3. SITE 1244[1]

Shipboard Scientific Party[2]

INTRODUCTION

Site 1244 (proposed Site HR1a) is located in 895 m of water on the eastern flank of Hydrate Ridge ~3 km northeast of the southern summit (see Fig. F1C, p. 51, in the "Leg 204 Summary" chapter). The three-dimensional (3-D) seismic data available from a Leg 204 site survey show that the bottom-simulating reflector (BSR) is present at a depth of ~125 meters below seafloor (mbsf) at this site (see Fig. F5, p. 55, in the "Leg 204 Summary" chapter). The temperature and pressure at the seafloor are well within the gas hydrate stability zone (GHSZ) (see Fig. F3, p. 53, in the "Leg 204 Summary" chapter), indicating that gas hydrates can exist within the entire stratigraphic section above the BSR if hydrate-forming gases are available in concentrations that exceed their in situ solubility. The 3-D seismic data also image a zone of incoherent seismic reflections that forms the core of Hydrate Ridge. At Site 1244, the top of this incoherent zone, denoted as Horizon AC in the seismic sections, is located at a depth of ~300 mbsf. This facies has been interpreted to comprise fractured accretionary complex material. Dipping, faulted, and strongly reflective strata interpreted to be an uplifted and deformed slope basin, overlie this facies.

The primary drilling objectives at this site were the following:

1. Determine the distribution and concentration of gas hydrate within the GHSZ;
2. Determine the nature of a pair of strong reflections (referred to as Reflections B and B') that underlies much of the eastern flank of Hydrate Ridge;
3. Determine the composition, structure, and fluid regime within the seismically incoherent unit underlying the stratified sediments; and
4. Sample the subsurface biosphere associated with these features.

Five holes were cored at Site 1244, and an additional hole was drilled (Fig. F1). Hole 1244A was abandoned when the first core overshot and did not record a mudline. Hole 1244B was abandoned at 53.1 mbsf after six cores were obtained because the bottom-hole assembly (BHA) had to be brought to the surface to retrieve a downhole instrument (Fugro piezoprobe) that had become unscrewed from the Schlumberger conductor cable. One advanced piston corer temperature (APCT) tool measurement was taken at 35.1 mbsf in this hole. Hole 1244C, which comprises 39 cores, began at the seafloor and continued to 334 mbsf. Special tools in Hole 1244C included three APCT tool (63, 82, and 110 mbsf), one Davis-Villinger Temperature Probe (DVTP) (64 mbsf), one Davis-Villinger Temperature-Pressure Probe (DVTPP) (150 mbsf), and three pressure core sampler (PCS) (120, 131, and 142 mbsf) runs. Hole 1244C was abandoned 17 m above the target depth of 350 mbsf when hole conditions suggested that a change from extended core barrel (XCB) to rotary core barrel (RCB) coring would be appropriate. We returned later in the leg to drill Hole 1244D to 380 mbsf, which was dedicated to wireline logging and seismic work. This was followed by Hole 1244E (cored to 136 mbsf), which was extensively sampled for geochemistry, hydrates, and microbiology, and Hole 1244F (cored to 24 mbsf), primarily for high-resolution microbiological sampling.
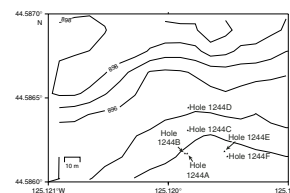
OPERATIONS

Transit from Victoria, British Columbia, Canada

The last line was cast away and the ship left Victoria, British Columbia, Canada, from Berth "B" north at 1017 hr on 11 July 2002. We passed the sea buoy and sent the pilot away at 1048 hr to get under way at full speed for Site 1244 (proposed Site HR1a). The transit to Site 1244 ended at 1348 hr on Friday, 12 July, when we began lowering the ship's thrusters and hydrophones. The initial site location was moved 50 m due west of the original coordinates.

Site 1244

Six holes were cored at Site 1244 (Table T1). Holes 1244A–1244D were drilled consecutively on 13–17 July; we returned to this site on 19 August to core Holes 1244E and 1244F. During both periods of time, wind speed was 4–21 kt (gusting to 25 kt), seas were 2–5 ft, swell was 6–10 ft, and the prevailing sea-surface current was from the north at ~0.5 kt.

The APCT tool was deployed ten times. In addition there were four DVTPP, two Fugro-McClelland piezoprobe, eight Ocean Drilling Program (ODP) PCS, and one Fugro Pressure Corer (FPC) runs at this site. No Hydrate Autoclave Coring Equipment (HYACE) Rotary Corer (HRC) cores were taken (see Table T4, p. 75, in the "Leg 204 Summary" chapter).

Hole 1244A was abandoned when the first core overshot and did not record a mudline.

Hole 1244B was spudded at 1325 hr on 13 July. The hole was cored using the advanced piston corer (APC), and one APCT measurement was taken at 35.1 mbsf in this hole. After collecting six APC cores (Cores 204-1244B-1H through 6H), the Fugro piezoprobe was deployed for its first test on the *JOIDES Resolution.* During this deployment, the

connection between the top of the tool, the electric logging line failed and the tool was left sitting on the landing ring in the BHA. We therefore had to pull out of the hole with the logging line and the drill string.

Hole 1244C was cored from the seafloor using the APC. The second Fugro piezoprobe test was conducted after Core 204-1244C-6H was taken at a depth of 53.0 mbsf. This was an excellent run with excellent data. A good decay curve was achieved after the tool sat for ~30 min in the formation. The drill string did not become stuck. There were three runs of the APCT tool in this hole, and the PCS was deployed three times. The cores were gassy (with methane), but no H_2S was detected. We continued to conduct continuous XCB coring operations in Hole 1244C until we reached the total depth (TD) in Hole 1244C at 333.5 mbsf and concluded coring because of hole instability. Examination of Core 204-1244C-39X (331.5 mbsf) and the initial chemical data from this depth suggested we had reached the deepest target (i.e., the accretionary complex). We had thus fulfilled the Pollution Prevention and Safety Panel (PPSP) requirement that we core the primary facies that we expected to encounter during logging while drilling (LWD) prior to proceeding with LWD at all sites. Acquiring LWD data at all of our sites at the beginning of the leg enabled us to use these data in concert with the previously collected 3-D seismic data to anticipate the nature of horizons prior to drilling and better plan the use of special tools for the rest of the leg.

Hole 1244D was spudded at 1505 hr on 16 July with the Anadrill LWD tools, to begin the LWD program of Leg 204. The LWD tools ($6^3/_4$-in collars) include the resistivity at the bit (RAB)-6 with $9^1/_8$-in button sleeve, measurement while drilling (MWD) (Powerpulse), Nuclear Magnetic Resonance porosity (NMR-MRP) tool, and Vision Neutron Density (VND) tool. Drilling proceeded at ~25 m/hr to TD (380 mbsf) without difficulty, and real-time data were transmitted to the surface at a rate of 6 Hz. Some extraneous pump noise affected the data transmission for 2–5 min after each pipe addition but caused minimal real-time data loss. Above TD, the tools were pulled out of the hole without rotating to ~355 mbsf to evaluate the effect of drilling motion on the NMR log. LWD tools and data were retrieved at the rig floor at ~1730 hr on 17 July. Total bit run was ~38 hr.

Hole 1244E was spudded at 0614 hr on 19 August and APC cored to 135.8 mbsf as a dedicated hole for microbiological studies and retrieval of cores under pressure. The PCS was deployed four times at this site. Core 204-1244E-3P (18.2–19.2 mbsf) was retrieved under pressure, but it had little or no core recovery. The other three PCS cores were successfully recovered from above the BSR, which at this site lies at ~124 mbsf. A deployment of the HYACINTH FPC tool in Hole 1244E resulted in the recovery of Core 204-1244E-8Y (FPC 9) at 50.70 mbsf. This core was recovered under full pressure and was successfully transferred from the autoclave into transfer and logging chambers (see **"Downhole Tools And Pressure Coring,"** p. 29). Other special tools at this site include six APCT measurements and two deployments of the DVTPP. Whirl-Paks and perfluorocarbon tracer (PFT) used for microbiology were obtained with Cores 204-1244E-4H, 5H, 7H, 9H, 10H, 12H, 13H, 14H, 16H, 17H, 18H, and 19H. Coring to refusal of the APC tool was followed with two wireline logging runs using the triple combination (triple combo) and Formation MicroScanner (FMS)-sonic tool and vertical, constant offset, and one to two stations of walkway vertical seismic profile (see **"Downhole Logging,"** p. 34).

Hole 1244F was APC cored to 24 mbsf to collect sediment samples for high-resolution microbiologic and geochemical sampling. Whirl-Paks and PFT were used in this hole.

LITHOSTRATIGRAPHY

Site 1244 is located on the eastern flank of southern Hydrate Ridge (see Figs. F1, p. 51, and F5, p. 55, both in the "Leg 204 Summary" chapter). Six holes were drilled at Site 1244, and five of these (Holes 1244A–1244C, 1244E, and 1244F) were cored. Hole 1244C was cored to 333.5 mbsf (142.5 m with the APC and 191 m with the XCB), and Hole 1244E was cored to 135.8 mbsf (APC). These two holes provide the primary data for this chapter. Holes 1244A, 1244B, and 1244F were cored to 9.5, 54.1, and 24.1 mbsf, respectively (primarily using the APC), and provide some additional data for the shallow part of the lithostratigraphic sequence at this site.

The sedimentary sequence at Site 1244 is dominated by clay and silty clay, with intervals of silt to very fine sand layers (Fig. F2). Recovered sediments were divided into three lithostratigraphic units based on the visual description of sedimentary structure, grain size, sediment color, smear slide analyses, and comparison with the 3-D seismic data. Other parameters, such as calcium carbonate content (expressed as $CaCO_3$ weight percent), total organic carbon (TOC), mineral information from X-ray diffraction (XRD), and physical property measurements of magnetic susceptibility (MS) and bulk density (see "Sediment Density from Multisensor Track and Moisture and Density," p. 26, in "Physical Properties") were also used to characterize lithologic changes. Correlation of the lithostratigraphic units defined here with the other Leg 204 sites is summarized in Figure F10, p. 60, in the "Leg 204 Summary" chapter.

F2. Lithostratigraphic summary, p. 45.

Lithostratigraphic Units

Lithostratigraphic Unit I

Intervals: Core 204-1244A-1H; Cores 204-1244B-1H through 6H; Core 204-1244C-1H through Section 8H-5; Core 204-1244E-1H through Section 12H-3; and Cores 204-1244F-1H through 4P

Depths: Hole 1244A: 0.00–9.99 mbsf; Hole 1244B: 0.00–54.10 mbsf; Hole 1244C: 0.00–69 mbsf; Hole 1244E: 0.00–77.6 mbsf; and Hole 1244E: 0.00–23.10 mbsf

Age: mid to late Pleistocene

The major lithology of lithostratigraphic Unit I consists of dark greenish gray (5GY 4/1) clay, with scattered thin layers of silty clay and fine silt (minor lithology) 3–17 cm thick (Fig. F2). The biogenic content of lithostratigraphic Unit I varies from 5% to 40% in the recovered sedimentary section. The sedimentary sequence observed in the cores is extensively fractured, likely the result of gas expansion upon core recovery. Cracks and voids increase throughout the lithostratigraphic unit from top to bottom and are particularly prominent features in Cores 204-1244C-3H through 7H. This gas expansion can increase the recovered length of the cores by as much as ~50 cm. Extensive whole-round sampling of the first three cores in Hole 1244C resulted in the removal of a substantial portion of the recovered section before it reached the core
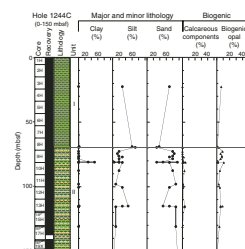
description table. However, Cores 204-1244A-1H through 3H and 204-1244E-1H through 3H were used to fill in the sampled intervals so that a complete description could be made.

Smear slide analysis of the mineralogic components of lithostratigraphic Unit I indicates that the major lithology (dark greenish gray clay) typically consists of 5% quartz, 10% feldspar, and 70% clay minerals (Fig. F2). Some silty clay samples (minor lithology) contain a minor amount of sand-sized grains (2%). Glauconite (2%), pyrite (3%), and volcanic glass (3%) are present as accessory minerals in these layers. Biotite, muscovite, and micronodules are also present in trace amounts (~1%–3%) throughout lithostratigraphic Unit I. Authigenic calcite needles, ranging in length from 1 to 5 mm, were estimated to compose ~80% of Sample 204-1244E-4H-7, 45 cm, and were identified during visual observation by the presence of light-colored patches and bands (1–4 cm thick) within the sediment in the upper 20 mbsf in both Holes 1244C and 1244E. In certain, but not all, cases the light-colored authigenic carbonate-rich sediments surrounded a cemented carbonate nodule that ranged in diameter from 1 to 4 cm (Fig. F3).

Dispersed patches of slightly lighter-colored sediment, not associated with carbonate precipitates, were observed in the middle of lithostratigraphic Unit I (Sample 204-1244C-4H-3, 35–38 cm, and interval 4H-4, 17–47 cm). Based on smear slide analyses, these color changes do not reflect a major change in mineralogy. However, color changes from dark greenish gray (5GY 4/1) to dark gray (N3) do occur throughout the core because of variations in the amount of sulfides present. The presence of sulfide precipitates (<1 mm) also helps to identify bioturbated zones within the sedimentary section. Nodular sulfide precipitates from Sections 204-1244C-5H-4 and 204-1244B-3H-5 were analyzed by XRD and found to be composed of pyrrhotite.

Calcitic components were also identified in XRD analyses of Samples 204-1244C-1H-3, 28–29 cm; 1H-3, 74–75 cm; 2H-4, 34–35 cm; and, especially, 4H-3, 26–27 cm. Although XRD analyses are less accurate for quantitative comparisons, variations in the height of the d(104) calcite spacing documents the pattern of downhole changes in the abundance of biogenic and authigenic carbonate constituents. Changes in the peak position of d(104) values of 3.035 to 3.018 indicate low-Mg calcite. Calcite was identified in Samples 204-1244B-1H-3, 73–74 cm; 1H-3, 137–138 cm; and 204-1244C-6H-4, 74–75 cm, where it is abundant (23%) in the silt fraction of silty clay and silt layers.

The biogenic microfossil content of lithostratigraphic Unit I is dominated by diatoms that compose ~5% of the major lithology. Silicoflagellates, radiolarians, sponge spicules, and organic debris are typically only present in trace amounts (~1%) but can exceed 5% of the sedimentary components, locally (Fig. F4). Calcareous nannofossils and foraminifers compose, on average, 10%–20% of the minor lithology in the upper 20 mbsf of lithostratigraphic Unit I in Hole 1244E and are all but absent between 20 and 77 mbsf (Fig. F2). Shell fragments and sponge spicules were noted in the visual core descriptions throughout lithostratigraphic Unit I and are present in all holes at Site 1244.

Lithostratigraphic Unit II

Intervals: Sections 204-1244C-8H-6 through 29X-CC and 204-1244E-12H-4 through 19H-CC
Depths: Hole 1244C: 69.00–245.00 mbsf; and Hole 1244E: 77.60–140.79 mbsf

F3. Carbonate nodule, p. 48.
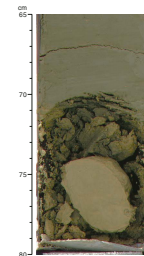
F4. Biogenic opal–rich clay, p. 49.
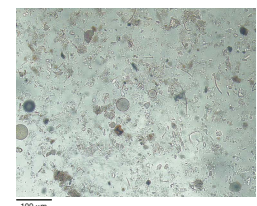
Age: early to mid-Pleistocene

The distinction between lithostratigraphic Units I and II is based primarily on the increased presence of very fine sand layers in Unit II (Fig. F2). Lithostratigraphic Unit II is composed of dark greenish gray (5GY 4/1) silty clay. This silty clay is interlayered with lighter-colored layers of fine sand and coarse silt, which we interpret as turbidites. The major sedimentary components of lithostratigraphic Unit II are clay minerals, quartz, feldspar, and muscovite. The biogenic component, which consists of mainly siliceous microfossils (sponge spicules, silicoflagellates, and diatoms), typically composes 3%–8% of the total sedimentary components in Holes 1244C and 1244E (Fig. F2). Extensive degassing cracks and voids, often associated with silt or sand layers, are observed throughout the upper 50 m of lithostratigraphic Unit II.

High-frequency turbidites, the bases of which contain fine to very fine sand that grades to silt and clay, characterize the upper 77 m of lithostratigraphic Unit II (69–146 mbsf) (Fig. F5). These turbidites range in total thickness from 0.2 to 2.1 m (coarse base to fine tail of turbidite), with an average thickness of 0.8 m. Between 146 and 245 mbsf, the frequency of the turbidites drops significantly. Within this interval, the turbidites range from 1 to 20 cm thick and the bases of individual events are separated by ~8 m on average. The sand and silt layers that form the sharp erosional bases of the turbidite sequences are commonly 1 to 3 cm thick, although occasionally, they reach 30 cm thick. The turbidites grade upward to become dominated by homogeneous silty clay and clay. Above many of the sand and silt bases, the silt and silty clay layers occur in thin (~1 mm) finely spaced layers over intervals that span as much as 15 cm. Sulfide mottles and halos, which may indicate a chemical-reaction front linked to bioturbation intensity, are preserved in the hemipelagic sediments between turbidites and help to distinguish these sediments from the graded turbidite tails. The turbidite tail in Section 204-1244C-13H-4 is characterized by a light gray homogeneous silty clay ~70 cm thick, whereas the uppermost hemipelagic layer, which consists of highly bioturbated clay with dark gray sulfide mottles, is ~30 cm thick (Fig. F5). MS data also show these graded turbidites throughout this interval in lithostratigraphic Unit II (see "Magnetic Susceptibility," p. 27, in "Physical Properties"). Of particular interest are the large MS spikes near ~170 mbsf, which correspond to seismic Horizon B and turbidites in the core.

Smear slide analyses indicate that the coarse fraction (major and minor lithologies) of the sampled sediments is dominated by silt-sized grains and typically composes 10%–35% (rarely from 50% to 70%) of the total sediment. Sands, when present, compose only a few percent (1%–2%) of the major lithology, although locally (e.g., in the minor lithology of Hole 1244E) they were observed to compose as much as 30%–50% (e.g., Samples 204-1244C-9H-6, 143 cm, and 204-1244E-13H-1, 51 cm, respectively). The mineralogy of the silt- and sand-sized fraction in both the major and minor lithologies is mainly dominated by quartz, feldspar, muscovite, and biotite. Glauconite (up to 8%) is observed in the silt layers of smear slide Samples 204-1224C-8H-6, 147 cm; 9H-6, 143 cm; 9H-7, 81 cm; and 13H-4, 115 cm. Pyrrhotite-rich layers are often present from 75 to 110 mbsf (e.g., Cores 204-1224C-9H, 10H, and 12H), occasionally representing up to 3% of the coarse fraction. Dark gray (N3) sulfide-rich bands (10–40 cm thick) with pyrrhotite nodules (up to 0.4 cm in diameter) are often observed in Cores 204-1244C-23X through 29X.

F5. Turbidite, p. 50.
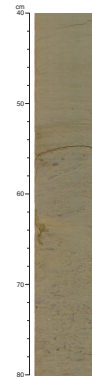
Core 204-1244C-27X contains a 60-cm-thick volcanic ash horizon at 216 mbsf (Fig. F6), with 50% glass content identified in the smear slide (Sample 204-1224C-27X-1, 8 cm). Most glass shards are very fine sand size and are present as both pristine, unaltered shards and altered shards (now clay minerals) (Fig. F7). XRD analyses show that glass, quartz, feldspar, muscovite, and clay minerals are present throughout this layer (Fig. F8). The ash layer displays a sharp subhorizontal base and is clearly correlated with a prominent peak on the MS and density data (see "Magnetic Susceptibility," p. 27, and "Sediment Density from Multisensor Track and Moisture and Density," p. 26, both in "Physical Properties"). This layer corresponds to the B′ reflector identified in the 3-D seismic reflection data and is also found at Site 1246 west of Site 1244.

Lithostratigraphic Unit III

Interval: Sections 204-1244C-30X-1, 30 cm, through 39X-CC
Depth: 244.70–333.50 mbsf
Age: late Pliocene to early Pleistocene

Lithostratigraphic Unit III is composed of hard, indurated silty clay and clayey silt with scattered glauconite sand layers. The silty clay is predominantly dark greenish gray (5GY 4/1); however, lighter variations in color are present in Cores 204-1244C-32X through 35X and typically indicate the presence of calcareous sediments (positive reaction to HCl) (Fig. F9). Core 204-1244C-36X exhibits a range of colors, from very dark gray (N3) to dark olive gray (5Y 3/2) to light bluish gray (5B 5/1). Lithostratigraphic Unit III is distinguished from lithostratigraphic Unit II by its general lack of sulfide precipitates, bioturbation, and silt layers as well as its higher state of lithification. The Unit II/III boundary lies directly below a silt layer at 244.5 mbsf in Hole 1244C, which represents the lowermost major turbidite in lithostratigraphic Unit II. Additional evidence for this unit boundary is seen in the bulk density data, which indicate a significant shift in physical properties below 245 mbsf (see "Sediment Density from Multisensor Track and Index Properties," p. 26, in "Physical Properties"). There is also a change to lower total calcium carbonate content at the same depth and a correlation with the onset of borehole breakouts imaged with the LWD-RAB tool (see "Downhole Logging," p. 34).

Core recovery in lithostratigraphic Unit III was high (90%), although the cores were generally highly disturbed, with drilling biscuits heavily fractured, making primary sedimentary structures difficult to identify. Bedding laminations, delineated by subtle color and grain size changes, were observed within intact drilling biscuits in Cores 204-1244C-32X, 35X, and 36X, and zones of bioturbation ranging from 3 to 10 cm thick were identified in intervals 204-1244C-32X-1, 44–54 cm; 32X-6, 114–118 cm; and 33X-6, 95–98 cm. Only one interval of mottled sulfide was identified in the entire unit (interval 204-1244C-30X-4, 65–145 cm).

The major sedimentary components of lithostratigraphic Unit III (only cored in Hole 1244C) are primarily clay minerals, quartz, and feldspar. Clay-size grains typically compose 70% of the sedimentary components, although local variations occur throughout the lithostratigraphic unit (Fig. F2). Pyrrhotite, biotite, and muscovite occur as accessory minerals in Cores 204-1244C-31X, 32X, 33X, and 35X. The upper sequence (from 255 to 299 mbsf) is rich in calcite, which constitutes as much as 61% of the sediment in Section 204-1244C-35X-5. The

F6. Ash layer, p. 51.
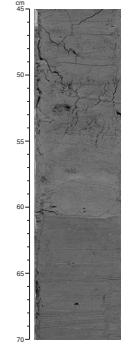
F7. Glass shards, p. 52.
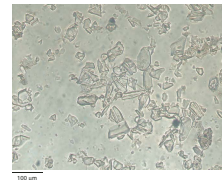
F8. XRD profile, p. 53.
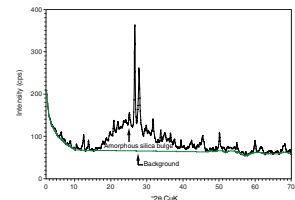
F9. Carbonate color change, p. 54.
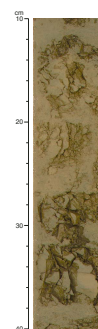
calcite is present as uniform needles (5 to 10 mm long) in smear slides and is interpreted to be authigenic from the regularity of its shape and size (Fig. F10). The carbonate silt is present in patches rather than layers.

The lowermost 43 m of lithostratigraphic Unit III contains glauconite in two discrete silty layers and dispersed among the dominant silty clay lithology. The glauconite grains, which are present as both pristine, unaltered green and oxidized brownish forms, tend to be rounded and range in size from <0.0039 mm (clay fraction) to 0.275 mm (medium sand) (Fig. F11).

The biogenic components (diatoms, foraminifers, nannofossils, silicoflagellates, sponge spicules, and organic debris) of lithostratigraphic Unit III compose 1%–30% of the total sedimentary components (Fig. F2). Diatoms are abundant, composing as much as 25% of the total sediment, and are found in association with authigenic carbonate silt layers in Samples 204-1244C-35X-4, 19 cm, and 35X-5, 16 cm. Foraminifers are only found in Cores 204-1244C-35X and 36X.

Quartz, feldspar, and mica are all present in varying amounts throughout the lithostratigraphic unit, depending on the overall grain size. Quartz content ranges from 1% in a clay horizon at 264 mbsf (Sample 204-1244C-32X-1, 44 cm) to 30% in a silt layer directly below at 265.04 mbsf (Section 204-1244C-32X-1). Feldspar follows the same trend and ranges from 1% to 14% of the total sediment.

Carbonate and gypsum nodules are also found in lithostratigraphic Unit III. Carbonate nodules are present in Sections 204-1244C-34X-1 and in 35X-1 (283.9 and 293.2 mbsf, respectively) in clay-rich layers with higher biogenic carbonate contents. The surrounding sediment is highly fractured and disturbed from the core-splitting process, which drags the rigid carbonate nodules through the surrounding sediment. Unlike the carbonates, gypsum nodules are small (<2 mm) and are typically found within hard clay fragments (Sections 204-1244C-35X-6, 38X-1, 38X-4, and 38X-CC).

A hard silty clay breccia layer containing angular clasts up to 2 cm in size is present toward the base of lithostratigraphic Unit III at 307.65 mbsf (interval 204-1244C-36X-4, 55–100 cm). The change in lithification from clay to claystone and the shift in the bulk density data at the lithostratigraphic Unit II/III boundary suggest a transition into the deeper accretionary complex, although alternately, this layer may simply represent an unconformity.

Sedimentary Evidence of Gas Hydrate

Gas hydrate was sampled in cores from lithostratigraphic Unit I in both Holes 1244C and 1244E. The uppermost hydrate sample taken from Hole 1244C was at 63 mbsf (Core 204-1244C-8H); that from Hole 1244E was at 50 mbsf (Core 204-1244E-7H). However, Core 204-1244C-7H (at ~59 mbsf) contains a linear zone of mousselike textured sediment that crosscuts bedding at an angle of ~45° (Fig. F12). A review of the infrared (IR) thermal images from this interval shows a thermal anomaly of –5.1°C (see "Physical Properties," p. 24) (Table T2), which suggests that gas hydrate may have dissociated within this interval prior to splitting the core liner. Similar indications of dissociated gas hydrate are present in Cores 204-1244C-6H and 7H. Gas hydrate was also sampled from intervals 204-1224C-8H-1, 47–52 cm; 8H-5, 50–80 cm; and 10H-2, 70–110 cm, in lithostratigraphic Unit II. Additionally, thermal anomalies were matched to disrupted sedimentary structures in

F10. Calcite needles, p. 55.
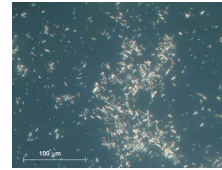
F11. Glauconite, p. 56.

F12. Mousselike texture and sediment disruption, p. 57.
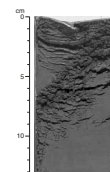
T2. Presence of gas hydrate based on IR images, p. 105.

lithostratigraphic Unit II, indicating that not all the gas hydrate recovered in this lithostratigraphic unit was sampled. Smear slide analyses of the mousselike textures attributed to gas hydrate–related disruption of the sediment do not indicate that the hydrate prefers to form in sediment with a different composition than that of the dominant lithology. However, it should be noted that the mousselike texture associated with hydrate dissociation may itself be biased toward clay sediments.

Environment of Deposition

Lithostratigraphic Unit III encompasses the oldest sediments recovered at Site 1244 and is composed of well-lithified claystone. Examination of the 3-D seismic data indicates that this unit lies within the deeper accretionary complex beneath Hydrate Ridge (see Fig. F5, p. 55, in the "Leg 204 Summary" chapter). This indurated claystone may have originated from either a slope basin or abyssal plain environment of deposition and has since been uplifted and deformed during the tectonic evolution of the ridge. The upper boundary of lithostratigraphic Unit III is well characterized on the 3-D seismic profiles as an abrupt change in reflectivity and reflects the change from the deeper accretionary complex sediments, which form the core of Hydrate Ridge, to the overlying slope basin sediments of lithostratigraphic Units I and II.

A thick ash layer (>60 cm thick), bearing >40% detrital volcanic glass shards, is present near the base of lithostratigraphic Unit II (Horizon B′) and indicates a volcanic influence near the source area for this deposit. The detrital nature of the glass in this deposit suggests that the ash, which was probably derived from the Cascade volcanic arc, was delivered to the continental shelf by rivers and, subsequently, transported to the lower slope and/or abyssal plain by turbidity currents. The mid-Holocene Mt. Mazama (Crater Lake) eruption, air fall ash distribution, and spatial distribution of volcanic glass–bearing turbidites across the Cascadia abyssal plain (Nelson et al., 1968) may serve as an analog for this type of process.

Overlying the volcanic glass in lithostratigraphic Unit II is a series of turbidites that are typically fine grained (silt to fine sand) and thin (1–3 cm) at their bases and contain a thicker (up to 80 cm) clay tail near their upper extent. These characteristics are suggestive of a distal turbidite facies, which could have originated from either (1) the continental shelf, resulting in fine-grained deposition near the lower slope and abyssal plain, or (2) the continental slope, where slumping or turbidity currents are sourced in the local slope region and fed by bathymetric highs composed of uplifted and accreted fine-grained abyssal plain deposits. Because both mechanisms result in fine-grained turbidite deposition, determining the source region for these deposits within the accretionary wedge is difficult. However, because of the lack of modern or ancient submarine canyons along this part of the margin, a local source region for these turbidites seems more likely. That is, the uplifted and folded sediments of the lower slope must have shed their sediments during slope failure and deposited these recycled sediments into an actively forming slope basin.

The boundary between lithostratigraphic Units I and II is characterized by a dramatic decrease in the presence of turbidites in the younger lithostratigraphic unit. This difference in turbidite frequency suggests that one or both of the above mechanisms may have operated during the deposition of Unit II (turbidites common), whereas only one, or potentially neither, was dominant during the deposition of Unit I, result-

ing in mainly hemipelagic clay accumulation. Alternatively, the higher frequency of turbidites in lithostratigraphic Unit II could represent increased slumping along the lower slope during a sea level lowstand. Lower sea level would result in more sediment delivery to the middle and lower slope, potentially causing oversteepening of slopes and sediment failure. A lower sea level might also destabilize gas hydrate on the slope, causing sediments to fail. Ultimately, better age control within this sedimentary section may help determine which mechanism is responsible for the observed change in turbidite frequency.

Three-dimensional seismic reflection data suggest that at Site 1244 both lithostratigraphic Unit I and II lie within the same deformed and uplifted slope basin sedimentary sequence that was cored at Site 1246 and potentially at Site 1245 (above Horizon Y) (see Fig. F5, p. 55, in the "Leg 204 Summary" chapter). Seismic Horizons B and B′ are present within lithostratigraphic Unit II at both Sites 1244 and 1246 (see Fig. F11, p. 61, in the "Leg 204 Summary" chapter) and have the same lithologic signatures; Horizon B contains a thick turbidite couplet and Horizon B′ is a volcanic glass–rich horizon. Neither Horizon B nor B′ is present at Site 1245; however, on the 3-D seismic data, Horizon Y is nearly coincident with the BSR at the bottom of Site 1246, suggesting deeper coring at Site 1246 might have recovered it and provided a marker horizon to tie Sites 1245 and 1246. The stratigraphy at Sites 1245 and 1246 in both lithostratigraphic Units I and II is also very similar, adding support for the correlation among Sites 1245, 1246, and 1244.

BIOSTRATIGRAPHY

Six holes were drilled at Site 1244, and five holes were cored. Hole 1244C contains the most complete sequence, a 333-m-thick upper Pliocene–Quaternary sedimentary sequence. The biostratigraphy determined for Site 1244 was based on an examination of all core catcher samples and a few of the samples taken from cores at Hole 1244C.

Diatoms

Diatoms are common to abundant and moderately to well preserved in the interval from the seafloor to 120 mbsf, whereas diatom abundances below 120 m to the bottom of Hole 1244C vary significantly from barren to abundant. Diatom assemblages at Hole 1244C are dominated by species such as *Stephanopyxis* spp., *Neodenticula* spp., and *Thalassionema nitzschioides*. A few warm-water taxa, such as *Hemidiscus cuneiformis, Fragilariopsis doliolus,* and *Thalassiosira oestrupii,* are frequently present (Table T3).

The interval between the seafloor and Sample 204-1244C-9H-CC (0–82.16 mbsf) contains *Neodenticula seminae* but lacks *Proboscia curvirostris*. This interval was assigned to North Pacific Diatom Zone (NPD) 12 (*N. seminae* Zone). The last occurrence (LO) of *P. curvirostris* was found in Sample 204-1244C-10H-CC (91.13 mbsf), marking NPD 12/11 (*P. curvirostris* Zone). A fragment of *Actinocyclus oculatus* was found in Sample 204-1244C-25X-CC (206.04 mbsf); thus, the LO of *A. oculatus* is tentatively placed between this sample and Sample 204-1244C-24X-CC (195.95–206.04 mbsf). Further study is needed to confirm this LO because, at present, no more than one fragment of *A. oculatus* has been found from the Hole 1244C samples. The interval between these two

T3. Bioevents, p. 107.

LOs (91.13–195.5 mbsf) was assigned to NPD 11 (*P. curvirostris* Zone). The LO of *Neodenticula koizumii* was found in Sample 204-1244C-34X-CC (292.05 mbsf). The interval between this LO and the LO of *A. oculatus* (206.64–283.17 mbsf) was assigned to NPD 10 (*A. oculatus* Zone). The first occurrence (FO) of *P. curvirostris* was placed in Sample 204-1244C-28X (235.24 mbsf) in NPD 10. The interval between the LO of *N. koizumii* and the bottom of Hole 1244C (292.05–333.64 mbsf) contains *N. koizumii* but lacks *Neodenticula kamtschatica* and was assigned to NPD 9 (*N. koizumii* Zone). The FO of *N. seminae* was placed in Sample 204-1244C-36X-CC (312.34 mbsf) from the middle part of this zone. The age of the bottom of Hole 1244C was estimated to be 2.4–2.7 Ma, based on the presence of *N. koizumii* and the absence of *N. seminae* and *N. kamtschatica* in Sample 204-1244C-39X-CC (333.64 mbsf).

Calcareous Nannofossils

Calcareous nannofossils from Hole 1244C were investigated in smear slides from core catcher samples and from selected samples to better constrain the biohorizons. Calcareous nannofossils are barren or of trace abundance for the majority of samples investigated (e.g., between Samples 204-1244C-2H-CC and 7H-CC [15.46–62.59 mbsf], 12H-CC and 25X-CC [110.38–206.04 mbsf], 30X-CC and 34X-CC [253.5–292.05 mbsf], and 38X and 39X [331.70–333.64 mbsf]). Rare to few and moderately preserved calcareous nannofossils were observed in samples in a few intervals (e.g., between Samples 204-1244C-8H-CC and 11H-CC [71.6–100.64 mbsf], 26X-CC and 29X-CC [214.31–244.54 mbsf], and 35X and 37X [302.70–314.89 mbsf]). The calcareous nannofossil biostratigraphy determined for Site 1244 was mainly based on the nannofossil record deduced from these samples (Table T3).

A Pliocene–Quaternary calcareous nannofossil assemblage was found in the 333-m sequence from Hole 1244C. This assemblage is characterized by dominance of cold-water species (e.g., *Coccolithus pelagicus* and *Gephyrocapsa carribeanica*) and by the common to rare presence of cosmopolitan species, such as several small-sized *Gephyrocapsa* species. Warm-water species (e.g., species of *Discoaster*) are absent in the assemblage. For the same reason, many Pliocene and Quaternary age-diagnostic species (e.g., various *Discoaster* species, *Sphenolithus abies,* *Helicosphaera sellii,* and *Reticulofenestra asanoi*) are absent too.

The poor preservation of calcareous nannofossils in sediments and the absence of a number of age-diagnostic species together made the biostratigraphic determination based on calcareous nannofossils very difficult. However, several Pliocene and Quaternary age diagnostic species, such as *Emiliania huxleyi, Pseudoemiliania lacunosa,* and *Calcidiscus macintyrei,* are rarely present in relatively good nannofossil samples from Hole 1244C, allowing us to recognize a few nannofossil events.

Since calcareous nannofossils are barren or found in trace amounts in sediments from the interval from 15.46 to 62.59 mbsf, the presence of *E. huxleyi* was only observed in Samples 204-1244C-1H-CC and 8H-CC, and this interval was assigned to the Zone NN21. Sample 204-1244C-9H-CC contains a few *Gephyrocapsa* species but lacks *E. huxleyi* and *P. lacunosa;* this sample was assigned to Zone NN20. The LO of *P. lacunosa* was found in Sample 204-1244C-10H-CC (91.13 mbsf), which marks the NN19b/NN20 zonal boundary. Sediments are barren or have trace abundances of calcareous nannofossils below 91.13 down to 187.26 mbsf. The dominance of various small *Gephyrocapsa* spp. in the calcareous nannofossil assemblage was observed only in one sample

(Sample 204-1244C-24X-CC [195.95 mbsf]) that contains rare calcareous nannofossils. This sample can be definitely assigned to a part of the mid-Pleistocene small *Gephyrocapsa* spp. Acme Zone (1.0–1.2 Ma). However, considering that a ~100-m interval above 195.95 mbsf lacks or contains poor nannofossils, it was not possible to accurately assign this sample to the top or to the bottom of the small *Gephyrocapsa* spp. Acme Zone, so an age interval of 1.0 to ~1.2 Ma was estimated for this sample (Table T3). *C. macintyrei* is frequently present in samples that contain rare and well-preserved calcareous nannofossils from 214.31 to 312.32 mbsf. The LO of *C. macintyrei* in Sample 204-1244C-26X-CC (214.31 mbsf) indicates an age of 1.59 Ma (NN19) for this stratigraphic level. Common *Gephyrocapsa lumina* is present continuously from 214.31 down to 235.25 mbsf; the FO of *G. lumina* (1.67 Ma) was placed at the level of 235.25 mbsf.

Based on calcareous nannofossils, the Pliocene/Pleistocene boundary (1.77 Ma) (Berggren et al., 1995) is located below the FO of medium-sized *Gephyrocapsa* spp. (>4 µm). The FO of a few medium-sized *Gephyrocapsa* spp. was observed in Sample 204-1244C-29X-CC (244.54 mbsf) in the 333-m sequence of Hole 1244C, indicating a Quaternary age for sediments at 244.54 mbsf. Based on this estimate, the Pliocene/Pleistocene boundary (1.77 Ma) was placed just below 244.54 mbsf.

Samples below 244.54 mbsf are generally barren of calcareous nannofossils, except for three samples (Samples 204-1244C-35X-CC, 36X-CC, and 37X-CC), which yielded rare and moderately preserved calcareous nannofossils. The calcareous nannofossil assemblage found in these samples is composed of *C. pelagicus, P. lacunosa, Reticulofenestra productus, Reticulofenestra minuta,* and *Reticulofenestra minutula,* indicating these samples are Pliocene in age. This assemblage lacks diagnostic species of Pliocene (e.g., a number of *Discoaster* and *Sphenolithus* species), which are warm-water species and absent in high latitudes and cold-current regions. The absence of these age-diagnostic species leads to difficulty in subdividing the lower part of the sequence in Hole 1244 by means of calcareous nannofossil events.

Reticulofenestra ampla was found in Samples 204-1244C-36X-CC and 37X-CC (314.89–312.34 mbsf); thus, the LO of *R. ampla* (2.78 Ma) was placed at 314.89 mbsf.

Discoaster spp. are absent in almost the whole sequence at Hole 1244C. However, a few *Discoaster* variabilis are present in Sample 204-1244C-37X-CC (314.89 mbsf). According to Perch-Nielsen's study (1985), *D. variabilis* disappears in the lower upper Pliocene Zone NN16; however, discoasters disappear before the LO of *Reticulofenestra pseudoumbilicus* in high latitudes. Furthermore, a few specimens of an the lower Pliocene event marker, *R. pseudoumbilicus,* are also present in Sample 204-1244C-37X-CC; the LO of *R. pseudoumbilicus* (3.82 Ma) marks the top of the lower Pliocene Zone NN15 (Martini and Müller, 1986). Unfortunately, the two samples below 314.89 mbsf are barren of calcareous nannofossils, and we were unable to track down the presence of this species in these deeper sediments. There are two possibilities for interpreting the presence of *D. variabilis* and *R. pseudoumbilicus* at 314.89 mbsf—either assigning sediments at 314.89 to the lower Pliocene Zone NN15 or considering them as reworked fossils in upper Pliocene sediments. There is a lack of evidence to support either of these possibilities based on the nannofossil data obtained during the cruise.

However, based on the evidence derived from both the calcareous nannofossil assemblage and these age-diagnostic species, sediment at

the bottom of Hole 1244C was roughly assigned to the lower Pliocene Zone NN15 and the early Pliocene Zone NN16.

Summary

Twelve microfossil (five diatom and seven nannofossil) events were recognized at Site 1244 (Table T3). The age-depth plot shows that biohorizons from these two fossil groups generally agree well with each other (Fig. F13). The Pleistocene/Pliocene boundary is located between 244.54 and 253.50 mbsf based on the FO of medium *Gephyrocapsa* spp. (Table T3). The age of the bottom of Hole 1244C is estimated to be 2.4–2.7 Ma (based on diatoms) and is estimated to be older than 2.8 Ma (based on nannofossils). Both estimations indicate that the bottom of Hole 1244C is of late Pliocene age, although some small discrepancies regarding the age remain.

The linear sedimentation rates at Site 1244 were calculated based on biostratigraphic data (Table T3). The sedimentation rates are estimated to be 27 cm/k.y. for the interval from the top of Hole 1244C to 80 mbsf, 6 cm/k.y. for the interval from 80 to 90 mbsf, 19 cm/k.y. for the interval from 90 to 200 mbsf, 7 cm/k.y. for the interval from 200 to 240 mbsf, 12 cm/k.y. for the interval from 240 to 290 mbsf, and 7 cm k.y. for the interval 290 mbsf to the bottom of Hole 1244C (Fig. F13). The sedimentation rate is generally higher above than below 200 mbsf.

INTERSTITIAL WATER GEOCHEMISTRY

A total of 113 whole-round samples were collected for interstitial water (IW) analyses at this site (12 samples from Hole 1244B, 72 samples from Hole 1244C, 23 samples from Hole 1244E, and 6 samples from Hole 1244F). Routine samples were collected at a frequency of approximately two whole-round samples per core in the upper 150 m, followed by a sampling resolution of one whole-round sample per core below this depth. A higher-resolution sampling protocol was used within the anaerobic methane oxidation (AMO) zone in Hole 1244C (approximately two whole-round samples per section) in a coordinated program with the shipboard microbiologists. The purpose of this high-resolution sampling was threefold: (1) to clearly define biogeochemical zones within the sedimentary sequence, (2) to estimate the presence and abundance of gas hydrate within the GHSZ using interstitial chloride concentration as proxy for the presence of gas hydrate, and (3) to provide supporting data for studies on the microbial dynamics of the sulfate/methane interface (SMI). The IW geochemistry data are tabulated in Table T4 and are illustrated in Figure F14.

Chloride Concentration and the Presence of Gas Hydrate

The downhole chloride content exhibits overall features similar to those previously observed in IW samples recovered from gas hydrate–bearing sediments during ODP drilling (e.g., Cascadia margin: Westbrook, Carson, Musgrave, et al., 1994; Blake Ridge: Paull, Matsumoto, Wallace, et al., 1996; Chile Triple Junction: Behrmann, Lewis, Musgrave, et al., 1992). The most striking feature of the chloride profile at Site 1244 is the zone defined by excursions to significantly lower values (519 mM) in the GHSZ, followed by a linear decrease from 70 mbsf to

F13. Age-depth plots, p. 58.
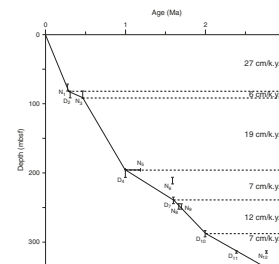
T4. IW data, p. 108.

F14. Concentration profiles of various dissolved species, p. 59.
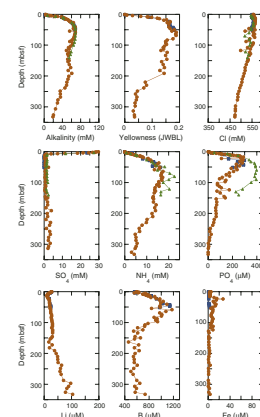
the bottom of the hole, where the chloride concentration is 472 mM (Fig. F15).

The linear profile of dissolved Cl^- is strongly suggestive of diffusion between low-salinity fluids in the accretionary wedge and a chloride concentration of 540 mM at 70 mbsf, apparently with a negligible advective component. The onset of low-chloride fluids corresponds to the depth of seismic Reflector AC, which is thought to represent the top of the accreted sedimentary wedge (see "Introduction," p. 1). The high lithium content measured in the deeper samples recovered from this site is consistent with a source deeper than 1 km, which is similar to the interpretation based on IW data from Sites 889 and 890 (Fig. F16) on the Cascadia margin off Vancouver Island (Kastner et al., 1995). Inferences about the source depth of low-chlorinity, high-lithium fluids are supported by field and laboratory observations that document remobilization of lithium from aluminosilicates at temperatures ranging from 70° to 100°C (Edmond et al., 1979; Seyfried et al., 1984). The geothermal gradient for this site is 61°C/km (see "Downhole Tools and Pressure Coring," p. 29).

Superimposed on the IW freshening trend that results from contact with the deeper fluids, excursions with anomalous low-chlorinity values above the BSR are thought to represent gas hydrate dissociation during core retrieval and can be used to estimate the amount of hydrate in the sediments (Hesse and Harrison, 1981; Kastner et al., 1995; Behrmann, Lewis, Musgrave, et al., 1992; Paull, Matsumoto, Wallace, et al., 1996; Hesse, 2003). The uncertainties in these estimates arise from a paucity of information on (1) the in situ chlorinity values of the IW, (2) the chloride content potentially trapped within the pores of the gas hydrates, (3) the spatial sampling bias, and (4) fluid transport and diffusion rates.

Because we have no data on the amount of Cl^- sequestered by the hydrate cage, we have assumed here (as has been previously done) that hydrate formation excludes all dissolved ions and that dissociation of hydrate will release water with a chloride concentration of 0 mM.

Gas hydrate is present at irregular intervals within the GHSZ, as evidenced by the recovery of gas hydrate samples and thermal anomalies seen in IR data (see "Infrared Scanner," p. 25, in "Physical Properties"). Because of this irregular gas hydrate distribution, uncertainties are introduced into gas hydrate distribution estimates based on chloride concentration data. For example, in Core 204-1244C-7H, the IR data indicate the presence of hydrate at 57–58 mbsf (prior to cutting the core) but no hydrate was actually sampled from this core. The IW sample at 54.8 mbsf does indeed show an excursion to 514 mM, whereas the sample collected at 64.37 mbsf shows no significant anomaly (Cl^- = 556 mM). Hydrate was sampled in Section 204-1244C-8H-2, but an IW sample that was collected ~5 m away from it shows no chloride anomaly. Another sample of nodular hydrate was recovered in Section 204-1244C-10H-2; in this case, the IW sample collected from sediments adjacent to the gas hydrate has a chloride concentration of 533 mM. Similarly, hole-to-hole variability in the predicted presence of gas hydrate based on the chloride data reflects lateral heterogeneity in hydrate distribution as well as limitations of sampling resolution, which, at two samples per core, is not enough to identify every occurrence of gas hydrate. For example, a chloride anomaly recorded at ~70 mbsf in Hole 1244E was not observed in Hole 1244C (Fig. F15).

The lower sampling resolution in Hole 1244E does not allow identification of the majority of gas hydrate horizons observed in Hole

F15. Chloride concentration profile, p. 61.
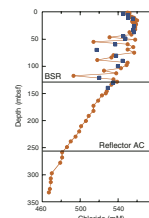
F16. Profile of the lithium to chloride concentration ratio, p. 62.
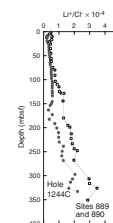
1244C. In addition to the whole-round samples collected on the catwalk, we collected three IW samples from the working half of Core 204-1244E-8Y. This core was collected with the FPC, and the density logs were obtained under pressure to image the presence of gas hydrate (see "HYACINTH Pressure Coring and Logging," p. 32, in "Downhole Tools and Pressure Coring"). The chloride analyses, listed in Table T5, show a well-defined anomaly in Sample 204-1244E-8Y-1, 10–15 cm, which was collected from the zone where density anomalies indicate the presence of gas hydrate.

It is difficult to determine the background in situ Cl⁻ content, particularly in the upper 70 m of the sedimentary sequence. Chloride concentration from 70 mbsf to the BSR form a linear trend that extends below 250 mbsf, and we have used this trend as a baseline for in situ Cl⁻ concentration, as shown in Figure F17. However, in the upper 15 m of Site 1244, there is an increase in dissolved Cl⁻ equivalent to 0.84 mM/m. A similar increase in dissolved Cl⁻ was reported at hydrate-bearing sites from the Blake Ridge (Paull, Matsumoto, Wallace, et al., 1996) and the Cascadia margin (Kastner et al., 1995). Two possible scenarios could account for this increase. It might represent a diffusion gradient resulting from ion exclusion during gas hydrate formation. Alternatively, the positive gradient in the shallow samples might reflect nonsteady-state conditions induced by glacial–interglacial salinity variations driven by changes in global ice volume (McDuff, 1985; Schrag and DePaolo, 1993).

Because of uncertainties in our knowledge of the background dissolved Cl⁻ in the upper 80 mbsf at Site 1244, we have estimated a range of values for gas hydrate occupying sediment pore space at Site 1244 (Fig. F17). These data suggest that in the GHSZ, 2%–8% of the pore space is occupied by gas hydrate. With the present data set it is not possible to ascertain the exact value and distribution of hydrate occupancy; however, several lines of evidence lead us to believe that the amount of hydrate is closer to our conservative estimate (Fig. F17B). The hydrate onset, which is predicted to occur at 40 mbsf using the minimum hydrate estimates, corresponds to the base of a zone where there are no major excursions in the chloride distribution. The upper 40 m also shows a more coherent pattern in downhole LWD resistivity data (see "Downhole Logging," p. 34). In contrast, LWD resistivity data between 40 mbsf and the depth of the BSR exhibit high variability, which perhaps reflects the patchiness of the gas hydrate distribution. These data all suggest that in the upper 40 mbsf there is not enough methane within the sediments to stabilize a gas hydrate structure (see "Hydrocarbon Gases," p. 19, in "Organic Geochemistry"). Although the two end-member interpretations affect the predicted stratigraphic distribution of gas hydrate, the total gas hydrate inventory predicted by each interpretation differs by only ±10%.

In addition, we have compared the chloride profile from Site 1244 with that of Site 888, which was drilled west of the Cascadia accretionary margin as a reference site during Leg 146 (Westbrook, Carson, Musgrave, et al., 1994). The sedimentary section at Site 888 is unaffected by the accretionary tectonics that deform and consolidate sediments within the wedge. At this site there is no seismic, geochemical, or physical evidence for the presence of gas hydrate (Westbrook, Carson, Musgrave, et al., 1994). A comparison of the chloride distribution between Sites 888 and 1244 (Fig. F18) suggests that the true background in situ Cl⁻ content in Site 1244 is closer to that assumed for our conservative

T5. Concentrations of dissolved chloride and sulfate, p. 111.

F17. Estimates of gas hydrate, p. 63.
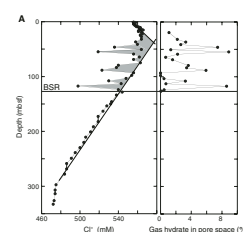
F18. Comparison of the chloride concentration profiles, Sites 1244, p. 65.
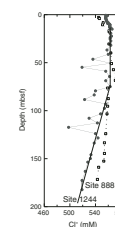
gas hydrate estimate (Fig. **F17B**). Because there is no evidence for hydrate formation at Site 888, we conclude that the increase in Cl⁻ in the upper 80 mbsf is likely to reflect global ocean changes rather than hydrate formation. Moreover, we also conclude that the presence of gas hydrate at Site 1244 is limited to between 40 and 130 mbsf.

Sulfate, Methane, and the Sulfate/Methane Interface

The SMI is a fundamental microbial and geochemical boundary in marine sediments and was the subject of integrated microbiological and geochemical investigations during Leg 204. Above the interface, sulfate reducers utilize interstitial sulfate to oxidize sedimentary organic matter; below the interface, methanogens generate methane. At the interface, a unique consortium of microbes interacts in AMO, a net biogeochemical process described by

$$CH_4 + SO_4^{2-} \rightarrow HCO_3^- + HS^- + H_2O$$

(Reeburgh, 1976) that involves carbon and sulfur cycling at the interface and also affects the geochemisty above and below the zone of AMO (Alperin et al., 1988; Borowski et al., 1997; Hoehler et al., 2000; Rodriguez et al., 2000).

In Hole 1244C, the SMI is located at ~8.5 mbsf, where interstitial sulfate first reaches a minimum concentration concomitant with increasing methane concentration as documented by headspace gas data (see **"Organic Geochemistry,"** p. 19) (Fig. **F19**). The zone where AMO occurs was sampled extensively by the microbiology team at this site (see **"Microbiology,"** p. 21).

The maximum sulfate concentration is 29.7 mM just below the sediment/water interface (Sample 204-1244C-1H-1, 65–75 cm) and falls below 1 mM at 9.15 mbsf (Sample 2H-3, 66–75 cm) (Table **T4;** Fig. **F19**). Below this depth, sulfate does not reach zero but remains at concentration <1 mM. These nonzero sulfate concentrations are likely to represent sulfate contamination from seawater in the borehole. Larger amounts of sulfate (>1 mM), derived from seawater circulating in the borehole, invaded the IW samples during XCB drilling below 189 mbsf. The sulfate profile is approximately linear between 4 and 7.5 mbsf, with curvature at both the top and the bottom of the profile, which probably represents sulfate depletion from oxidation of sedimentary organic matter (SOM) and transport by advecting fluids.

Borowski et al. (1996) hypothesized that downward sulfate flux is balanced by upward methane flux under conditions of high upward methane diffusion (such as is present in gas hydrate terranes) and low sulfate reduction rates in the sulfate reduction zone. These conditions are most often present within continental margin sediments that harbor gas hydrate. Under these conditions, sulfate and methane are coupled geochemical species because AMO occurring at the SMI involves the microbially mediated co-consumption of sulfate and methane. Because the stoichiometric ratio between sulfate and methane consumed by AMO is 1/1, these respective fluxes should be equivalent at the interface. Thus, the rate of upward methane diffusion can be estimated using the sulfate gradient, assuming that the middle and lower portions of the sulfate profile are dominated by sulfate depletion resulting from AMO. Sulfate gradients are an important proxy for methane flux because true methane gradients have only rarely been measured as a result

F19. Sulfate concentration profile, p. 66.
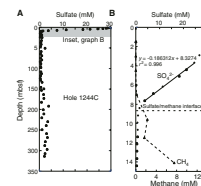
of methane gas loss that occurs during core retrieval (Dickens et al., 1997; Paull and Ussler, 2001).

Fick's First Law allows the delivery of sulfate to the SMI to be calculated. If the diffusion coefficient of sulfate (D_o), sediment porosity (ϕ), and the sulfate concentration gradient (δC) with depth (δx) are known, the diffusive flux (J) may be estimated by

$$J = D_o \, \phi^3 \, \delta C / \delta x.$$

Compared to other localities displaying linear sulfate profiles (e.g., the Blake Ridge and ODP Sites 994, 995, and 997) (Paull, Matsumoto, Wallace, et al., 1996), the sulfate distribution at Site 1244 in the lower sulfate reduction zone may not be sufficiently dominated by AMO to produce a meaningful estimate of methane flux. Nevertheless, an estimated methane flux at Site 1244 of 2.7×10^{-3} mM/cm²/yr was calculated based on a sulfate gradient of 5.5 mM/m between 4 and 8 mbsf (equivalent to a slope of 0.18 m/mM) (see Fig. F19B), a sulfate diffusion coefficient of 5.8×10^{-6} cm²/s at 5°C and average porosity of 0.65. For comparison, at the Blake Ridge (offshore southeastern North America), the steepest measured sulfate gradient predicts a methane flux of 1.8×10^{-3} mM/cm²/yr (Borowski et al., 1996, 2000), so the flux at Site 1244 is ~33% higher than that reported to date for any large passive margin gas hydrate terrane. These estimates assume methane delivery through diffusion only and assume that the linear portion of the sulfate curve is mainly created by sulfate demand at the SMI. If significant water or methane advection occurs or if sulfate depletion through AMO is of minor importance, then this estimate is invalid.

Organic Matter Decomposition

The early diagenesis of marine sediments is most often dominated by organic matter decomposition (e.g., Berner, 1980). Interstitial alkalinity, ammonium (NH_4^+), and phosphate (PO_4^{3-}) concentration increase rapidly with increasing depth, reaching maximum concentration at 58.97, 64.37, and 17.90 mbsf, respectively (Table T4; Fig. F14). These IW constituents reflect the activity of interstitial microbes that are metabolizing SOM through a reaction cascade that ultimately produces inorganic metabolic by-products. From the shape of the profiles, it is likely that the microbial decomposition of SOM is most active in the upper 100 m of the sedimentary section, where production outpaces depletion for each constituent. During postcruise research, we will have the opportunity to correlate microbial abundance and activity to key interstitial constituents that identify organic matter decomposition.

Major and Minor Element Distributions

As discussed in the previous sections, the distribution of dissolved chloride and sulfate provide the major clues to understanding the processes involved in gas hydrate dynamics and methane fluxes at this site. Further clues about the nature of fluid sources, diagenetic reactions, and microbiological processes within these sediments can be obtained from the distribution of other dissolved ions in the pore fluids shown in Figure F14 and listed in Table T4.

We have documented a zone of low chloride and high lithium concentration within the accreted sediments of the wedge (Fig. F16), which

is similar in composition to that reported for Sites 889 and 890 in the northern section of the accretionary prism (Kastner et al., 1995). Superimposed on the lithium increase there is a significant decrease in the concentration of this element in pore fluids recovered from 160 to 180 mbsf (Fig. F14). This depth interval corresponds to the reflector identified as Horizon B on the seismic data (see "Introduction," p. 1). The lithium distribution within this depth interval reflects incorporation of this element into solid geochemical phases associated with low-temperature diagenetic alteration of material present in Horizon B, even though we have not identified the phases that are incorporating lithium at this time. The sediments from this depth horizon also show variations in their physical properties and are characterized by high-density (~1.9 g/cm^3) and low porosity (~50%) values (see "Physical Properties," p. 24). Postcruise analyses of lithium and its isotopic composition in various geochemical phases will provide constraints on the diagenetic processes occurring at Horizon B.

In addition to low chlorinity and high lithium values, the deep-seated fluid at Site 1244 is also enriched in Sr^{2+} (Fig. F14). The dissolved strontium signature within the GHSZ at this site (0–130 mbsf) is more complex than that of lithium because strontium is involved in carbonate diagenetic reactions, which in turn are dependent on temperature, pressure, and pH. The increase in dissolved boron within the gas hydrate–bearing section may also be related to carbonate diagenesis (e.g., Deyhle et al., 2001), as evidenced by the similarity between alkalinity and boron distributions.

Iron and manganese have similar profiles, showing coincident maxima in their concentration (Fe = 52 µM and Mn = 6 µM) at depths ranging from 29 to 31 mbsf or ~20 m below the depth of sulfate depletion (Fig. F14; Table T4). This distribution may reflect cycling of iron manganese minerals, which precipitate as sulfides below the SMI and are remobilized at a depth in the sediment section where sulfide is depleted. A similar distribution was observed at Site 1230 on the Peru margin (D'Hondt, Jørgensen, Miller, et al., 2003). The dissolved manganese concentration remains level at ~1 µM within the GHSZ, followed by an increase downhole, which is probably associated with the composition of the deep-seated fluids. In contrast, the dissolved iron remains higher than background (<1 µM) throughout the GHSZ. Postcruise analyses of the distribution and isotopic composition of dissolved sulfide and of solid sulfide minerals will likely provide constraints to the nature of the Fe-Mn biogeochemical cycling at this site.

The distribution of dissolved and solid-phase barium in continental margin sediments has received recent attention because preservation of barite fronts within the sediments may serve as an indication of methane fluxes in the past. Dickens (2001) has presented a model based on the diagenetic behavior of barium-bearing phases in marine reducing sediments. Barite is a widespread component of oceanic sediment and is particularly abundant in areas characterized by high-productivity waters (e.g., Dehairs et al., 1980; Collier and Edmond, 1984; Dymond et al., 1992; Paytan and Kastner, 1996). In spite of the low solubility and, hence, high stability of barite in seawater, this mineral is dissolved under conditions of sulfate depletion:

$$BaSO_4 \rightarrow Ba^{2+} + SO_4^{2-}.$$

Such conditions are frequently present in organic-rich coastal sediments accumulating at high rates, in which sulfate concentration in the IWs approaches zero, as a result of microbial sulfate reduction of SOM (Brumsack and Gieskes, 1993). In these settings, dissolved barium accumulates in the pore fluids, reaching concentrations that are several orders of magnitude higher than those observed in seawater (e.g., Torres et al., 1996). The dissolved barium distribution at Site 1244 follows this general trend, reaching a concentration of ~60 µM at 20 mbsf (Fig. **F20**).

ORGANIC GEOCHEMISTRY

Shipboard organic geochemical studies of cores from Holes 1244A–1244C and 1244E included monitoring of hydrocarbon gases, carbonate carbon (IC), organic carbon, total sulfur (TS) and total nitrogen (TN) content and Rock-Eval pyrolysis characterization of organic matter. Procedures are summarized in **"Organic Geochemistry,"** p. 16, in the "Explanatory Notes" chapter.

Hydrocarbon Gases

Hydrocarbon gas measurements using the headspace method are listed in Table **T6.** Results are reported in parts per million by volume (ppmv) of methane (C_1), ethane (C_2), ethylene ($C_{2=}$), and propane (C_3) in the air headspace of a 21-cm^3 vial containing a nominal 5-cm^3 sediment sample. Results are plotted as ppmv of hydrocarbon gas component vs. depth in Figure **F21.** Methane contents increase rapidly from just above background levels, 9 ppmv at 0.05 mbsf, to ~40,000 ppmv at 14.1 mbsf and generally remain in the range of 20,000–40,000 ppmv to the base of the cored section at 333 mbsf. Dissolved sulfate is essentially depleted in the pore fluids in the uppermost 7 mbsf (see **"Sulfate, Methane, and the Sulfate/Methane Interface,"** p. 16, in "Interstitial Water Geochemistry"), and this depth effectively divides the zones of methanotrophy and methanogenesis. Trace amounts of ethane and propane are present below 7 mbsf but are not consistently present in the gas until depths of 130 and 260 mbsf, respectively. The unsaturated compound ethylene is sporadically present throughout the cored section (Table **T6**).

The composition of gas from voids or expansion gaps in the core liner is shown in Table **T7.** The void gas (vacutainer [VAC]) samples are relatively pure methane, generally with minimal air contamination, as shown by the ppmv values that approach or, in two cases, exceed 100%. Void gas samples reflect the composition of gas in the subsurface but not the amount. The subsurface gas content is probably proportional to the general abundance and internal pressure of core voids, but it is difficult to quantify.

Gas composition, as expressed by the C_1/C_2 value of headspace gas, is plotted vs. depth in Figure **F22** and vs. sediment temperature in Figure **F23.** The sediment temperature was estimated assuming the measured geothermal gradient of 61°C/km (see **"Downhole Tools and Pressure Coring,"** p. 29). The trend of C_1/C_2 values shows a general exponential increase in ethane content relative to methane with increasing depth. The C_1/C_2 values for the void gas samples show some consistent offsets in the trend that may be related to presence of methane hydrate in the

F20. Dissolved sulfate and barium profiles, p. 67.
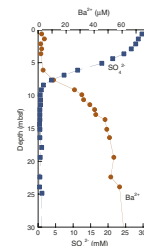
T6. Concentrations of C_1, C_2, and C_3, p. 112.

F21. Concentrations of C_1, C_2, and C_3 vs. depth, p. 68.
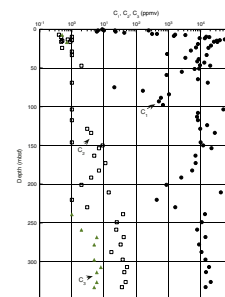
T7. Concentrations of C_1, C_2, and C_3 in VAC samples, p. 113.

F22. C_1/C_2 ratio vs. depth, p. 69.
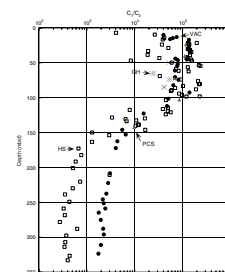
F23. C_1/C_2 ratio vs. temperature, p. 70.
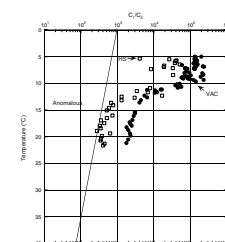
cores. Specifically, there are apparent step offsets to lower C_1/C_2 values at depths of ~40 and 130 mbsf, possibly indicating the top and base of the zone of gas hydrate presence, respectively.

When the C_1/C_2 ratio of the void gas is plotted vs. temperature (Fig. F23), the C_1/C_2 trend falls within the normal range associated with in situ low-temperature ethane generation but approaches the "anomalous" field that indicates possible migrated thermogenic hydrocarbons (Pimmel and Claypool, 2001). Headspace methane values above ~10,000 ppmv are residual concentrations, representing only the gas retained by sediments after outgassing has taken place during retrieval of the core to the surface (Kvenvolden and Lorenson, 2000; Paull and Ussler, 2001). Moreover, there is variability in the results of the headspace technique resulting from nonuniform sample size. Accordingly, the methane ppmv in air concentrations were converted to an equivalent methane concentration in IW by the procedure outlined in "Organic Geochemistry," p. 16, in the "Explanatory Notes" chapter. Gas concentrations expressed in millimoles of methane per liter of water are shown in Table T8 and plotted in Figure F24. Also shown in Figure F24 is the dissolved sulfate concentration ("Sulfate, Methane, and the Sulfate/Methane Interface," p. 16, in "Interstitial Water Geochemistry"). Below ~7 mbsf, the residual dissolved CH_4 content in the IW increases at about the depth which sulfate concentration approaches zero.

Gas Hydrate and Pressure Cores

Gas hydrate pieces and gas hydrate–cemented sediments were physically recovered from Sections 204-1244C-8H-1 and 10H-2 and 204-1244E-7H-6 and 12H-1. Evidence from electrical logs (see "Downhole Logging," p. 34) and dissolved chloride profiles (see "Major and Minor Element Distributions," p. 17, in "Interstitial Water Geochemistry") indicates that gas hydrates are definitely present in the subsurface at depths below ~40 mbsf and are possibly present at depths below ~32 mbsf. Gas hydrate–bearing intervals exist down to the base of the GHSZ, which is at ~127 mbsf at Site 1244. The composition of gas given off by decomposed hydrate pieces (Table T9) shows enrichment in ethane relative to the void gas samples analyzed at comparable depth intervals. The gas hydrate pieces from Hole 1244C were analyzed after storage at –80°C for 3 or 4 days, but the gas hydrate pieces from Hole 1244E were analyzed immediately. The general trend of the C_1/C_2 ratio of the void gas (Fig. F22) is offset in the direction of ethane depletion over the general interval where gas hydrate is present. A similar trend was observed in void gas samples from gas hydrate–bearing sediments at Blake Ridge during ODP Leg 164. Whether or not these shifts in the C_1/C_2 ratio are valid indicators of the presence of gas hydrate will be evaluated in cores from other sites during Leg 204.

In addition to the gas samples obtained from the decomposition of gas hydrate pieces recovered in the core, the gas composition of samples taken during controlled degassing of the PCS (for details on the PCS, see "Pressure Core Sampler," p. 30, in "Downhole Tools and Pressure Coring") was also analyzed. The results are listed in Table T10 and shown in Figure F22. The gas from PCS experiments is enriched in air but generally has the same C_1/C_2 composition as the void gas samples from adjacent cores.

T8. Headspace methane, p. 115.

F24. Dissolved residual methane and sulfate, p. 71.
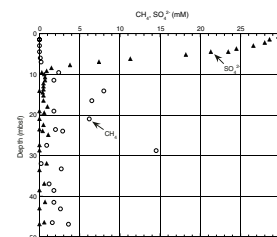
T9. Gas from decomposition of gas hydrate, p. 117.

T10. Gas composition of samples from the PCS experiments, p. 118.

Carbon Analyses, Elemental Analyses, and Rock-Eval Characterization

A total of 34 sediment samples (one per core in Holes 1244A–1244C, except for PCS cores) were analyzed for IC, total carbon (TC), organic carbon (OC) (by difference), TN, and TS. The results are reported in Table **T11**. IC content (plotted against depth of burial in Fig. **F25**) is relatively low (0.04–0.75 wt%). When calculated as $CaCO_3$, the IC from sediments in Hole 1244C varies from 0.33 to 6.25 wt% (Fig. **F25**), reflecting primary changes in biogenic and authigenic carbonate. The sediments below 250 mbsf contain relatively low amounts of IC, reflecting a major change to lithostratigraphic Unit III. (see **"Lithostratigraphic Unit III,"** p. 7, in "Lithostratigraphic Units" in "Lithostratigraphy").

OC content of sampled intervals (Table **T11**; Fig. **F25**) is relatively high in comparison to other marine sediments, ranging from 0.87 to 1.83 wt% (average = 1.27 wt%). The analyzed sample with the highest OC content is at a depth of 28.26 mbsf. The C/N ratios are <10. Based on the C/N ratios, organic matter in the sediment is mainly marine in origin.

TN in the sediments varies between 0.13 and 0.22 wt% (Table **T11**; Fig. **F25**). The nitrogen data show no apparent trends vs. either depth or OC content. The sediment samples have TS contents ranging from 0.09 to 1.84 wt% (Table **T11**; Fig. **F25**). There is no apparent relationship between sulfur and OC. The sediments contain less sulfur relative to carbon in the depth interval from 18.76 to 237.99 mbsf. TS content in the sediment increases in cores below 238 mbsf.

Fourteen samples from Hole 1244C were characterized by Rock-Eval pyrolysis (Table **T12**). Samples with >1 wt% OC were selected for analysis. All samples have significant levels of pyrolyzable organic matter contents, with S_2 yields ranging from 1.4 to 3.1 mg of hydrocarbons per gram (HC/g) of sediment. The low T_{max} values and the well-defined S_2 peak shapes in the pyrograms (not shown) indicate that samples contain mostly thermally immature primary organic matter. The measured S_1 (0.2–0.6 mg/g) and production index ($S_1/[S_1+S_2]$) values (0.12–0.18) are relatively high for thermally immature sediments, suggesting possible low levels of staining by migrated hydrocarbons. The hydrogen index values range from 100 to 200 mg HC/g C but are not diagnostic for organic matter type at this level of maturity.

MICROBIOLOGY

The goals of microbiological sampling and study during Leg 204 were to determine the rate of microbial methane production and consumption, the composition of the microbial communities responsible for this methane production and consumption, and the effect of high methane concentrations and methane hydrates on sedimentary microbial biomass and community structure. Most of the onboard work was devoted to deciding where and how to sample and collecting subsamples to meet these goals. The bulk of the analyses necessary to achieve these goals are to be performed on shore.

Site 1244, located on the eastern slope of Hydrate Ridge, was the primary site chosen for comparison of microbiology with the Hydrate Ridge summit. The methane flux estimated from the sulfate gradient at this Site 1244 is 2.7×10^{-3} mmol/cm²/yr (see **"Interstitial Water**

T11. IC, OC, TN, and TS contents and C/N ratios, p. 119.

F25. Contents of IC, $CaCO_3$, OC, TS, and TN, and C/N ratios, p. 72.
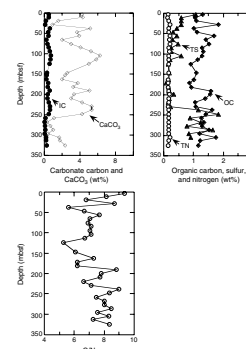
T12. Rock-Eval pyrolysis of samples, p. 120.

Geochemistry," p. 13), as compared to the summit, which has methane fluxes estimated at over 10,000 times these rates (see "Interstitial Water Geochemistry," p. 11, in the "Site 1249" chapter and references therein). The methane flux at Site 1244 is comparable to the maximum fluxes found at the Blake Ridge (1.8×10^{-3} mmol/cm²/yr) (Borowski et al., 1996), where previous microbiological study on Leg 164 samples (Wellsbury et al., 2000) will also provide a framework for comparison.

Microbiological Sampling

Site 1244 was both the first and last site sampled for microbiology during Leg 204, and the samples taken and methods used reflect our learning process. Sampling in the upper sediment layers targeted the SMI, where microbial consumption of methane should peak. AMO, using sulfate as the electron acceptor, has been a topic of much recent study (Boetius et al., 2000; Orphan et al., 2002; Michaelis et al., 2002; Zhang et al., 2002) and is a major focus for the Leg 204 microbiological program. The initial holes drilled at Site 1244 were sampled for geochemistry, and once the sulfate and methane data had been examined, the SMI was targeted for intensive coupled microbiological and geochemical sampling. We found that this interface could also be estimated quickly by noting the presence of cracks (expanded gas) by eye, and more accurately, but still rapidly, by observing the sharp transition between high and low *P*-wave signal strength, causing dropouts in velocity values (see "Physical Properties," p. 22, in the "Explanatory Notes" chapter). The SMI at Site 1244 was at 8.5 mbsf, based on measurements of sulfate (see "Interstitial Water Geochemistry," p. 13) and methane (see "Hydrocarbon Gases," p. 19, in "Organic Geochemistry"). The top three cores from Holes 1244C and 1244F were sampled intensively (one to two samples per section) in coordination with the geochemistry program (Table T13).

Methanogenesis can proceed in most anaerobic environments, but it becomes the major process when other electron donors such as nitrate and sulfate are depleted. We sampled regularly downhole to below the base of the GHSZ (Table T13) to quantify methanogenesis in these sediments. At the Blake Ridge, microbial biomass (as measured by direct counts) increased just below the GHSZ and then returned to background values (Wellsbury et al., 2000). Site 1244 will provide a comparison with these values.

Iron is another electron acceptor that can be used by microorganisms, but the iron data from the first hole at most sites were not available by the time microbiological sampling was initiated in the second hole. Because sampling at Site 1244 took place at both the beginning and the end of the leg, we had IW iron data available to guide microbiological sampling. Onboard IW analyses at Site 1244 indicated unusual iron geochemistry with a soluble iron maximum of 27.5 mM at 21 mbsf. Samples targeting this zone were taken from Holes 1244E and 1244F and placed in enrichment media for iron- or manganese-reducing organisms and for methanogens (see "Enrichment Cultures," p. 21, in "Microbiology" in the "Explanatory Notes" chapter).

Sediments associated with hydrates were not deliberately sampled at this hole; however, IR anomalies indicated small amounts of disseminated or veined hydrates in Hole 1244E, which was sampled for microbiology.

The emphasis in sample processing was to work as quickly as possible without compromising microbiological technique, to maintain samples

T13. Intervals sampled for microbiology, p. 121.

at or below ambient temperature of the formations from which they were taken, and to minimize exposure to oxygen. Cores were kept at 4°C and left undisturbed in their liners until they could be completely processed. When supply exceeded the rate of processing, cores were handled on a last-in, first-out basis. The processing of samples from Hole 1244C was conducted prior to completion of the refrigerated van laboratory, so the hold refrigerator was set up as a temporary sample processing laboratory and maintained at 4°C.

Contamination Tests

Perfluorocarbon Tracer

Samples for PFT analysis were not taken from Hole 1244C. Subsequent cores had 5-g subsamples taken from outer and inner layers for gas chromatography (GC) analysis, as described in **"Perfluorocarbon Tracer,"** p. 20, in "Shipboard Microbiological Procedures and Protocols" in the "Explanatory Notes" chapter. Samples have been analyzed as described, and raw data are presented in Table **T14.** Differences between outside and inside samples generally indicate minimal penetration. Notable exceptions may reflect penetration along fractures in sediments or discrepancies in handling and sampling, particularly when dealing with XCB cores.

Fluorescent Microspheres

A comparison of fluorescent microsphere penetration in core interiors and exteriors is summarized in Table **T14.** Microscopic analysis of outer core layers showed numbers of microspheres ranging upward from 104 spheres per gram of sediment, whereas microspheres were generally below the detection limit of 10 spheres per gram in samples taken from core interiors.

Onboard Analyses

Samples were taken as described in the **"Shipboard Microbiological Procedures and Protocols,"** p. 20, in "Microbiology" in the "Explanatory Notes" chapter for inoculation of enrichment cultures targeting methane producing and iron- and manganese-reducing organisms. For methanogenic enrichments, one section from active upper sediments well below the SMI was sampled (Section 204-1244E-4H-5) as well as another section deeper in the hole (Section 204-1244E-18H-5). Samples were maintained at low temperature, and dilution series were inoculated to culture for microorganisms that produce methane from the disproportionation of acetate as well as from hydrogen and carbon dioxide. One series will be maintained at <10°C while a duplicate will be kept at 20°C. Deoxyribonucleic acid (DNA) sequence information from these enrichments will be used for comparison to nucleic acids extracted from frozen sediments, and isolates developed will be used for planned minimum metabolic energy, continuous culture experiments.

Enrichments in metal reducers were taken from regular intervals in Holes 1244F (0–15 mbsf) and 1244E to transect the dissolved iron peak near 30 mbsf. A total of 16 quadruplicate sets were inoculated. Media for growth of iron- and manganese-reducing organisms were inoculated with 1–2 g of freshly collected sediment. Four media formulations were used: acetate plus ferrihydrite, acetate plus manganese dioxide, formate

T14. Core quality indicators, p. 122.

plus ferrihydrite, and formate plus manganese dioxide. Formate-containing media were subsequently pressurized with 1-atm hydrogen gas.

PHYSICAL PROPERTIES

In this section, we describe the downhole distribution of physical property data collected from Site 1244. Three holes were drilled at this site. Hole 1244A contained only one core and missed the mudline. Hole 1244B was drilled to a depth of 62 mbsf. Hole 1244C, which was drilled to a depth of 330 mbsf, contains a total of 39 cores. Several pressure cores were taken with the PCS (Cores 204-1244C-14P, 16P, and 18P) in Hole 1244C. No continuous measurements with the multisensor track (MST) and thermal conductivity were possible on these PCS cores. However, subsampling for moisture and density (MAD) was conducted. This site was revisited on 19 August 2002, and Holes 1244E and 1244F were cored. Physical property measurements were acquired from Hole 1244E to a total depth of 140 mbsf, and complete IR scans of all cores recovered were acquired.

Routine physical property measurements were collected on whole-round core sections at this site (see "Physical Properties," p. 22, in the "Explanatory Notes" chapter). A scan of IR emission along the entire core-liner surface was recorded for most cores at this site prior to sectioning and sampling on the catwalk.

Samples were taken from split cores to measure sediment MAD properties. We also measured compressional (P)-wave velocities (V_P) on the split cores using the standard ODP Hamilton Frame device, and occasionally, we used the handheld Torvane to measure shear strength on selected core sections.

The sampling strategy at this site was designed to address specific leg-related research objectives as well as to provide a first test for all systems (Holes 1244A–1244C). Sampling rates for MAD measurements were much higher at this site (minimum of one sample per section) compared to the other sites. The objective of this strategy was to obtain a high-resolution data set of bulk density and related properties (porosity, grain density, and moisture content) to compare to the LWD measurements. The MAD data provide good ground truth and a reliable comparison to the in situ measurements of the logging tools.

Measurement spacing, count times, and data acquisition schemes (DAQ) used for the MST were the following: MS: spacing = 2.5 cm, count time = 3×1 s; gamma ray attenuation (GRA): spacing = 2.5 cm, count time = 5 s; and PWL: spacing = 2.5 cm, DAQ = 50.

In Hole 1244A and partially in Hole 1244B (up to a depth of ~35 mbsf), we also began testing the new Geotek Non Contact Resistivity (NCR) system. The new ODP software and electronics interface was not functional at this stage, and hence, there is no usable data at this site. There was a problem with acquiring MS data while the NCR was running, but this was resolved by turning off the NCR system below 35 mbsf.

Most of the physical property data show breaks or variations in downhole trends that match well with the data acquired by LWD and partially agree with the lithostratigraphic boundaries defined by the sedimentologists (see "Lithostratigraphy," p. 4).

Infrared Scanner

IR imaging of cores drilled at Site 1244 provided on-catwalk identification of hydrate zones in each core (see "Physical Properties," p. 22, in the "Explanatory Notes" chapter). Dissociation of hydrate is an endothermic reaction that produces decreased temperature in intervals of the core containing hydrate. The butyrate core liners are opaque in the IR range detected by the camera used (8–12 μm). However, the cooled zones associated with hydrates are transmitted through the core liner by thermal conduction, creating an image of the core temperature on the surface of the core liner, which is then detected by the IR-imaging camera.

Each thermal image covered ~20 cm of core. The spatial resolution of the thermal images is lower than a direct image of the core itself but, nonetheless, provides previously unavailable information on the overall shape and character of hydrate occurrences. This information was used to facilitate hydrate sampling and preservation starting at Core 204-1244C-8H.

The shapes of thermal anomalies in the images were compared to the actual hydrate samples observed and photographed after they were taken from the core liners (Fig. F26). The thermal images provide a distinction between nodular, vein-filling, and layered hydrate, if hydrate abundance is relatively low, as is the case at this site. In addition, disseminated hydrate is detectable on the IR images as thermal anomalies with a ΔT of ~1°C or less. The IR thermal anomalies are cataloged in Table T2, including an interpretation of the overall hydrate texture.

Successive thermal images were also used to produce a downcore thermal log for each core recovered at Site 1244 (Fig. F27). The logs show the overall thermal structure of each core and include both positive thermal anomalies associated with voids and the tendency of cores to be warmer at the bottom than at the top. This tendency becomes stronger with depth and is especially true for XCB cores. The warmer base of each core may result from the shorter time since exposure to the frictional heating of the bit as well as local frictional heating associated with removal of the cutting shoe and core catcher from the bottom of the core barrel. In addition, the warmer temperatures at the base of the core could reflect thermal transfer associated with gas expansion. The extreme positive thermal anomalies are artifacts associated with the partial absence of core in the last image of the core sequence. Also, note that the XCB-cored interval is cooler than the APC-cored interval at this site, which is presumably caused by the poorer quality of the XCB core and greater contact with cool drilling fluid during core recovery.

A more detailed plot of the zone of negative thermal anomalies in Holes 1244C and 1244E (Fig. F28A) shows the distribution of IR temperature anomalies as a function of depth. The larger anomalies are present between 47 and 85 mbsf, indicating that this is the zone containing the greatest abundance of hydrate at this site. Figure F28B also shows the LWD resistivity log for Hole 1244D, which has been interpreted using Archie's Relation to predict the abundance of hydrate (see "Downhole Logging," p. 34). Recognizing that Hole 1244D is 15 m away from Hole 1244C, the plot shows that observed hydrate corresponds reasonably well to the resistivity estimate. The poorest matches are from ~15 to 40 mbsf, from ~100 to 115 mbsf, and below ~125 mbsf. Lack of agreement between the two methods is likely to reflect a combination of disseminated hydrate not detected by IR imaging, uncertainty of hydrate resisitivity logs, heterogeneity in hydrate occurrence be-

F26. IR images and photographs of corresponding hydrates, p. 73.
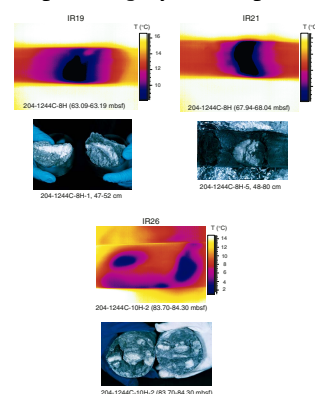
F27. IR downcore temperature profiles, p. 74.
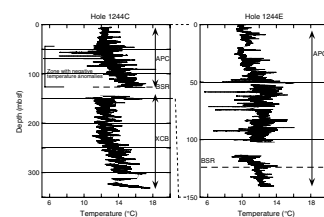
F28. Downcore temperature anomalies, p. 75.
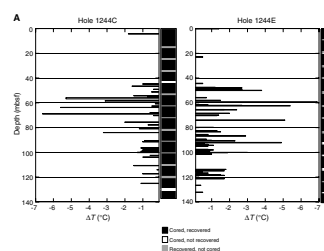
tween Holes 1244A and 1244D, and the response of the resisitivity log to the presence of gas below the BSR.

The absence of negative thermal anomalies below 126 mbsf is consistent with a BSR depth of 125 mbsf derived from seismic data. PCS and XCB drilling were conducted between 141 mbsf and the bottom of the hole (BOH). At present, it is not known if the use of the XCB reduces the sensitivity of the IR image, but it seems likely given the greater temperature reduction in XCB cores in Figure **F27.** PCS cores do not permit collection of IR data.

Sediment Density from Multisensor Track and Moisture and Density

GRA densities were measured by the GRA instrument on the MST, and bulk density and grain density were calculated from the MAD data (Table **T15;** Fig. **F29**). These density values and inferred porosities are compared to the LWD data (Fig. **F30**).

In general, all three data sets are in good agreement. However, there are distinct discrepancies between the GRA measurements and the MAD/LWD data. The GRA measurements are most affected by gas expansion effects and voids in the core liner (**"Physical Properties,"** p. 22, in the "Explanatory Notes" chapter). This data set shows the largest scatter (accurately reflecting the core material in the liner) and consistently produces much lower density values than the two other techniques, especially at greater depth. However, the measurements for Holes 1244A and 1244B show that for depths shallower than 50 mbsf and especially for the upper 10 mbsf before gas expansion occurs, the MAD and GRA measurements are a perfect match (Fig. **F31**). At those shallow depths, the LWD did not produce reliable results because of poor borehole conditions. The LWD and MAD data do not always show a perfect match. For example, the two data sets show similar density to 175 mbsf, below which the MAD data are consistently lower than LWD data, to 245 mbsf. The two data sets are, again, in good agreement below 245 mbsf. We have no explanation for these differences. They do not coincide with a change in coring technique from APC to XCB at 145 mbsf or any obvious lithologic boundaries.

Overall, the density increases slightly with depth, starting with values at ~1.6 g/cm³ near the seafloor and reaching maximum values of ~1.85 g/cm³ at a depth of ~155 mbsf. This general increase is an expected effect of compaction of soft marine clayey-silty sediments. Just above the boundary separating lithostratigraphic Units I and II, a low-density layer is present, which is best resolved with the high-resolution LWD data.

Between 155 and 180 mbsf, a unit characterized by high density values (~1.9 g/cm³) and low porosity values of ~50% is found. This unit has a relatively sharp top and smooth base. Below 175 mbsf, density values start to decrease downhole to a value of ~1.85 g/cm³. Density then remains almost constant to a depth of 235 mbsf. A second high-density, low-porosity unit, with similar density and porosity values as the shallower unit, is present from 235 to 245 mbsf. This sequence is sharply truncated at the bottom, where density values drop to ~1.72 g/cm³. This drop in density is associated with the boundary between slope-basin sediments and the deeper accretionary wedge complex (see **"Lithostratigraphy,"** p. 4). The density increases within lithostratigraphic Unit III from 1.72 (245 mbsf) to ~1.8 g/cm³ (~285 mbsf). Below

F29. Physical property measurements, p. 77.
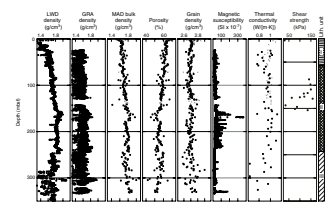
F30. GRA, MAD, and LWD density, p. 78.
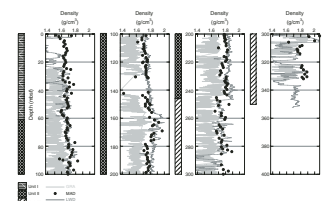
F31. Comparison of shallow measurements of bulk density from GRA and MAD, p. 79.
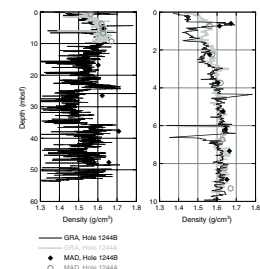
285 mbsf, there are large fluctuations in density, with values varying from ~1.4 to ~2.1 g/cm³. There is partial agreement between the discrete MAD, LWD, and GRA density measurements within this unit, especially at 300 mbsf, where all three independent techniques gave very high density values of ~1.9 g/cm³. This suggests that the fluctuations may not be an artifact of poor borehole condition (in case of the LWD), gas expansion, or drilling slurry (in case of the XCB coring). However, the origin of these fluctuations remains enigmatic.

The discrete measurements of MAD were used to calculate grain densities and porosities. The inferred grain density values are rather uniform throughout the hole (values of 2.7 ± 0.2 g/cm³), with the largest deviations occurring at depths >210 mbsf. Since the grain density lacks any significant variation, porosity is essentially proportional to bulk density.

Magnetic Susceptibility

MS was not measured in Hole 1244A or in the uppermost 35 m of Hole 1244B. Multiple measurements between 35 and 53 mbsf in Holes 1244B and 1244C show the same data trend (Fig. F29). However, minor deviations occur as a result of difference in hole locations as well as difference in gas-expansion cracks and voids.

Since the sediment sequence of Hole 1244C provides the most complete MS profile, we describe the MS characteristics based on results of this hole. Overall, three MS units can be identified (Fig. F29). MS Unit I has relatively uniform MS values of ~40 × 10^{-7} (SI). This unit extends from the seafloor down to 160 mbsf. MS Unit II is characterized by large variations of up to 380 × 10^{-7} (SI). This unit is truncated sharply at 233 mbsf and is followed by MS Unit III, which again has relatively uniform susceptibility of ~40 × 10^{-7} (SI).

Compressional Wave Velocity from the Multisensor Track and Hamilton Frame

V_P was measured with the Hamilton Frame (PWS3) on split cores only in the upper 12 m of Holes 1244A–1244C. In deeper parts of the holes, velocity measurements were strongly affected by gas expansion in the cores and by the XCB coring technique, which disturbed the entire core.

The V_P measured with the PWS3 device vary between 1530 and 1600 m/s (Table T16). These values are, however, ~50 m/s higher than the V_P measured with the MST (Fig. F32). It was subsequently discovered that the PWS3 measurement error of 50 m/s was caused by a worn displacement transducer.

In Hole 1244E, a new set of velocity measurements were carried out to investigate the structure in the upper 10 mbsf (Fig. F33). The measurements in Hole 1244E show an almost linear increase with depth. This increase is consistent with the trend observed in the GRA density, shear strength, and electrical resistivity, which is related to the early compaction of the sediments.

Thermal Conductivity

Thermal conductivity measurements were made routinely after the cores were equilibrated to ambient room temperatures. The general pro-

T16. V_P values from split-core analyses, p. 126.

F32. V_P, p. 80.
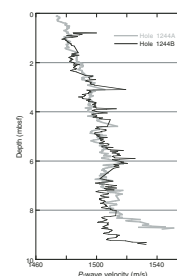
F33. Physical property data, p. 81.
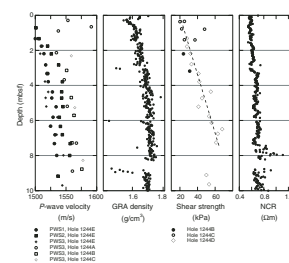
cedure was to measure thermal conductivity once per core in Section 3. On cores adjacent to downhole temperature measurements, thermal conductivity was measured at Sections 1, 3, and 5 of the core.

Measured values vary between 0.64 and 1.12 W/(m·K), with an average value of 0.94 W/(m·K) (Table **T17;** Fig. **F29**). A small increase in thermal conductivity was observed downhole to a depth of 240 mbsf. However, data are scattered, probably as a result of gas expansion. No correlation between bulk density and thermal conductivity was therefore observed. Thermal conductivity apparently decreased at depths below 240 mbsf. However, we believe this to be mainly the effect of gas expansion and the XCB coring technique, which introduces cracks and lower-density drilling slurry.

Shear Strength

Vane shear strength measurements were not routinely conducted because of the disturbed nature of the sediments. Occasionally, a hand-held Torvane was used to measure shear strength (see **"Physical Properties,"** p. 22, in the "Explanatory Notes" chapter). Measurements were made on the working half of the split-core sections at locations where the sediment appeared undisturbed. Intervals within the core sections with abundant cracks and voids resulting from gas expansion were avoided. Measured values vary between 23 and 160 kPa (Table **T18;** Fig. **F29**). Within the upper 10 mbsf, there is good correlation between shear strength and V_P, bulk density, and electrical resistivity. All parameters indicate compaction of the sediment. However, no further correlation to other physical properties or lithostratigraphic units at greater depth was attempted because of the sparse and scattered data set.

Summary and Discussion

At this site, we implemented the use of an IR camera as a tool to identify the presence of gas hydrate in the cores. These data provided a new means of estimating the spatial distribution of hydrate in cores. Further analyses should result in quantification of hydrate concentrations.

The physical properties measured at Site 1244 are generally in good agreement with the other data acquired at this site. The high-resolution sampling procedure for discrete MAD analyses provides ground truth for the LWD experiment. Density measurements from the MST, the MAD analyses, and the LWD data agree very well and show similar trends; however, there are discrepancies between MST and MAD/LWD densities that were caused by gas expansion and voids in the cores.

There is good correlation of density and MS with major lithostratigraphic units. The boundary between lithostratigraphic Units I and II at 62 mbsf was not clearly detected in the MS. The MS data suggest a boundary at a depth of 165 mbsf where a sudden change in the MS pattern was observed. Unit II shows higher MS values and is characterized by large variations, which may correlate to individual turbidite sequences. Although turbidites were also observed in Unit I, the MS data do not show as strong variations here. This may be an indication of different source material.

The boundary between lithostratigraphic Units II and III is identified as the change from slope-basin sediments to the AC. This boundary is marked by a sudden drop in average density and MS values.

T17. Thermal conductivity, p. 127.

T18. Shear strength values, p. 128.

DOWNHOLE TOOLS AND PRESSURE CORING

Downhole Temperature Measurements

Ten measurements of in situ temperature, including one mudline temperature taken prior to coring, were made with the APCT tool at this site in Holes 1244B, 1244C, and 1244E. APCT 12 was used in Holes 1244B and 1244C, and APCT 11 was used in Hole 1244E. Four additional temperature measurements were made with the DVTPP, generally at depths greater than those suitable for the APCT tool.

Measurements were taken at ~30-m intervals and span the depth range of 35.1–149.4 mbsf (Table **T19**). All downhole temperature-tool deployments resulted in temperature histories that showed clear penetration and extraction pulses and smooth temperature decay (see **"Downhole Tools and Pressure Coring,"** p. 34, in the "Explanatory Notes" chapter). Raw data are shown in Figure **F34.** Only the portion of the data from the immediate time period before, during, and after tool insertion is shown.

APCT data were modeled using the software program TFIT (as described in **"Downhole Tools and Pressure Coring,"** p. 34, in the "Explanatory Notes" chapter) using measured thermal conductivities (see **"Physical Properties,"** p. 24) and are plotted in Figure **F35.** Uncertainty in the extrapolated value of in situ temperature resulting from the subjective analyst picking of t_p, t_i, and t_f is <0.02°C for these high-quality records. Uncertainty resulting from possible errors in measured values of thermal conductivity is also estimated to be ~0.02°C.

DVTPP temperatures were picked from the measured temperature recorded late in the time series. For these relatively long deployments, the temperature appears to have approached equilibrium, so no further extrapolation of the DVTPP temperature data was done at this site. Uncertainties in the in situ temperature estimated from DVTPP data are estimated to be ~ 0.1°C because the DVTPP data are noisier than the APCT data. Because mudline temperatures recorded by the DVTPP tip 3 were consistently higher than those recorded by APCT 12, an empirically determined shift of –1.40°C was applied to the DVTPP data measured with tip 3 before plotting the data to determine the subsurface temperature gradient. APCT and DVTPP temperature estimates made at depths of 62.5 and 63.5 mbsf, respectively, yield temperatures that differ by only 0.074°C, verifying this empirical calibration.

During the course of the leg, an unexpectedly important source of uncertainty in APCT measurements became apparent. After APCT 12 showed an apparent temperature jump of >2°C during the course of drilling at Site 1246, we decided to calibrate each APCT tool using an ice-water bath (see **"Downhole Tools and Pressure Coring,"** p. 14, in the "Site 1246" chapter). This simple experiment revealed considerable variability among the tools. APCT 11, which was used in Hole 1244E, yielded a temperature for ice water of –0.513°C. We do not have a "prejump" calibration for APCT 12, which was used in Holes 1244B and 1244C, as well as at Sites 1245, 1246, and 1248–1251. To estimate the offset between APCT 11 and APCT 12, we calculated the temperature gradient and extrapolated seafloor temperature for each instrument separately (excluding the mudline temperature). Slopes are similar (slope = 0.0615 for APCT 12 and slope = 0.0632 for APCT 11) and their intercepts differ by 0.58°C (intercept = 3.99 for APCT 12 and intercept = 3.41 for APCT 11). This suggests that APCT 12 was calibrated to within
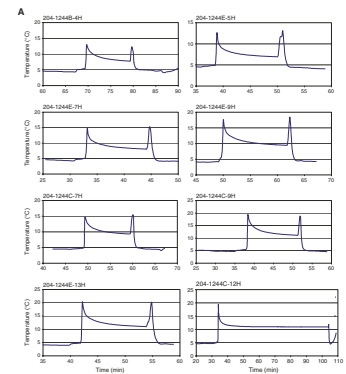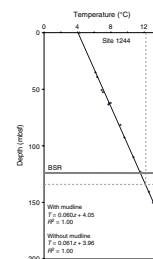
~0.1°C prior to its use at Site 1246. In the remainder of this report, in situ temperatures derived from APCT 11 are corrected by +0.51°C for determination of thermal gradients (but not in the tables); calibration correction is applied to data from APCT 12.

Figure F35 shows the temperature gradient determined at this site and the position of the BSR, as determined from seismic reflection data and confirmed by downhole acoustic logging. The dashed horizontal line shows the predicted depth to the gas hydrate stability field, assuming the temperature gradient determined for Site 1244 and hydrostatic pressure for a pure methane and seawater system (Maekawa et al., 1995). The predicted stability boundary is ~10 m below the BSR, and the temperature at the BSR appears to be ~0.6°C too cold. Possible explanations for this mismatch will be discussed elsewhere.

In Situ Pressure Measurements

The DVTPP pore pressure measurement at 62.5 mbsf in Hole 1244C (Fig. F34B) yields a rapid decay to a pressure that is within ~20 psi of the predicted hydrostatic pressure. In contrast, the signal from the DVTPP pressure measurement in Hole 1244C decays gradually (Fig. F34B), suggesting that the pressure probe was inserted into an intact formation at 150.2 mbsf and measured a true formation pore pressure. Pressure had clearly not reached equilibrium after 35 min in the formation, requiring additional modeling to extrapolate from the data to derive an estimate of in situ pressure. This modeling will be part of a shore-based effort. All of the DVTPP runs yield temperature data that are consistent with in situ temperatures measured by the APCT tool but only one of the runs appears to yield an accurate in situ pressure measurement. This suggests that the pressure measurements are more sensitive to minor cracking of the formation around the probe than the temperature measurements.

The first run of the piezoprobe in Hole 1244B was unsuccessful. A second deployment of the piezoprobe in Hole 1244C produced a well-defined pressure-dissipation curve. These results will be used with the data collected from postcruise geotechnical testing of sediment from this site to evaluate the in situ state of stress and permeability of the formation. In addition, the piezoprobe data will be compared with data from the DVTPP as part of a postcruise study.

Pressure Core Sampler

The PCS was successfully deployed seven times at Site 1244. The main objectives of the deployments were (1) to construct a detailed profile of concentration and composition of natural gases in the upper part of the section and (2) to identify the presence/absence and concentration of gas hydrate within the GHSZ.

Specific depth intervals were targeted for deployment of the PCS. Five cores (Core 204-1244F-4P [23.1–24.1 mbsf]; 204-1244E-6P [39.2–40.2 mbsf], 11P [71.6–72.6 mbsf], and 15P [102–103.1 mbsf]; and 204-1244C-14P [119.5–120.5 mbsf]) were recovered from above the BSR at ~124 mbsf. The other two cores (Cores 204-1244C-16P [130.5–131.5 mbsf] and 18P [141.5–142.5 mbsf]) were recovered from below the BSR.

The PCS cores were degassed for periods of 450–2999 min after recovery on board (Table T20). No pressure was recorded during degassing of Cores 204-1244C-14P, 16P, and 18P because of the lack of equipment. Pressure transducers were not properly calibrated during degassing of

T20. Results from degassing experiments, p. 130.

Cores 204-1244E-6P and 15P and 204-1244F-4P, and the pressure record is not reported here. Pressure was recorded during degassing of Core 204-1244E-11P (Fig. **F36**). Gas was collected in a series of sample increments (splits), and most were analyzed for molecular composition (see **"Organic Geochemistry,"** p. 19). In addition, gas splits were subsampled for onshore analyses. After degassing, the PCSs were disassembled. The lengths of the cores were measured (Table **T20**), and samples were taken for analysis of physical properties (see **"Physical Properties,"** p. 24).

Gas was collected in 2.5- to 580-mL increments. The measured incremental and cumulative volumes are plotted vs. time in Figure **F36.** The cumulative volume of released gas varies from 595 mL (Core 204-1244E-4P) to 4530 mL (Core 11P) (Table **T20**). The volume of the last gas splits varies from 0 mL (Core 204-1244E-15P) to 120 mL (Core 204-1244C-14P). This observation suggests that, in some cases, not all gas was collected.

Gases released from the PCS are mixtures of air (N_2 and O_2), CH_4, CO_2, and C_{2+} hydrocarbon gases (see **"Gas Hydrate and Pressure Cores,"** p. 20, in "Organic Geochemistry"). The abundance of air components in the PCS gas samples (1.4%–33.33% of gas mixtures) suggests that air was not always properly displaced from the PCS by seawater during deployments. Methane is the dominant natural gas present in collected gas splits. The molecular composition of gases from the PCS is similar to the composition of gas voids at adjacent depths (see Fig. **F24**).

Sediments in cores recovered by the PCS have lithology similar to sediments recovered by APC and XCB at adjacent depths (see **"Physical Properties,"** p. 24). Porosity values measured in APC and XCB cores taken near the PCS were used to estimate the methane concentration in situ (Table **T20**).

The concentration of methane in situ was estimated based on data from the degassing experiments (i.e., total volume of methane) and core examination (i.e., length of recovered core and the porosity of sediments). The calculation yields equivalent concentrations varying from 23.7 to 221.2 mM (Table **T20**). These concentrations have been compared with the theoretical methane-solubility curve extrapolated from values that were calculated for higher pressures (depths) (Handa, 1990; Duan et al., 1992) (Fig. **F37**). Preliminary analysis suggests that gas hydrates have been present in relatively low concentrations in Cores 204-1244E-11P (~2% pore volume) and 15P (~0.5% pore volume). Interestingly, no evidence of the presence of gas hydrate was found in the pressure record during degassing of Core 204-1244E-11P (Fig. **F36E**). The presence of gas hydrate in these two cores correlates well with the observed distribution of gas hydrate at Site 1244.

The concentration of methane in cores taken ~4 m above the BSR (Core 204-1244C-14P), ~7 m below the BSR (Core 16P), and ~18 m below the BSR (Core 18P) is estimated to be below saturation. The measurements suggest that there is neither gas hydrate nor free gas in the intervals sampled near the BSR.

Based on PCS measurements, gas hydrate appears to be more abundant in the middle part of the GHSZ. This observation is consistent with visual observations on the catwalk, Cl^- anomalies (see **"Interstitial Water Geochemistry,"** p. 13), and well-logging data (see **"Downhole Logging,"** p. 34). However, the gas hydrate concentration in sediments appears to be lower than that estimated by other methods. Additional comparison of measured methane concentrations with theoretical methane solubility above and below the BSR will be performed on

F36. Volume-time plots, p. 85.
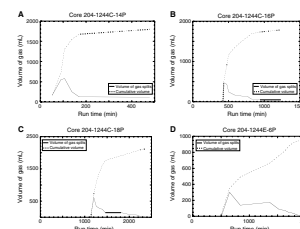
F37. Methane concentrations, p. 87.
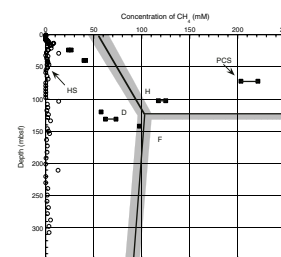
shore to better estimate if methane was present in situ in solution, in free phase, or as gas hydrate.

HYACINTH Pressure Coring and Logging

Coring Summary

The only HYACINTH pressure core taken at Site 1244 was Core 204-1244E-8Y (FPC 9) at 50.70 mbsf. This core was recovered under full pressure well above the BSR (located at 124 mbsf) and in the GHSZ. Hydrate samples had been collected in the previous core (Core 204-1244E-7H) at 49.94 mbsf and were collected from the core beneath Core 8Y (FPC 9; Core 9H) at 58.08 mbsf. It was therefore anticipated that this short pressure core might contain some hydrate.

HYACE Rotary Corer Operations

No HRC cores were taken at Site 1244.

Fugro Pressure Corer Operations

A single FPC deployment was made at Site 1244 (Core 204-1244D-2Y; FPC 9) (see Table T21). After a number of adjustments based on experience from previous deployments, the outstanding problem was effective and reliable sealing of the lower autoclave valve. For this deployment further minor adjustments were made to the valve and plans were made to adjust the speed profile of the drill string when withdrawing the tool from the bottom.

After assembly and making up in the drill string, the tool was lowered while rotating at 20 revolutions per minute (rpm) and pumping at 160 gallons per minute (gpm), with the APC on (maximum heave = ~1 m). As the tool approached the BHA, the bit was picked up 2 m above TD and rotating was stopped. The tool was landed slowly while some flow was taking place. The pump pressure was increased to 200 psi, and 5 m slack was given on the sandline. Following this procedure, the bit was lowered to the bottom and the weight was set at ~10 kips. The pump pressure was increased to ~700 psi while the operator held his fingertips to the drill string. This sophisticated sensor system detected the pins shearing and a small amount of hammering. After hammering, the pump pressure was increased to 800 psi to ensure that the end of stroke had been reached. To withdraw the core from the formation, the drill string was lifted ~1 m at a moderate speed (290 m/hr) and then lifted for 3 m at a slower rate (100 m/hr). The tool was then lifted through the drill string on the sand line (slowly at first at a rate of 6 m/min).

Once the tool was laid on the piperacker, a visual observation indicated full closure of the lower valve. The autoclave was removed and placed in the ice trough while the data logger was analyzed. This showed that the valve had closed at the seabed. A maximum pressure of 92 kbar was recorded just prior to the autoclave being immersed in the ice bath. The core was transferred from the autoclave to the shear transfer chamber, sheared, and then transferred into the logging chamber. This proved to be a difficult operation due to the tight tolerances of the ball valves. To help the core from increasing in temperature, ice bags were laid over the transfer chambers during this operation. The logging chamber was placed in the ice bath overnight (which reduced the pres-

sure to ~60 kbar) before being transferred to the Geotek V-MSCL for analysis.

Core Logging and Analysis

After having been stored in an ice bath overnight, the HYACINTH logging chamber containing Core 204-1244E-8Y (FPC 9) was loaded into the Geotek Vertical Multi-Sensor Core Logger (V-MSCL). Initially, the pressure at this stage was 60 bar. Over the next 12 hr, 17 high-resolution GRA logs were recorded. Between the logging runs, the pressure was slowly and incrementally released, and 3.8 L of gas was collected and analyzed in a process similar to that performed on Core 204-1249F-2E (HRC 4) (see "Downhole Tools and Pressure Coring," p. 20, in the "Site 1249" chapter). The initial gamma density profile indicated a single distinct zone of low density (at the logging interval of 31–37 cm), provisionally interpreted as a hydrate layer, which when depressurized formed a thin gas layer. Figure F38 shows the following three density profiles:

"Run 1" = in situ pressure before any degassing, which is assumed to be the same as the in situ density profile.
"Run 12" = during the depressurization/degassing process, showing two gas layers developing from the hydrate and the general reduction in density caused by gas exsolving from solution.
"Run 16" = the last density profile after all the gas had been removed from the system leaving only the sediments.

The density anomaly interpreted to be a hydrate in Run 1 can be accounted for by 0.5 cm of hydrate (crystal density = 0.92 g/cm³) in the 5-cm-diameter core. The lower gas layer, which formed at the base of the core, may indicate the possible presence of another discrete hydrate zone in the core catcher (below the level of logging). After all the gas had been removed, the core was X-rayed, run through the MST, split, and digitally imaged. Three IW samples were taken from Core 204-1244E-8Y (FPC 9), two near the suspected hydrate zones and one in the center of the core. These data fit well with the IW samples collected elsewhere in this hole (see "Interstitial Water Geochemistry," p. 13). It is also interesting to note that the sulfate data indicated no contamination from surface seawater, despite using surface seawater as the pressurizing fluid. It is anticipated that a detailed analysis of these data sets will provide pertinent information on the nature and structure of this region where gas hydrate forms at relatively low concentrations.

It is interesting to note that in the APC cores immediately above and below Core 204-1244E-8Y (FPC 9; Cores 7H and 9H), the thermal images from the IR camera show approximately six to eight low-temperature anomalies per core (see "Physical Properties," p. 24). This frequency of one to two anomalies per meter is commensurate with the two anomalies in density provisionally interpreted from Core 204-1244E-8Y (FPC 9). It is possible that all the hydrate in these regions of low concentration exists in the hydrate veins, and none is disseminated in the pore space.

F38. FPC core gamma density profile, p. 88.
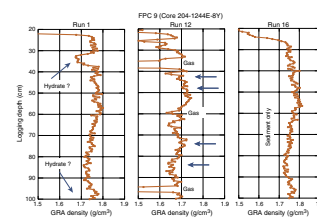
DOWNHOLE LOGGING

Logging While Drilling

Operations

Leg 204 LWD operations began on 16 July 2002 at 1330 hr, with initial BHA makeup, tool initialization, and calibration. The LWD tools (6¾-in collars) included the GeoVision Resistivity (GVR) (RAB) with a $9^{1}/_{8}$-in button sleeve, MWD (Powerpulse), NMR-MRP tool, and VND tool. The U.S. Department of Energy provided funding support to deploy the NMR-MRP tool. Memory and battery life allowed for at least 24 hr of continuous drilling. Hole 1244D was spudded at ~2300 hr at 906.00 meters below rig floor (mbrf) water depth (drillers depth) on the eastern flank of Hydrate Ridge. Drilling proceeded at ~25 m/hr to TD at 380 mbsf without difficulty, and real-time data were transmitted to the surface at a rate of 6 Hz. Some extraneous pump noise affected the data transmission for 2–5 min after each pipe addition but caused minimal real-time data loss. From the BOH, the tools were pulled out of the hole without rotating to ~355 mbsf to evaluate the effect of drilling motion on the NMR-MRP log. LWD tools and data were retrieved at the rig floor at ~0130 hr on 18 July. The total bit run was ~38 hr.

Logging Quality

Figure F39 shows the quality control logs for Hole 1244D. The target rate of penetration (ROP) of 25 m/hr (±5 m/hr) in the interval from the seafloor to TD was generally achieved. This is sufficient to record one sample per 4-cm interval (~25 samples per m), which was obtained over 85% of the total section of the hole. Using slow drilling rates enhanced the NMR-MRP porosity data, and the data sampling resolution is approximately one sample per 15-cm interval. The quality of RAB images is good, and no significant resolution loss is observed with variation in ROP in Hole 1244D. However, the quality of the RAB images in the upper 38 m of Hole 1244D (Fig. F40) is degraded by an apparent problem associated with low rates of bit rotation.

The differential caliper log (DCAL), which gives the distance between the tool sensor and the wall of the borehole as recorded by the LWD density tool, is the best indicator of borehole conditions. The differential caliper values are <1 in over 92% of the total section in Hole 1244D. Only the uppermost 38 m of the hole shows washouts >1 in. The bulk density correction (DRHO), calculated from the difference between the short- and long-spaced density measurements, varies from 0 to 0.1 g/cm³ (Fig. F39), which shows the good quality of the density measurements. A standoff of <1 in between the tool and the borehole wall indicates high-quality density measurements with an accuracy of ±0.015 g/cm³. The interval below 250 mbsf shows minor washouts resulting from borehole breakouts, with differential caliper measurements up to 1 in. Density measurements below 250 mbsf are not accurate.

Time-after-bit (TAB) measurements are 10 ± 2 min for ring resistivity and gamma ray logs and 87 ± 5 min for density and neutron porosity logs (Fig. F39). TAB values remain relatively constant, coinciding with steady ROP while drilling over most of the hole, although some large variations in ROP are observed during pipe additions toward the bottom of the hole. Large values on the DCAL and DRHO logs near the bottom of the hole also indicate that the borehole was enlarged.

F39. Quality control LWD logs, p. 89.
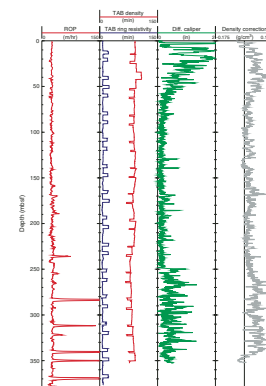
F40. LWD data, p. 90.
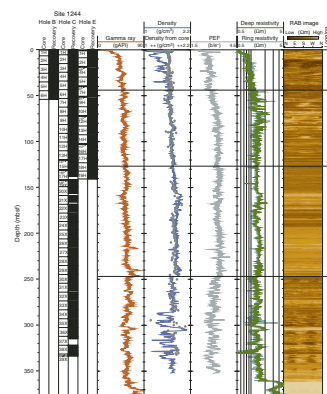
The depths, relative to seafloor, for all of the LWD logs were fixed by identifying the gamma ray signal associated with the seafloor and shifting the log data to the appropriate depth as determined by the drillers pipe tallies. For Hole 1244D, it was determined that the gamma ray log pick for the seafloor was at a depth of 906.0 mbrf. The rig floor logging datum was located 10.9 m above sea level for this hole.

Wireline Logging

Operations

Hole 1244E was APC cored to a depth of 135.8 mbsf and then drilled to a TD of 250 mbsf. Rig-up for conventional wireline logging (CWL) operations began at 2230 Universal Time Coordinated (UCT) on 20 August and final rig-down was completed by 0945 UCT on 21 August. See Table T22 for detailed information on the Hole 1244E CWL program.

CWL operations in Hole 1244E began with the deployment of the triple combo tool (Temperature/Acceleration/Pressure [TAP] tool/Dual Induction Tool [DIT]/Hostile Environment Litho-Density Tool [HLDT]/Accelerator Porosity Sonde [APS]/Hostile Environment Gamma Ray Sonde [HNGS]/Inline Checkshot Tool [QSST]) (Table T22). The triple combo tool string initially reached TD of the hole (250 mbsf) without difficulty and with no sticking problems. Excellent quality data were acquired during the main uphole pass (see below), and the tool was run back to the bottom of the hole for a second log pass. Before the start of the second log pass, several checkshots were performed with the QSST. A one-way traveltime of 733 ms was recorded at the TD of Hole 1244E (250 mbsf). To calculate a checkshot interval velocity with depth, a 32-m uphole shift is necessary to take into account the positioning of the QSST at the top of the triple combo tool string. The repeat pass of the triple combo tool was performed over an interval from 245.5 up into the drill pipe at a depth of 72.5 mbsf. TAP tool temperature data and associated depth data were recorded without problems. The triple combo logging run ended with the rig-down of the tool string, which was completed at ~0515 hr on 21 August.

For the second CWL run in Hole 1244E, the FMS-sonic string (FMS/Dipole Shear Sonic Imager [DSI]/Scintillation Gamma Ray Tool [SGT]) was deployed. The FMS-sonic tool string reached maximum depth of 250.5 mbsf on two consecutive passes. The two FMS-sonic runs confirmed the excellent condition of the hole, as observed during the triple combo log run. Both passes of the FMS-sonic tool string appeared to follow a helicoidal path throughout the entire borehole. DSI modes used in Hole 1244E were medium-frequency monopole for the first pass, low-frequency monopole for the second pass, and for both passes low-frequency mode for the lower dipole standard frequency for the upper dipole. The recorded sonic waveforms are of very high quality, particularly the dipole recordings, but the very low velocity of this formation made it difficult for the automatic slowness/time coherence (STC) picking program to select accurate V_P. Some adjustment of the STC parameters allowed for improved P-wave picks but further reprocessing was required. The quality of the recorded shear (S-) wave data was very high, but it will also require additional processing.

A final run was made for seismic experiments which will be discussed elsewhere.

T22. CWL operations summary, p. 132.

Logging Quality

All logging data from the triple combo and FMS-sonic runs in Hole 1244E are of very high quality (Figs. F41, F42, F43, F44). The hole conditions were excellent, with an almost straight HLDT caliper measurement from 11.4 to 12.0 in, on average. Comparison of logs from successive passes shows good repeatability of the data. The two passes of the FMS calipers also showed that the hole was nearly cylindrical, consistent with the HLDT log caliper recorded on the triple combo runs.

The absolute depths, relative to seafloor, for all of the CWL logs were fixed by identifying the gamma ray signal associated with the seafloor and depth shifting the log data appropriately. The gamma ray pick for the seafloor in Hole 1244E was 904.5 mbrf for all of the CWL runs.

Interpretation of Logging-While-Drilling and Wireline Logs

Holes 1244D and 1244E show excellent quality LWD and CWL logs. The presence of gas hydrate was identified from ~40 to 127 mbsf by high resistivities, high acoustic velocities, and RAB image anomalies, allowing quantitative estimates of gas hydrate saturations. RAB imaging also revealed evidence of fractures filled with gas hydrate. Low- and high-density interbedding is observed below the GHSZ (~127 mbsf), which may indicate lithologic changes within lithostratigraphic Unit II associated with turbidites, ash layers, and/or the presence of gas. Borehole breakouts, which result from horizontal stress differences, are observed in the lower portion of the hole. NMR-MRP data were transmitted to shore for processing, to estimate bound fluid volume and total free-fluid porosity and for comparison with neutron, density, and core porosity estimates.

Comparison of Logging-While-Drilling and Wireline Logs

Figure F43 shows a comparison of downhole LWD and CWL data from Holes 1244D and 1244E, using the gamma ray, neutron porosity, density, photoelectric factor, and deep-resistivity logs. The highly variable CWL logging data within the upper 75 mbsf of Hole 1244E was obtained through the drill pipe. Comparison of similar logging signatures on Figure F43 reveals that the CWL logging data from Hole 1244E are ~4 m deeper than the LWD from Hole 1244D. This difference is best shown with the deep resistivity and density logs from the two holes. At a depth of ~156 mbsf in Hole 1244D, the LWD density and resistivity logs show a distinct increase in value; however, this same log response is at a depth of ~160 mbsf on the CWL data from Hole 1244E. This difference is best explained by local variability in the geology of this site, with Hole 1244E being drilled more than 90 m southeast of Hole 1244D. After taking into account the apparent depth offset between Holes 1244D and 1244E, it can be seen that the LWD and CWL data from each hole match relatively well (Fig. F43), exhibiting similar curve shapes and absolute log values. The CWL (Hole 1244E) and LWD (Hole 1244D) resistivity logs exhibit differences in measured values with depth and a difference in the apparent vertical resolution of each device, with the RAB (LWD) tool yielding a log with a higher vertical resolution.

F41. CWL data, p. 91.
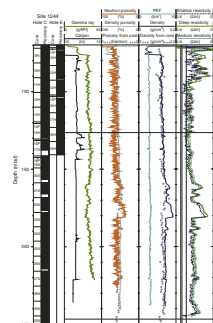
F42. CWL gamma ray data, p. 92.
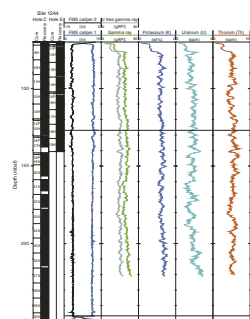
F43. Comparison of LWD and CWL, p. 93.
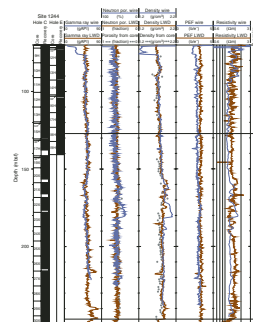
F44. CWL acoustic logging data, p. 94.
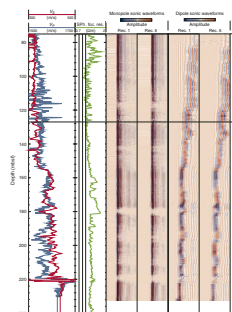
Logging Units

The logged section in Holes 1244D and 1244E is divided into four "logging units" on the basis of obvious changes in the LWD and CWL gamma ray, density, electrical resistivity (Figs. **F40, F41, F42**), and acoustic transit-time measurements (Fig. **F44**).

Logging Unit 1 (0–43 mbsf) is characterized by increasing resistivities and densities with depth as measured by the LWD tools. However, this trend in the downhole log data is probably due in part to degraded log measurements within the enlarged portion of the near-surface borehole as shown in Figure **F39** and evidenced by the discrepancy between the core and LWD log density data between 0 and 30 mbsf (Fig. **F40**). The base of logging Unit 1 does not coincide with the base of lithostratigraphic Unit I (0–62 mbsf), which is composed of clay to silty clay sediments. The transition from of logging Unit 1 to 2 is defined by a sharp increase in electrical resistivity.

Logging Unit 2 (43–127 mbsf) is characterized by zones of distinct high resistivities and high compressional velocities (V_P), with peak resistivity values exceeding 2 Ωm and V_P recorded at >1.65 km/s. The gamma ray logs in this unit show a characteristic cyclicity of values that may reflect the interbedded sand and clay turbidite sequences as described by the shipboard sedimentologists for lithostratigraphic Unit II (62–250 mbsf) (see **"Lithostratigraphic Unit II,"** p. 5, in "Lithostratigraphic Units" in "Lithostratigraphy"). The downhole log-measured density increases with depth in logging Unit 2 (1.7 g/cm³ at the top to near 2.0 g/cm³ at the bottom). In Hole 1244E (Fig. **F44**), the acoustic transit-time log has been used to precisely select the depth of the boundary between logging Units 2 and 3, which is marked by a drop in V_P to <1.55 km/s. Also noted on the LWD density log is a subtle drop in bulk density at the contact from logging Unit 2 into 3, which corresponds to the depth of the BSR at this site.

Logging Unit 3 (127–247 mbsf) correlates with the lower part of lithostratigraphic Unit II (62–250 mbsf), which is described as an interbedded sand, silt, and clay turbidite sequence. Logging Unit 3 is generally characterized by lower and more uniform resistivities and acoustic velocities compared to logging Unit 2. The transition from logging Unit 3 to 4 is marked by an abrupt drop in electrical resistivity (from ~1.3 to 1.0 Ωm) and bulk density (from ~1.9 to 1.6 g/cm³) (Fig. **F40**), which appears to mark the contact with the deformed sediments of the accretionary complex.

Logging Unit 4 (247–380 mbsf; TD of Hole 1244D), reflecting the upper portion of the deformed sediments of the accretionary complex, is characterized by highly variable resistivity and density measurements that are in part the result of enlarged borehole breakouts (with DCAL values >1 in) but also reflect lithologic variation. The breakouts appear consistent with a northeast-southwest orientation in the borehole.

Resistivity-at-the-Bit and Formation MicroScanner Images

Both the RAB and FMS tools produce high-resolution images of the electrical resistivity of the borehole wall that can be used for detailed sedimentological and structural interpretations. It is also possible to use the RAB and the FMS tools to make high-resolution electrical images of gas hydrates in the borehole thus yielding information about the nature and texture of gas hydrates in sediments. The resolution of the images from the RAB tool is considerably lower than the resolution of the

images from the FMS. For example, the RAB images have about a 5- to 10-cm vertical resolution, whereas the FMS tool can resolve features such as microfractures with widths <1 cm. However, the RAB tool provides 360° coverage of the borehole, whereas FMS images cover only ~30% of the hole.

The RAB image in Figure F45 is from within the zone of expected gas hydrate stability in Hole 1244D. This RAB image is characterized by light (high resistivity) to dark (low resistivity) bands, which, in many cases, can be traced across the display as sine waves. These light continuous high-resistivity sine wave bands likely represent gas hydrate occupying moderately to steeply dipping fractures (east-northeast dip direction) in Hole 1244D.

In Figure F46, we have cross correlated a RAB image (Hole 1244D) and an FMS image (Hole 1244E) of an ash layer, as identified by the shipboard sedimentologists at a depth of ~216 mbsf in Hole 1244C (see "Lithostratigraphic Unit II," p. 5, in "Lithostratigraphic Units," in "Lithostratigraphy"). As shown in Figure F46, the ash layer, imaged by the RAB and FMS tools, appears as a complex interbedded zone of high and low resistivities. More detailed examination of the FMS image shows distinct lateral variability within this ash layer.

As described above, logging Unit 3 (127–247 mbsf) correlates with the lower part of lithostratigraphic Unit II (62–250 mbsf) (see "Lithostratigraphic Unit II," p. 5, in "Lithostratigraphic Units," in "Lithostratigraphy"), which is described as an interbedded sand, silt, and clay turbidite sequence. The RAB and FMS images in Figure F47, from logging Unit 3 in Holes 1244D and 1244E, are characterized by interbedded light (resistive) and dark (conductive) layers. The darker, more conductive layers usually represent the more porous, coarser-grained fraction of the turbidite sequence where the conductive drilling fluids have penetrated more deeply into the formation.

During Leg 204, the RAB images proved to be a very useful tool with which to evaluate the occurrence of borehole breakouts, which are the product of differential horizontal stress acting on the borehole. In Figure F48, the RAB image from Hole 1244D shows a dominant set of parallel borehole breakouts oriented approximately east-northeast to west-southwest.

Logging Porosities

Sediment porosities can be determined from analyses of recovered cores and from numerous borehole measurements (see p. 22, and "Downhole Logging," p. 43, in the "Explanatory Notes" chapter). Data from the LWD density, neutron, and nuclear magnetic resonance logs have been used to calculate sediment porosities for Hole 1244D. Core-derived physical property data, including porosities (see "Physical Properties," p. 24), have been used to both calibrate and evaluate the log-derived sediment porosities.

The VND LWD log-derived measurements of density in Hole 1244D (Fig. F40) are relatively consistent within the upper 285 mbsf of the hole, with values ranging from ~1.4 g/cm³ near the seafloor to over 1.8 g/cm³ at the bottom of logging Unit 3 at 247 mbsf. The density log measurements are degraded in logging Unit 4 as discussed earlier in this chapter. The LWD log-derived density measurements (ρ_b) from Hole 1244D were used to calculate sediment porosities (ϕ) using the standard density-porosity relation,

F45. RAB image showing the presence of gas hydrate, p. 95.
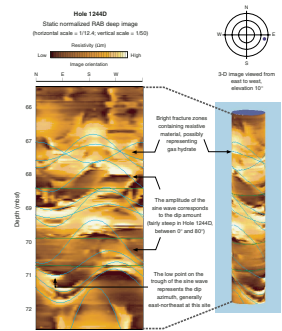
F46. RAB and FMS images showing an ash layer, p. 96.
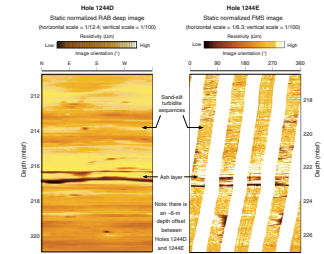
F47. RAB and FMS images showing turbidites, p. 97.
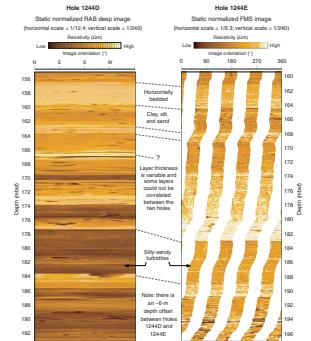
F48. RAB image showing borehole breakouts, p. 98.
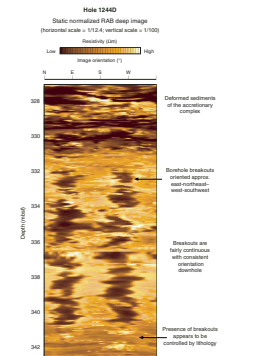
$$\phi = (\rho_m - \rho_b)/(\rho_m - \rho_w).$$

Water densities (ρ_w) were assumed to be constant and equal to 1.05 g/cm³; however, variable core-derived grain/matrix densities were assumed for each log density-porosity calculation. The core-derived grain densities (ρ_m) for Hole 1244D ranged from an average value at the seafloor of 2.69 g/cm³ to about 2.71 g/cm³ at the bottom of the hole (see "Physical Properties," p. 24). The density log-derived porosities in logging Units 1–3 (0–247 mbsf) of Hole 1244D range from ~40% to 70% (Fig. F49). However, the density log porosities in logging Unit 4 (247–380 mbsf) are more variable, ranging from 35% to 95%, which is in part controlled by poor borehole conditions.

The LWD neutron porosity log from Hole 1244D (Fig. F49) yielded sediment porosities ranging from an average value at the top of the logged section of ~70% to ~60% in logging Unit 4. The "total" sediment porosities derived by the NMR-MRP tool in Hole 1244D (Fig. F49) ranged from ~80% near the seafloor to ~0% near the bottom of the hole.

In studies of downhole log data it is common to compare porosity data from different sources to evaluate the results of particular measurements. The comparison of core-derived and LWD log-derived porosities in Figure F49 reveals that the density log-derived porosities are generally similar to the core porosities in logging Units 1 though 3 (0–247 mbsf). However, the density log-derived porosities are generally higher than the core porosities in Unit 4. The neutron log-derived porosities are generally similar to the core-derived porosities in logging Units 1 and 2, but the neutron log porosities are higher than the core-derived porosities throughout most of logging Unit 3. The NMR-MRP porosities are generally lower than the core-derived porosities in logging Units 2 through 3. The NMR-MRP porosities in logging Unit 1 (above ~25 mbsf) appear to have been significantly degraded by washouts in the upper part of the hole. The NMR-MRP porosity log also exhibits numerous low-porosity zones throughout the entire hole, which will be further evaluated after the cruise.

Gas Hydrate

The presence of gas hydrates at Site 1244 was documented by direct sampling, with several pieces of gas hydrate being recovered in Holes 1244C and 1244E within the depth interval from 49.94 to 126.70 mbsf. Despite these limited occurrences of visible gas hydrates, it was inferred, based on geochemical core analyses (see "Interstitial Water Geochemistry," p. 13), IR image analysis of cores (see "Physical Properties," p. 24), and downhole logging data, that disseminated gas hydrate is present in logging Unit 2. As previously discussed in "Downhole Logging," p. 43, in the "Explanatory Notes" chapter, gas hydrate occurrences are generally characterized by increases in log-measured electrical resistivities and acoustic velocities. Logging Unit 2 at Site 1244 is characterized by a distinct stepwise increase in both electrical resistivities and acoustic velocities. In addition, the RAB images reveal several thin high-resistivity zones within logging Unit 1 (0–43 mbsf), suggesting the possible occurrence of gas hydrate.

Resistivity log data have been used to quantify the amount of gas hydrate at Site 1244. For the purpose of this discussion, it is assumed that the high resistivities and velocities measured in logging Unit 2 are due to the presence of gas hydrate. Archie's Relation,

F49. Comparison of LWD and core-derived porosities, p. 99.
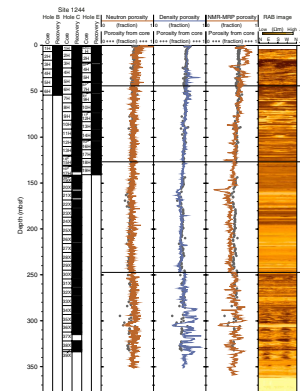
$$S_w = (aR_w/\phi^m R_t)^{1/n}$$

(see **"Downhole Logging,"** p. 43, in the "Explanatory Notes" chapter), was used with resistivity data (R_t) from the LWD-RAB tool and porosity data (ϕ) from the LWD density tool to calculate water saturations in Hole 1244D. It should be noted that gas hydrate saturation (S_h) is the measurement of the percentage of pore space in sediment occupied by gas hydrate, which is the mathematical complement of Archie-derived pore water saturations (S_w), with

$$S_h = 1 - S_w.$$

For Archie's Relation, the formation water resistivity (R_w) was calculated from recovered core water samples and the Archie a and m variables were calculated using a crossplot technique, which compares the downhole log-derived resistivities and density porosities. See Collett and Ladd (2000) for the details on how to calculate the required formation water resistivities and Archie variables. The values used at Site 1244 were: a = 1, m = 2.8, and u = 1.9386.

The Archie Relation yielded water saturations (Fig. **F50**) ranging from an average minimum value of ~75% to a maximum of 100% in logging Unit 2 (43–127 mbsf) of Hole 1244D, which implies the gas hydrate saturations in logging Unit 2 range from 0% to 25%. It also appears that logging Unit 1 may contain several thin gas hydrate–bearing intervals. However, the low water saturations shown in logging Unit 3 (Fig. **F50**) correspond to zones that exhibit low acoustic velocities on the downhole-recorded acoustic wireline logs (Fig. **F44**), which is indicative of free gas–bearing sediments.

Temperature Data

The LDEO TAP tool was deployed on the triple combo tool string in Hole 1244E (F48. **F51**). During the process of coring and drilling, cold seawater is circulated in the hole cooling the formation surrounding the borehole. Once drilling ceases, the temperature of the fluids in the borehole gradually rebound to the in situ equilibrium formation temperatures. Thus, the temperature data from the TAP tool can not be easily used to assess the nature of the in situ equilibrium temperatures. However, the plot of the first pass downgoing temperature profile in Figure **F51** reveals several gradient changes that were caused by borehole temperature anomalies. The temperature anomaly at 87.5 mbsf is the base of the drill pipe during the initial descent of the triple combo tool string. The break in the slope of first pass down going temperature log at a depth ~120 mbsf is near the depth of the BSR (127 mbsf) at this site.

F50. LWD-derived water saturations, p. 100.
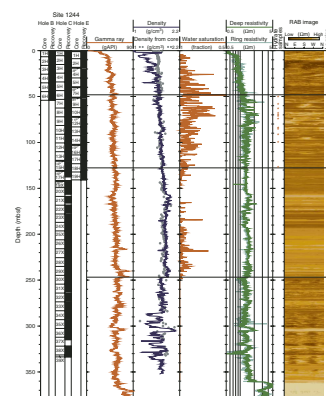
F51. Borehole temperatures recorded with the TAP tool, p. 101.
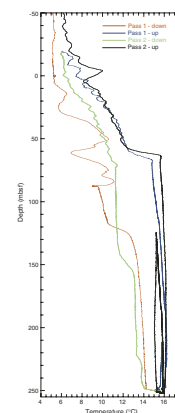
REFERENCES

Alperin, M.J., Reeburgh, W.S., and Whiticar, M.J., 1988. Carbon and hydrogen fractionation resulting from anaerobic methane oxidation. *Global Biogeochem. Cycles,* 2:279–288.

Behrmann, J.H., Lewis, S.D., Musgrave, R.J., et al., 1992. *Proc. ODP, Init. Repts.,* 141: College Station, TX (Ocean Drilling Program).

Berggren, W.A., Kent, D.V., Swisher, C.C., III, and Aubry, M.-P., 1995. A revised Cenozoic geochronology and chronostratigraphy. *In* Berggren, W.A., Kent, D.V., Aubry, M.-P., and Hardenbol, J. (Eds.), *Geochronology, Time Scales and Global Stratigraphic Correlation.* Spec. Publ.—SEPM, 54:129–212.

Berner, R.A., 1980. *Early Diagenesis: A Theoretical Approach:* Princeton, NJ (Princeton Univ. Press).

Boetius, A., Ravenschlag, K., Schubert, C.J., Rickert, D., Widdel, F., Gieseke, A., Amann, R., Jørgensen, B.B., Witte, U., and Pfannkuche, O., 2000. A marine microbial consortium apparently mediating the anaerobic oxidation of methane. *Nature,* 407:623–626.

Borowski, W.S., Hoehler, T.M., Alperin, M.J., Rodriguez, N.M., and Paull, C.K., 2000. Significance of anaerobic methane oxidation in methane-rich sediments overlying the Blake Ridge gas hydrates. *In* Paull, C.K., Matsumoto, R., Wallace, P.J., and Dillon, W.P. (Eds.), *Proc. ODP, Sci. Results,* 164: College Station, TX (Ocean Drilling Program), 87–99.

Borowski, W.S., Paull, C.K., and Ussler, W., III, 1996. Marine pore-water sulfate profiles indicate in situ methane flux from underlying gas hydrate. *Geology,* 24:655–658.

————, 1997. Carbon cycling within the upper methanogenic zone of continental rise sediments: an example from the methane-rich sediments overlying the Blake Ridge gas hydrate deposits. *Mar. Chem.,* 57:299–311.

Brumsack, H.-J., and Gieskes, J.M., 1983. Interstitial water trace-metal chemistry of laminated sediments from the Gulf of California, Mexico. *Mar. Chem.,* 14:89–106.

Clague, D., Maher, N., and Paull, C.K., 2001. High-resolution multibeam survey of Hydrate Ridge, offshore Oregon. *In* Paul, C.K., and Dillon, W.P. (Eds.), *Natural Gas Hydrates: Occurrence, Distribution, and Detection.* Am. Geophys. Union, Geophys. Monogr. Ser., 124:297–306.

Collett, T.S., and Ladd, J., 2000. Detection of gas hydrate with downhole logs and assessment of gas hydrate concentrations (saturations) and gas volumes on the Blake Ridge with electrical resistivity log data. *In* Paull, C.K., Matsumoto, R., Wallace, P.J., and Dillon, W.P. (Eds.), *Proc. ODP, Sci. Results,* 164: College Station, TX (Ocean Drilling Program), 179–191.

Collier, R., and Edmond, J., 1984. The trace element geochemistry of marine biogenic particulate matter. *Prog. Oceanogr.,* 13:113–199.

Dehairs, F., Chesselet, R., and Jedwab, J., 1980. Discrete suspended particles of barite and the barium cycle in the open ocean. *Earth Planet. Sci. Lett.,* 49:528–550.

Deyhle, A., Kopf, A., and Eisenhauer, A., 2001. Boron systematics of authigenic carbonates: a new approach to identify fluid processes in accretionary prisms. *Earth Planet. Sci. Lett.,* 187:191–205.

D'Hondt, S.L., Jørgensen, B.B., Miller, D.J., et al., 2003. *Proc. ODP, Init. Repts.,* 201 [CD-ROM]. Available from: Ocean Drilling Program, Texas A&M University, College Station TX 77845-9547, USA.

Dickens, G.R., 2001. Sulfate profiles and barium fronts in sediment on the Blake Ridge: present and past methane fluxes through a large gas hydrate reservoir. *Geochim. Cosmochim. Acta,* 65:529–543.

Dickens, G.R., Paull, C.K., and Wallace, P., 1997. Direct measurement of in situ methane quantities in a large gas-hydrate reservoir. *Nature,* 385:426–428.

Duan, Z., Møller, N., Greenberg, J., and Weare, J.H., 1992. The prediction of methane solubility in natural waters to high ionic strengths from 0° to 250°C and from 0 to 1600 bar. *Geochim. Cosmochim. Acta,* 56:1451–1460.

Dymond, J., Suess, E., and Lyle, M., 1992. Barium in deep-sea sediment: a geochemical proxy for paleoproductivity. *Paleoceanography,* 7:163–181.

Edmond, J.M., Measures, C., McDuff, R.E., Chan, L.H., Collier, R., and Grant, B., 1979. Ridge crest hydrothermal activity and the balances of the major and minor elements in the ocean: the Galapagos data. *Earth Planet. Sci. Lett.,* 46:1–18.

Handa, Y.P., 1990. Effect of hydrostatic pressure and salinity on the stability of gas hydrates. *J. Phys. Chem.,* 94:2652–2657.

Hesse, R., 2003. Pore anomalies of submarine gas-hydrate zones as tool to assess hydrate abundance and distribution in the subsurface. What have we learned in the past decade? *Earth Sci. Rev.,* 61:149–179.

Hesse, R., and Harrison, W.E., 1981. Gas hydrates (clathrates) causing pore-water freshening and oxygen isotope fractionation in deep-water sedimentary sections of terrigenous continental margins. *Earth Planet. Sci. Lett.,* 55:453–462.

Hoehler, T.M., Borowski, W.S., Alperin, M.J., Rodriguez, N.M., and Paull, C.K., 2000. Model, stable isotope, and radiotracer characterization of anaerobic methane oxidation in gas hydrate–bearing sediments of the Blake Ridge. *In* Paull, C.K., Matsumoto, R., Wallace, P.J., and Dillon, W.P. (Eds.), *Proc. ODP, Sci. Results,* 164: College Station, TX (Ocean Drilling Program), 79–85.

Kastner, M., Kvenvolden, K.A., Whiticar, M.J., Camerlenghi, A., and Lorenson, T.D., 1995. Relation between pore fluid chemistry and gas hydrates associated with bottom-simulating reflectors at the Cascadia margin, Sites 889 and 892. *In* Carson, B., Westbrook, G.K., Musgrave, R.J., and Suess, E. (Eds.), *Proc. ODP, Sci. Results,* 146 (Pt 1): College Station, TX (Ocean Drilling Program), 175–187.

Kvenvolden, K.A., and Lorenson, T.D., 2000. Methane and other hydrocarbon gases in sediment from the southeastern North American continental margin. *In* Paull, C.K., Matsumoto, R., Wallace, P.J., and Dillon, W.P. (Eds.), *Proc. ODP, Sci. Results,* 164: College Station, TX (Ocean Drilling Program), 29–36.

Maekawa, T., Itoh, S. Sakata, S., Igari, S., and Imai, N., 1995. Pressure and temperature conditions for methane hydrate dissociation in sodium chloride solutions. *Geochem. J.,* 29:325–329.

Martini, E., and Müller, C., 1986. Current Tertiary and Quaternary calcareous nannoplankton stratigraphy and correlations. *Newsl. Stratigr.,* 16:99–112.

McDuff, R.E., 1985. The chemistry of interstitial waters, Deep Sea Drilling Project Leg 86. *In* Heath, G.R., Burckle, L.H., et al., *Init. Repts. DSDP,* 86: Washington (U.S. Govt. Printing Office), 675–687.

Michaelis, W., Seifert, R., Nauhaus, K., Treude, T., Thiel, V., Blumenberg, M., Knittel, K., Gieseke, A., Peterknecht, K., Pape, T., Boetius, A., Amann, R., Jørgensen, B.B., Widdel, F., Peckmann, J., Pimenov, N.V., and Gulin, M.B., 2002. Microbial reefs in the Black Sea fueled by anaerobic oxidation of methane. *Science,* 297:1013–1015.

Nelson, C.H., Kulm, L.D., Carlson, P.R., and Duncan, J.R., 1968. Mazama ash in the northeastern Pacific. *Science,* 161:47–49.

Orphan, V., House, C.H., Hinrichs, K.-U., McKeegan, K.D., and DeLong, E.F., 2002. Multiple archaeal groups mediate methane oxidation in anoxic cold seep sediments. *Proc. Natl. Acad. Sci. U.S.A.,* 99:7663–7668.

Paull, C.K., Matsumoto, R., Wallace, P.J., et al., 1996. *Proc. ODP, Init. Repts.,* 164: College Station, TX (Ocean Drilling Program).

Paull, C.K., and Ussler, W., III, 2001. History and significance of gas sampling during DSDP and ODP drilling associated with gas hydrates. *In* Paull, C.K., and Dillon, W.P. (Eds.), *Natural Gas Hydrates: Occurrence, Distribution, and Detection.* Am. Geophys. Union, Geophys. Monogr. Ser., 124:53–66.

Paytan, A., and Kastner, M., 1996. Benthic Ba fluxes in the central equatorial Pacific, implications for the oceanic Ba cycle. *Earth Planet. Sci. Lett.,* 142:439–450.

Perch-Nielsen, K., 1985. Cenozoic calcareous nannofossils. *In* Bolli, H.M., Saunders, J.B., and Perch-Nielsen, K. (Eds.), *Plankton Stratigraphy:* Cambridge (Cambridge Univ. Press), 427–554.

Pimmel, A., and Claypool, G., 2001. Introduction to shipboard organic geochemistry on the *JOIDES Resolution. ODP Tech. Note,* 30 [Online]. Available from World Wide Web: <http://www-odp.tamu.edu/publications/tnotes/tn30/INDEX.HTM>. [Cited 2002-07-03]

Reeburgh, W.S., 1976. Methane consumption in Cariaco Trench waters and sediments. *Earth Planet. Sci. Lett.,* 28:337–344.

Rodriguez, N.M., Paull, C.K., and Borowski, W.S., 2000. Zonation of authigenic carbonates within gas hydrate-bearing sedimentary sections on the Blake Ridge: offshore southeastern North America. *In* Paull, C.K., Matsumoto, R., Wallace, P.J., and Dillon, W.P. (Eds.), *Proc. ODP, Sci. Results,* 164, 301–312 [CD-ROM]. Available from: Ocean Drilling Program, Texas A&M University, College Station, TX 77845-9547, U.S.A.

Schrag, D.P., and DePaolo, D.J., 1993. Determination of $\delta^{18}O$ of seawater in the deep ocean during the last glacial maximum. *Paleoceanography,* 8:1–6.

Seyfried, W.E., Jr., Janecky, D.R., and Mottl, M.J., 1984. Alteration of the oceanic crust: implications for geochemical cycles of lithium and boron. *Geochim. Cosmochim. Acta,* 48:557–569.

Torres, M.E., Brumsack, H.-J., Bohrmann, G., and Emeis, K.C., 1996. Barite fronts in continental margin sediments: a new look at barium remobilization in the zone of sulfate reduction and formation of heavy barites in diagenetic fronts. *Chem. Geol.,* 127:125–139.

Wellsbury, P., Goodman, K., Cragg, B.A., and Parkes, R.J., 2000. The geomicrobiology of deep marine sediments from Blake Ridge containing methane hydrate (Sites 994, 995, and 997). *In* Paull, C.K., Matsumoto, R., Wallace, P.J., and Dillon, W.P. (Eds.), *Proc. ODP, Sci. Results,* 164: College Station, TX (Ocean Drilling Program), 379–391.

Westbrook, G.K., Carson, B., Musgrave, R.J., et al., 1994. *Proc. ODP, Init. Repts.,* 146 (Pt. 1): College Station, TX (Ocean Drilling Program).

Zhang, C.L., Li, Y., Wall, J.D., Larsen, L., Sassen, R., Huang, Y., Wang, Y., Peacock, A., White, D.C., Horita, J., and Cole, D.R., 2002. Lipid and carbon isotopic evidence of methane-oxidizing and sulfate-reducing bacteria in association with gas hydrates from the Gulf of Mexico. *Geology,* 20:239–242.

Figure F1. Bathymetric map showing locations of holes drilled at Site 1244. Bathymetry from EM300 data acquired by Monterey Bay Aquarium Research Institute (MBARI) (Clague et al., 2001).
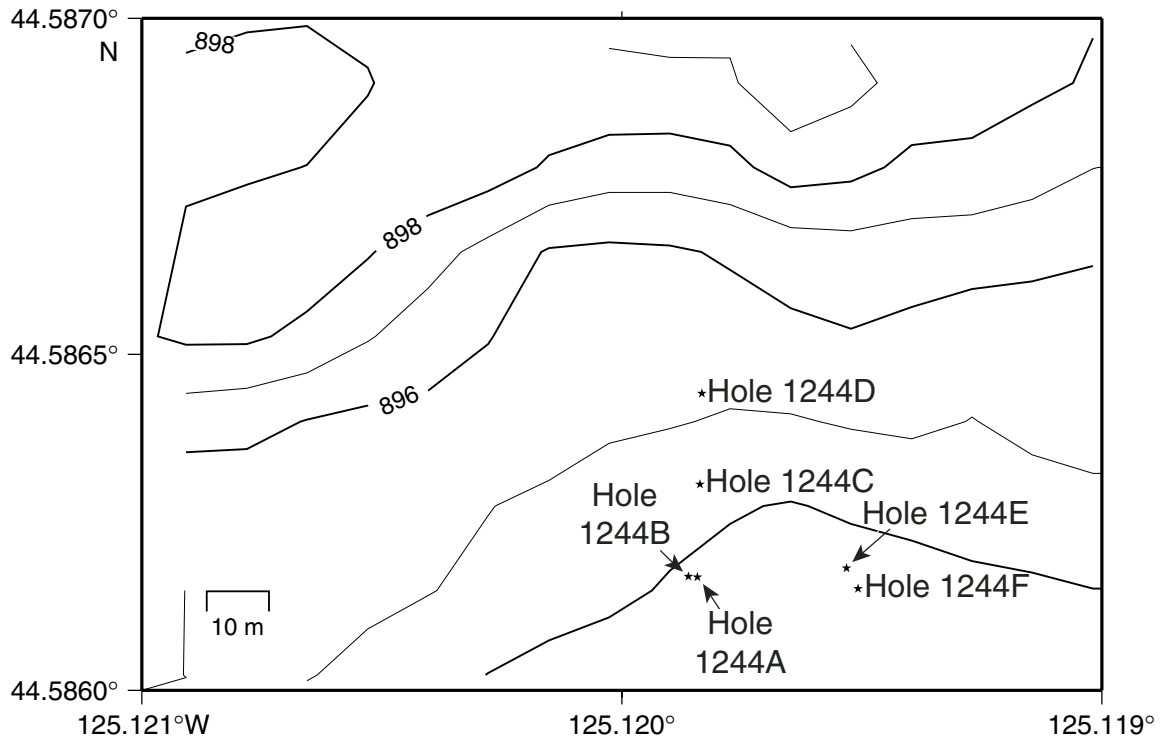
Figure F2. Lithostratigraphic summary for Holes 1244C and 1244E. (Continued on next two pages.)
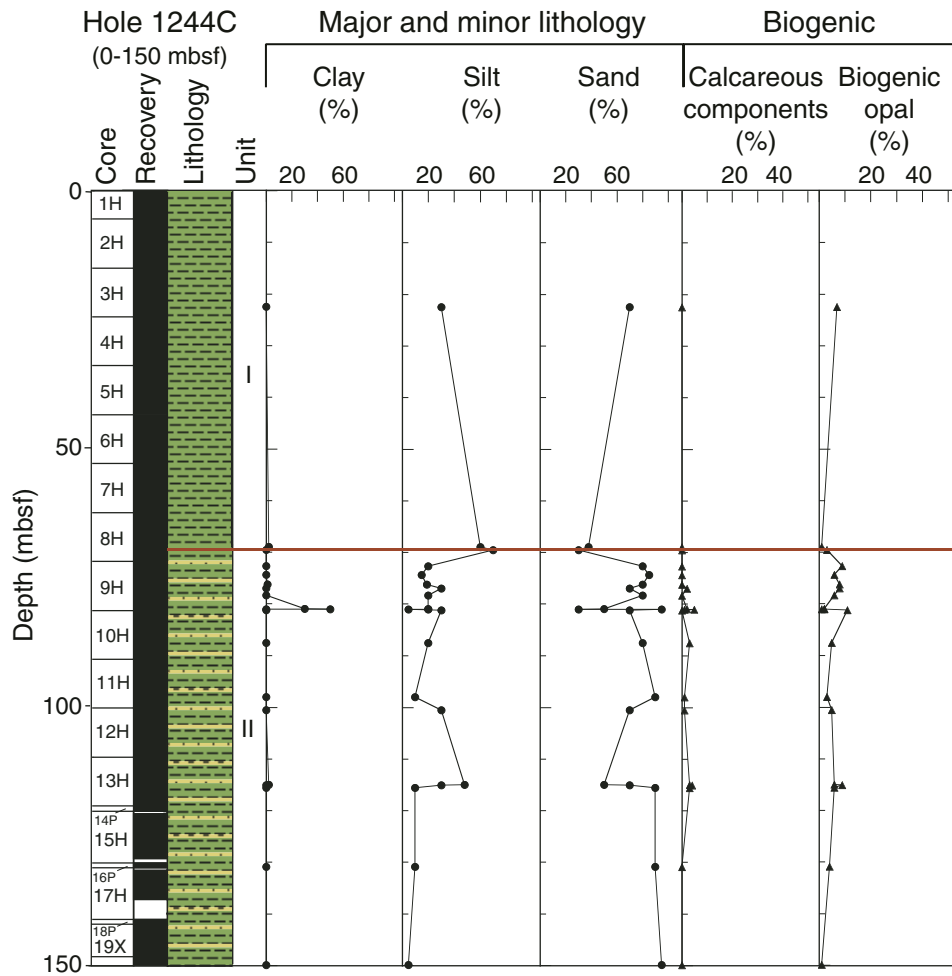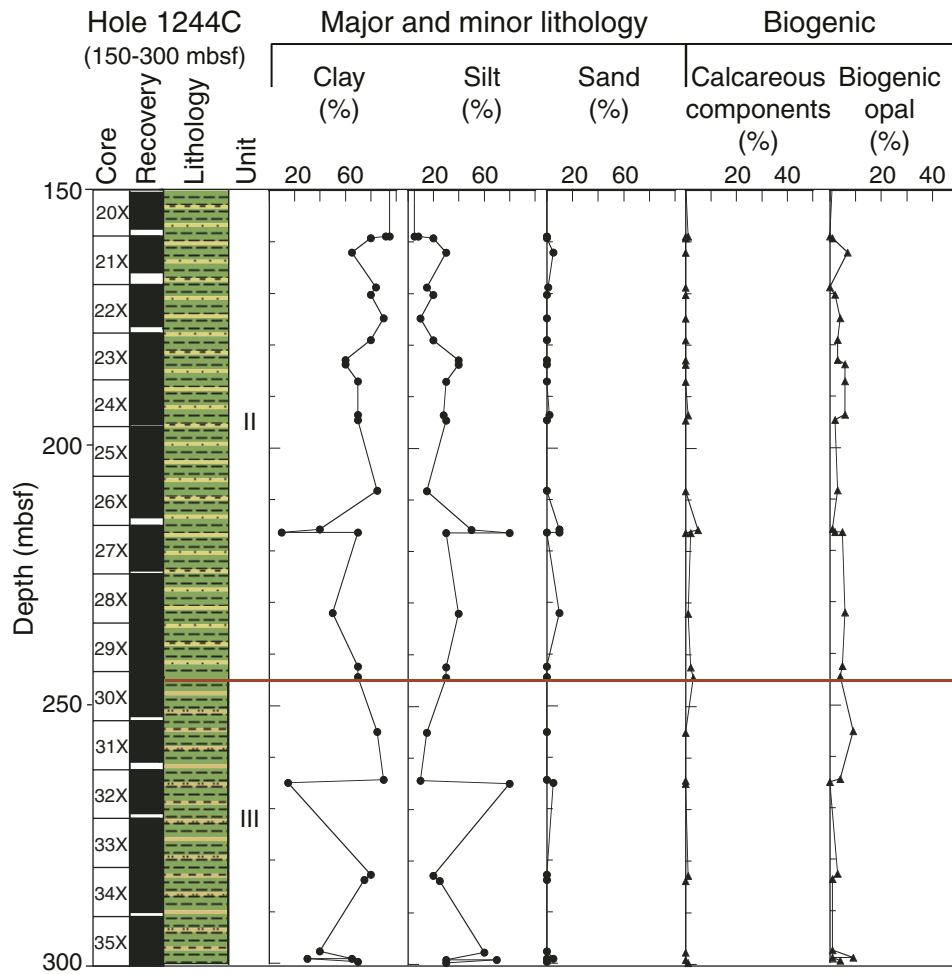
Figure F2 (continued).

Figure F2 (continued).

Clay with silty clay interlayers

Silty clay with silt and sand interlayers

Claystone and silty claystone with silt interlayers

● Major lithologies

◇ Minor lithologies

▲ Biogenic components in major and minor lithologies
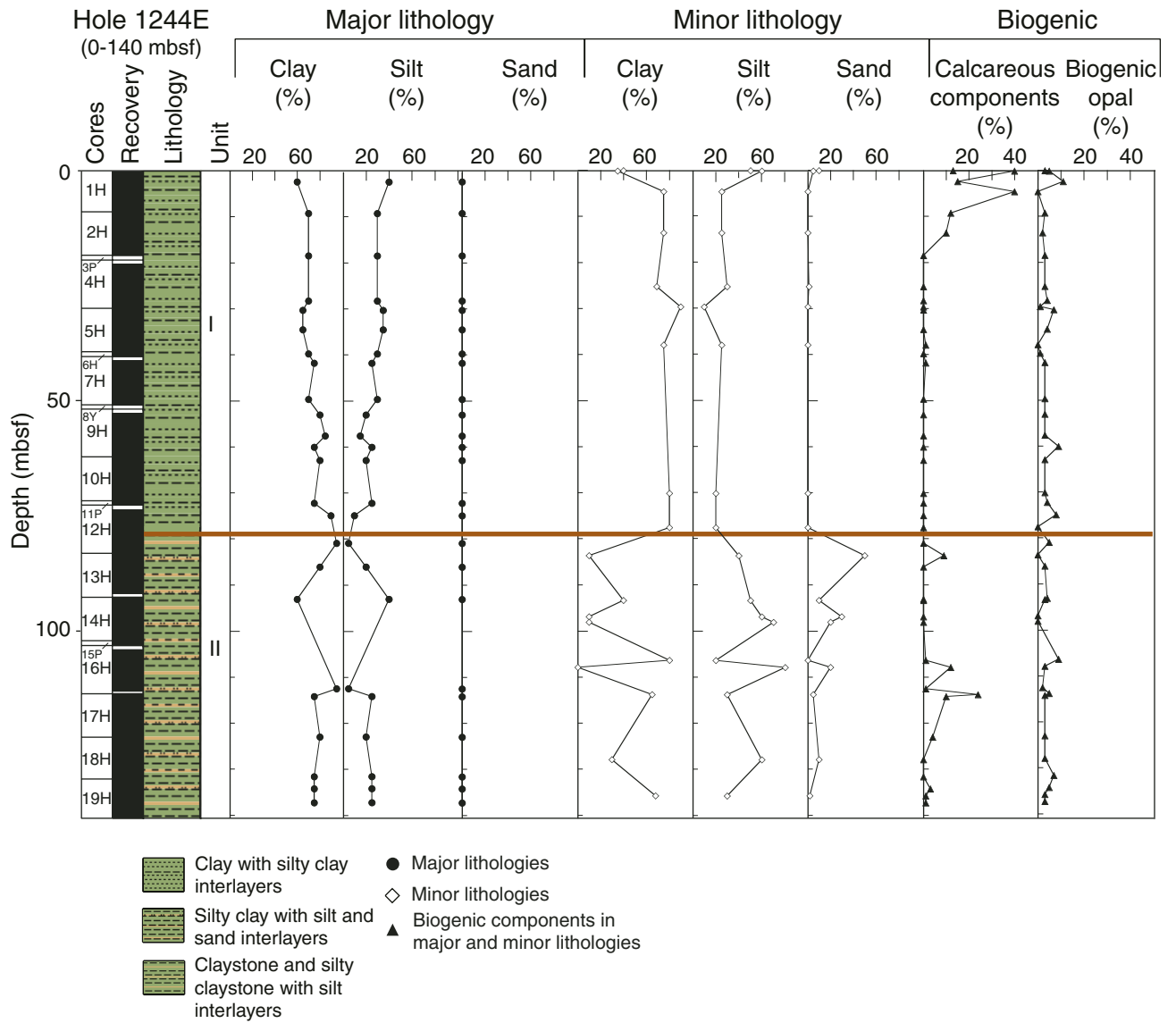
Figure F3. Close-up photograph of a carbonate nodule from lithostratigraphic Unit I (interval 204-1244B-3H-7, 65–80 cm).
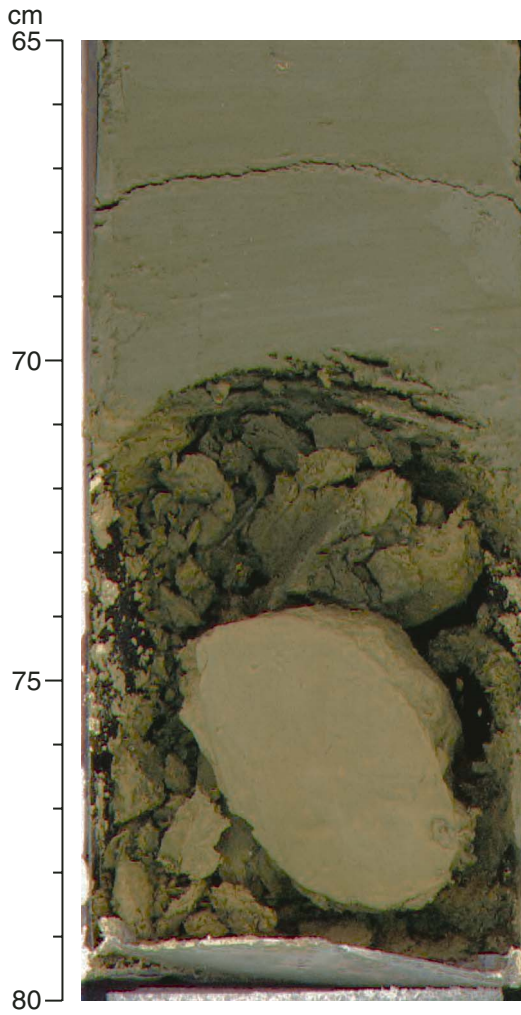
Figure F4. Photomicrograph of biogenic opal-rich clay from lithostratigraphic Unit I (Sample **204-1244C-9H-4, 50 cm**).
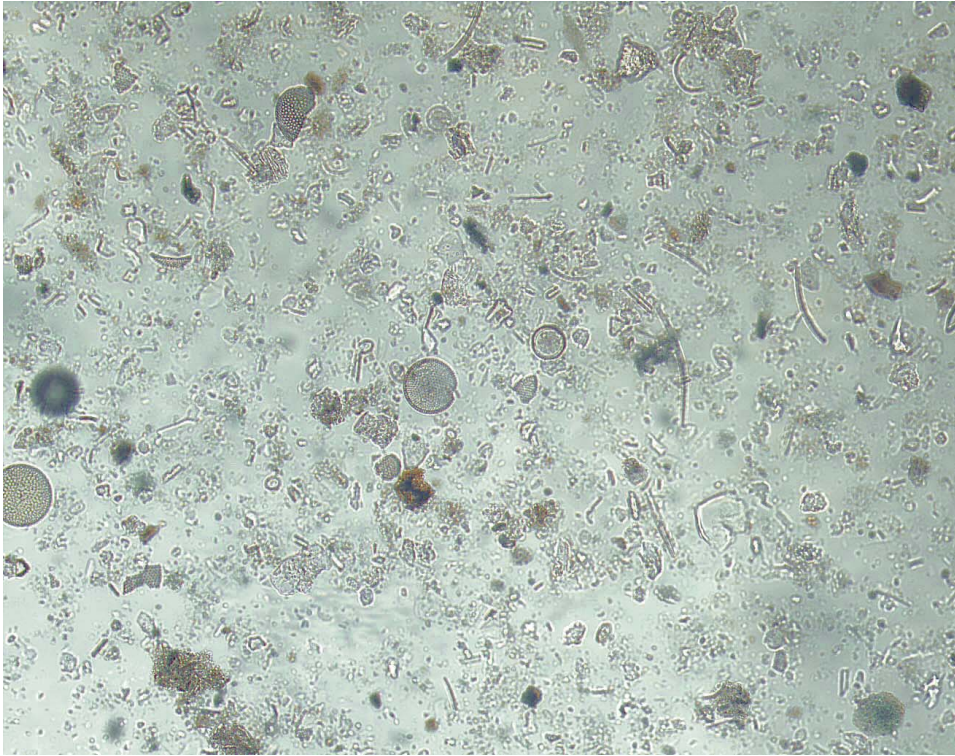
100 µm

Figure F5. Close-up photograph of a turbidite from lithostratigraphic Unit II (interval 204-1244C-13H-4, 40–80 cm). The sand layer at 54 cm marks the base of the turbidite. Above this coarse base, the sediment grades to the silty clay of the turbidite tail. Below the base of the turbidite, the sediment is highly bioturbated. These characteristics are common to most of the turbidites found throughout lithostratigraphic Unit II.
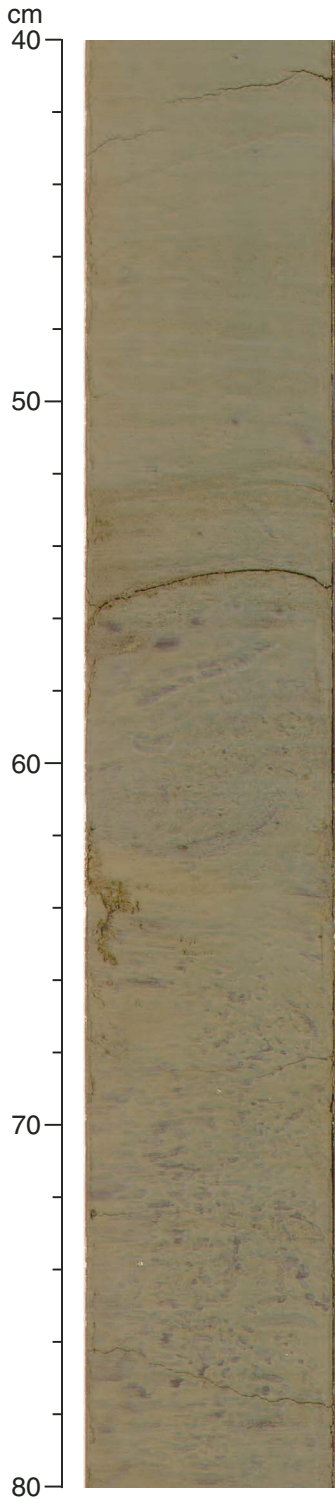
Figure F6. Close-up photograph of ash layer (Horizon B′) in lithostratigraphic Unit II (interval 204-1244C-27X-1, 45–70 cm). The base of the ash is present at 61 cm. This horizon extends to the top of the section but is not seen in the previous core because of poor recovery.
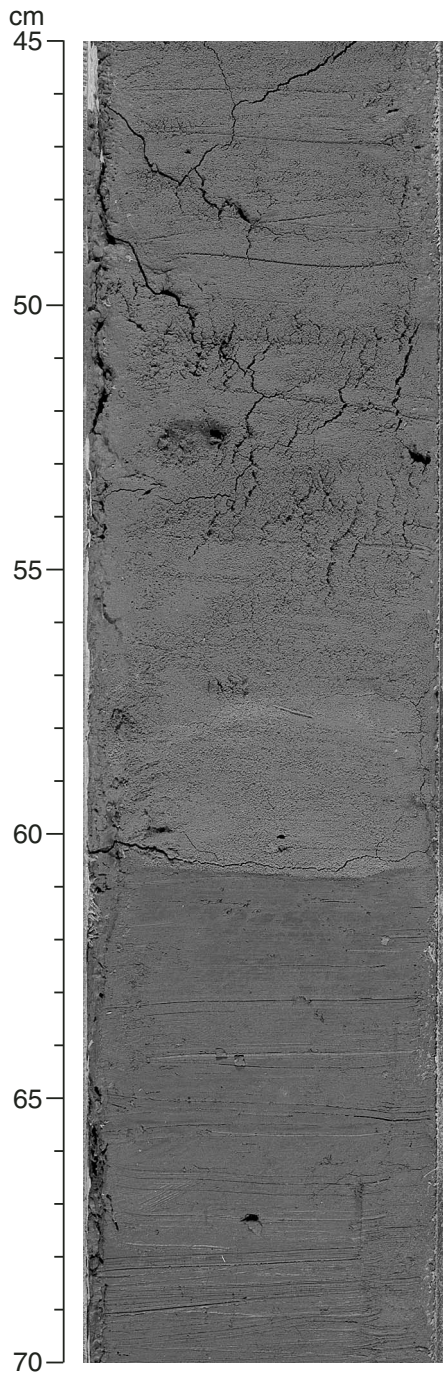
Figure F7. Photomicrograph of glass shards from lithostratigraphic Unit II (Sample 204-1244C-27X-1, 8 cm).
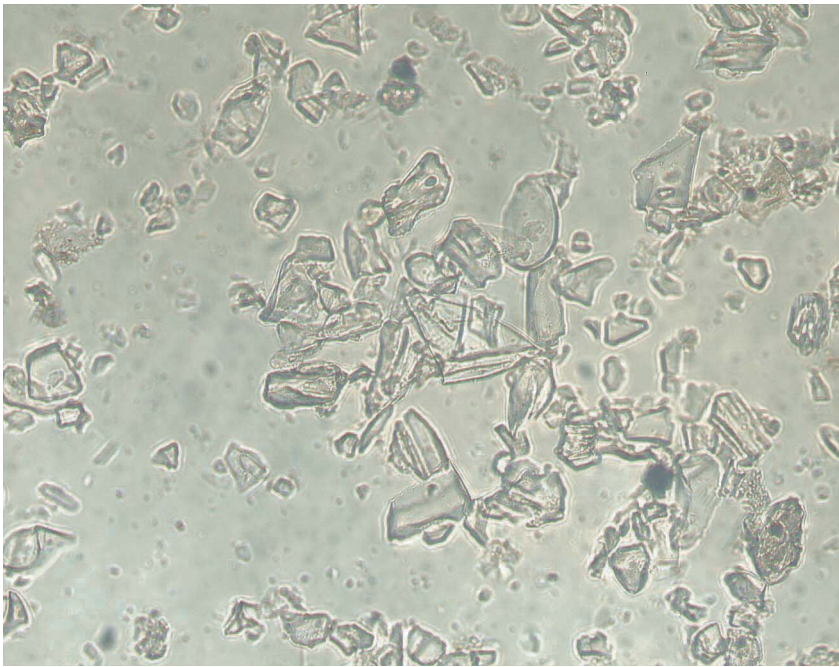
100 µm

Figure F8. XRD profile of Sample 204-1244C-27X-1, 23–24 cm. This sample, from the volcanic glass–rich silt layer (Horizon B′) in lithostratigraphic Unit II, contains abundant amorphous silica (volcanic glass shards), which causes the bulge in the background peak levels.
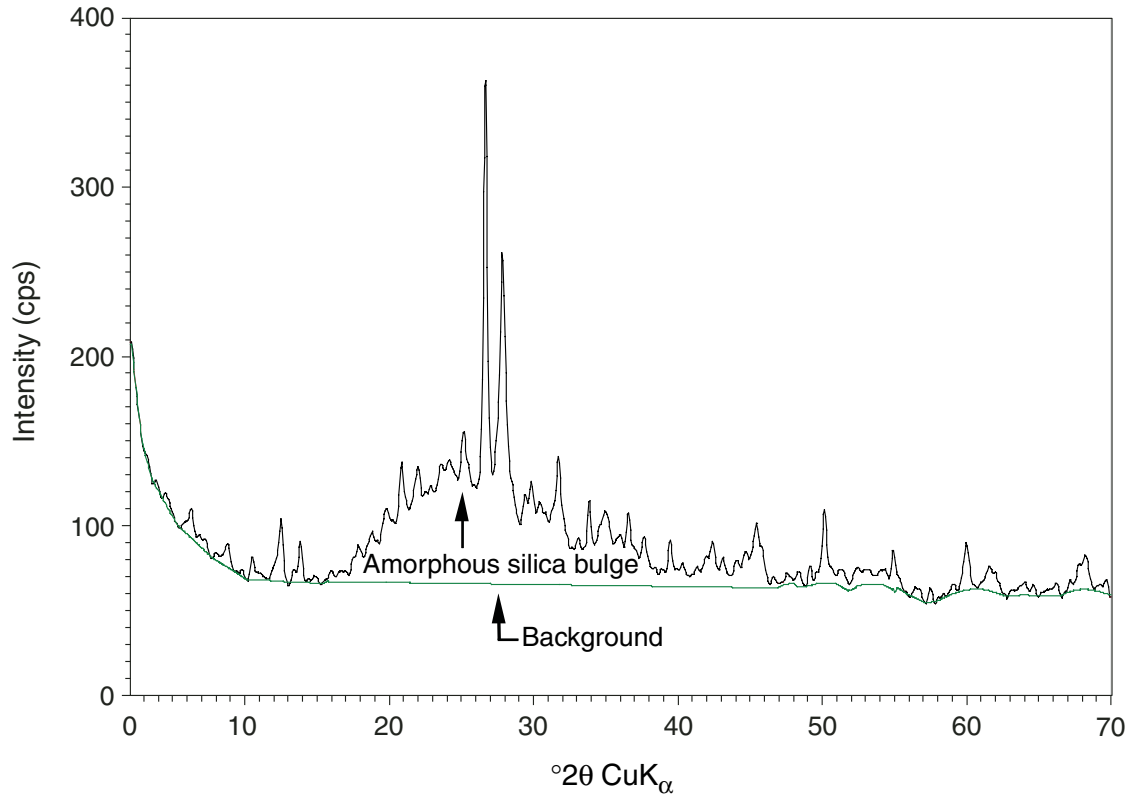
Figure F9. Close-up photograph of carbonate color change in lithostratigraphic Unit III (interval 204-1244C-35X-4, 10–40 cm).
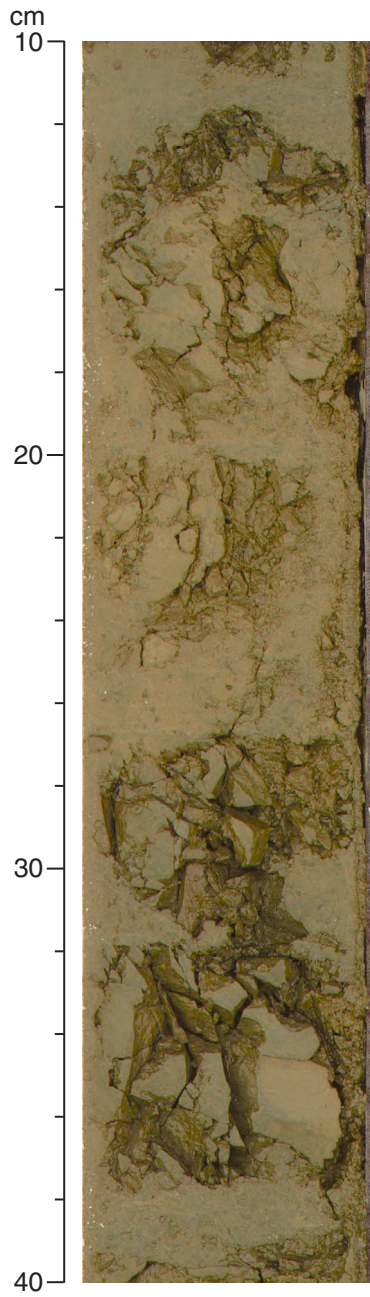
Figure F10. Photomicrograph of authigenic calcite needles (Sample 204-1244C-35X-5, 16 cm).
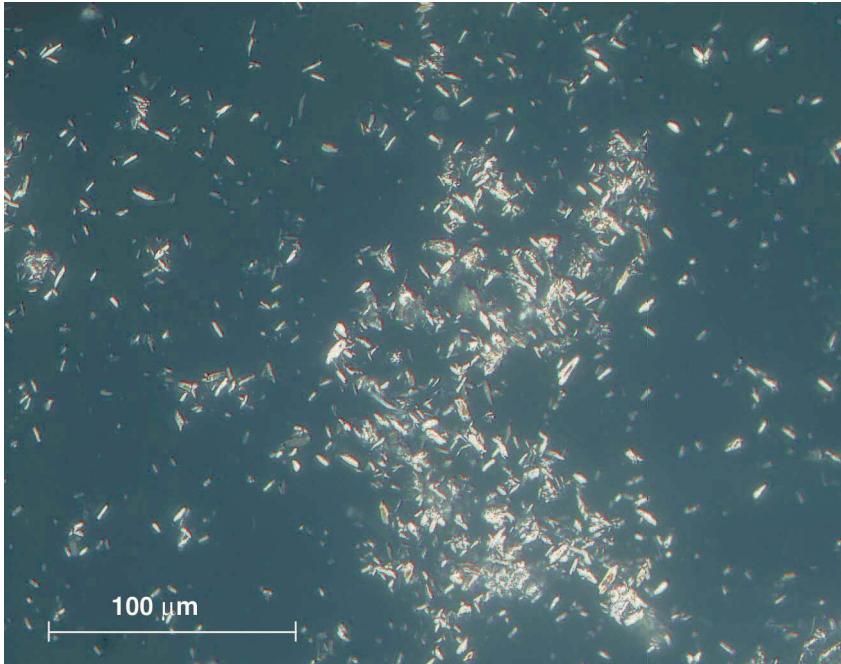
Figure F11. Photomicrograph of glauconite from lithostratigraphic Unit III (Sample 204-1244C-36X-3, 98 cm).
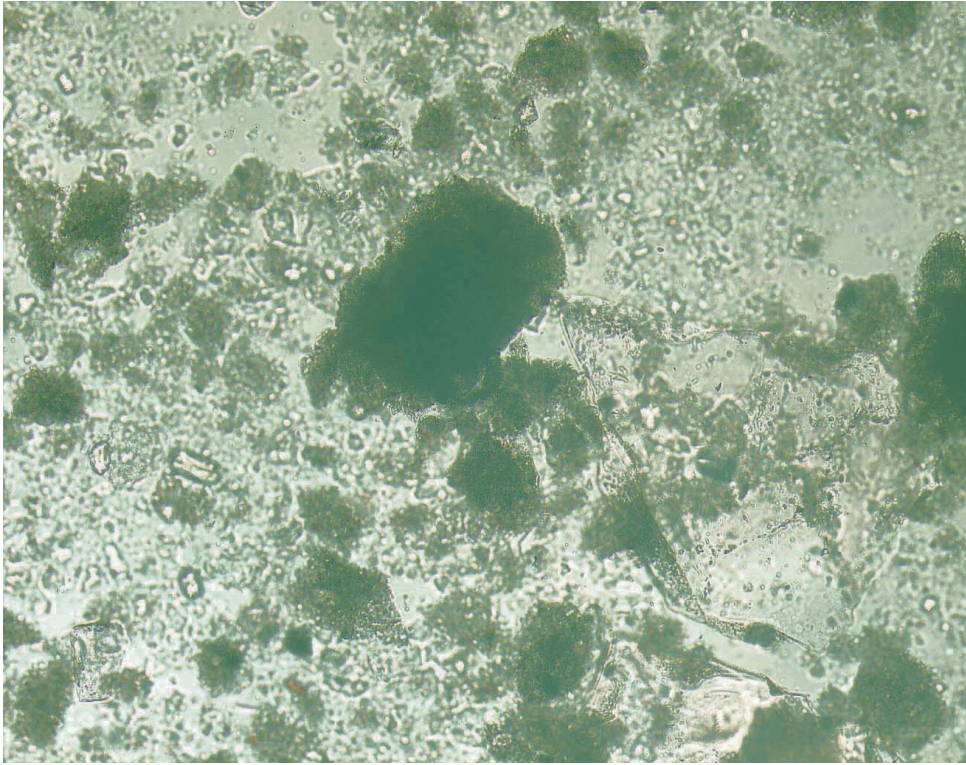
100 μm

Figure F12. Close-up photograph of mousselike texture and sediment disruption presumed to be related to the dissociation of gas hydrate (interval 204-1244C-7H-5, 0–13 cm). See "Physical Properties," p. 24, for corresponding IR anomalies (see Fig. F28A, p. 75).
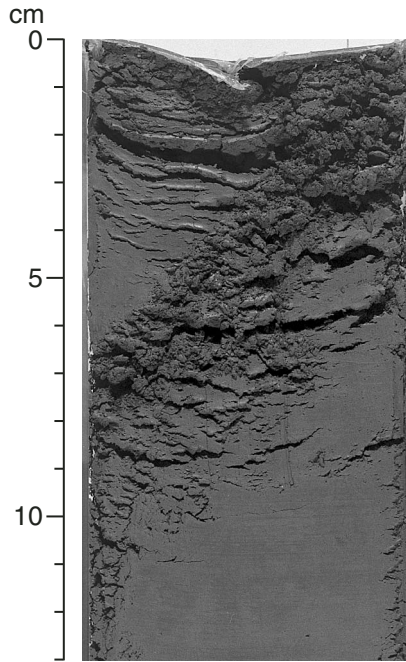
Figure F13. Age-depth plots for Hole 1244C based on diatom and calcareous nannofossil bioevents. The detailed age and depth of control points are shown in Table T3, p. 107. D = diatom event, N = nannofossil event.
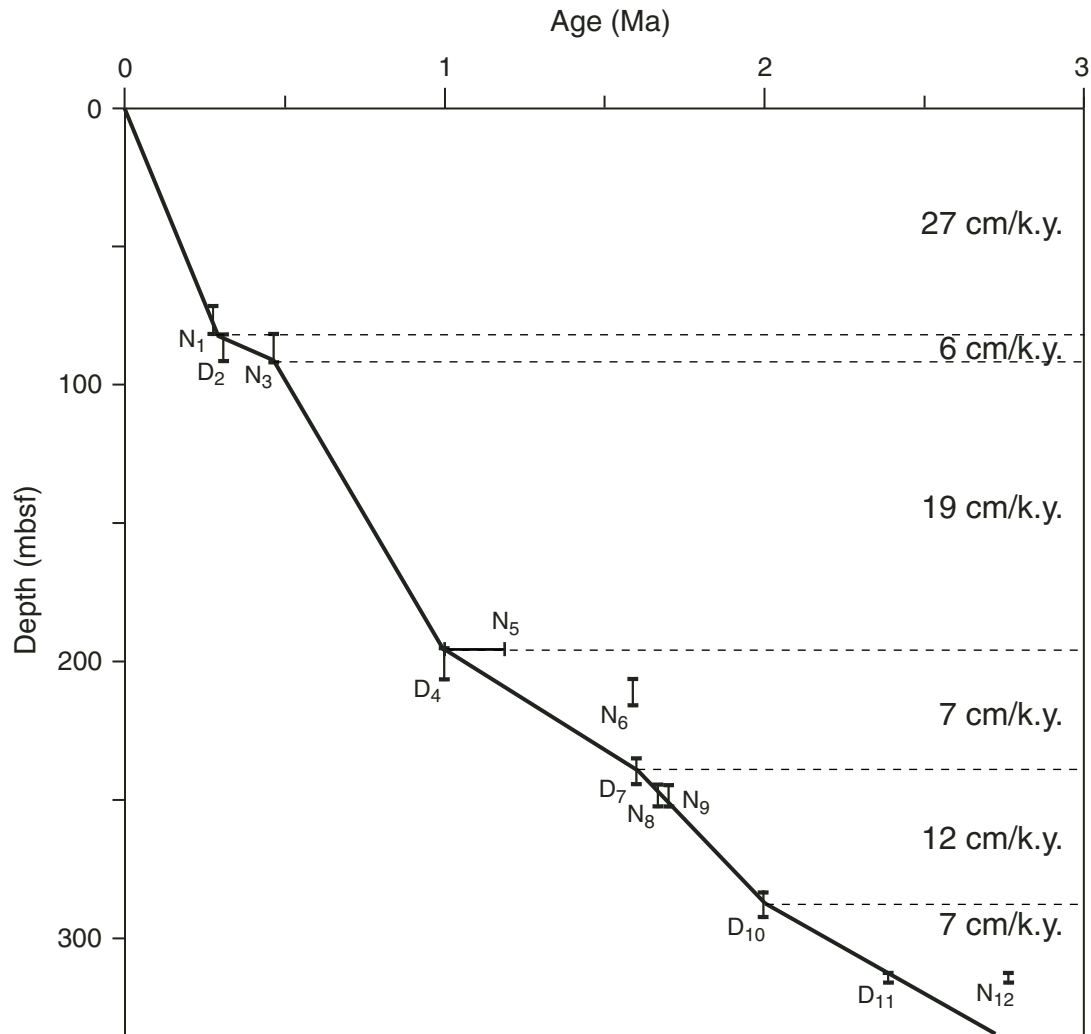
Figure F14. Concentration profiles of various dissolved species in pore waters from Holes 1244B (blue dots), 1244C (red circles), and 1244E (green triangles). (Continued on next page.)
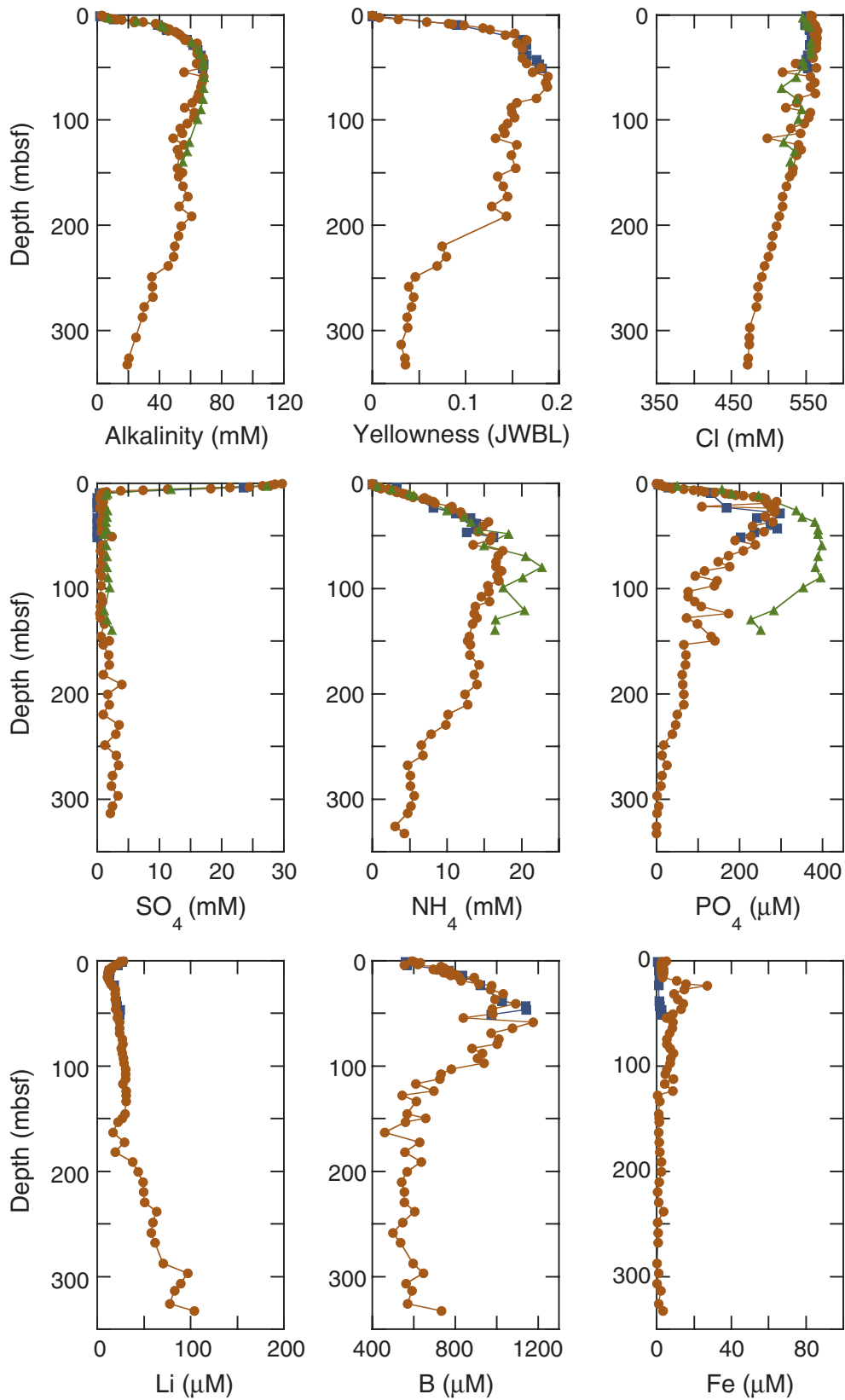
Figure F14 (continued).
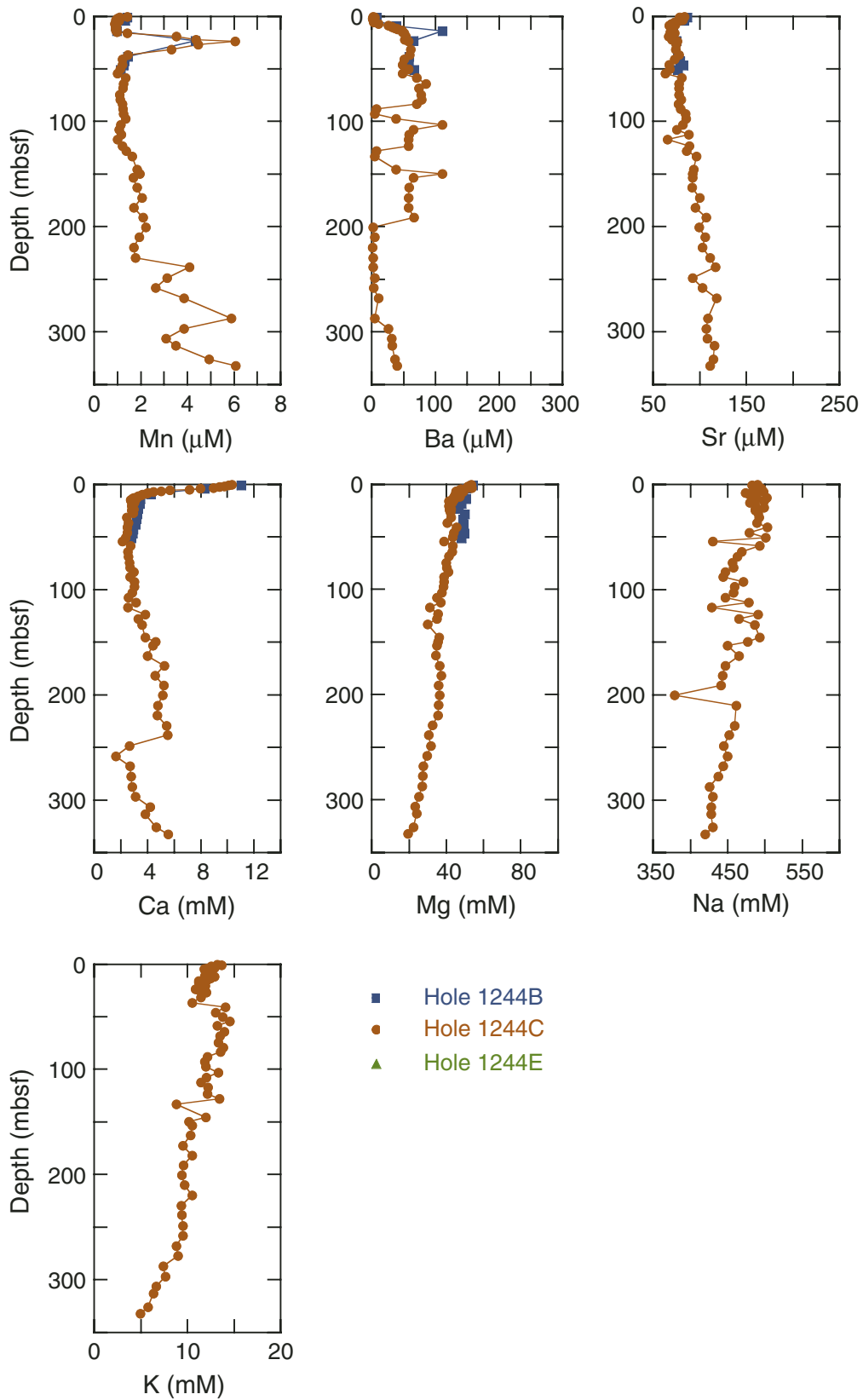
Figure F15. Chloride (Cl⁻) concentration profile at Site 1244 showing the Cl⁻ relationship to the position of the bottom-simulating reflector (BSR) at the base of the GHSZ and reflector AC. Although the chloride anomalies in both Holes 1244B (red circles) and 1244E (blue squares) are limited to the depth interval ranging from 40 mbsf to the depth of the BSR, the depth of individual chloride anomalies varies from hole to hole because of the heterogeneous presence of gas hydrate and pore water sampling resolution.
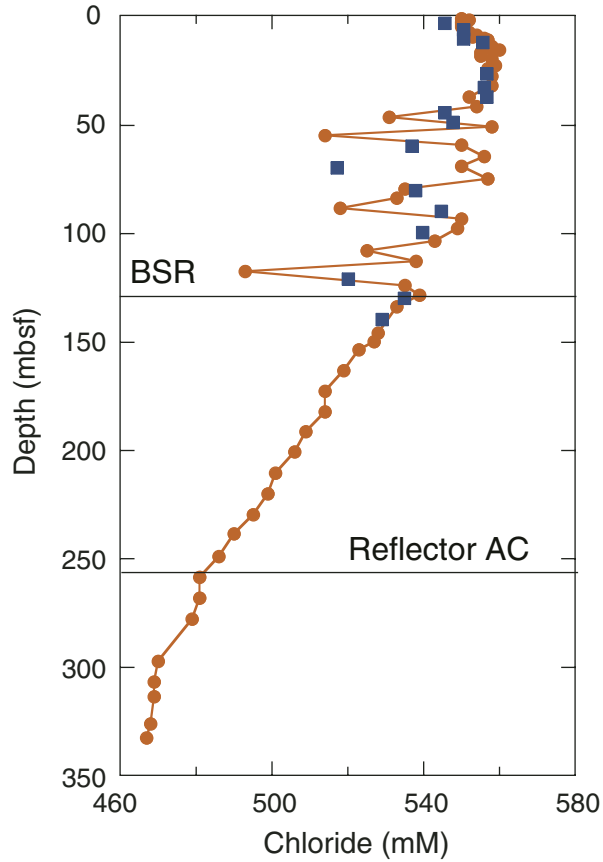
Figure F16. Profile of the lithium (Li$^+$) to chloride (Cl$^-$) concentration (molar $\times$ 10^{-4}) ratio at Site 1244 compared to the distribution reported for Site 888, which was drilled west of the deformation zone during ODP Leg 146 (Westbrook, Carson, Musgrave, et al., 1994; Kastner et al., 1995). The similarity between these distributions suggests a common source of fluids deep within the accreted sediments of the Cascadia prism.
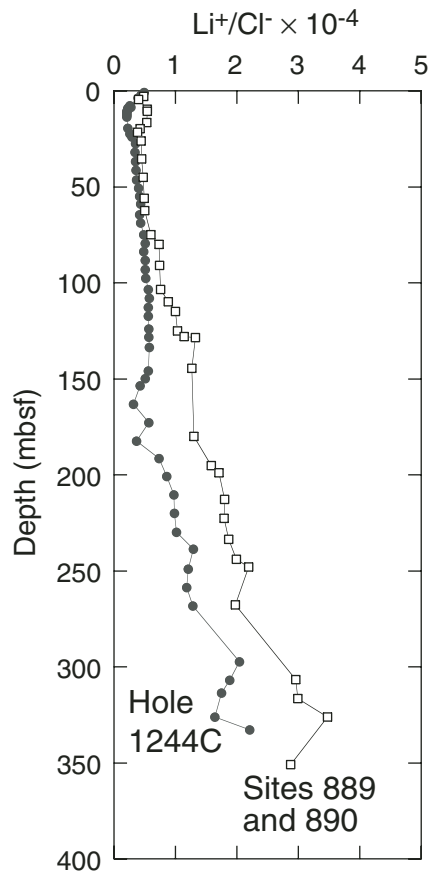
Figure F17. Estimates of gas hydrate amounts based on two interpretations of the chloride (Cl⁻) concentration profile. **A.** Interpretation based on extending two linear trends of chloride data seen above (0–20 mbsf) and below (130–330 mbsf) the GHSZ. This interpretation predicts that gas hydrate is present from 20 to 130 mbsf and results in a larger gas hydrate inventory estimate. (Continued on next page.)
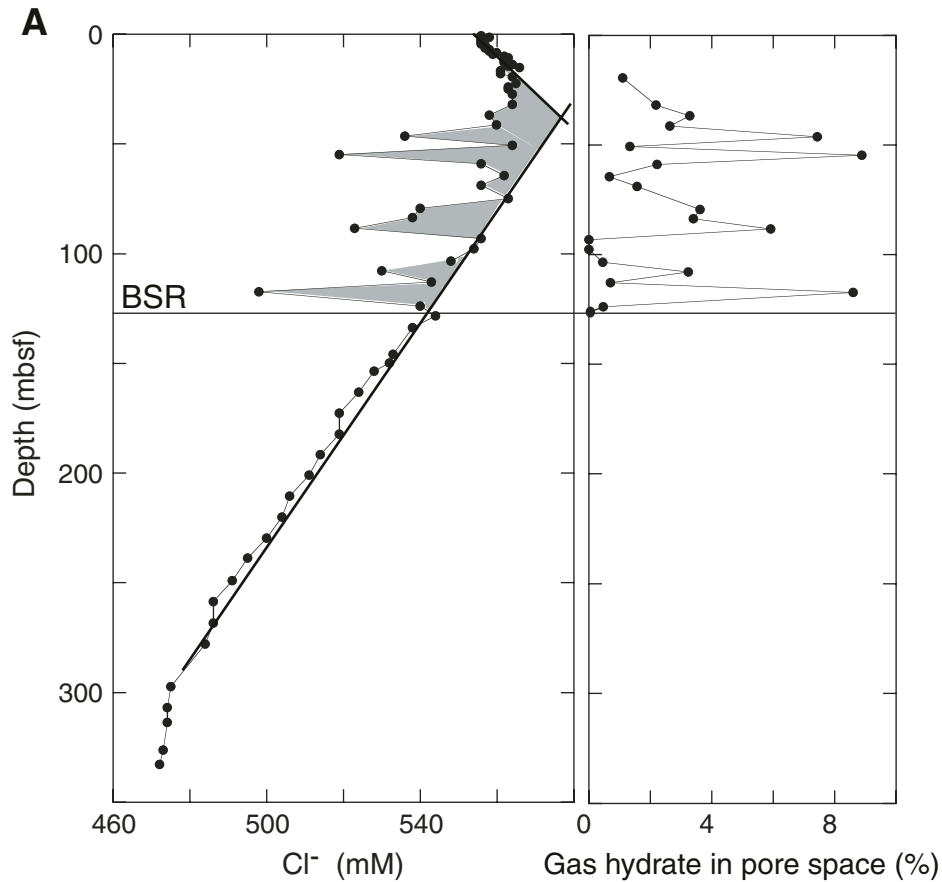
Figure F17 (continued). B. Interpretation based on extending the lower chloride concentration trend into the GHSZ and using a similar baseline chloride concentration observed at ODP Site 888 (see Fig. F18, p. 65). This interpretation predicts that gas hydrate is present in the region between 40 and 120 mbsf and results in a more conservative estimate of in situ gas hydrate. Based on comparison with sediment resistivity distributions and seismic records and on the data from Site 888, we favor the more conservative approach in estimating the gas hydrate inventory at this site. BSR = bottom-simulating reflector.
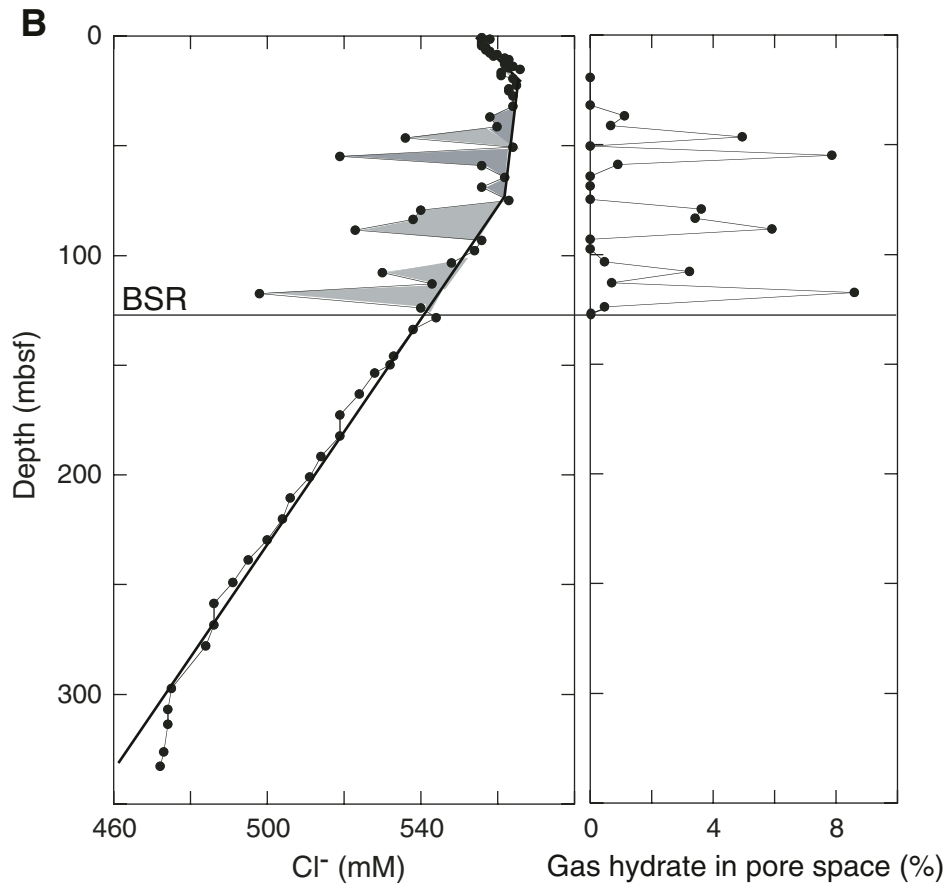
Figure F18. Comparison of the chloride (Cl⁻) concentration profiles in Sites 1244 (solid circles, solid line) and 888 (open squares, dashed line). Note that the data from each site trace similar background chloride profiles in the upper 50–60 m. This similarity is the basis for our preferred estimate of the gas hydrate inventory at Site 1244.
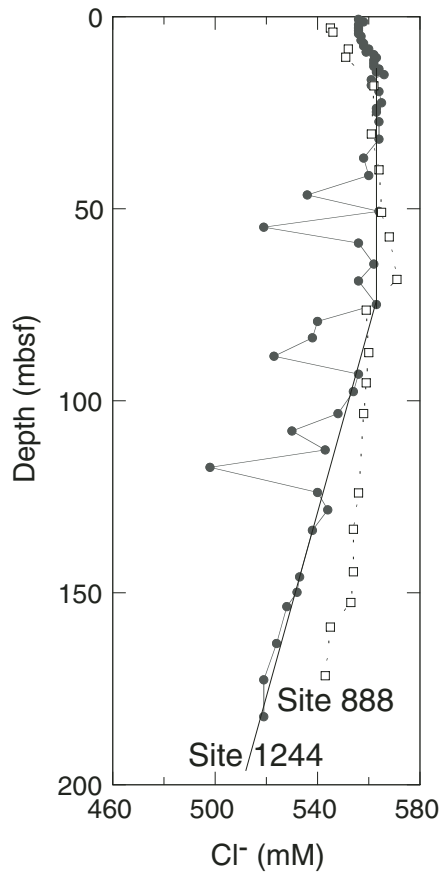
Figure F19. Sulfate (SO_4^{2-}) concentration profile at Hole 1244C including (**A**) the entire penetrated sedimentary section and (**B**) a detailed profile from the seafloor to 15 mbsf that also shows interstitial methane concentration from headspace data (see **"Organic Geochemistry,"** p. 19). In A, note that the sulfate concentration decreases rapidly from 29.7 mM (Sample 204-1244C-1H-1, 65–75 cm [0.65 mbsf]) to levels <1 mM (Sample 2H-3, 65–75 cm [9.15 mbsf]). Samples below ~9 mbsf contain residual amounts of sulfate <1 mM, and this amount increases below ~135 mbsf coincident with the onset of XCB drilling. The shaded portion of the profile appears in B, where the curvature of the sulfate profile at both the top and bottom of the sulfate reduction zone can be clearly observed. A linear portion of the curve is present between ~4 and 8 mbsf, and this portion was used to calculate upward methane flux at Site 1244 based on the shown linear regression. The SMI is also shown at a depth of ~8.5 mbsf, where sulfate concentration falls below 1 mM with a concomitant increase in interstitial methane concentration.
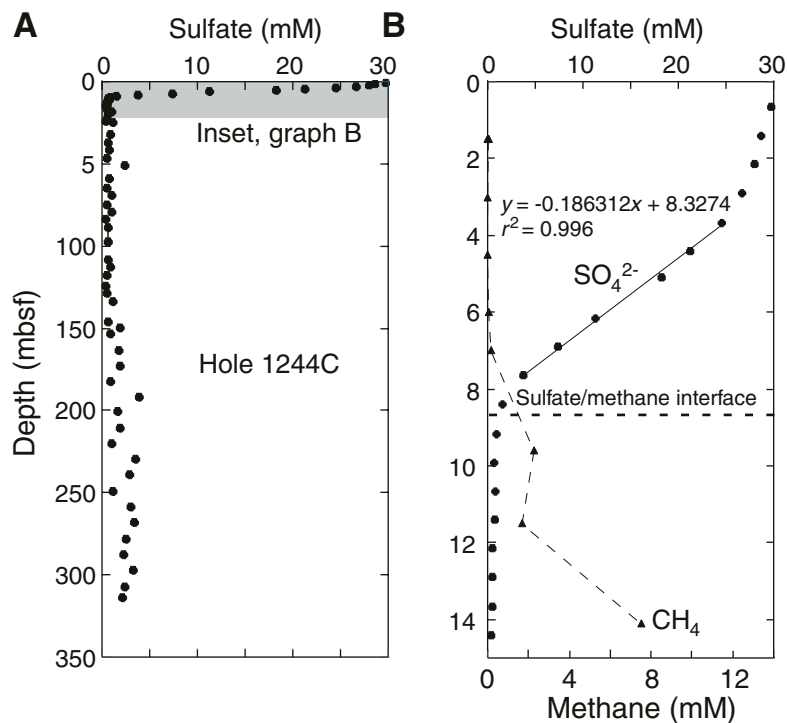
Figure F20. Dissolved sulfate and barium profiles in the upper 30 mbsf at Site 1244, illustrating barium remobilization at the zone of sulfate depletion.
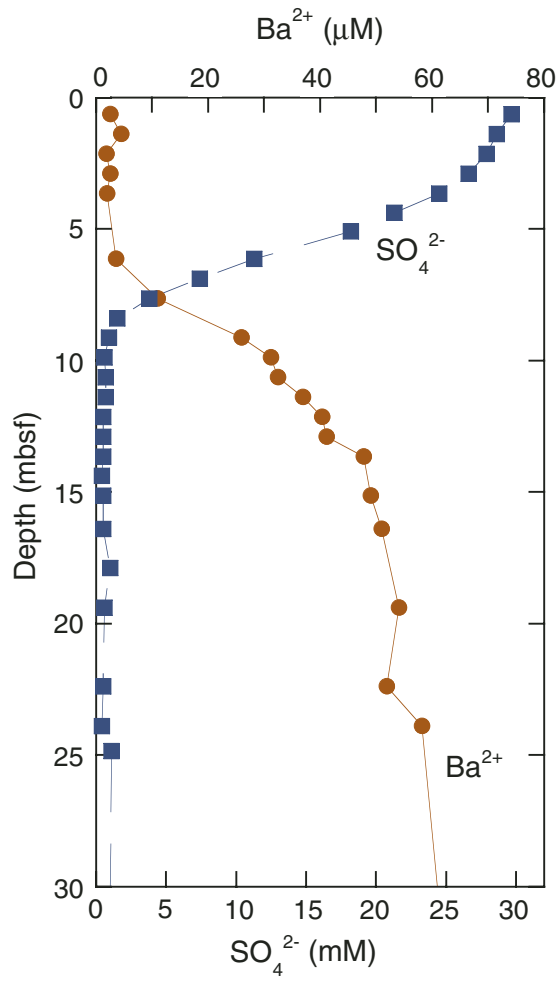
Figure F21. Concentrations of C_1, C_2, and C_3 vs. depth for Holes 1244A, 1244B, 1244C, and 1244E. Circles = C_1, squares = C_2, triangles = C_3.
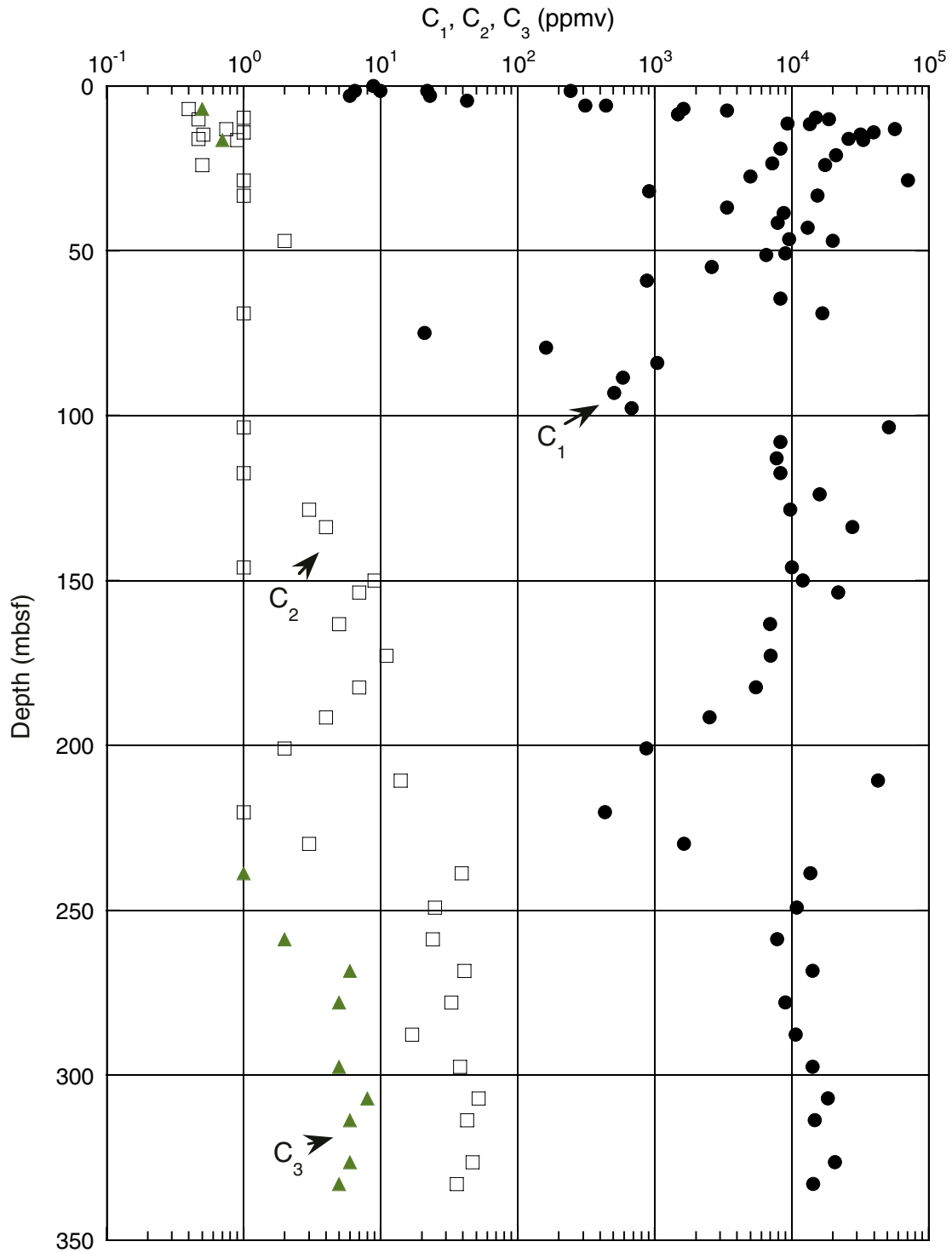
Figure F22. C_1/C_2 ratio vs. depth for Holes 1244A, 1244B, 1244C, and 1244E. VAC = vacutainer, HS = headspace gas, GH = gas hydrate, PCS = pressure core sampler.
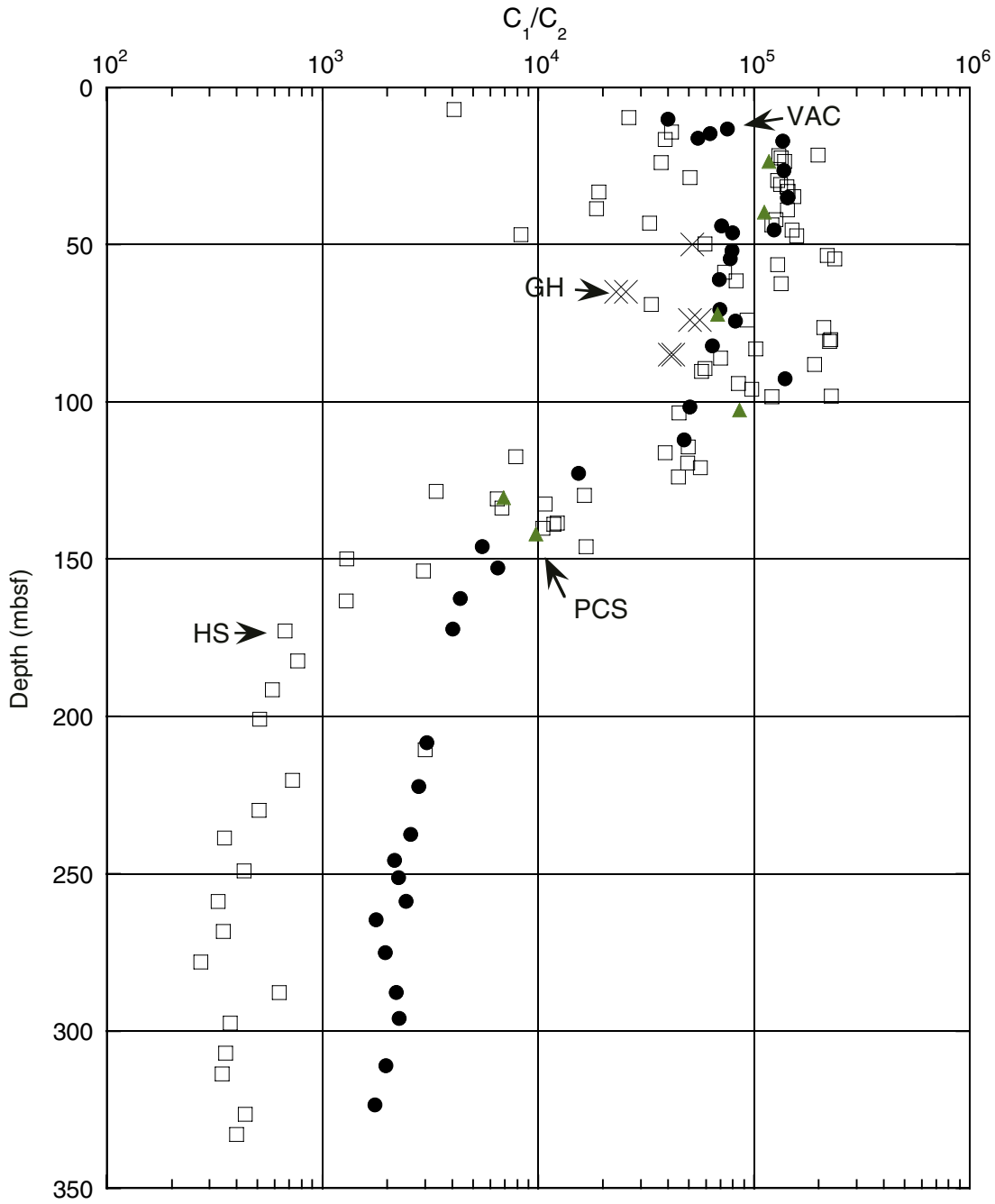
Figure F23. C_1/C_2 ratio vs. temperature for Holes 1244A, 1244B, 1244C, and 1244E. VAC = vacutainer, HS = headspace.
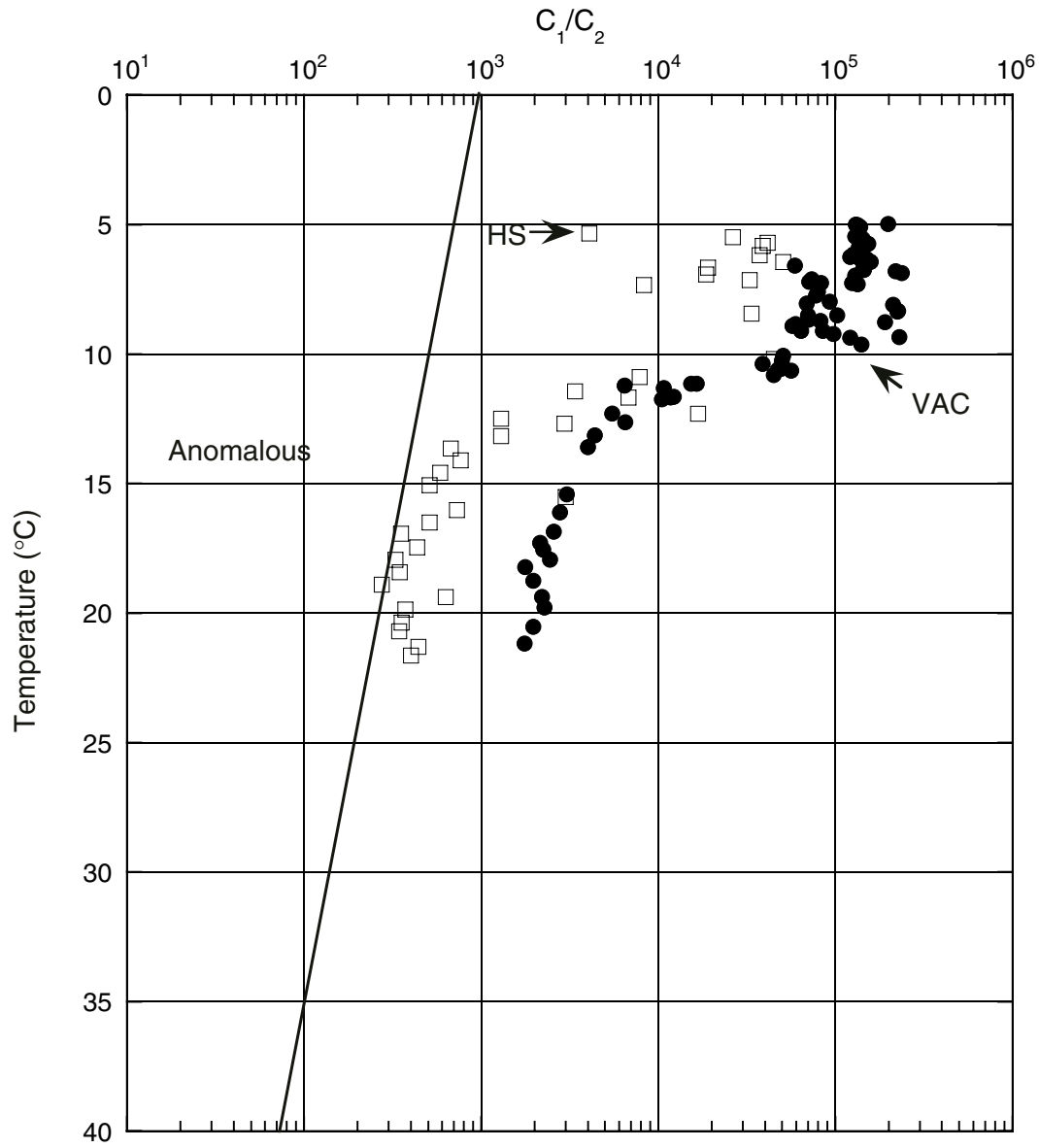
Figure F24. Dissolved residual methane (CH_4) and sulfate (SO_4^{2-}) in pore water. Methane concentration increases at the depth where sulfate concentration is depleted. Circles = CH_4; triangles = SO_4^{2-}.
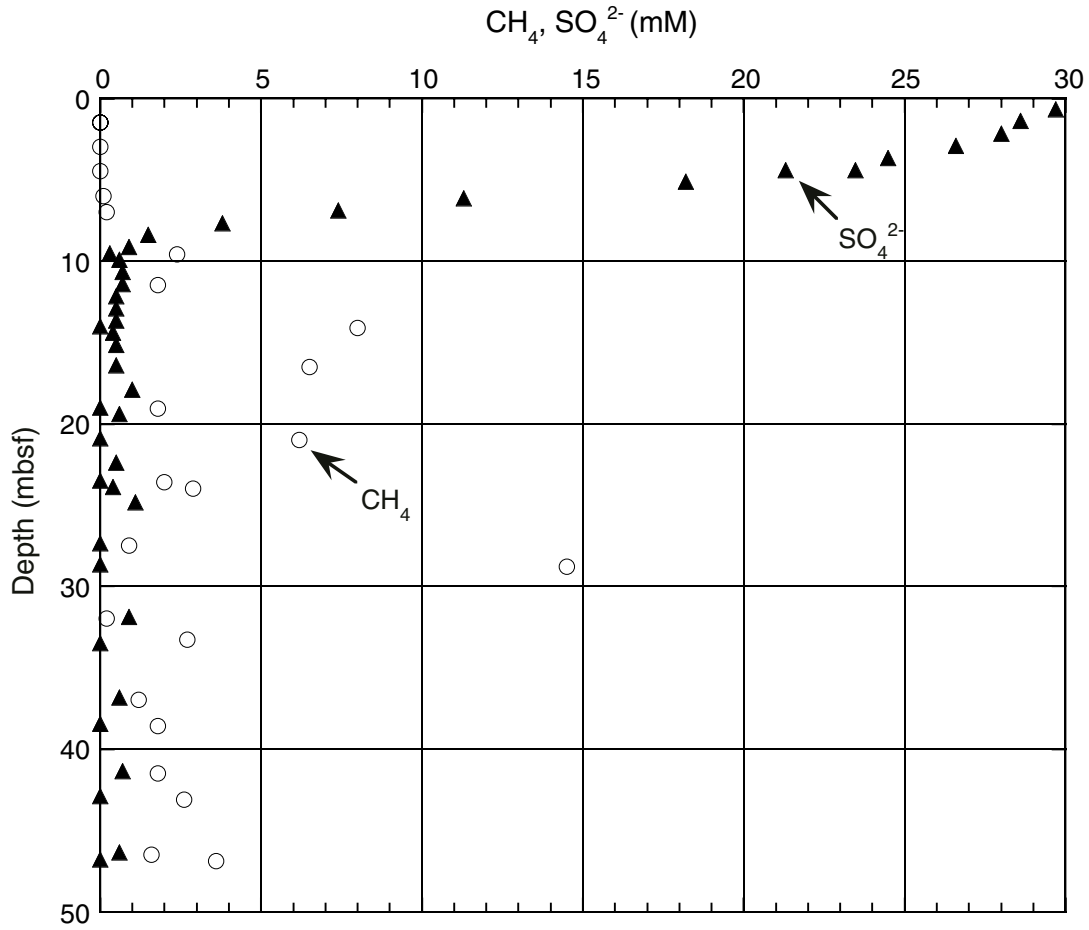
Figure F25. Contents of carbonate carbon (IC) and CaCO$_3$, organic carbon (OC), total sulfur (TS), total nitrogen (TN), and C/N ratios in sediments from Holes 1244A, 1244B, 1244C, and 1244E.
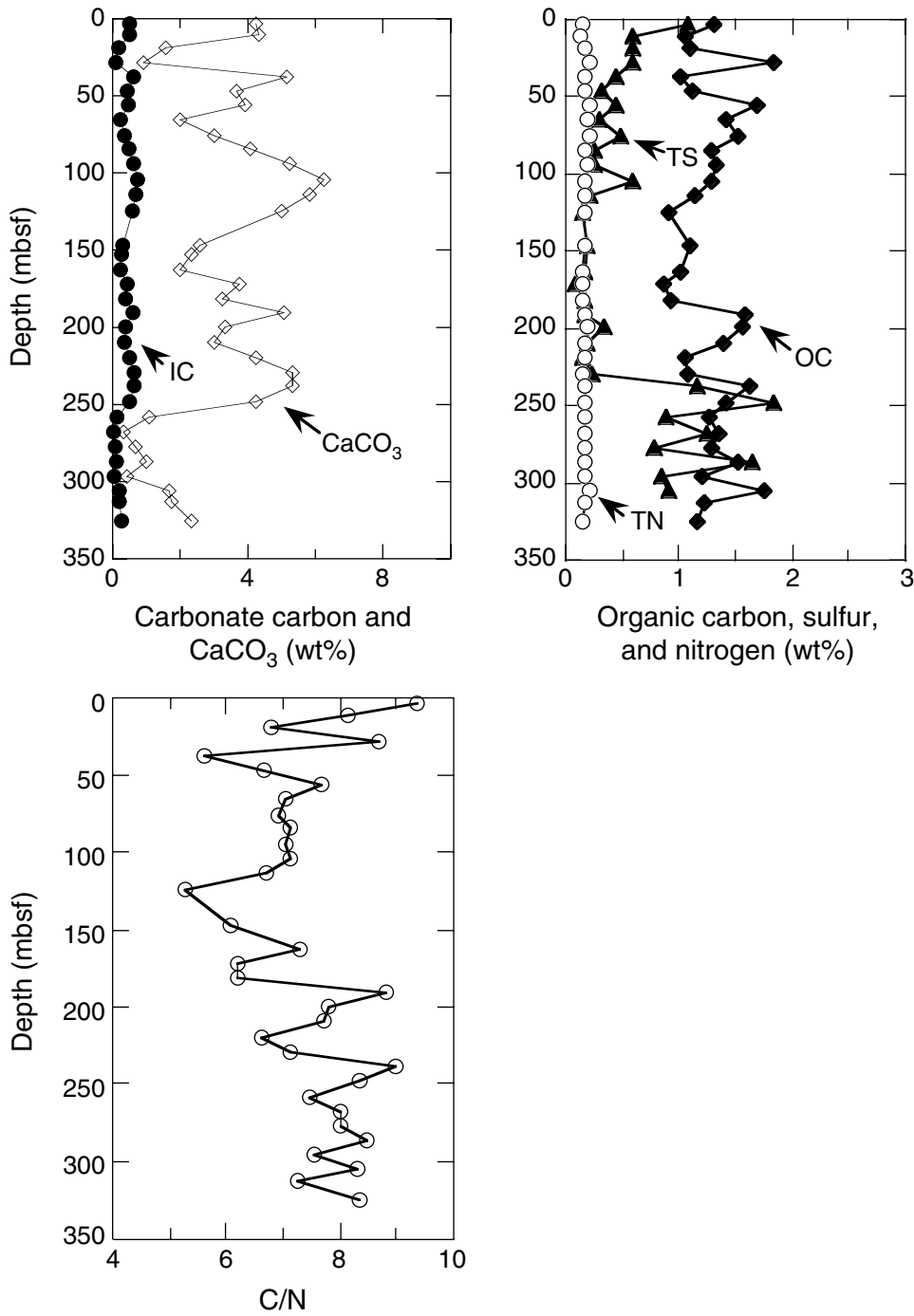
Figure F26. Comparison of IR images of core liners with photographs of corresponding hydrate occurrences after freezing in liquid nitrogen and extraction of core from the core liner. For IR anomaly designations, see Table T2, p. 105.

IR19

204-1244C-8H (63.09-63.19 mbsf)

204-1244C-8H-1, 47-52 cm

IR21

204-1244C-8H (67.94-68.04 mbsf)

204-1244C-8H-5, 48-80 cm

IR26

204-1244C-10H-2 (83.70-84.30 mbsf)

204-1244C-10H-2 (83.70-84.30 mbsf)
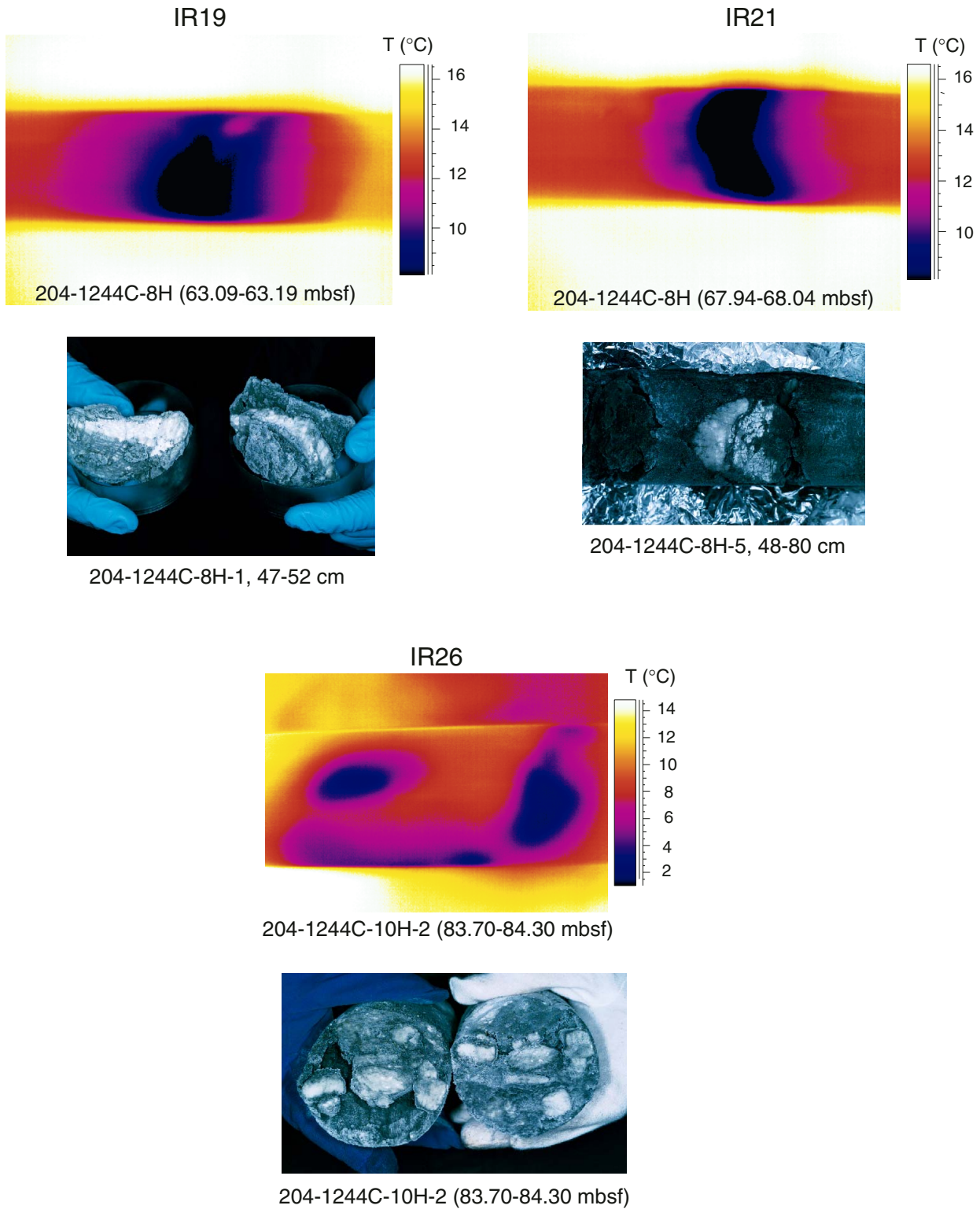
Figure F27. Downcore temperature profiles from IR imaging for Holes 1244C and 1244E. APC = advanced piston corer; BSR = bottom simulating reflector; XCB = extended core barrel.
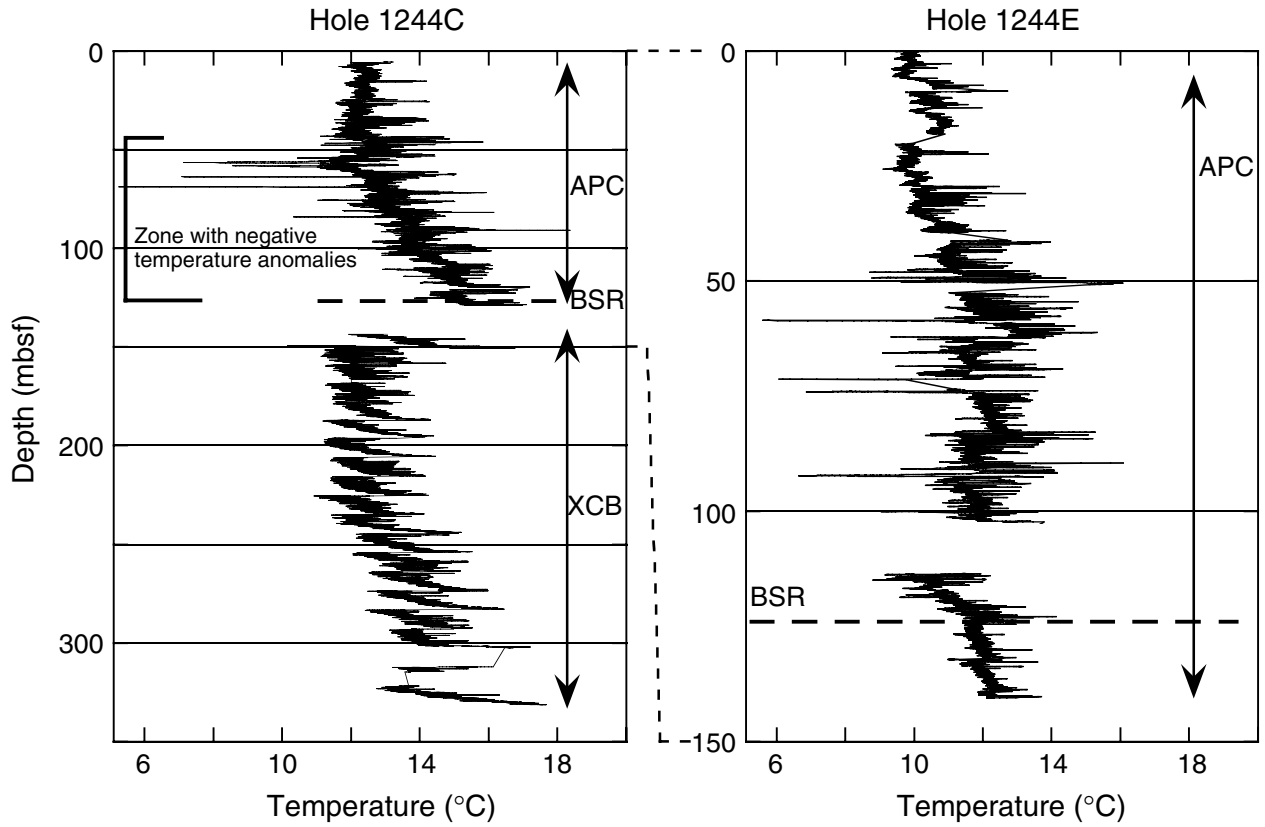
Figure F28. A. Comparison of downcore temperature anomalies (Δ*T*) from IR imaging of Holes 1244C and 1244E. (Continued on next page.)
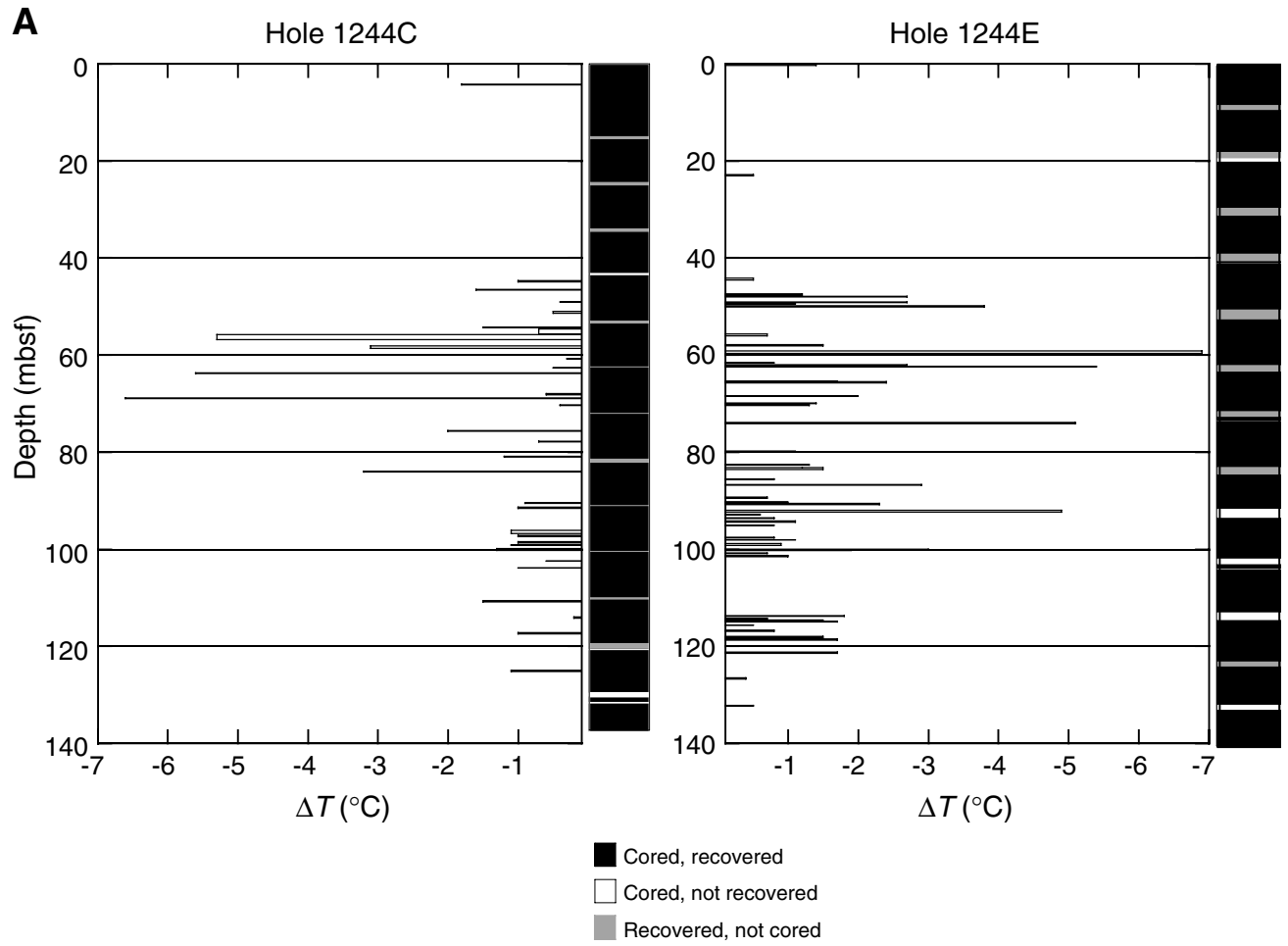
Figure F28 (continued). B. Downcore temperature anomalies (ΔT) from IR imaging for Hole 1244E compared with estimated hydrate concentrations from LWD resistivity in Hole 1244D. Resisitivity data are plotted in terms of apparent pore water saturation using Archie's Relation; the estimated hydrate concentration is 1.0 S_w (see **"Downhole Logging,"** p. 34).

B

Hole 1244E   Hole 1244D

ΔT (°C)

Pore water saturation

(S_w = proportion of pores saturated by water)

■ Cored, recovered
□ Cored, not recovered
▨ Recovered, not cored
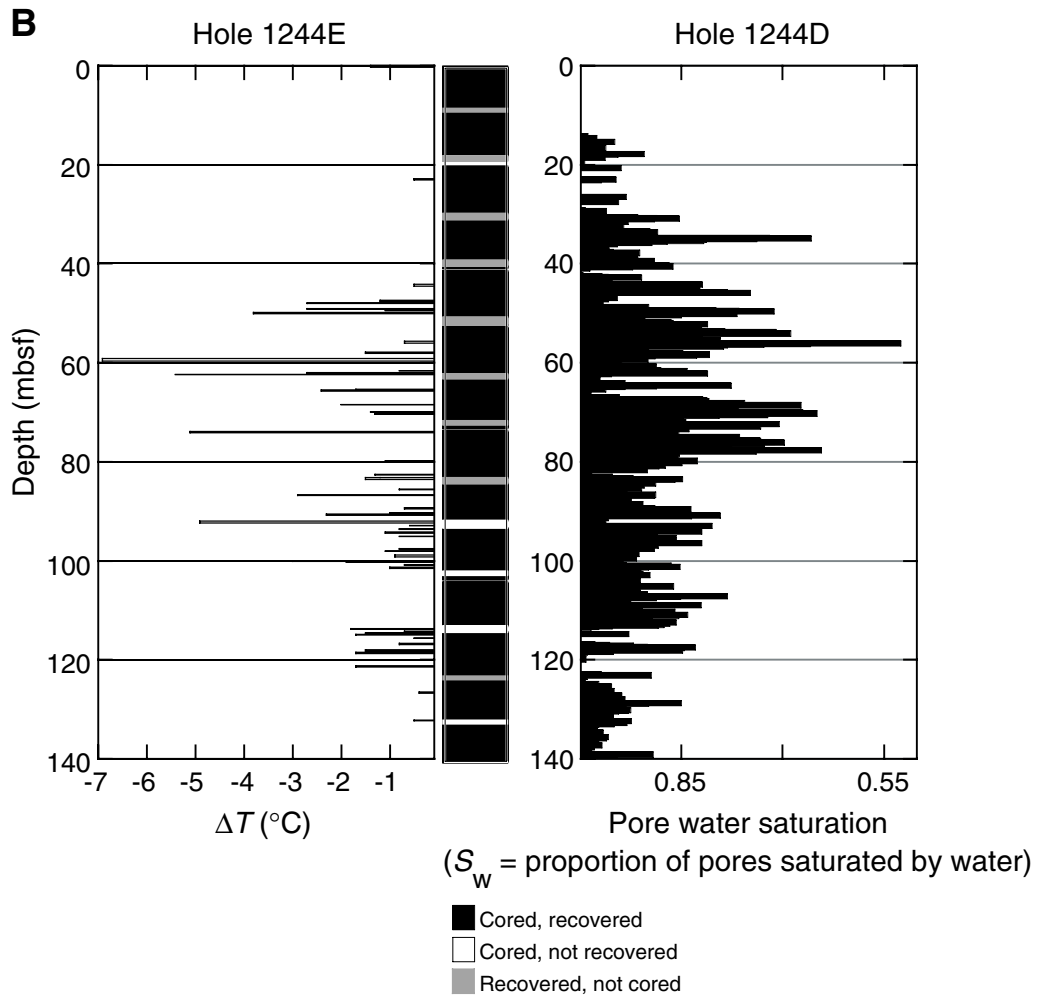
Figure F29. Summary of physical property measurements at Site 1244. LWD = logging while drilling, GRA = gamma ray attenuation, MAD = moisture and density.
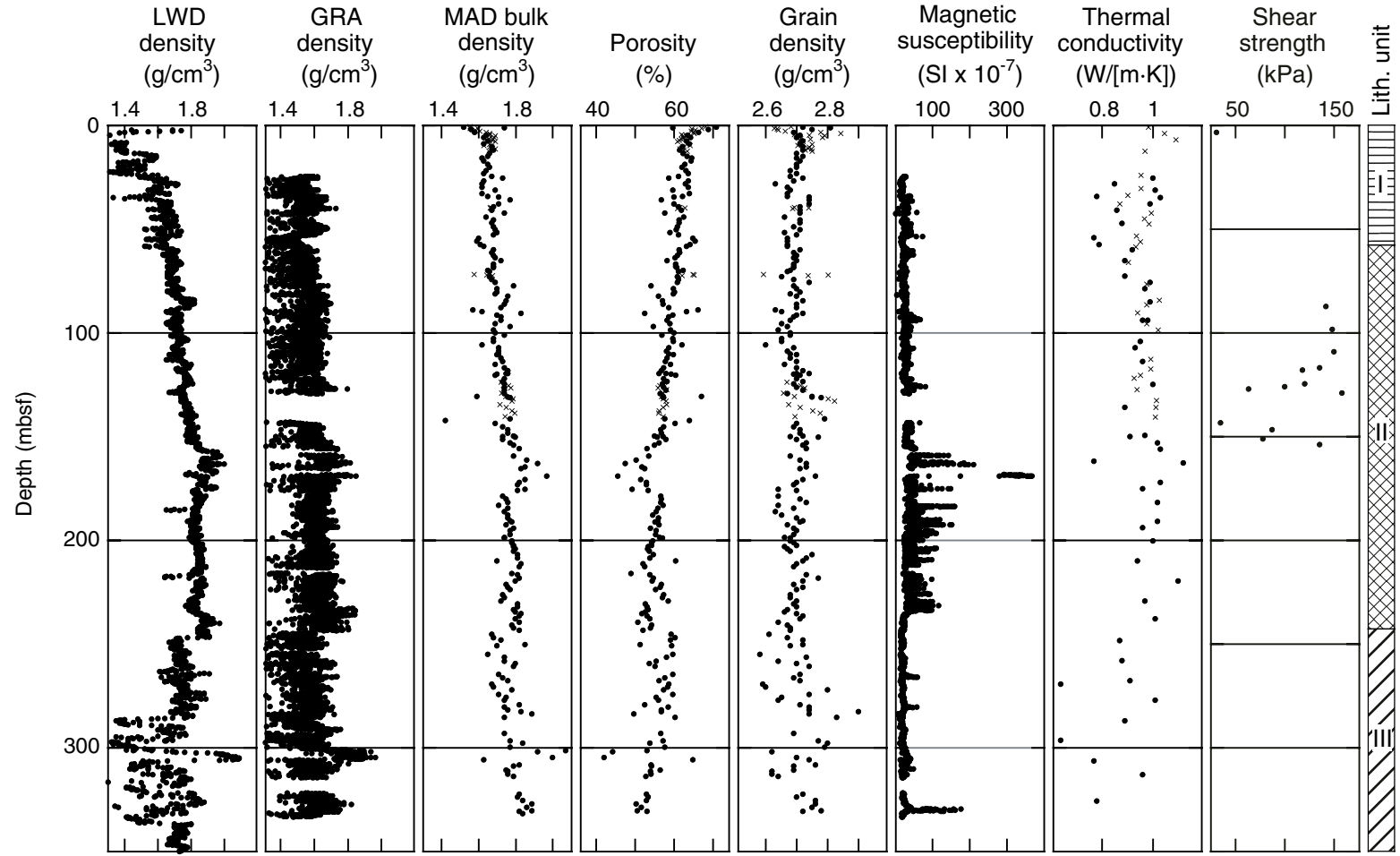
Figure F30. Detailed comparison of density measurements from gamma ray attenuation (GRA), moisture and density (MAD), and logging while drilling (LWD) at Site 1244.
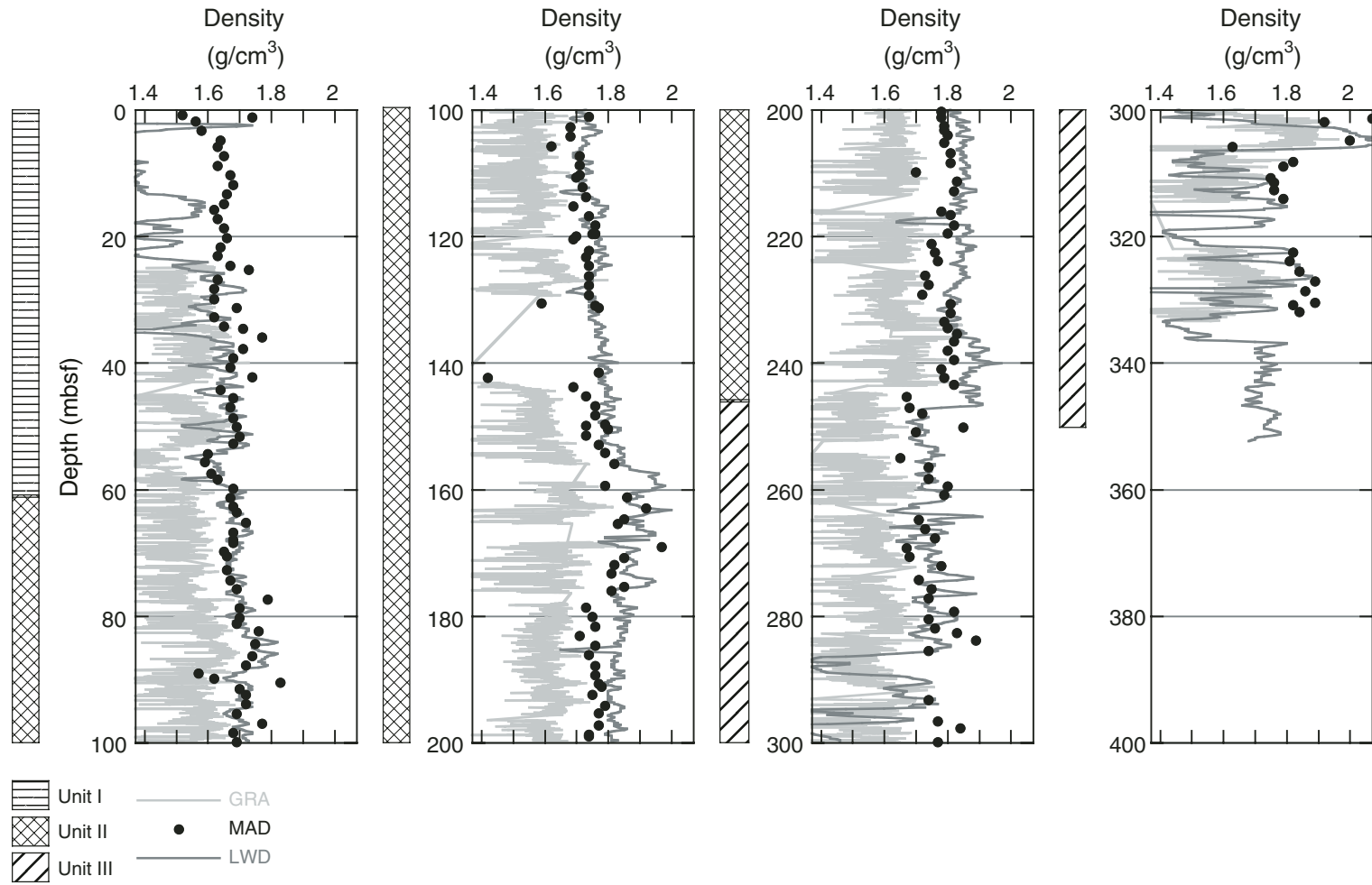
Figure F31. Comparison of shallow measurements of density from gamma ray attenuation (GRA) and moisture and density (MAD) samples in Holes 1244A and 1244B.
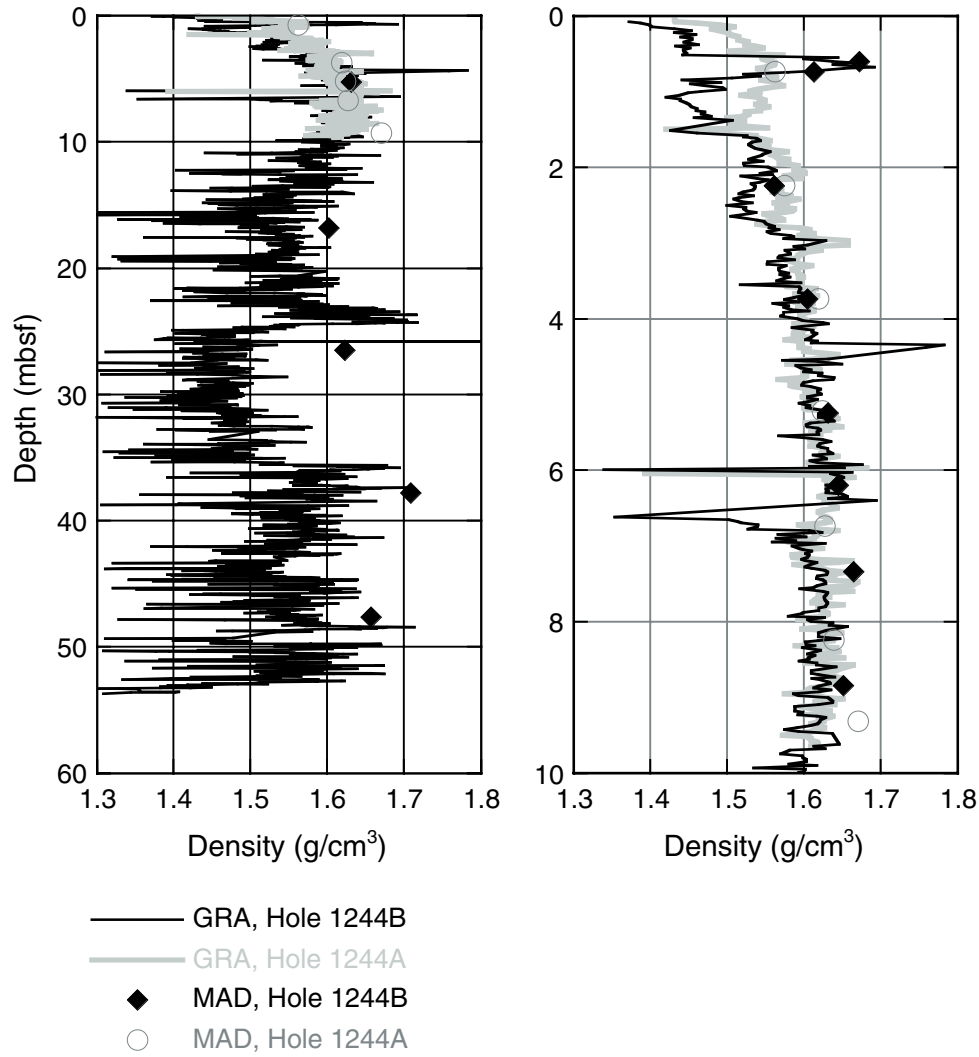
Figure F32. V_P measured on the MST in Holes 1244A and 1244B.
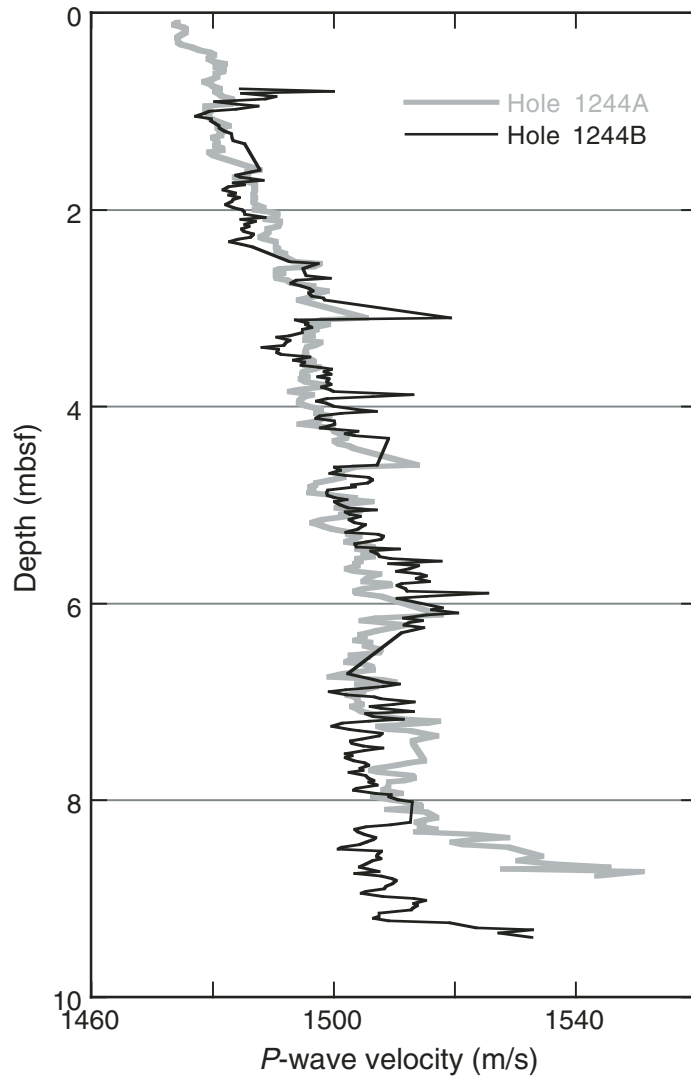
Figure F33. Comparison of physical properties in the upper 10 mbsf at Site 1244. GRA = gamma ray attenuation, NCR = noncontact resistivity.
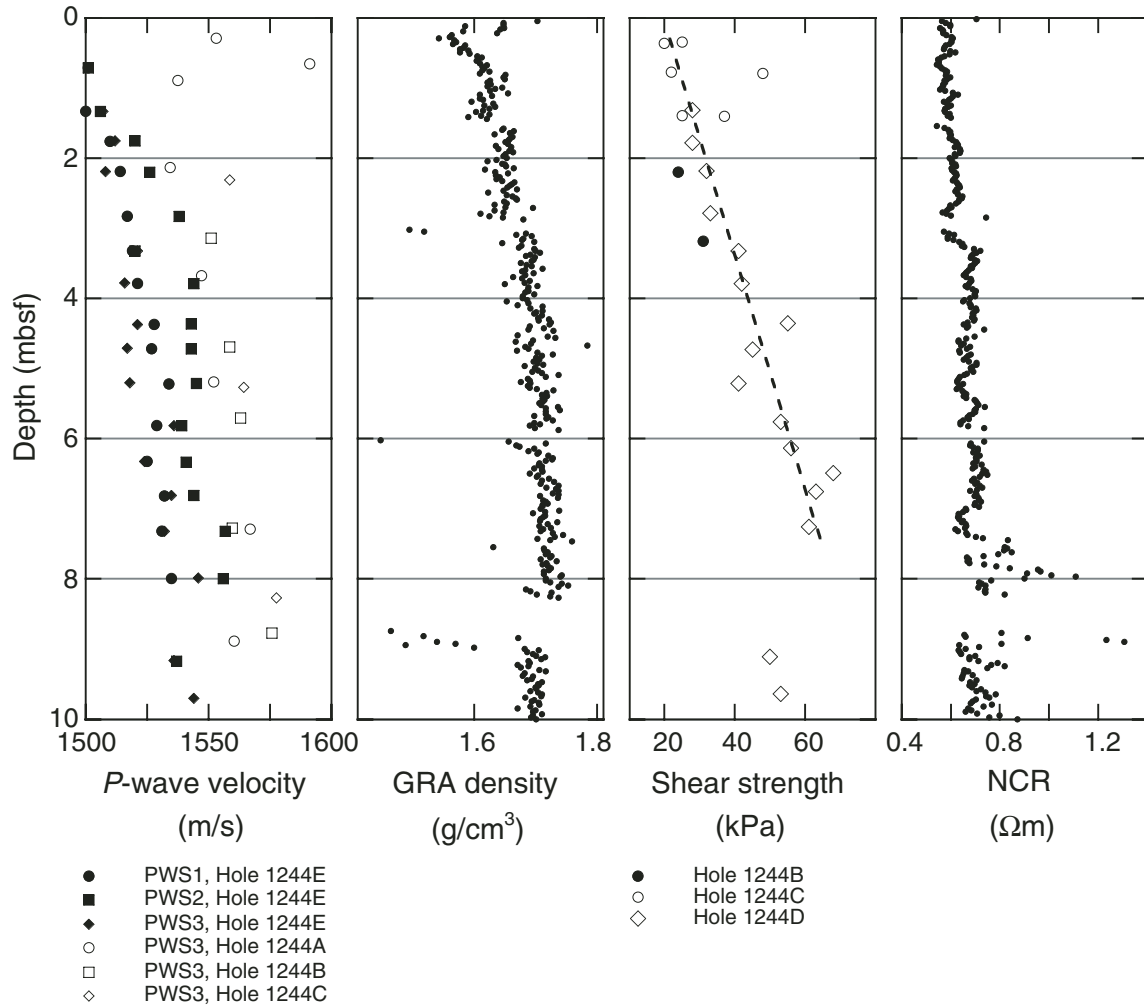
Figure F34. Raw data for estimating in situ temperatures. **A.** APCT tool data. Only the portion of data immediately before, during, and immediately after penetration of the probe into the subsurface is shown. For an example of the entire temperature history of a deployment see **"Downhole Tools and Pressure Coring,"** p. 34, in the "Explanatory Notes" chapter. The ODP core identification number associated with each run of the APCT tool is indicated in the upper left corner of the graph. (Continued on next page.)

A
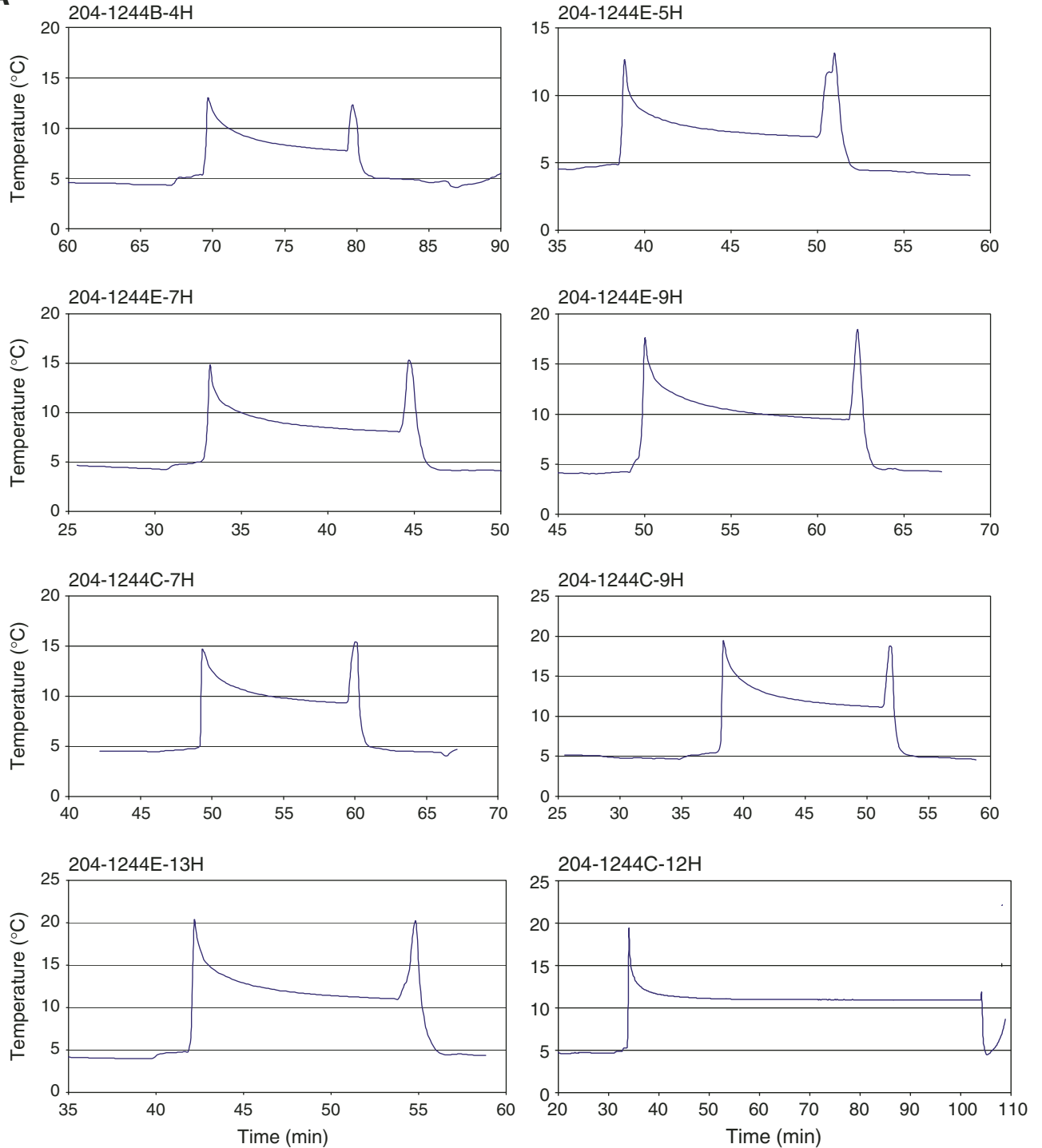
Figure F34 (continued). B. DVTPP temperature (T) and pressure (P) data. The ODP identification for the cores preceding and following tool deployment is indicated.

A (continued).

204-1244E-17H

B

Between 204-1244E-8Y and 9H

Between 204-1244C-7H and 8H

Between 204-1244E-19H- and BOH

Between 204-1244C-19X and 20X
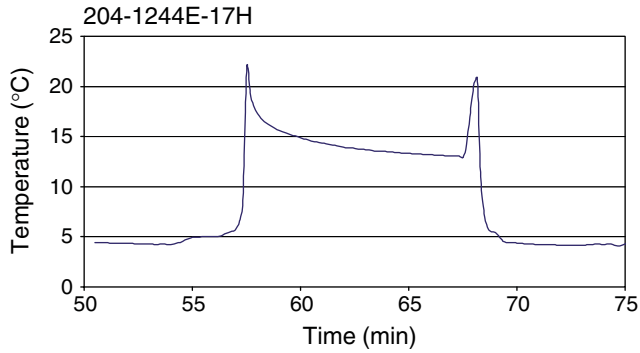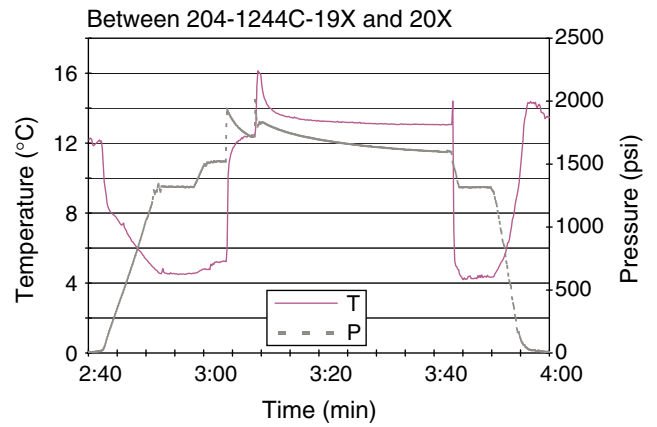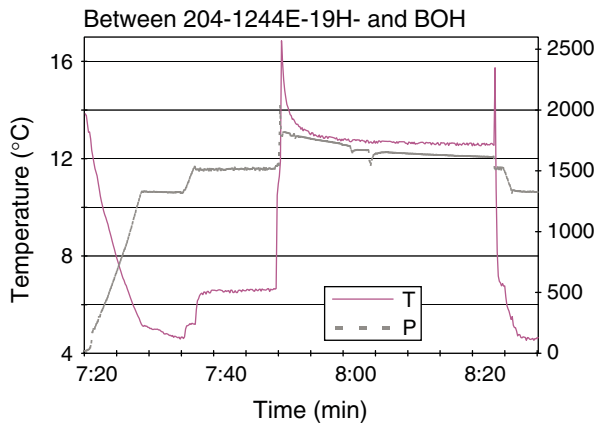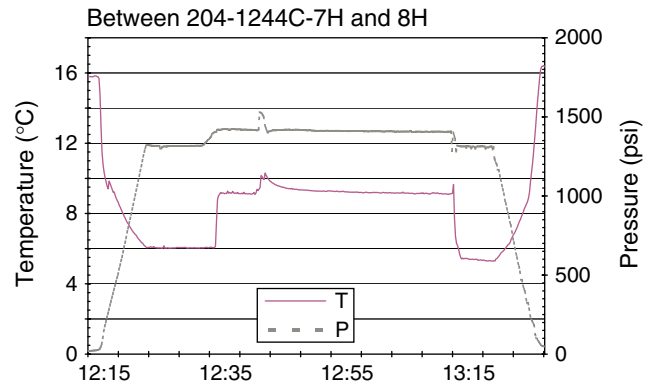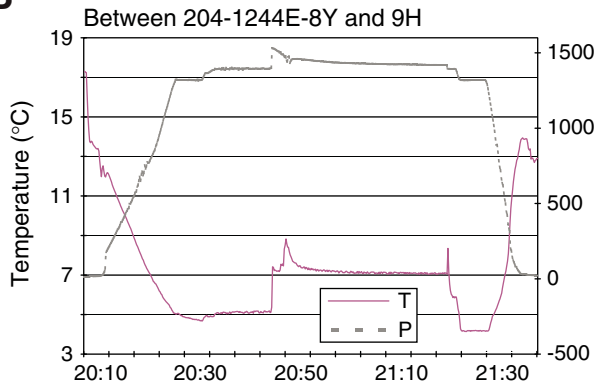
Figure F35. Subsurface temperatures plotted vs. depth beneath the seafloor at Site 1244. Data from APCT 11 were corrected as discussed in the text. The equation for the best fitting linear thermal gradient for all the data is also shown.

Site 1244

BSR

With mudline
$T = 0.060z + 4.05$
$R^2 = 1.00$

Without mudline
$T = 0.061z + 3.96$
$R^2 = 1.00$
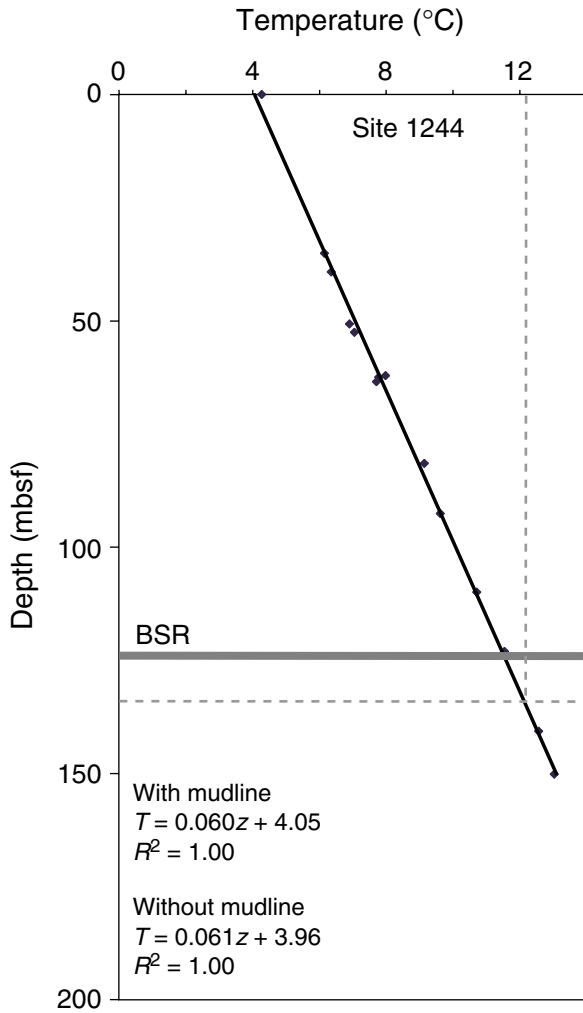
Figure F36. A–D. Volume-time plots obtained while degassing PCSs deployed at Site 1244. The cumulative volume and the volume of gas splits are also shown. (Continued on next page.)
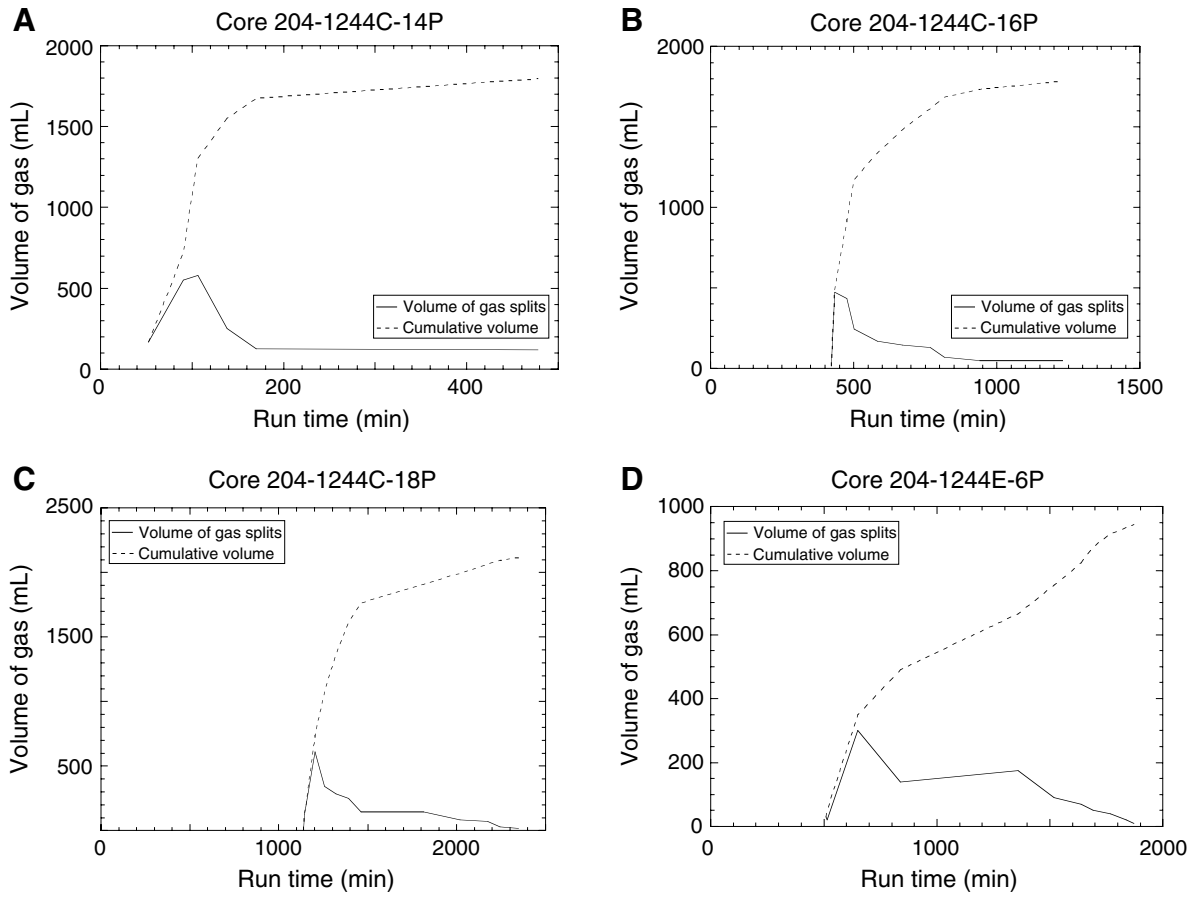
Figure F36 (continued). E–G. Volume-time plots.

Figure F37. Methane concentration in sediments at Site 1244 based on headspace (HS) and pressure core sampler (PCS) data. Estimated theoretical solubility of methane in pore water (extrapolated from values calculated for higher pressures) (depths) (Handa, 1990; Duan et al., 1992) is shown, and fields of dissolved methane (D), methane hydrate (H), and free methane (F) are depicted. The gray area indicates the uncertainties in the position of the boundaries. Note that the headspace technique fails to determine accurate concentration values above ~2 mM because methane is relatively abundant in situ and it rapidly escapes from sediments upon core retrieval.

Figure F38. Gamma ray attenuation (GRA) density profile along Core 204-1244E-8Y (Fugro Pressure Corer [FPC] 9), showing the density before, during, and after degassing.

FPC 9 (Core 204-1244E-8Y)
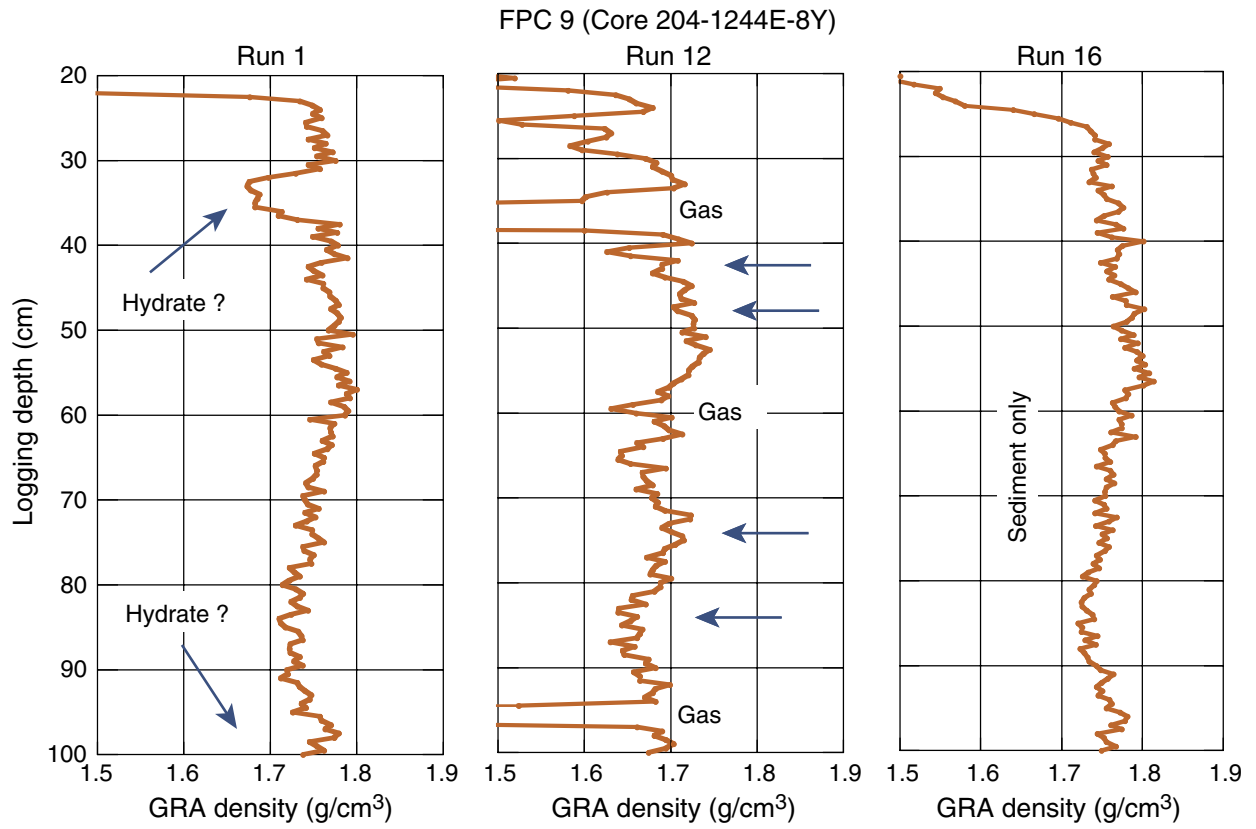
Figure F39. Quality control LWD logs from Hole 1244D. ROP = rate of penetration, TAB = time after bit.
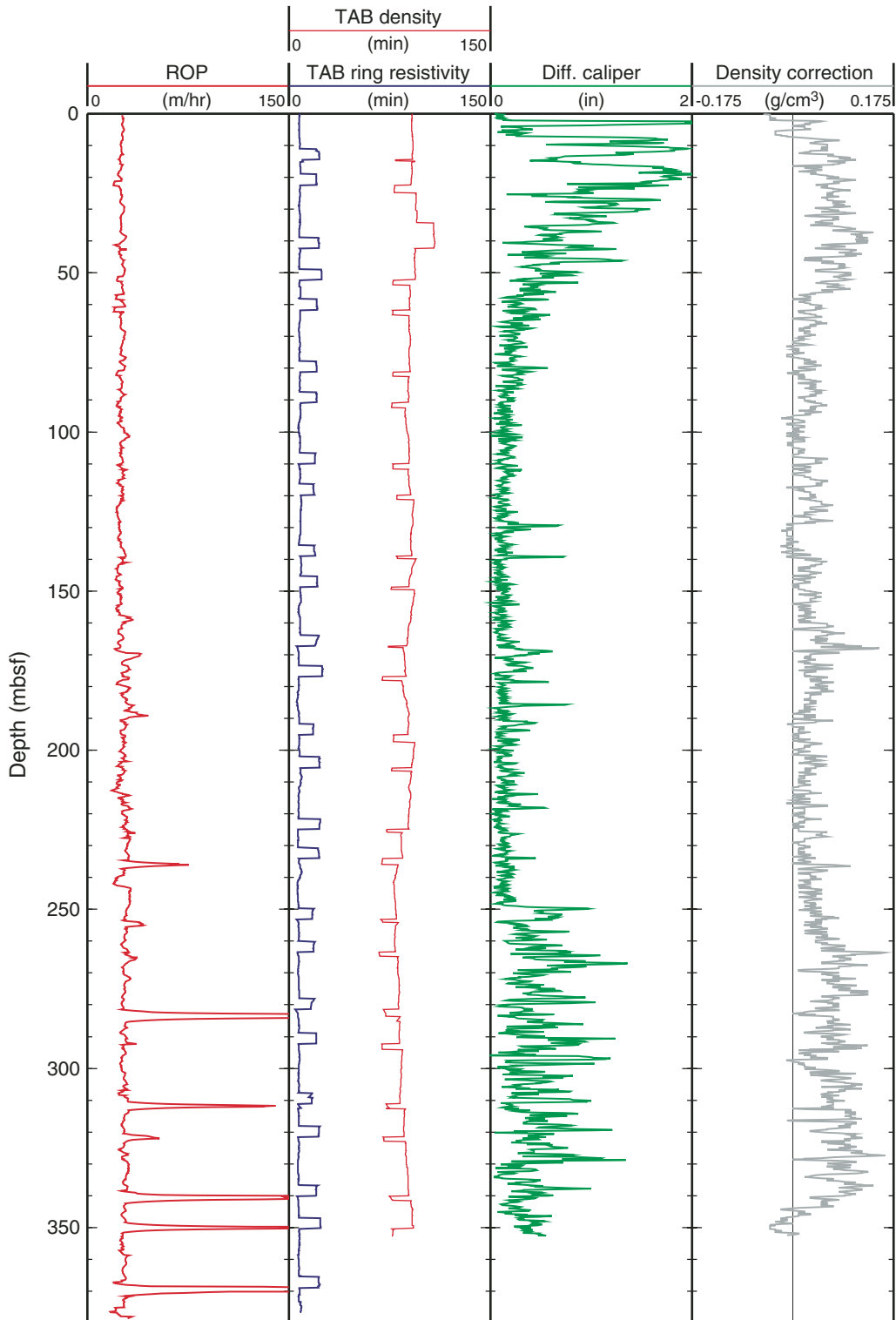
Figure F40. Summary of LWD data from Hole 1244D. gAPI = American Petroleum Institute gamma ray emission units, PEF = photoelectric factor, RAB = resistivity at the bit.
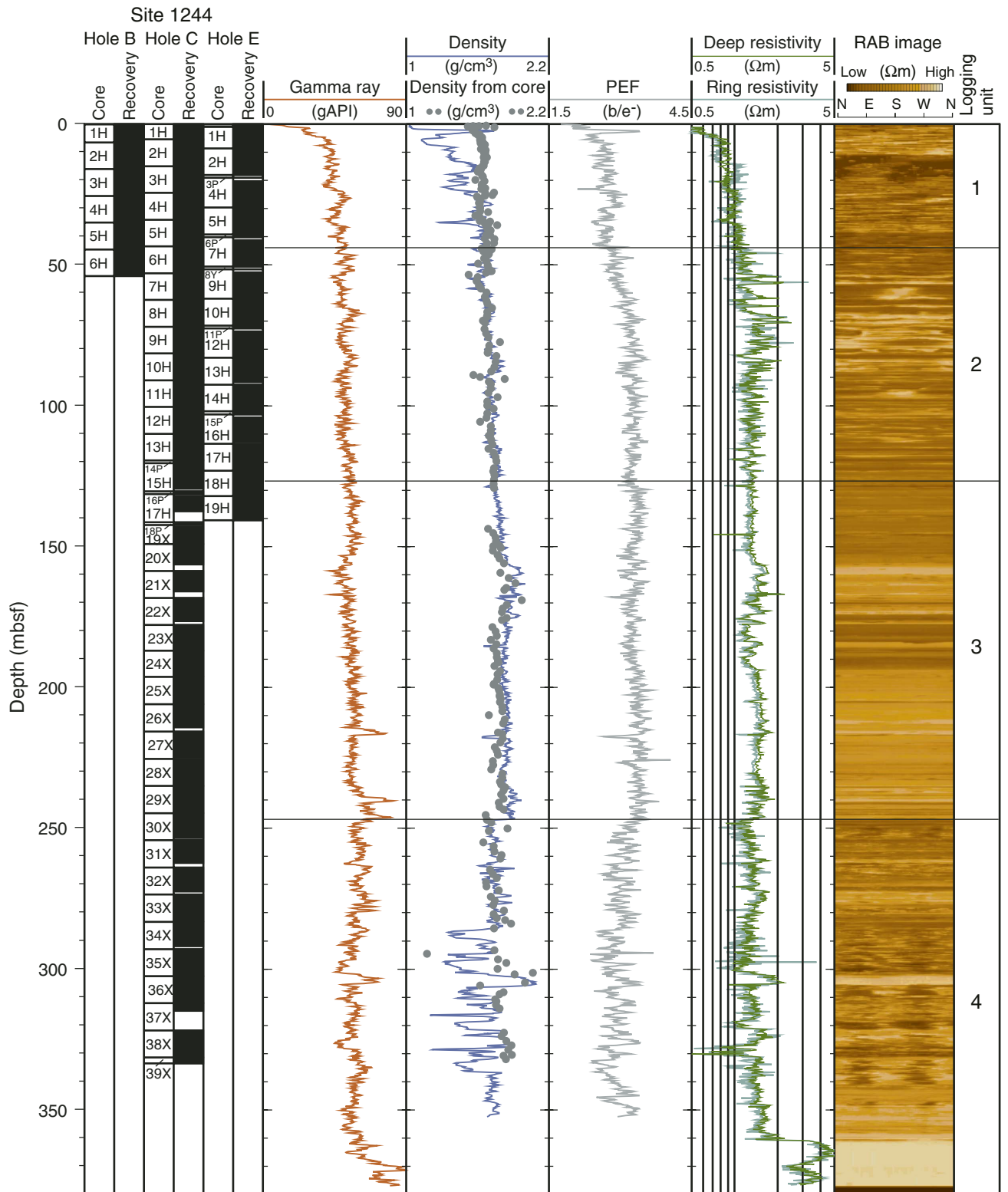
Figure F41. Summary of Hole 1244E CWL log data. gAPI = American Petroleum Institute gamma ray emission units, PEF = photoelectric factor.
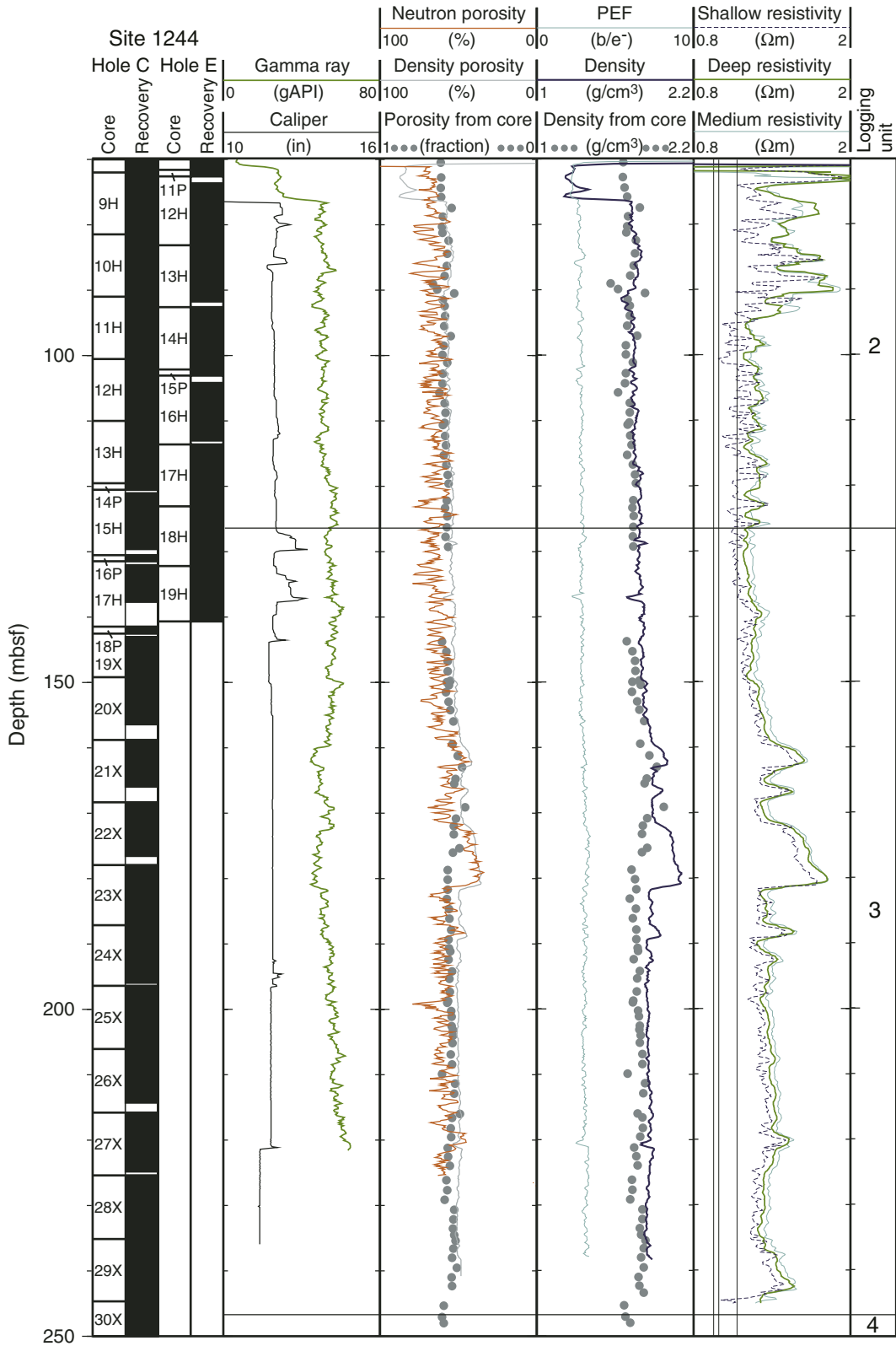
Figure F42. CWL gamma ray logging data from Hole 1244E. gAPI = American Petroleum Institute gamma ray emission units, FMS = Formation MicroScanner.
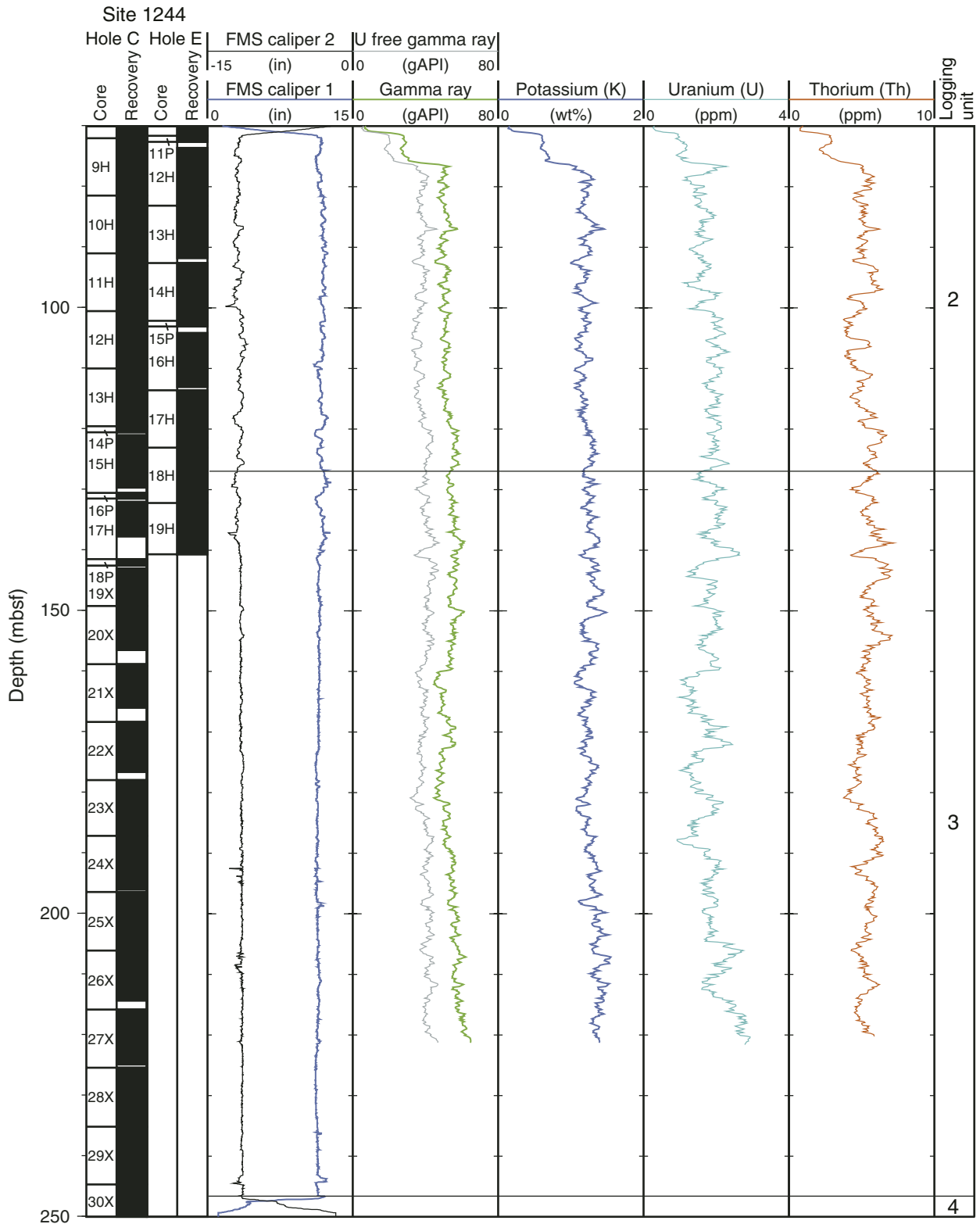
Figure F43. Comparison of logging-while-drilling (LWD) and CWL downhole logging data from Holes 1244D and 1244E. por. = porosity, PEF = photoelectric factor, gAPI = American Petroleum Institute gamma ray emission units, LWD = logging while drilling.
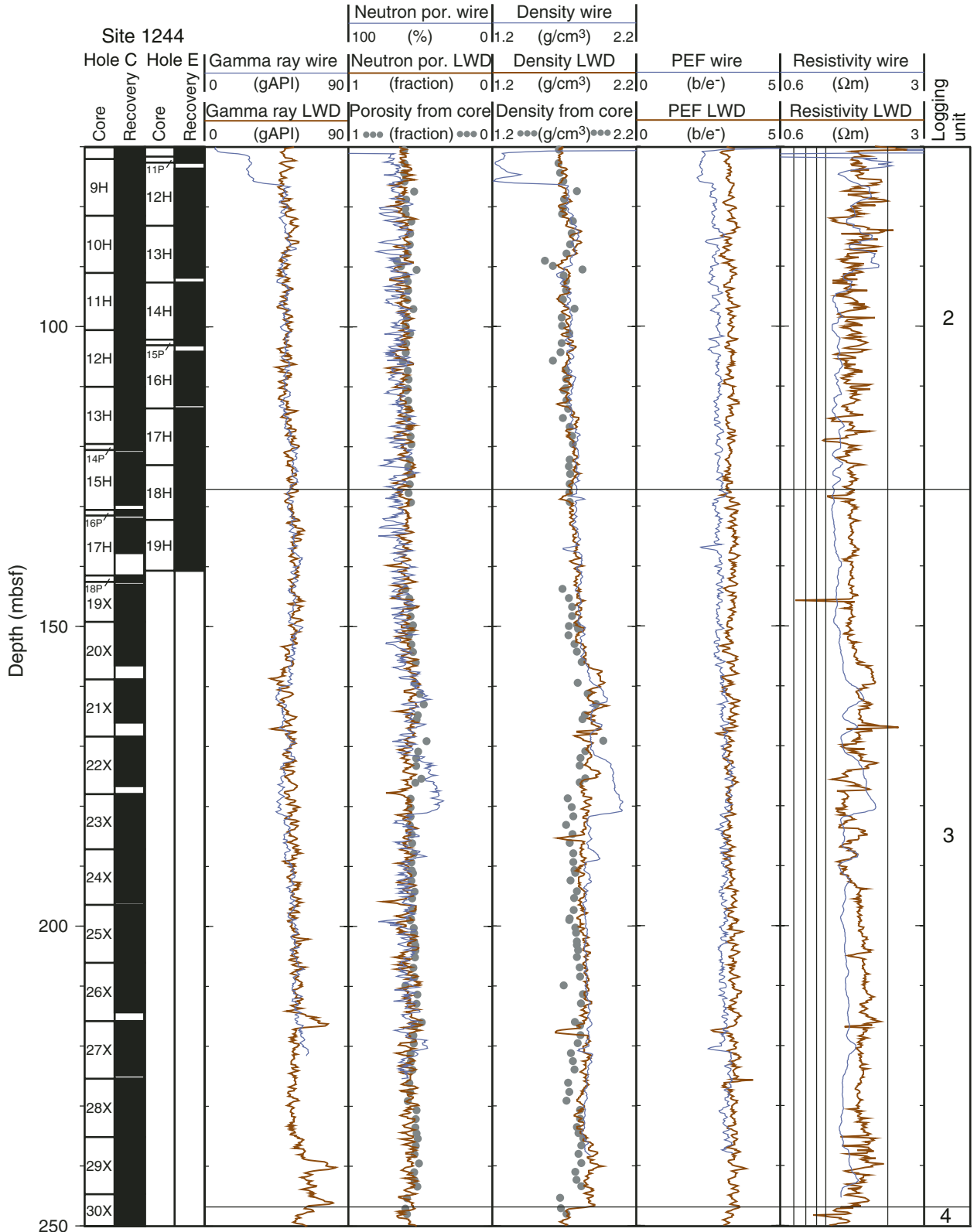
Figure F44. CWL acoustic logging data from Hole 1244E. The resistivity log is used as a reference indicator of the presence of gas hydrate. Low waveform amplitudes are also possible indicators of gas hydrate. SPh. foc. res. = spherically focused resistivity.
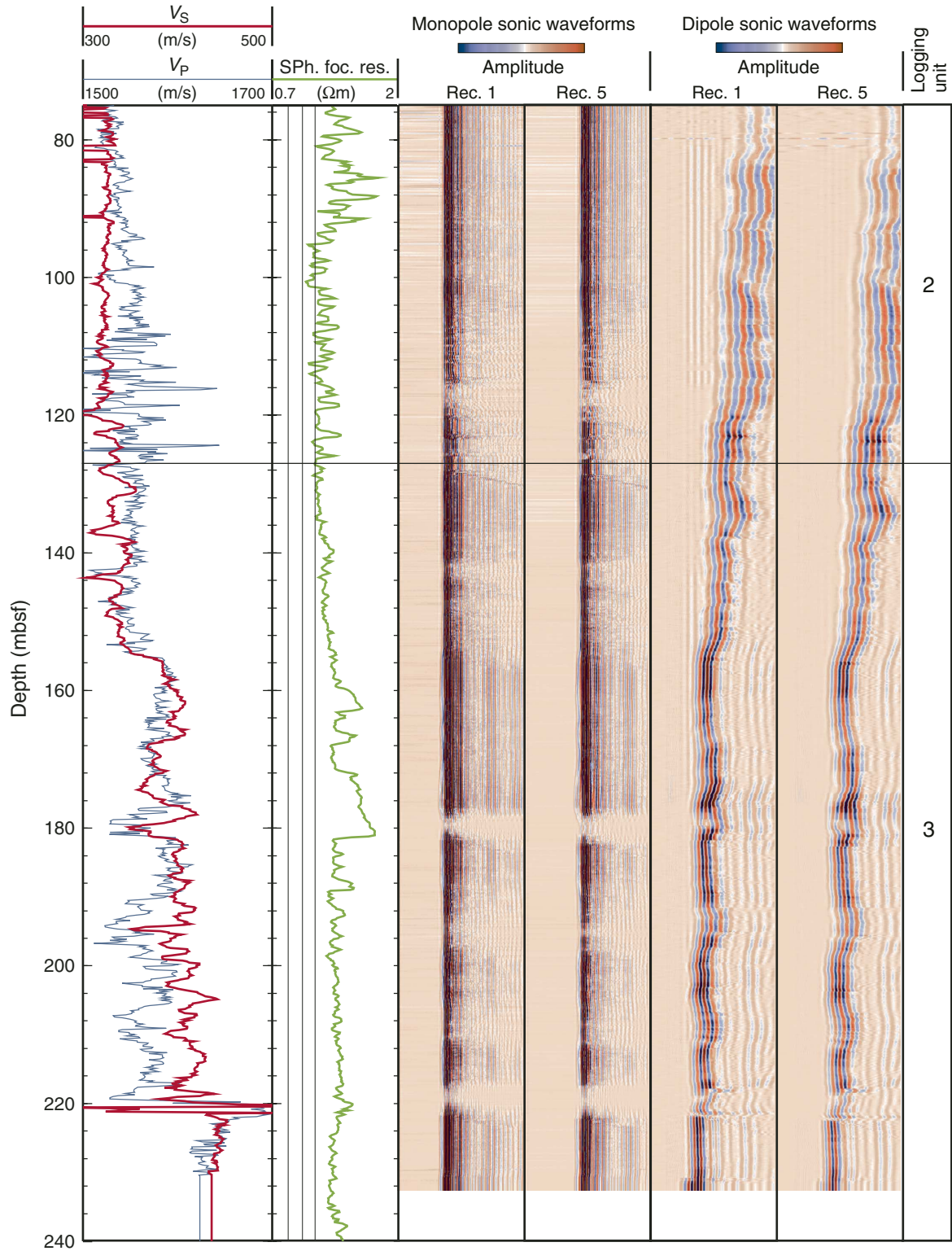
Figure F45. Resistivity-at-the-bit (RAB) image showing the presence of gas hydrate as bright resistive material occupying dipping fractures in Hole 1244D. 3-D = three-dimensional.
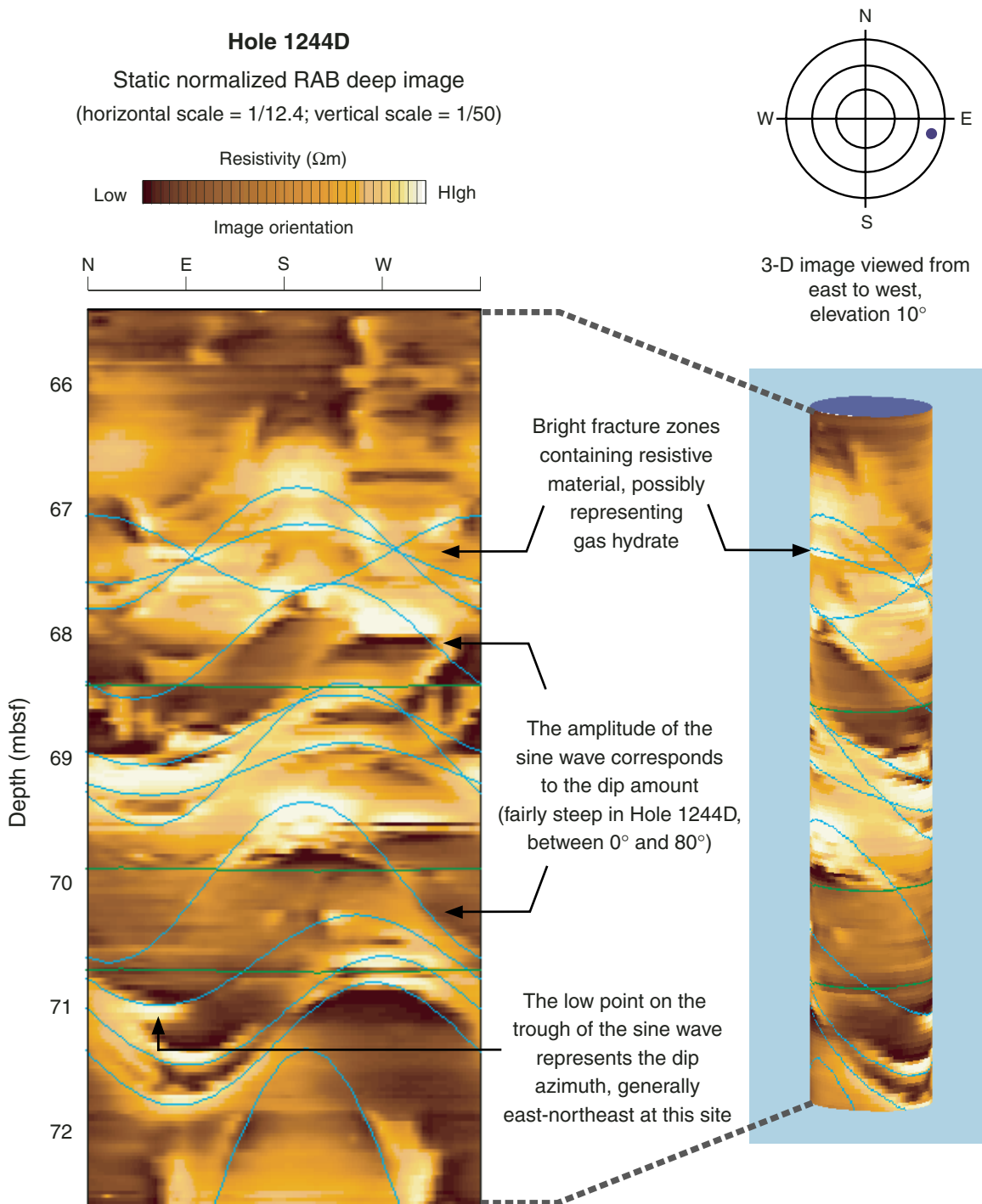
Figure F46. Resisitivity-at-the-bit (RAB) tool and Formation MicroScanner (FMS) images showing detail of an ash layer in Holes 1244D and 1244E.
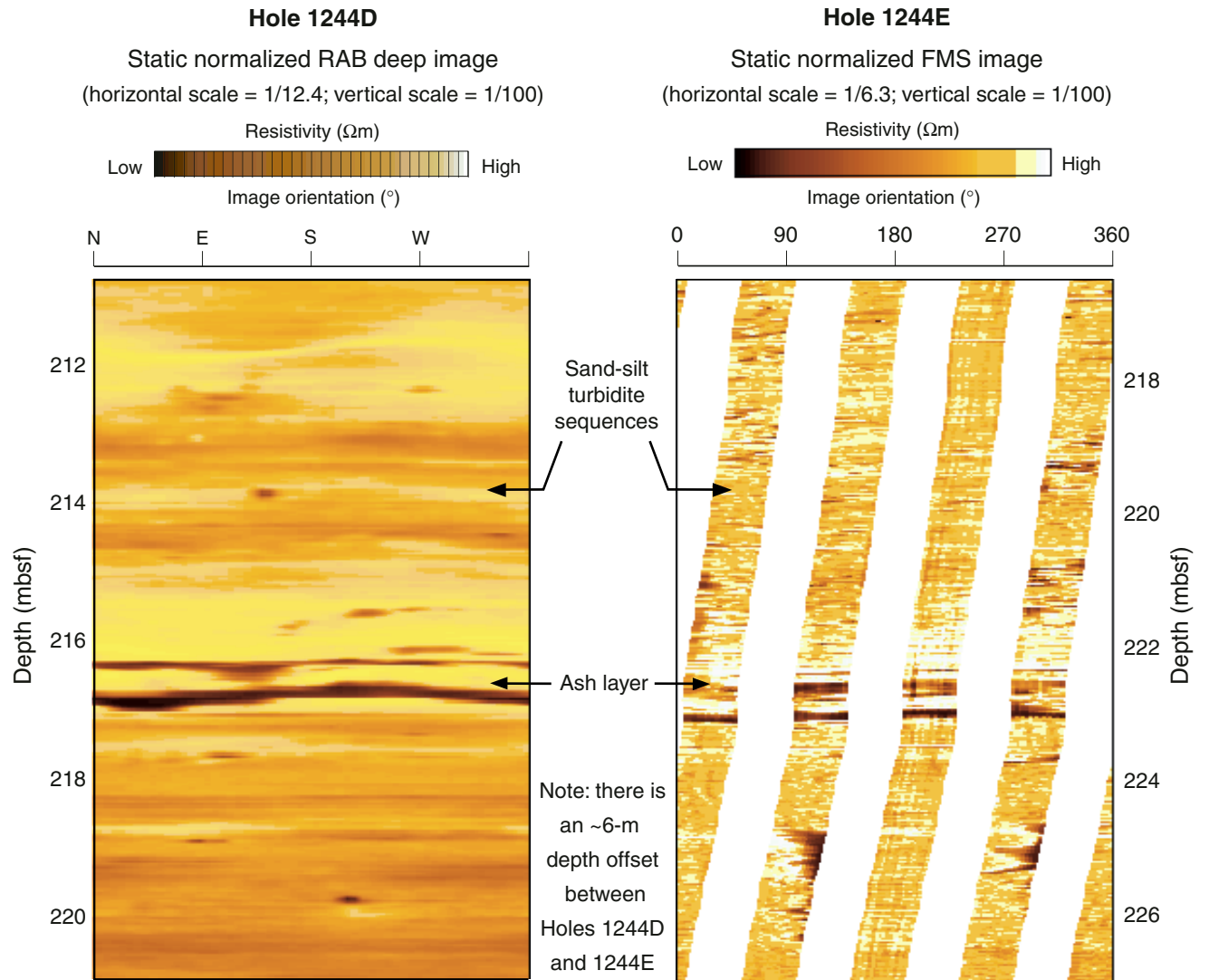
Figure F47. Resisitivity-at-the-bit (RAB) tool and Formation MicroScanner (FMS) images showing turbidites characterized by interbedded bright resistive and dark conductive layers in Holes 1244D and 1244E.

Hole 1244D

Static normalized RAB deep image

(horizontal scale = 1/12.4; vertical scale = 1/240)

Hole 1244E

Static normalized FMS image

(horizontal scale = 1/6.3; vertical scale = 1/240)

Horizontally bedded

Clay, silt, and sand

?

Layer thickness is variable and some layers could not be correlated between the two holes

Silty-sandy turbidites

Note: there is an ~6-m depth offset between Holes 1244D and 1244E
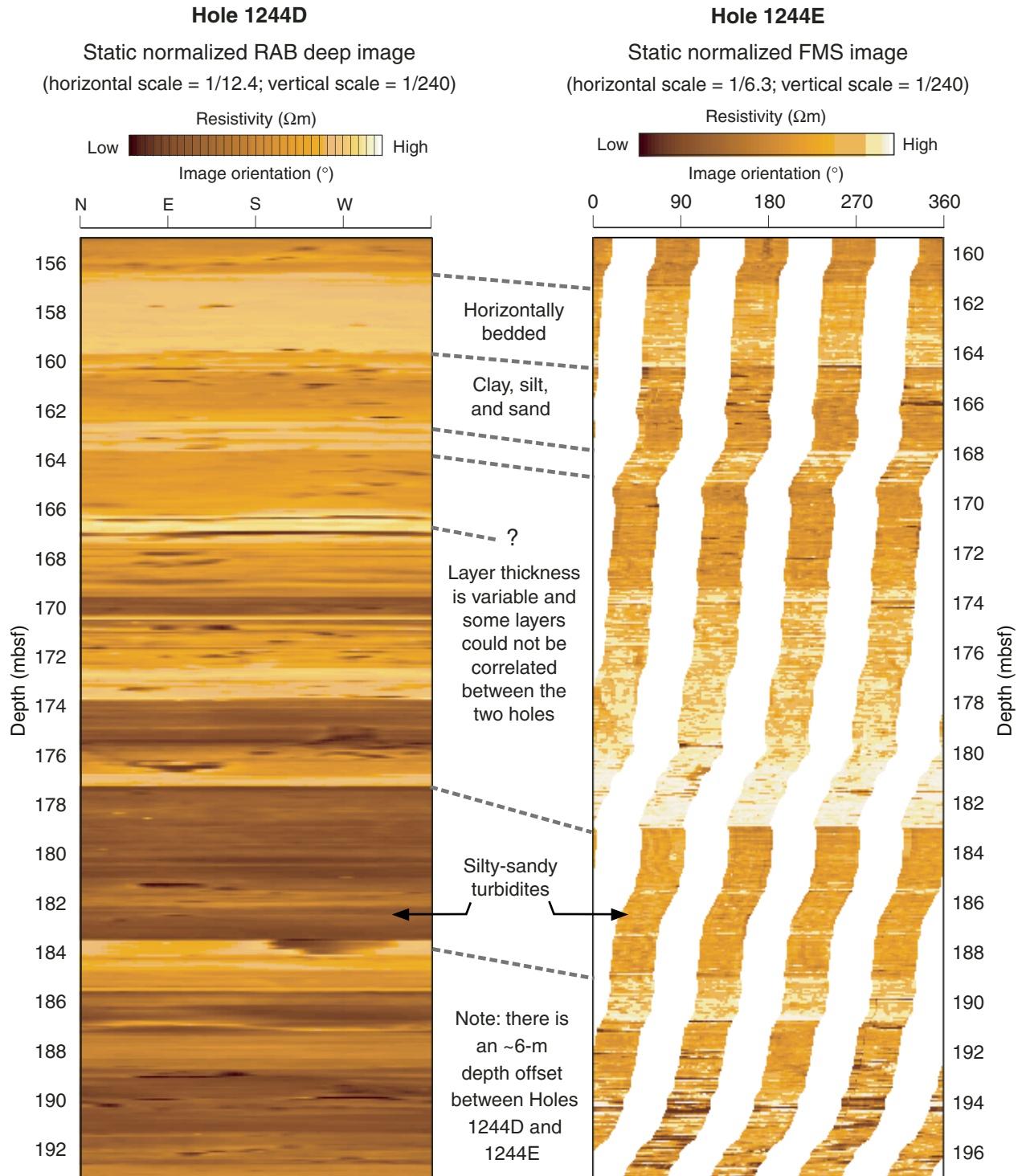
Figure F48. Resisitivity-at-the-bit (RAB) tool image showing borehole breakouts occurring as irregular, dark, conductive features oriented east-northeast and west-southwest. approx. = approximately.

Hole 1244D

Static normalized RAB deep image

(horizontal scale = 1/12.4; vertical scale = 1/100)
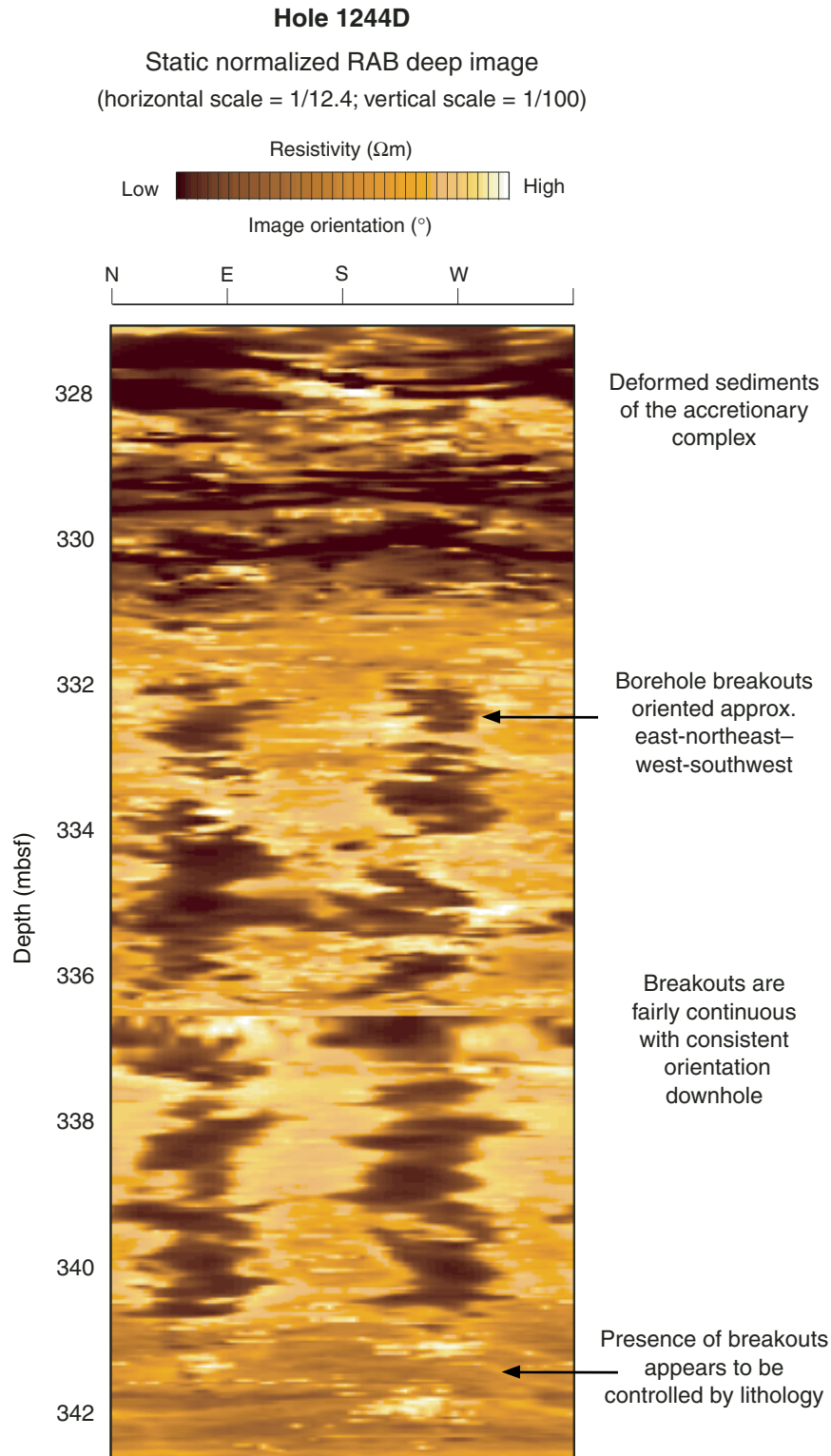
Figure F49. Comparison of logging-while-drilling (LWD)- and core-derived porosities from Hole 1244D. NRM-MRP = Nuclear Magnetic Resonance tool, RAB = resistivity-at-the-bit.
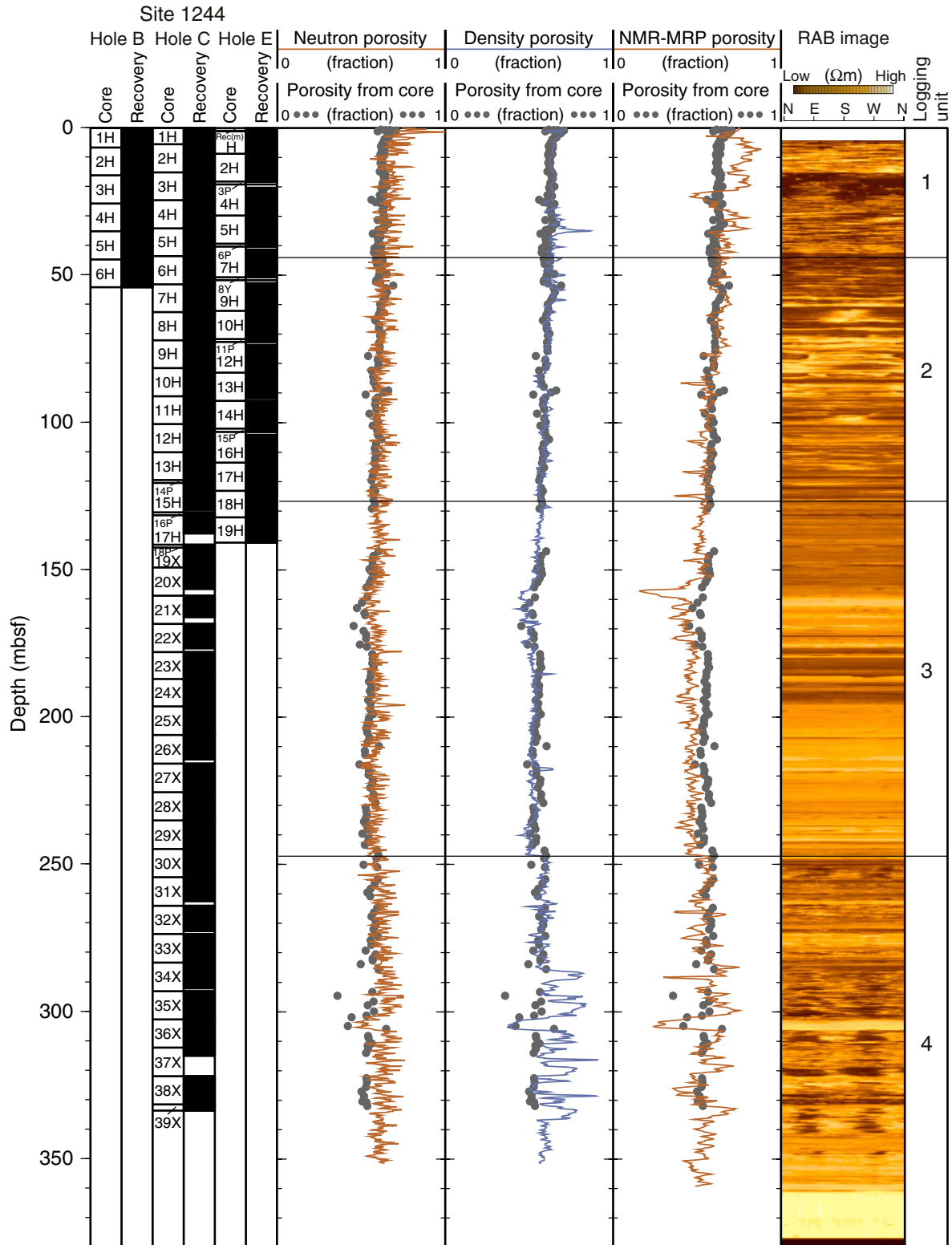
Figure F50. Logging-while-drilling (LWD) derived water saturations from Hole 1244D. gAPI = American Petroleum Institute gamma ray emission units, RAB = resistivity-at-the-bit.
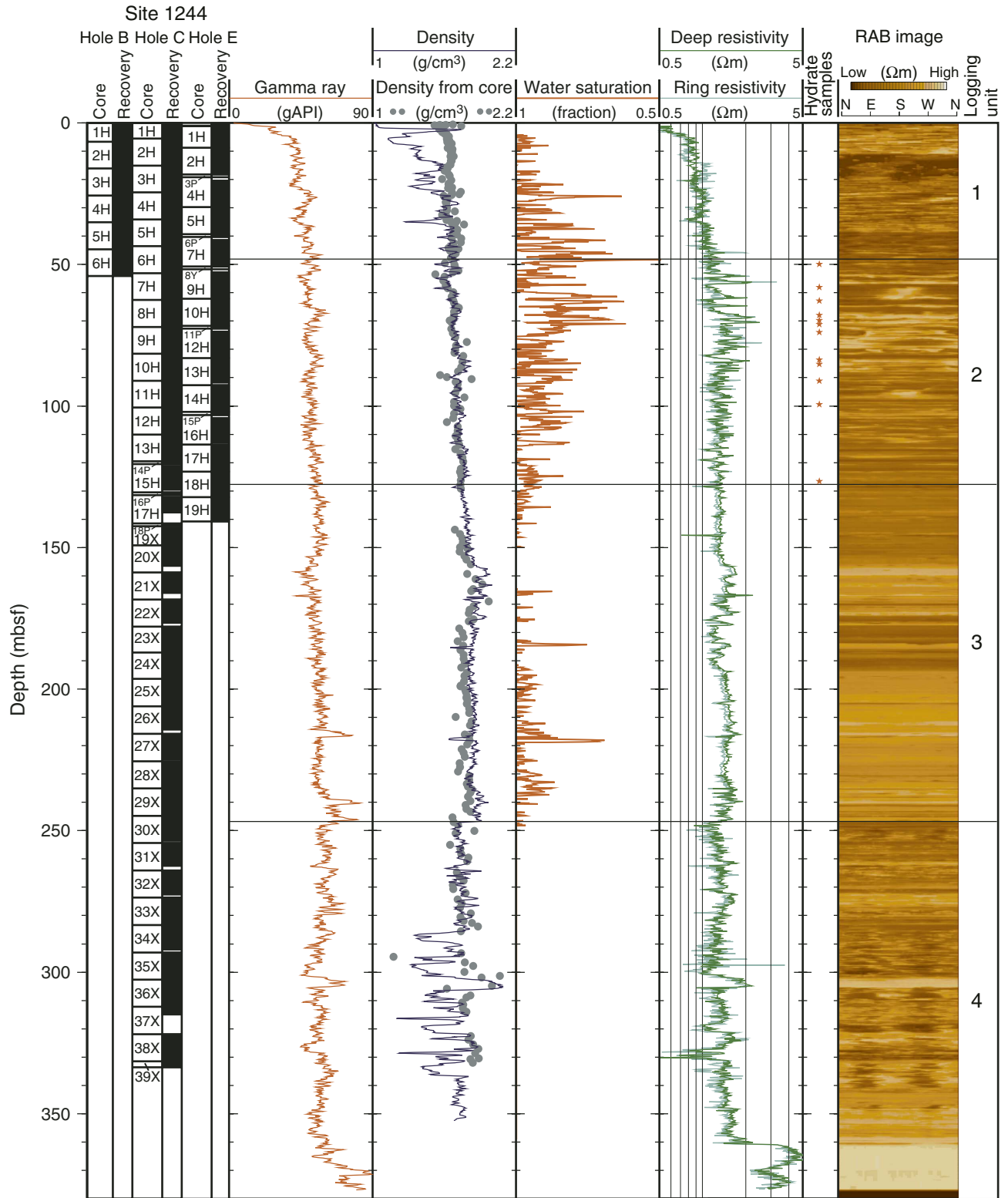
Figure F51. Borehole temperatures recorded with the TAP tool during the down and up pass of the two runs of the triple combo tool string in Hole 1244E.
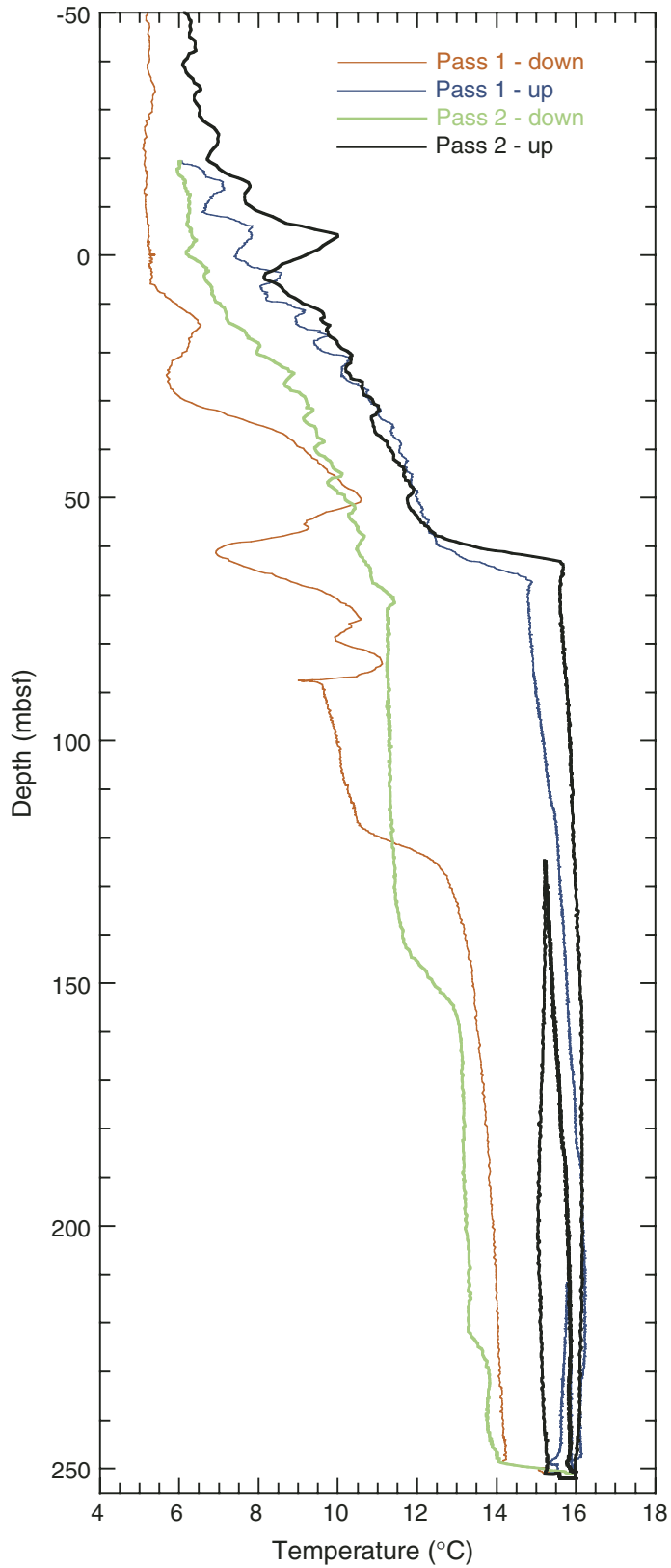
Table T1. Coring summary, Site 1244. (Continued on next two pages).

Hole 1244A
Latitude: 44°35.1701′N
Longitude: 125°7.1906′W
Time on site (hr): 204.50 (1415 hr, 12 Jul–1900 hr, 12 July 2002)
Time on hole (hr): 10.75 (1415 hr, 12 Jul–0100 hr, 13 Jul 2002)
Seafloor (drill pipe measurement from rig floor, mbrf): 907.6
Distance between rig floor and sea level (m): 10.9
Water depth (drill pipe measurement from sea level, m): 896.7
Total depth (drill pipe measurement from rig floor, mbrf): 917.5
Total penetration (meters below seafloor, mbsf): 9.5
Total number of cores: 1
Total number of drilled intervals: 0
Total length of cored section (m): 9.5
Total core recovered (m): 9.99
Core recovery (%): 105.2

Hole 1244B
Latitude: 44°35.1702′N
Longitude: 125°7.1917′W
Time on hole (hr): 11.75 (0100 hr, 13 Jul–1245 hr, 13 Jul 2002)
Seafloor (drill pipe measurement from rig floor, mbrf): 906.8
Distance between rig floor and sea level (m): 10.8
Water depth (drill pipe measurement from sea level, m): 896.0
Total depth (drill pipe measurement from rig floor, mbrf): 961
Total penetration (meters below seafloor, mbsf): 54.1
Total number of cores: 6
Total number of drilled intervals: 0
Total length of cored section (m): 54.1
Total core recovered (m): 56.85
Core recovery (%): 105.1

Hole 1244C
Latitude: 44°35.1784′N
Longitude: 125°7.1902′W
Time on hole (hr): 64.75 (1245 hr, 13 Jul–0530 hr, 16 Jul 2002)
Seafloor (drill pipe measurement from rig floor, mbrf): 906.0
Distance between rig floor and sea level (m): 10.9
Water depth (drill pipe measurement from sea level, m): 895.1
Total depth (drill pipe measurement from rig floor, mbrf): 1239.5
Total penetration (meters below seafloor, mbsf): 333.5
Total number of cores: 39
Total number of drilled intervals: 3
Total length of cored section (m): 332
Total core recovered (m): 315.50
Core recovery (%): 95.0

Hole 1244D
Latitude: 44°35.1865′N
Longitude: 125°7.1900′W
Time on hole (hr): 37.50 (0530 hr, 16 Jul–1900 hr, 17 Jul 2002)
Seafloor (drill pipe measurement from rig floor, mbrf): 906.0
Distance between rig floor and sea level (m): 10.9
Water depth (drill pipe measurement from sea level, m): 895.1
Total depth (drill pipe measurement from rig floor, mbrf): 1286
Total penetration (meters below seafloor, mbsf): 380
Total number of cores: 0
Total number of drilled intervals: 1
Total length of cored section (m): 0
Total core recovered (m): 0
Core recovery (%): 0

Hole 1244E
Latitude: 44°35.1709′N
Longitude: 125°7.1719′W
Time on hole (hr): 74.75 (2300 hr, 18 Aug–0145 hr, 22 Aug 2002)
Seafloor (drill pipe measurement from rig floor, mbrf): 904.8
Distance between rig floor and sea level (m): 11.2
Water depth (drill pipe measurement from sea level, m): 893.6
Total depth (drill pipe measurement from rig floor, mbrf): 1154.8
Total penetration (meters below seafloor, mbsf): 250
Total number of cores: 19
Total number of drilled intervals: 6
Total length of cored section (m): 135.8
Total core recovered (m): 137.73
Core recovery (%): 101.4

Table T1 (continued).

Hole 1244F
Latitude: 44°35.1691′N
Longitude: 125°7.1705′W
Time on hole (hr): 5.00 (0145 hr, 22 Aug–0645 hr, 22 Aug 2002)
Seafloor (drill pipe measurement from rig floor, mbrf): 907.4
Distance between rig floor and sea level (m): 11.1
Water depth (drill pipe measurement from sea level, m): 896.3
Total depth (drill pipe measurement from rig floor, mbrf): 931.5
Total penetration (meters below seafloor, mbsf): 0
Total number of cores: 4
Total number of drilled intervals: 0
Total length of cored section (m): 24.1
Total core recovered (m): 24.9
Core recovery (%): 103.3

Core	Date (2002)	Local time (hr)	Depth (mbsf) Top	Bottom	Length (m) Cored	Recovered	Recovery (%)
204-1244A-							
1H	13 Jul	0100	0.0	9.5	9.5	9.99	105.2
			Cored totals:		9.5	9.99	105.2
			Drilled total:		0.0		
			Total:		9.5		
204-1244B-							
1H	13 Jul	0135	0.0	6.6	6.6	6.66	100.9
2H	13 Jul	0220	6.6	16.1	9.5	9.93	104.5
3H	13 Jul	0300	16.1	25.6	9.5	10.11	106.4
4H	13 Jul	0425	25.6	35.1	9.5	10.56	111.2
5H	13 Jul	0500	35.1	44.6	9.5	9.96	104.8
6H	13 Jul	0555	44.6	54.1	9.5	9.63	101.4
			Cored totals:		54.1	56.85	105.1
			Drilled total:		0.0		
			Total:		54.1		
204-1244C-							
1H	13 Jul	1945	0.0	5.5	5.5	5.50	100.0
2H	13 Jul	2020	5.5	15.0	9.5	10.01	105.4
3H	13 Jul	2055	15.0	24.5	9.5	10.19	107.3
4H	13 Jul	2135	24.5	34.0	9.5	10.15	106.8
5H	13 Jul	2200	34.0	43.5	9.5	9.29	97.8
6H	13 Jul	2250	43.5	53.0	9.5	10.01	105.4
7H	14 Jul	0450	53.0	62.5	9.5	9.64	101.5
8H	14 Jul	0720	62.5	72.0	9.5	9.65	101.6
9H	14 Jul	0815	72.0	81.5	9.5	10.21	107.5
10H	14 Jul	0910	81.5	91.0	9.5	9.68	101.9
11H	14 Jul	1000	91.0	100.5	9.5	9.69	102.0
12H	14 Jul	1145	100.5	110.0	9.5	9.98	105.1
13H	14 Jul	1245	110.0	119.5	9.5	10.38	109.3
14P	14 Jul	1410	119.5	120.5	1.0	1.18	118.0
			*****Drilled from 120.5 to 121 mbsf*****				
15H	14 Jul	1505	121.0	130.5	9.5	8.68	91.4
16P	14 Jul	1610	130.5	131.5	1.0	1.00	100.0
			*****Drilled from 131.5 to 132 mbsf*****				
17H	14 Jul	1650	132.0	141.5	9.5	5.70	60.0
18P	14 Jul	1830	141.5	142.5	1.0	1.08	108.0
			*****Drilled from 142.5 to 143 mbsf*****				
19X	14 Jul	1925	143.0	149.2	6.2	7.82	126.1
20X	14 Jul	2215	149.2	158.8	9.6	7.25	75.5
21X	14 Jul	2325	158.8	168.3	9.5	7.21	75.9
22X	15 Jul	0055	168.3	177.9	9.6	8.31	86.6
23X	15 Jul	0155	177.9	187.1	9.2	9.41	102.3
24X	15 Jul	0250	187.1	196.4	9.3	8.90	95.7
25X	15 Jul	0400	196.4	206.1	9.7	9.69	99.9
26X	15 Jul	0515	206.1	215.8	9.7	8.26	85.2
27X	15 Jul	0625	215.8	225.4	9.6	9.05	94.3
28X	15 Jul	0730	225.4	235.1	9.7	9.90	102.1
29X	15 Jul	0850	235.1	244.7	9.6	9.49	98.9
30X	15 Jul	0945	244.7	254.3	9.6	8.85	92.2
31X	15 Jul	1055	254.3	264.0	9.7	8.17	84.2
32X	15 Jul	1200	264.0	273.6	9.6	8.63	89.9
33X	15 Jul	1300	273.6	283.3	9.7	9.62	99.2

Table T1 (continued).

Core	Date (2002)	Local time (hr)	Depth (mbsf) Top	Depth (mbsf) Bottom	Length (m) Cored	Length (m) Recovered	Recovery (%)
34X	15 Jul	1400	283.3	293.0	9.7	8.80	90.7
35X	15 Jul	1525	293.0	302.6	9.6	9.75	101.6
36X	15 Jul	1620	302.6	312.2	9.6	9.59	99.9
37X	15 Jul	1750	312.2	321.9	9.7	2.74	28.2
38X	15 Jul	1920	321.9	331.5	9.6	9.85	102.6
39X	15 Jul	2030	331.5	333.5	2.0	2.19	109.5
			Cored totals:		332.0	315.50	95.0
			Drilled total:		1.5		
			Total:		333.5		

204-1244D-

*****Drilled from 0 to 380 mbsf*****

204-1244E-

Core	Date (2002)	Local time (hr)	Depth (mbsf) Top	Depth (mbsf) Bottom	Length (m) Cored	Length (m) Recovered	Recovery (%)
1H	19 Aug	0640	0.0	8.7	8.7	8.76	100.7
2H	19 Aug	0745	8.7	18.2	9.5	9.94	104.6
3P	19 Aug	0840	18.2	19.2	1.0	0.00	0.0
			*****Drilled from 19.2 to 20.2 mbsf*****				
4H	19 Aug	0910	20.2	29.7	9.5	10.24	107.8
5H	19 Aug	1000	29.7	39.2	9.5	10.11	106.4
6P	19 Aug	1105	39.2	40.2	1.0	1.00	100.0
			*****Drilled from 40.2 to 41.2 mbsf*****				
7H	19 Aug	1155	41.2	50.7	9.5	10.59	111.5
8Y	19 Aug	1310	50.7	51.7	1.0	0.92	92.0
			*****Drilled from 51.7 to 52.6 mbsf*****				
9H	19 Aug	1530	52.6	62.1	9.5	9.91	104.3
10H	19 Aug	1625	62.1	71.6	9.5	9.78	102.9
11P	19 Aug	1725	71.6	72.6	1.0	1.00	100.0
			*****Drilled from 72.6 to 73.6 mbsf*****				
12H	19 Aug	1750	73.6	83.1	9.5	10.11	106.4
13H	19 Aug	1855	83.1	92.6	9.5	8.69	91.5
14H	19 Aug	1925	92.6	102.1	9.5	9.40	98.9
15P	19 Aug	2040	102.1	103.1	1.0	1.00	100.0
			*****Drilled from 103.1 to 104.1 mbsf*****				
16H	19 Aug	2100	104.1	113.6	9.5	8.94	94.1
17H	19 Aug	2200	113.6	123.1	9.5	9.66	101.7
18H	19 Aug	2300	123.1	132.2	9.1	9.09	99.9
19H	19 Aug	2340	132.2	140.7	8.5	8.59	101.1
			*****Drilled from 140.7 to 250 mbsf*****				
			Cored totals:		135.8	137.73	101.4
			Drilled total:		114.2		
			Total:		250		

204-1244F-

Core	Date (2002)	Local time (hr)	Depth (mbsf) Top	Depth (mbsf) Bottom	Length (m) Cored	Length (m) Recovered	Recovery (%)
1H	22 Aug	0300	0.0	4.1	4.1	4.10	100.0
2H	22 Aug	0335	4.1	13.6	9.5	9.72	102.3
3H	22 Aug	0415	13.6	23.1	9.5	10.08	106.1
4P	22 Aug	0515	23.1	24.1	1.0	1.00	100.0
			Cored totals:		24.1	24.90	103.3
			Drilled total:		0.0		
			Total:		24.1		

Table T2. Presence of gas hydrate based on infrared images of cores in liners, Holes 1244C and 1244E. (**See table notes.** Continued on next page.)

Core, section	ΔT (°C)	Gas hydrate texture*	Depth interval (mbsf)[†] Top	Bottom	Anomaly designation[‡]	Sampled interval Top (cm)	Bottom (cm)	Depth (mbsf)
204-1244C-								
6H	−1.0	Disseminated	44.70	45.00	IR8			
6H	−1.6	Vein, slight dip	46.60	46.69	IR9			
6H	−1.8	Nodular	47.83	47.96	IR10			
6H	−0.4	Disseminated	49.20	49.10	IR11			
6H	−0.5	Disseminated	51.10	51.50	IR12			
7H	−1.5	Vein; horizontal or dipping; may be gas expansion	54.30	54.45	IR13			
7H	−0.7	Disseminated; variable ΔT	54.70	55.70	IR14			
7H	−5.3	Vein (10 cm thick) with disseminated hydrate above and below	55.85	56.90	IR15			
7H	−3.1	Nodular	58.20	58.70	IR16			
7H	−0.3	Disseminated	60.84	60.90	IR17			
8H	−0.5	Disseminated	62.70	62.76	IR18			
8H-1	−5.6	Nodular (large single nodule); vein	63.72	63.90	IR19	47	52	62.97
8H	−0.6	Disseminated	68.00	68.30	IR20			
8H-5	−6.6	Vein; low dip 5-cm thick	68.95	69.07	IR21	48	80	68.00
8H	−0.4	Nodular	70.40	70.45	IR22			
9H	−2.0	Vein; disseminated	75.66	75.79	IR23			
9H	−0.7	Disseminated	77.92	78.01	IR24			
9H	−1.2	Disseminated; vein	80.90	81.10	IR25			
10H-2	−3.2	Nodular; vein; steep dip; 2-cm nodules	84.01	84.18	IR26	70	103	83.70
10H	−0.9	Disseminated	90.55	90.60	IR27			
11H	−1.0	Disseminated	91.50	91.71	IR28a			
11H	−1.1	Disseminated	96.21	96.90	IR29a			
11H	−1.0	Disseminated	97.25	97.46	IR30a			
11H	−1.0	Disseminated	98.54	98.82	IR31a			
11H	−1.1	Disseminated	99.15	99.30	IR32a			
11H	−1.3	Disseminated; vein	100.00	100.40	IR33a			
12H	−0.6	Vein; disseminated	102.55	102.60	IR34a			
12H	−1.0	Disseminated	103.92	104.01	IR35a			
13H	−1.5	Disseminated	110.63	110.92	IR36a			
13H	−0.2	Disseminated	114.10	114.24	IR37a			
13H	−1.0	Disseminated	117.33	117.50	IR38a			
15H	−1.1	Disseminated	125.03	125.31	IR39a			
204-1244E-								
4H	−0.5	Disseminated	22.90	23.20	IR491			
7H	−0.5	Disseminated; vein	44.25	44.65	IR492			
7H	−1.2	Disseminated	47.50	47.70	IR493			
7H	−2.7	Vein; slight dip; nodular	48.01	48.15	IR494			
7H	−2.7	Vein; slight dip	49.15	49.32	IR495			
7H	−1.1	Disseminated	49.50	49.59	IR496			
7H-6	−3.8	Vein; moderate dip; nodular	49.99	50.16	IR497	124	141	49.94
9H	−0.7	Disseminated	55.73	56.10	IR498			
9H	−1.5	Disseminated	57.90	58.24	IR499			
9H-4	−6.9	Vein; moderate to steep dip	59.30	59.70	IR500	98	106	58.08
10H	−2.7	Vein?	62.10	62.17	IR501			
10H	−1.4	Nodular	62.70	62.72	IR502			
10H	−1.7	Nodular	65.40	65.50	IR503			
10H	−2.4	Vein; steep dip; nodular	65.56	65.79	IR504			
10H	−2.0	Nodular	68.53	68.56	IR505			
10H-6	−1.4	Nodular	70.03	70.05	IR506	20	28	69.80
10H	−1.3	Vein; disseminated	70.40	70.45	IR507			
10H	−0.8	Nodular	70.65	70.74	IR508			
10H	−5.4	Vein; steeply dipping; nodular	71.40	71.50	IR509			
12H-1	−5.1	Nodular	73.95	74.25	IR510	50	60	74.10
12H	−1.1	Vein	79.90	79.95	IR511			
12H	−1.3	Disseminated	82.67	82.75	IR512			
13H	−1.2	Disseminated; includes gas void	83.30	83.65	IR513			
13H	−0.8	Vein; shallow dip; nodular	85.65	85.72	IR514			
13H-2	−2.9	Disseminated	86.75	86.90	IR515	70	80	85.30
13H	−0.7	Nodular; with disseminated above and below	89.31	89.65	IR516			
13H	−1.0	Disseminated	90.35	90.44	IR517			
13H	−2.3	Disseminated; vein	90.69	90.93	IR518			
13H-6	−4.9	Vein; thick; steep dip; nodular	92.05	92.48	IR519	107	150	90.97
14H	−0.6	Disseminated	92.96	93.01	IR520			
14H	−0.8	Vein; disseminated	93.68	93.77	IR521			
14H	−1.1	Nodular; disseminated	94.30	94.48	IR522	41	51	93.01

Table T2 (continued).

Core, section	ΔT (°C)	Gas hydrate texture*	Depth interval (mbsf)† Top	Depth interval (mbsf)† Bottom	Anomaly designation‡	Sampled interval Top (cm)	Sampled interval Bottom (cm)	Sampled interval Depth (mbsf)
14H-2	−0.8	Disseminated	95.15	95.23	IR523			
14H	−0.8	Disseminated	97.69	97.78	IR524			
14H	−1.1	Disseminated	98.08	98.15	IR525			
14H	−0.9	Disseminated	98.91	99.32	IR526			
14H	−3.0	Nodular	100.06	100.16	IR527			
14H	−1.9	Nodular; vein	100.30	100.37	IR528			
14H	−0.7	Disseminated	100.88	100.93	IR529			
14H	−1.0	Disseminated; vein; nodular	101.31	101.67	IR530			
17H-5	−1.8	Vein	113.78	113.90	IR531	39	62	113.09
17H	−0.7	Disseminated	114.30	114.41	IR532			
17H	−1.5	Disseminated	114.66	114.74	IR533			
17H	−1.7	Nodular	114.98	115.05	IR534			
17H	−0.5	Disseminated; vein	115.70	115.77	IR535			
17H	−0.8	Disseminated	116.75	117.00	IR536			
17H	−1.5	Nodular; disseminated	118.08	118.29	IR537			
17H	−1.7	Nodular	118.58	118.29	IR538			
17H	−1.7	Nodular	118.58	118.82	IR538			
17H	−1.7	Disseminated	121.25	121.25	IR539			

Notes: * = from anomaly characteristics and core description, if available. † = from uncut core liner. ‡ = used for reference to specific anomalies in text and figures. The difference between these depth intervals and the equivalent curated section depth intervals is typically <1 m.

Table T3. Bioevents, Hole 1244C.

Age (Ma)	Bioevent	Top Core, section, interval (cm)	Top Depth (mbsf)	Bottom Core, section, interval (cm)	Bottom Depth (mbsf)	Average depth (mbsf)	Event number*	Comment
		204-1244C-		204-1244C-				
0.27	FO *Emiliania huxleyi*	8H-CC	71.60	9H-CC	82.16	76.88	1	Nannofossil
0.30	LO *Proboscia curvirostris*	9H-CC	82.16	10H-CC	91.13	86.65	2	Diatom
0.46	LO *Pseudoemiliania lacunosa*	9H-CC	82.16	10H-CC	91.13	86.65	3	Nannofossil
1.00	LO *Actinocyclus oculatus*	24X-CC	195.95	25X-CC	206.04	201.00	4	Diatom
1.00–2.00	FO small *Gephyrocapsa* spp. Acme	24X-CC	195.95	24X-CC	195.95	195.95	5	Nannofossil
1.59	FO *Calcidiscus macintyrei*	25X-CC	206.04	26X-CC	214.31	210.18	6	Nannofossil
1.60	FO *Proboscia curvirostris*	28X-CC	235.25	29X-CC	244.54	239.90	7	Diatom
1.67	FO *Gephyrocapsa lumina*	29X-CC	244.54	30X-CC	253.50	249.02	8	Nannofossil
1.70	FO medium *Gephyrocapsa* spp.	29X-CC	244.54	30X-CC	253.50	249.02	9	Nannofossil
2.00	LO *Neodenticula koizumii*	33X-CC	283.17	34X-CC	292.05	287.61	10	Diatom
2.40	FO *Neodenticula seminae*	36X-CC	312.14	37X-CC	314.89	313.52	11	Diatom
2.78	FO *Reticulofenestra ampla*	36X-CC	312.14	37X-CC	314.89	313.52	12	Nannofossil

Notes: * = number in Figure F13, p. 58. FO = first occurrence, LO = last occurrence.

Table T4. Interstitial water data, Holes 1244A, 1244C, 1244E and 1244F. (**See table notes.** Continued on the next two pages.)

Core, section, interval (cm)	Depth (mbsf)	pH	Alkalinity (mM)	Salinity (g/kg)	Cl (mM)	SO$_4$ (mM)	NH$_4$ (mM)	PO$_4$ (µM)	Na (mM)	K (mM)	Mg (mM)	Ca (mM)	B (µM)	Ba (µM)	Fe (µM)	Li (µM)	Mn (µM)	Sr (µM)	Color*	DOC (mM)
204-1244B-																				
1H-1, 140–150	1.40	7.74	1.50	35	550	30.5	0.0	4	—	—	54.3	11.0	560	7.2	0.6	27.0	1.42	86.7	0.00	—
1H-3, 140–150	4.40	8.11	10.55	35	554	23.5	3.3	28	—	—	50.8	8.3	569	5.0	1.8	22.1	1.34	83.3	—	—
2H-2, 140–150	9.50	8.03	38.86	34	549	0.3	—	130	—	—	49.2	4.2	768	38.1	1.1	13.3	0.94	71.7	0.09	—
2H-5, 140–150	14.00	7.97	44.56	34	554	0	—	—	—	—	50.5	3.5	835	111.1	1.4	12.9	0.98	70.9	—	—
3H-2, 140–150	19.00	7.82	—	35	—	0	—	—	—	—	48.2	3.4	—	—	—	—	—	—	—	—
3H-5, 140–150	23.50	7.90	57.37	—	557	0	8.2	169	—	—	46.9	3.3	922	66.2	1.1	18.2	4.35	75.3	0.16	—
4H-3, 135–150	28.63	7.65	61.84	36	555	—	11.2	298	—	—	50.0	3.2	—	—	—	—	—	—	0.16	—
4H-7, 22–32	33.50	7.77	64.50	36	558	0	13.2	242	—	—	49.0	3.2	—	—	—	—	—	—	0.16	—
5H-3, 135–150	38.46	7.69	66.48	36	552	0	13.9	274	—	—	49.5	3.1	1027	58.7	1.3	20.2	1.46	76.8	0.17	—
5H-6, 129–150	42.90	7.63	67.28	36	550	—	13.9	291	—	—	46.9	3.0	1140	58.4	1.7	20.6	1.31	79.0	0.18	—
6H-3, 135–150	46.78	7.69	68.23	36	546	0	12.7	236	—	—	49.8	2.9	1141	58.5	2.6	24.3	1.26	82.4	0.18	—
6H-6, 135–150	51.28	7.94	67.69	36	552	0	16.2	203	—	—	48.1	2.8	972	66.8	2.5	23.8	1.13	76.8	0.18	—
204-1244C-																				
1H-1, 65–75	0.65	7.26	2.86	34	550	29.7	0.0	0	490	13.2	53.5	10.4	593	2.5	5.4	27.7	1.43	84.0	0.00	—
1H-1, 140–150	1.40	7.72	3.39	34	552	28.6	0.0	8	483	13.7	53.1	10.1	600	4.5	2.7	24.9	1.10	78.8	—	—
1H-2, 65–75	2.15	7.73	4.28	34	550	28.0	0.1	7	485	12.6	51.9	9.8	631	1.9	2.7	24.8	1.01	80.6	—	—
1H-2, 140–150	2.90	7.80	6.20	34	550	26.6	0.3	15	487	12.8	51.3	9.4	618	2.6	4.0	23.1	1.01	79.4	0.01	—
1H-3, 65–75	3.65	7.86	8.37	34	550	24.5	0.6	21	491	12.9	53.8	9.0	622	2.0	2.6	21.9	0.92	81.8	—	—
1H-3, 140–150	4.40	8.01	12.11	33	550	21.3	1.0	38	496	12.1	50.4	8.0	554	—	—	19.6	1.07	78.3	0.03	—
1H-4, 60–70	5.10	7.97	15.54	33	551	18.2	1.2	38	496	11.8	48.0	7.1	—	—	—	—	—	—	—	—
2H-1, 65–75	6.15	7.69	23.72	33	551	11.3	2.2	66	488	12.0	47.2	5.7	731	3.5	3.1	17.0	0.94	72.9	—	—
2H-1, 140–150	6.90	8.05	29.40	33	552	7.4	2.4	89	487	11.9	45.2	5.0	—	—	—	—	—	—	0.06	—
2H-2, 65–75	7.65	7.48	23.82	33	552	3.8	3.1	106	498	12.6	49.1	4.5	746	11.0	2.5	14.2	0.89	69.7	—	—
2H-2, 140–150	8.40	8.15	37.42	33	554	1.5	3.2	116	474	12.3	46.7	4.0	695	—	3.8	15.3	0.95	73.6	0.08	—
2H-3, 65–75	9.15	7.72	—	33	553	0.9	3.3	141	481	12.0	47.3	4.0	712	25.9	2.6	12.2	0.92	67.3	0.09	—
2H-3, 140–150	9.90	7.79	40.08	32	556	0.6	4.1	166	479	12.1	46.6	3.6	775	31.2	3.4	12.4	0.93	70.3	0.10	—
2H-4, 65–75	10.65	7.98	40.65	33	557	0.7	4.4	177	486	12.0	44.8	3.5	765	32.5	2.9	11.9	0.93	69.5	—	—
2H-4, 140–150	11.40	7.95	40.93	34	556	0.7	—	190	—	11.9	45.2	3.3	745	37.0	3.8	11.7	0.95	69.0	—	—
2H-5, 65–75	12.15	7.98	42.82	34	556	0.5	4.9	209	489	12.9	47.5	3.3	764	40.3	2.9	11.5	0.94	70.3	—	—
2H-5, 140–150	12.90	7.89	43.87	33	556	0.5	5.5	235	503	12.1	44.2	3.0	792	41.2	2.8	11.5	0.93	70.2	0.12	—
2H-6, 65–75	13.65	7.91	46.35	34	558	0.5	5.4	244	488	12.5	44.4	2.9	802	47.8	3.4	11.7	0.93	69.9	—	—
2H-6, 140–150	14.40	7.68	45.78	33	557	0.4	7.0	257	485	11.8	43.6	3.1	778	—	3.0	11.6	0.95	70.6	0.13	—
2H-7, 64–74	15.14	7.92	45.56	33	560	0.5	6.8	263	486	12.1	44.1	2.7	815	49.1	3.2	11.2	0.98	68.5	—	—
3H-1, 140–150	16.40	7.71	50.27	35	555	0.5	7.5	260	499	11.2	41.5	2.8	891	51.0	3.1	11.2	1.43	73.2	—	—
3H-2, 140–150	17.90	7.72	51.97	35	555	1.0	8.1	290	480	11.2	43.4	3.0	—	—	—	—	—	—	0.15	—
3H-3, 140–150	19.40	7.78	53.20	34	558	0.6	8.4	268	487	11.5	42.2	2.8	829	54.1	10.8	12.4	3.54	66.9	0.14	—
3H-4, 140–150	20.90	—	—	—	—	—	—	—	—	11.9	41.5	2.8	—	—	—	—	—	—	—	—
3H-5, 140–150	22.40	7.75	55.65	35	559	0.5	10.7	110	499	—	—	—	915	51.9	15.8	14.6	4.37	70.6	—	—
3H-6, 140–150	23.90	7.68	56.39	35	557	0.4	10.3	276	487	10.9	42.6	3.0	975	58.2	27.1	16.1	6.05	76.2	0.17	—
3H-7, 84–94	24.84	7.68	58.43	35	557	1.1	10.7	286	487	11.2	41.8	2.8	—	—	—	—	—	—	0.17	—
4H-2, 135–150	27.35	7.71	64.05	35	558	—	11.8	286	491	12.0	42.3	2.9	970	—	14.9	19.5	4.46	74.8	0.15	—
4H-5, 135–150	31.85	7.71	63.88	35	558	0.9	12.2	262	492	11.4	42.7	2.5	1033	61.9	9.3	19.3	3.32	74.2	0.16	—
5H-2, 135–150	36.85	7.68	64.10	35	552	0.6	15.6	280	490	10.5	40.7	2.6	992	59.6	11.4	19.3	1.44	77.9	—	—
5H-5, 135–150	41.35	7.80	68.10	35	554	0.7	14.9	232	504	14.1	45.6	2.5	1091	50.9	14.2	20.0	1.22	73.5	0.16	—
6H-2, 135–150	46.35	7.71	63.93	34	531	0.6	14.2	259	479	13.1	44.0	2.5	979	48.8	13.0	19.8	1.20	67.4	0.17	—
6H-5, 135–150	50.71	7.82	68.17	35	558	2.3	16.0	228	501	13.8	43.6	2.4	982	57.8	8.5	22.4	1.12	68.1	0.18	—
7H-2, 135–150	54.79	8.17	55.82	32	514	—	15.8	189	430	14.6	39.0	2.1	840	49.0	5.3	21.7	1.01	63.5	0.17	—
7H-5, 135–150	58.97	7.67	68.25	35	550	0.8	13.5	238	493	13.2	43.6	2.8	1175	70.6	8.7	23.9	1.35	81.1	0.19	—

Table T4 (continued).

Core, section, interval (cm)	Depth (mbsf)	pH	Alkalinity (mM)	Salinity (g/kg)	Cl (mM)	SO$_4$ (mM)	NH$_4$ (mM)	PO$_4$ (µM)	Na (mM)	K (mM)	Mg (mM)	Ca (mM)	B (µM)	Ba (µM)	Fe (µM)	Li (µM)	Mn (µM)	Sr (µM)	Color*	DOC (mM)
8H-2, 135–150	64.37	7.74	67.46	35	556	0.5	17.5	209	469	14.0	43.3	2.5	1075	85.6	8.5	23.6	1.26	77.9	0.19	—
8H-5, 135–150	68.87	7.90	66.47	35	550	1.0	16.9	174	463	13.5	41.5	2.6	973	74.6	7.1	24.1	1.23	78.0	0.19	—
9H-2, 135–150	74.85	7.87	65.27	35	557	0.6	16.6	148	457	13.3	39.9	2.6	1011	78.2	5.6	26.9	1.09	78.1	—	—
9H-5, 135–150	79.35	7.86	64.21	34	535	1.0	16.6	177	459	13.9	40.4	2.7	1002	79.0	5.5	27.4	1.11	80.1	0.18	—
10H-2, 55–70	83.55	7.78	60.89	34	533	0.4	17.3	116	447	13.6	41.3	3.0	882	70.9	7.3	25.8	1.22	77.4	0.15	—
10H-5, 135–150	88.38	7.77	56.00	33	518	0.7	16.7	93	444	12.2	38.8	2.7	931	7.2	9.0	26.6	1.24	79.5	0.15	—
11H-2, 135–150	93.08	7.75	62.55	35	550	—	16.9	147	472	11.9	38.9	3.0	908	5.0	7.6	28.2	1.26	85.1	0.15	—
11H-5, 135–150	97.58	7.68	62.16	35	549	0.6	15.5	139	460	12.0	38.6	3.0	940	38.1	7.3	28.6	1.35	85.8	0.15	—
12H-2, 135–150	103.35	7.88	57.69	34	543	—	15.6	77	458	13.3	37.6	2.9	780	111.1	5.5	30.4	1.14	82.2	0.15	—
12H-5, 135–150	107.85	7.90	53.36	33	525	0.6	14.6	77	447	12.1	35.1	2.6	730	66.2	4.6	30.4	1.08	75.6	0.14	—
13H-2, 135–150	112.85	8.00	54.69	34	538	0.9	15.7	91	478	11.5	37.1	3.1	725	58.7	8.9	30.3	1.17	88.4	0.14	—
13H-5, 135–150	117.35	8.06	48.63	30	493	0.5	13.8	108	429	12.2	31.1	2.5	610	58.4	4.5	27.7	1.01	66.0	0.13	—
15H-2, 135–150	123.85	7.79	55.83	34	535	0.4	13.7	174	491	12.2	35.7	3.8	698	58.5	8.7	30.7	1.20	89.1	0.16	—
15H-5, 135–150	128.35	8.04	51.43	33	539	0.5	14.1	72	466	13.4	35.2	3.3	543	7.2	0.6	30.9	1.37	86.4	—	—
17H-2, 30–45	133.70	7.74	53.09	33	533	1.1	13.5	98	487	8.8	30.1	3.6	612	5.0	1.8	30.9	1.63	96.4	0.15	—
19X-2, 135–150	145.85	7.74	51.42	33	528	0.6	13.0	131	493	12.0	36.4	3.8	568	38.1	1.1	29.6	1.85	93.6	0.15	—
19X-5, 85–100	149.85	7.59	54.56	32	527	1.9	12.8	141	477	10.2	35.5	4.6	658	111.1	1.4	27.0	1.96	92.5	—	—
20X-3, 135–150	153.55	7.81	52.38	32	523	0.9	13.2	65	450	10.5	35.2	4.4	561	66.2	1.5	22.3	1.67	92.7	0.13	—
21X-3, 135–150	163.15	8.15	54.90	32	519	1.8	13.1	71	466	10.3	34.6	4.0	459	58.7	1.1	16.6	1.85	92.0	0.14	—
22X-3, 135–150	172.65	7.58	58.26	32	514	1.9	14.3	70	447	9.6	36.4	5.3	629	58.4	1.3	29.2	2.06	100.3	0.15	—
23X-3, 135–150	182.25	7.73	52.59	32	514	0.9	13.7	61	444	10.6	37.3	4.6	557	58.5	1.7	19.0	1.70	95.8	0.13	—
24X-3, 135–150	191.45	7.52	60.58	32	509	3.9	14.0	63	441	9.6	35.9	5.2	635	66.8	2.6	37.7	2.11	107.2	0.14	—
25X-3, 135–150	200.75	7.72	53.99	30	506	1.7	12.4	66	379	9.4	36.5	5.2	567	2.5	2.5	43.7	2.22	99.6	—	—
26X-3, 135–150	210.45	7.60	52.22	32	501	1.9	12.8	65	462	9.7	36.1	4.8	542	4.5	1.5	49.2	1.94	105.8	—	—
27X-3, 130–150	220.10	7.65	49.83	31	499	1.0	10.2	50	—	10.5	35.6	4.8	554	1.9	0.5	49.5	1.70	102.9	0.07	—
28X-3, 130–150	229.70	7.62	48.96	30	495	3.5	9.8	46	459	9.4	32.8	5.5	554	2.6	1.1	51.1	1.78	111.1	0.08	—
29X-3, 130–150	238.56	7.71	45.71	30	490	2.9	7.9	38	452	9.4	30.5	5.5	606	2.0	3.6	63.8	4.08	117.3	0.07	—
30X-3, 130–150	249.00	7.65	35.00	30	486	1.2	6.5	17	445	9.5	31.9	2.6	547	5.1	0.5	59.3	3.14	92.7	0.05	—
31X-3, 130–150	258.60	7.72	35.25	30	481	3.0	6.8	13	450	9.5	29.9	1.6	500	3.5	1.0	57.6	2.63	103.2	0.04	—
32X-3, 130–150	268.24	7.69	35.74	29	481	3.4	4.8	24	444	8.8	27.7	2.7	535	11.0	0.9	62.2	3.85	118.5	0.04	—
33X-3, 130–150	277.84	7.82	30.14	24	479	2.5	5.1	13	438	9.0	27.4	2.8	—	—	—	70.5	—	—	0.04	—
34X-3, 130–150	287.60	7.59	29.14	29		2.3	5.1	11	426	7.4	27.2	2.7	598	4.6	0.3	70.5	5.89	109.1	0.04	—
35X-3, 130–150	297.33	7.66	—	28	470	3.3	5.6	1	431	7.6	25.3	3.1	647	25.9	1.1	97.1	3.85	107.2	0.04	—
36X-3, 130–150	306.90	7.70	24.72	28	469	2.4	5.1	5	428	6.7	23.5	4.2	562	31.2	0.3	89.3	3.08	108.2	—	—
37X-1, 130–150	313.50	7.63	—	25	469	2.1	4.7	1	428	6.4	24.2	3.8	591	32.5	2.3	83.1	3.50	116.1	0.03	—
38X-3, 130–150	326.20	7.61	20.22	27	468	—	3.1	0	430	5.8	22.6	4.7	570	37.0	1.0	77.8	4.94	114.6	0.03	—
39X-1, 130–150	332.80	7.63	19.39	27	467	—	4.3	0	420	5.0	19.5	5.5	733	40.3	3.3	104.3	6.07	111.5	0.04	—
204-1244E-																				
1H-2, 140–150	2.90	7.71	7.19	35	546	27.3	0.7	50	—	—	48.2	9.4	576	11.0	7.0	25.0	2.00	91.0	—	1.91
1H-4, 140–150	5.90	7.4	25.19	34	551	11.8	2.6	158	—	—	45.3	6.4	635	16.0	13.0	15.0	3.00	80.0	—	6.60
2H-1, 140–150	10.10	7.44	41.18	34	551	1.7	4.9	181	—	—	44.4	3.6	743	52.0	6.0	12.0	1.00	80.0	—	7.86
2H-2, 140–150	11.60	7.59	43.05	34	556	1.4	5.5	245	—	—	44.0	4.5	772	55.0	8.0	12.0	3.00	80.0	—	9.51
4H-5, 0–20	26.20	7.18	60.73	35	557	1.7	10.0	336	—	—	45.1	3.2	961	67.0	30.0	18.0	6.00	81.0	—	13.65
5H-2, 135–150	32.50	7.23	65.00	36	556	1.6	12.3	352	—	—	46.9	3.5	1052	73.0	52.0	21.0	5.00	87.0	—	14.42
5H-5, 135–150	37.00	7.10	66.34	36	557	1.4	13.3	381	—	—	46.4	3.4	1058	70.0	39.0	20.0	5.00	87.0	—	14.39
7H-2, 135–150	44.05	7.19	68.22	36	546	1.5	14.3	389	—	—	44.3	3.2	1131	65.0	20.0	21.0	2.00	91.0	—	14.59
7H-5, 135–150	48.55	7.18	68.18	36	548	1.0	18.3	389	—	—	44.0	3.5	1092	65.0	15.0	22.0	2.00	89.0	—	14.97
9H-5, 135–150	59.51	7.22	68.91	35	537	1.5	14.9	399	—	—	43.6	3.2	1163	74.0	27.0	24.0	3.00	90.0	—	16.46
10H-6, 0–20	69.60	7.33	68.34	34	517	1.6	20.5	389	—	—	41.0	3.1	1148	85.0	19.0	25.0	2.00	91.0	—	16.77

Table T4 (continued).

Core, section, interval (cm)	Depth (mbsf)	pH	Alkalinity (mM)	Salinity (g/kg)	Cl (mM)	SO$_4$ (mM)	NH$_4$ (mM)	PO$_4$ (µM)	Na (mM)	K (mM)	Mg (mM)	Ca (mM)	B (µM)	Ba (µM)	Fe (µM)	Li (µM)	Mn (µM)	Sr (µM)	Color*	DOC (mM)
12H-5, 135–150	80.05	7.20	67.90	35	538	1.6	22.7	383	—	—	40.6	3.6	1158	92.0	19.0	28.0	2.00	95.0	—	15.67
13H-5, 135–150	89.75	7.25	66.50	35	545	1.7	20.1	397	—	—	40.7	3.6	1100	91.0	13.0	29.0	2.00	101.0	—	15.11
14H-5, 125–140	99.37	7.11	64.63	34	540	2.0	17.5	354	—	—	41.4	3.9	1069	100.0	25.0	31.0	3.00	103.0	—	14.40
17H-5, 135–150	120.95	7.27	59.22	34	520	1.2	20.4	282	—	—	37.2	4.0	788	86.0	13.0	34.0	2.00	108.0	—	13.46
18H-5, 135–150	129.70	7.31	57.86	33	535	1.5	16.5	228	—	—	34.2	4.1	681	93.0	10.0	34.0	1.00	107.0	—	19.19
19H-5, 135–150	139.55	7.14	55.00	34	529	2.3	16.4	251	—	—	34.0	4.5	713	97.0	12.0	34.0	1.00	107.0	—	13.58
204-1244F-																				
1H-1, 140–150	1.40	7.25	3.29	35	—	29.4	—	14	487	11.9	46.7	11.4	541	10.0	6.0	26.0	2.00	91.0	—	—
1H-2, 140–150	2.90	7.28	6.04	34	—	25.7	—	72	488	12.0	47.9	9.3	579	13.0	6.0	24.0	1.00	91.0	—	—
2H-1, 140–150	5.50	7.71	34.55	34	—	5.2	—	182	491	11.9	45.1	5.1	676	22.0	8.0	14.0	3.00	76.0	—	—
2H-3, 140–150	8.50	7.60	43.71	34	—	1.9	—	319	497	12.1	43.8	3.4	769	50.0	9.0	12.0	1.00	78.0	—	—
3H-2, 140–150	16.50	7.31	52.06	35	—	1.3	—	334	513	12.4	45.6	3.0	883	56.0	23.0	12.0	3.00	79.0	—	—
3H-4, 140–150	19.50	7.21	56.30	35	—	1.5	—	332	503	12.3	44.2	3.0	916	61.0	54.0	14.0	4.00	80.0	—	—

Notes: DOC = dissolved organic carbon. * = relative to the JWBL standard used during Leg 201 (D'Hondt, Jørgensen, Miller, et al., 2003). — = no sample was available.

Table T5. Concentrations of dissolved chloride and sulfate in pore fluids, Hole 1244E.

Core, section, interval (cm)	Depth (mbsf)	Cl (mM)	SO$_4$ (mM)
204-1244E-			
8Y-1, 10–15	50.80	528.00	0.74
8Y-1, 40–45	51.10	558.00	0.57
8Y-1, 65–70	51.35	551.00	0.63

Table T6. Concentrations of methane, ethane, and propane in headspace gas, Hole 1244A, 1244B, 1244C, and 1244E.

Core, section, interval (cm)	Depth (mbsf)	C_1 (ppmv)	C_2 (ppmv)	$C_{2=}$ (ppmv)	C_3 (ppmv)	C_1/C_2
204-1244A-						
1H-2, 0–5	1.50	10				
1H-5, 0–5	6.00	443				
204-1244B-						
1H-2, 0–5	1.50	22				
1H-4, 0–5	4.50	43				
2H-3, 0–5	9.60	15,007	1	0.3		26,328
2H-6, 0–5	14.10	39,787	1	0.5		41,445
3H-3, 0–5	19.10	8,323				
3H-6, 0–5	23.60	7,248				
4H-4, 0–5	28.78	70,697	1			50,498
4H-7, 0–5	33.28	15,459	1	0.5		19,085
5H-4, 0–5	38.61	8,748	0	0.4		18,613
5H-7, 0–5	43.11	13,115	0			32,788
6H-4, 0–5	46.93	19,912	2	3.9		8,297
6H-7, 0–5	51.43	6,569		0.4		
204-1244C-						
1H-2, 0–5	1.50	245				
1H-3, 0–5	3.00	6				
2H-2, 0–5	7.00	1,632	0		0.5	4,080
2H-5, 0–5	11.50	9,362				
3H-2, 0–5	16.50	33,324	1	0.3	0.7	38,749
3H-5, 0–5	21.00	21,100		0.5		
3H-7, 0–5	24.00	17,504	0	0.4		37,243
4H-3, 0–5	27.50	5,029				
4H-6, 0–5	32.00	916				
5H-3, 0–5	37.00	3,379				
5H-6, 0–5	41.50	7,895		0.4		
6H-3, 0–5	46.50	9,600				
6H-6, 0–5	50.86	9,029		0.5		
7H-3, 0–5	54.94	2,622				
7H-6, 0–5	59.12	879				
8H-3, 0–5	64.52	8,286				
8H-6, 0–5	69.02	16,805	1	0.5		33,610
9H-3, 0–5	75.00	21		1.0		
9H-6, 0–5	79.50	161		0.8		
10H-3, 0–5	84.03	1,051				
10H-6, 0–5	88.53	587				
11H-3, 0–5	93.23	507				
11H-6, 0–5	97.73	685				
12H-3, 0–5	103.50	51,241	1			44,948
12H-6, 0–5	108.00	8,298				
13H-3, 0–5	113.00	7,802				
13H-6, 0–5	117.50	8,265	1			7,871
15H-3, 0–5	124.00	16,060				
15H-6, 0–5	128.50	9,778	3			3,372
17H-2, 40–45	133.80	27,858	4			6,795
19X-3, 0–5	146.00	10,028	1	0.7		16,713
19X-6, 0–5	150.00	12,073	9	1.2		1,298
20X-4, 0–5	153.70	21,974	7	0.4		2,946
21X-4, 0–5	163.30	6,971	5			1,291
22X-4, 0–5	172.80	7,056	11			672
23X-4, 0–5	182.40	5,512	7			766
24X-4, 0–5	191.60	2,520	4			586
25X-4, 0–5	200.90	871	2			512
26X-4, 0–5	210.60	42,962	14			3,004
27X-4, 0–5	220.30	436	1			727
28X-4, 0–5	229.90	1,643	3			510
29X-4, 0–5	238.76	13,733	39	0.9	0.6	352
30X-4, 0–5	249.20	10,886	25	0.8		435
31X-4, 0–5	258.80	7,882	24		1.6	328
32X-4, 0–5	268.44	14,244	41	0.6	5.5	347
33X-4, 0–5	278.04	9,012	33	0.7	5.1	273
34X-4, 0–5	287.80	10,727	17			631
35X-4, 0–5	297.53	14,212	38	0.6	4.8	374
36X-4, 0–5	307.10	18,438	52	0.8	7.9	355
37X-2,0,-5	313.70	14,749	43	0.5	5.7	343
38X-4, 0–5	326.40	20,735	47	0.5	5.5	440
39X-2, 0–5	333.00	14,375	36	0.6	5.1	400
204-1244E-						
1H-1, 0–5	0.00	8.9				
1H-2, 0–5	1.50	6.5				
1H-3, 0–5	3.00	23				
1H-5, 0–5	6.00	314				
1H-6, 0–5	7.50	3,369				
2H-1, 0–5	8.70	1,481				
2H-2, 0–5	10.20	18,787	0.47			39,972
2H-3, 0–5	11.70	13,656				
2H-4, 0–5	13.20	56,704	0.75			75,605
2H-5, 0–5	14.70	31,984	0.51			62,714
2H-6, 0–5	16.20	26,002	0.47			55,323

Notes: Blank space indicates that the component was not determined (either not present or is below detection limit). C_1 = methane, C_2 = ethane, $C_{2=}$ = ethylene, C_3 = propane.

Table T7. Concentrations of methane, ethane, and propane in VAC samples of core gas voids, Holes 1244B, 1244C, and 1244E. (**See table notes.** Continued on next page.)

Core, section, interval (cm)	Depth (mbsf)	C_1 (ppmv)	C_2 (ppmv)	C_3 (ppmv)	CO_2 (ppmv)	C_1/C_2
204-1244B-						
3H-1, 105–107	17.15	940,196	6.9	4.8	NA	136,260
4H-2, 72–73	26.50	800,870	5.8	5.3	NA	138,081
4H-8, 33–35	35.11	968,207	6.7	5.5	NA	144,509
5H-7, 101–104	44.12	1,002,297	14.1		NA	71,085
6H-3, 0–2	45.43	932,558	7.5	3.8	NA	124,341
6H-7, 60–62	52.03	1,031,228	13.0		NA	79,325
204-1244C-						
5H-1, 121–123	35.21	943,154	6.6	5.1	NA	142,902
6H-2, 136–137	46.36	951,689	11.9		NA	79,974
7H-2, 122–124	54.66	961,731	12.4		NA	77,559
7H-7, 60–62	61.22	961,550	13.9		NA	69,176
8H-7, 25–26	70.68	830,492	11.9		NA	69,789
9H-2, 85–87	74.35	849,730	10.3		NA	82,498
10H-1, 61–63	82.11	967,538	15.1		NA	64,075
11H-2, 103–108	92.76	953,130	6.8	2.9	NA	140,166
12H-1, 107–110	101.57	975,116	19.3	1.0	NA	50,524
13H-2, 69–71	112.19	960,577	20.2		NA	47,553
15H-2, 35–37	122.85	974,485	63.4	4.3	NA	15,370
19X-3, 10–11	146.10	799,427	145.2	6.6	NA	5,506
20X-3, 27–28	152.47	964,933	148.2	5.7	NA	6,511
21X-3, 88–89	162.68	853,666	195.1	6.9	NA	4,376
22X-3, 90–91	172.20	963,297	240.0	8.5	NA	4,014
26X-2, 80–81	208.40	941,517	308.0	10.9	NA	3,057
27X-5, 50–51	222.30	960,734	344.0	12.6	NA	2,793
29X-3, 37–38	237.63	909,200	353.0	13.0	NA	2,576
30X-1, 96–97	245.66	925,011	428.0	15.8	NA	2,161
30X-5, 67–70	251.37	629,777	280.0	10.6	NA	2,249
31X-3, 150–152	258.80	921,178	375.0	14.0	NA	2,456
32X-1, 75–77	264.75	905,857	510.0	19.5	NA	1,776
33X-2, 1–2	275.05	967,051	492.0	19.3	NA	1,966
34X-4, 1–2	287.81	977,042	443.0	16.8	NA	2,206
35X-3, 1–2	296.04	982,492	432.0	15.4	NA	2,274
36X-7, 5–6	311.09	931,724	473.0	19.7	NA	1,970
38X-2, 14–15	323.54	972,510	553.0	22.2	NA	1,759
204-1244E-						
4H-1, 140	21.60	912,664	4.6		20,122	198,837
4H-2, 10	21.80	927,566	7.1	5.2	19,871	130,827
4H-2, 68	22.38	942,322	7.0	4.6	17,071	133,853
4H-3, 32	23.52	936,681	6.8	4.5	15,157	138,358
4H-7, 47	29.67	942,704	7.3	6.0	29,611	129,492
5H-1, 113	30.83	906,066	6.8	6.2	24,320	132,854
5H-2, 48	31.63	925,053	6.5	4.9	17,062	142,535
5H-3, 45	33.10	925,870	6.4	4.5	13,653	144,217
5H-4, 58	34.73	937,355	6.1	4.9	10,756	153,163
5H-7, 31	38.63	947,970	6.6	5.0	19,960	143,198
7H-1, 99	42.19	927,354	7.3	5.3	27,043	126,343
7H-2, 103	43.73	903,039	7.4	4.9	20,843	121,540
7H-3, 124	45.44	776,341	5.2	4.6	15,958	150,746
7H-4, 146	47.16	937,916	5.9	5.7	27,077	158,432
7H-6, 101	49.71	902,674	15.2	2.9	49,103	59,308
9H-1, 83	53.43	952,447	4.4	5.8	22,667	218,451
9H-2, 42	54.52	949,963	4.0	5.6	17,764	237,491
9H-3, 72	56.32	952,528	7.4	3.4	10,145	129,244
9H-5, 15	58.31	928,038	12.6	2.7	18,140	73,421
9H-7, 1	61.17	890,784	10.8	2.5	9,822	82,633
10H-1, 36	62.46	947,722	7.1	4.8	17,790	133,482
12H-1, 28	73.88	910,611	9.8	3.9	25,393	92,919
12H-2, 119	75.39	946,445	4.5	6.9	20,821	211,260
12H-5, 68	79.38	947,438	4.2	6.7	16,542	226,660
12H-5, 116	79.86	963,726	4.3	9.5	NA	224,122
13H-1, 4	83.14	938,160	9.2	4.7	23,735	102,085
13H-3, 2	85.42	960,896	13.7		9,226	70,241
13H-4, 46	87.36	959,989	5.0	5.3	10,597	191,233

Table T7 (continued).

Core, section, interval (cm)	Depth (mbsf)	C_1 (ppmv)	C_2 (ppmv)	C_3 (ppmv)	CO_2 (ppmv)	C_1/C_2
13H-5, 30	88.70	952,303	16.0	1.8	12,978	59,408
13H-5, 120	89.60	881,539	15.5		19,452	57,058
14H-2, 3	93.65	944,231	11.1	4.2	18,210	84,837
14H-3, 50	95.62	957,725	9.8	4.4	10,084	97,727
14H-4, 139	98.01	968,912	8.0	7.0	NA	121,114
14H-4, 118	97.80	658,509	2.9	4.0	14,471	229,446
17H-1, 61	114.21	935,206	18.8	4.2	22,750	49,692
17H-2, 108	116.18	972,549	25.0	3.3	11,116	38,840
17H-4, 135	119.45	959,370	19.4	4.3	8,504	49,503
17H-5, 127	120.87	942,384	16.7	5.3	47,136	56,600
18H-1, 85	123.95	916,420	20.4	6.2	5,200	44,835
18H-5, 58	128.93	952,313	58.0	4.9	NA	16,411
18H-6, 26	130.11	939,237	145.5	4.7	NA	6,457
19H-1, 30	132.50	903,283	83.7	8.0	NA	10,794
19H-5, 36	138.56	966,829	79.0	4.1	NA	12,241
19H-5, 76	138.96	963,172	81.7	4.9	NA	11,789
19H-6, 52	140.22	388,987	37.1		NA	10,493

Notes: C_1 = methane, C_2 = ethane, C_3 = propane, CO_2 = carbon dioxide. NA = not analyzed.

Table T8. Headspace of methane gas in parts per million by volume converted to microliters per liter and millimoles, Holes 1244A, 1244B, 1244C, and 1244E. (**See table notes.** Continued on next page.)

Core, section, interval (cm)	Depth (mbsf)	C_1 (ppmv)	Sediment			C_1 (μL/L)[†]	C_1 (mM)[‡]
			Gross weight (g)	Net weight (g)	Volume (cm³)*		
204-1244A-							
1H-2, 0–5	1.5	10	25.0	9.3	6.0	23	0.0
1H-5, 0–5	6.0	443	25.7	10.0	6.2	995	0.1
204-1244B-							
1H-2, 0–5	1.5	22	23.9	8.2	5.3	62	0.0
1H-4, 0–5	4.5	43	24.8	9.1	5.7	108	0.0
2H-3, 0–5	9.6	15,007	26.1	10.4	6.4	32,137	2.4
2H-6, 0–5	14.1	39,787	24.7	9.0	5.5	106,014	8.0
3H-3, 0–5	19.1	8,323	24.3	8.6	5.2	23,832	1.8
3H-6, 0–5	23.6	7,248	22.9	7.2	4.3	26,371	2.0
4H-4, 0–5	28.8	70,697	24.8	9.1	5.4	189,995	14.5
4H-7, 0–5	33.3	15,459	26.0	10.3	6.1	35,080	2.7
5H-4, 0–5	38.6	8,748	25.0	9.3	5.5	23,039	1.8
5H-7, 0–5	43.1	13,115	25.3	9.6	5.7	33,172	2.6
6H-4, 0–5	46.9	19,912	25.9	10.2	6.0	46,690	3.6
6H-7, 0–5	51.4	6,569	22.2	6.5	3.8	27,816	2.2
204-1244C-							
1H-2, 0–5	1.5	245	24.2	8.5	5.5	654	0.0
1H-3, 0–5	3.0	6	26.0	10.3	6.5	12	0.0
2H-2, 0–5	7.0	1,632	28.8	13.1	8.1	2,422	0.2
2H-5, 0–5	11.5	9,362	25.1	9.4	5.7	23,322	1.8
3H-2, 0–5	16.5	33,324	24.9	9.2	5.6	86,597	6.5
3H-5, 0–5	21.0	21,100	22.5	6.8	4.1	82,234	6.2
3H-7, 0–5	24.0	17,504	26.2	10.5	6.3	38,191	2.9
4H-3, 0–5	27.5	5,029	25.8	10.1	6.0	11,744	0.9
4H-6, 0–5	32.0	916	23.6	7.9	4.7	2,985	0.2
5H-3, 0–5	37.0	3,379	21.8	6.1	3.6	15,321	1.2
5H-6, 0–5	41.5	7,895	24.4	8.7	5.1	22,824	1.8
6H-3, 0–5	46.5	9,600	26.5	10.8	6.4	20,571	1.6
6H-6, 0–5	50.9	9,029	25.7	10.0	5.9	21,683	1.7
7H-3, 0–5	54.9	2,622	24.6	8.9	5.2	7,417	0.6
7H-6, 0–5	59.1	879	25.9	10.2	6.0	2,063	0.2
8H-3, 0–5	64.5	8,286	26.0	10.3	6.0	19,232	1.5
8H-6, 0–5	69.0	16,805	26.4	10.7	6.2	37,004	2.9
9H-3, 0–5	75.0	21	24.1	8.4	4.9	65	0.0
9H-6, 0–5	79.5	161	25.3	9.6	5.6	415	0.0
10H-3, 0–5	84.0	1,051	26.7	11.0	6.4	2,238	0.2
10H-6, 0–5	88.5	587	26.4	10.7	6.2	1,304	0.1
11H-3, 0–5	93.2	507	24.9	9.2	5.3	1,394	0.1
11H-6, 0–5	97.7	685	25.3	9.6	5.6	1,780	0.1
12H-3, 0–5	103.5	51,241	23.4	7.7	4.5	178,928	14.5
12H-6, 0–5	108.0	8,298	25.1	9.4	5.4	22,265	1.8
13H-3, 0–5	113.0	7,802	22.9	7.2	4.2	29,754	2.4
13H-6, 0–5	117.5	8,265	27.4	11.7	6.7	16,240	1.3
15H-3, 0–5	124.0	16,060	25.9	10.2	5.9	38,628	3.2
15H-6, 0–5	128.5	9,778	24.8	9.1	5.2	27,574	2.3
17H-2, 40–45	133.8	27,858	26.2	10.5	6.0	64,457	5.4
19X-3, 0–5	146.0	10,028	27.0	11.3	6.5	20,912	1.8
19X-6, 0–5	150.0	12,073	24.5	8.8	5.0	35,789	3.0
20X-4, 0–5	153.7	21,974	26.1	10.4	6.0	51,779	4.4
21X-4, 0–5	163.3	6,971	29.1	13.4	7.7	11,213	1.0
22X-4, 0–5	172.8	7,056	24.2	8.5	4.9	21,999	1.9
23X-4, 0–5	182.4	5,512	24.3	8.6	4.9	16,949	1.5
24X-4, 0–5	191.6	2,520	25.7	10.0	5.7	6,321	0.6
25X-4, 0–5	200.9	871	25.2	9.5	5.4	2,349	0.2
26X-4, 0–5	210.6	42,962	23.4	7.7	4.4	153,213	13.8
27X-4, 0–5	220.3	436	25.2	9.5	5.4	1,179	0.1
28X-4, 0–5	229.9	1,643	28.8	13.1	7.4	2,776	0.3
29X-4, 0–5	238.8	13,733	27.8	12.1	6.9	26,287	2.5
30X-4, 0–5	249.2	10,886	28.3	12.6	7.1	19,608	1.9
31X-4, 0–5	258.8	7,882	26.9	11.2	6.3	16,979	1.6
32X-4, 0–5	268.4	14,244	26.4	10.7	6.1	32,822	3.2
33X-4, 0–5	278.0	9,012	26.1	10.4	5.9	21,650	2.1

Table T8 (continued).

Core, section, interval (cm)	Depth (mbsf)	C_1 (ppmv)	Sediment			C_1 (μL/L)[†]	C_1 (mM)[‡]
			Gross weight (g)	Net weight (g)	Volume (cm^3)*		
34X-4, 0–5	287.8	10,727	21.4	5.7	3.2	55,915	5.4
35X-4, 0–5	297.5	14,212	25.5	9.8	5.5	37,181	3.7
36X-4, 0–5	307.1	18,438	26.9	11.2	6.3	39,945	4.0
37X-2, 0–5	313.7	14,749	25.1	9.4	5.3	40,923	4.1
38X-4, 0–5	326.4	20,735	25.4	9.7	5.5	55,179	5.6
39X-2, 0–5	333.0	14,375	24.0	8.3	4.7	47,159	4.8
204-1244E-							
1H-1, 0–5	0.0	8.9	25.1	9.5	6.68	0.02	0.0
1H-2, 0–5	1.5	6.5	26.2	10.6	6.80	0.01	0.0
1H-3, 0–5	3.0	23	27.8	12.2	7.69	0.04	0.0
1H-5, 0–5	6.0	314	27.0	11.4	7.06	0.64	0.0
1H-6, 0–5	7.5	3,369	26.3	10.7	6.59	7.62	0.5
2H-1, 0–5	8.7	1,481	28.6	13.0	7.98	2.51	0.2
2H-2, 0–5	10.2	18,787	26.8	11.2	6.85	40.21	2.8
2H-3, 0–5	11.7	13,656	25.9	10.3	6.27	33.14	2.3
2H-4, 0–5	13.2	56,704	27.0	11.4	6.92	119.36	8.4
2H-5, 0–5	14.7	31,984	26.4	10.8	6.54	73.12	5.2
2H-6, 0–5	16.2	26,002	26.4	10.8	6.53	59.65	4.2

Notes: * = sample weight per density, where density = $[0.0403\ln(\text{depth}) + 1.5424]$. † = ppmv $CH_4 \times [(21 - \text{sample volume})/\text{sample volume})]$. ‡ = μL/L $CH_4/(f \times 1000 \times 22.4)$, where $f = -0.00053 \times \text{depth} + 0.64$.

Table T9. Gas from decomposition of gas hydrate measured by gas chromatography or NGA analysis, Holes 1244C and 1244E.

Core, section, interval (cm)	Depth (mbsf)	$C_1 + C_2$ (ppmv)	C_1 (ppmv)	C_2 (ppmv)	C_3 (ppmv)	$i\text{-}C_4$ (ppmv)	$n\text{-}C_4$ (ppmv)	$n\text{-}C_5$ (ppmv)	$i\text{-}C_6$ (ppmv)	O_2 (ppmv)	N_2 (ppmv)	CO_2 (ppmv)	C_1/C_2
204-1244C-													
8H-1, 47–52	62.97		400,346	15.6									25,647
10H-2, 70–103	83.70		21,695	0.5									40,934
10H-2, 70–103	83.70		23,776	0.6									42,456
204-1244C-													
8H-1, 47–52	62.97	406,062	395,995	17.2		0.2		3.4	0.5	100,306	445,680	5,014	22,970
10H-2, 70–103	83.70	11,880						1.5		180,467	767,841	927	
10H-2, 70–103	83.70	23,693			0.4	0.2	0.35	5.5	0.67	178,295	763,056	833	
204-1244E-													
7H-6, 124–141	49.94		343,207	6.6									51,922
12H-1, 50–60	74.10		839,671	16.6									50,583
12H-1, 50–60	74.10		940,699	18.6									50,467
12H-1, 50–60	74.10		908,292	16.1						10,568	35,327	5,571	56,311

Notes: C_1 = methane, C_2 = ethane, C_3 = propane, $i\text{-}C_4$ = isobutane, $n\text{-}C_4$ = normal butane, $n\text{-}C_5$ = normal pentane, $n\text{-}C_6$ = normal hexane, O_2 = oxygen, N_2 = nitrogen, CO_2 = carbon dioxide. Replicate analyses are shown; analyses containing values for O_2 or N_2 indicate NGA results.

Table T10. Composition of gas samples from PCS experiments, Hole 1244C.

Sample	Volume (mL)	C_1 (ppm)	C_2 (ppm)	C_3 (ppm)	$i\text{-}C_4$ (ppm)	$n\text{-}C_4$ (ppm)	$i\text{-}C_5$ (ppm)	$n\text{-}C_5$ (ppm)	$i\text{-}C_6$ (ppm)	$n\text{-}C_6$ (ppm)	O_2 (ppm)	N_2 (ppm)	CO_2 (ppm)
204-1244C-14P (119.5 mbsf)													
G1	170	436,079		1.6	0.8	0.4	0.3	6.1	0.6		85,989	439,689	669
G2	550	689,226		2.8	1.3	0.4	0.3				47,949	247,888	2,149
G3	580	667,865		3.3	2.2	1.4	0.7	18.2	1.9		55,396	257,047	4,666
G4	250	670,843		3.6	2.6	1.7	0.8	20.0	2.0	0.2	54,751	254,490	4,696
G5	125	705,012		3.6	2.3	1.4	0.8	21.7	2.1	0.2	49,213	227,366	4,506
G6	120	638,788		3.2	1.9	0.6	0.6	7.2	0.8		64,289	277,859	1,781
204-1244C-16P (130.5 mbsf)													
G1	15	5,634		0.8	3.7	2.3	0.4	19.2	2.1		183,744	765,307	87
G2	475	843,372		3.0	1.1	0.4	0.3	4.8	0.5		24,411	99,419	3,615
G3	435	560,012		2.2	3.0	0.3	0.2	1.3			75,549	341,868	1,921
G4	245	636,039		3.1	4.2	0.9	0.4	7.5	0.8		61,899	282,637	3,410
G5	170	679,387		3.4	1.5	0.6	0.4	0.9			55,204	247,197	3,881
G6	145	580,360	84.1	176	1.6	0.5	0.4	3.9	0.4		37,069	164,478	2,325
G7	130	640,898		4.3	1.6	0.5	2.9	1.1			50,109	221,322	2,295
G8	70	635,219		4.3	1.9	0.7	0.7	2.4	0.3		53,633	232,047	2,887
204-1244C-18P (141.5 mbsf)													
G1	125	772,473	80.6	2.3	1.0	0.7	0.1	5.7			35,347	167,384	495
G2	610	920,021	96.0	2.3	0.8	0.3	0.3	2.2			1,519	27,305	498
G3	345	882,178	92.1	3.1	1.5	1.2	0.5	13.8	1.5		8,695	78,080	556
G4	285	851,463	82.5	2.9	1.2	0.5	0.4	7.2	0.8		15,250	104,741	524
G5	250	881,000	85.4	3.3	1.4	0.4	0.3	5.9	0.7		9,606	66,977	1,030
G6	145	884,948	85.8	3.3	1.3	0.3	0.5	1.4	0.2		8,621	63,660	1,213
G7	145	843,935	87.2	3.4	1.6	0.4	0.5	3.1	0.5		15,308	105,297	576
G8	85	852,936	88.1	3.4	1.4	0.3	0.5	2.7	0.5		13,695	95,317	340
G9	70	701,437	79.9	3.7	1.4	0.4	0.6	2.1	0.2		36,677	246,037	563
G10	30	692,092	85.3	4.5	1.5	0.5	0.7	2.8	0.4		36,665	256,700	508
G11	20	663,382	84.5	4.5	1.8	0.8	0.7	5.7	0.6		43,299	276,725	480
204-1244E-6P (39.2 mbsf)													
G1	350	870,286	5.7								15,114	78,400	1,209
G2	140	937,758	10.0	4.9							7,561	38,339	629
G3	175	930,691	11.8	3.4							4,961	34,666	577
G4	90	953,158	9.2	5.6							1,224	21,812	695
G5	190	941,925	7.6	5.7							2,711	28,599	1,059
204-1244E-11P (71.6 mbsf)													
G1	210	810,427	14.0								28,500	140,287	303
G2	460	970,372	32.0								1,236	3,175	
G3	470	972,979	17.0								312	1,227	
G4	410	971,345	14.5								192	1,354	
G5	370	971,345	14.5								230	2,110	
G6	450	965,414	10.0	2.6								1,592	323
G7	410	966,128	9.2	3.3							117	3,471	656
G8	370	959,598	8.6	3.6								5,637	1,201
G9	390	957,788	9.4	3.7								8,191	1,137
G10	360	960,875	10.6	3.9							450	12,480	828
G11	180	957,634	10.6	4.1							562	11,397	2,111
G12	120	960,231	11.2	4.3							930	10,894	1,868
G13	70	959,952	11.2	4.1							869	12,212	1,502
G14	260	955,157	14.5	5.0							2,137	13,307	2,025
204-1244E-15P (102.1 mbsf)													
G1	90	268,925	5.5	1.2							72,741	633,256	224
G2	330	742,137	11.5								13,743	231,071	225
G3	410	690,349	9.3	2.1							13,443	287,268	
G4	380	668,665	7.0	6.1							9,894	305,853	193
G5	560	697,888	7.3								8,684	287,700	463
G6	460	747,744	7.5	3.2							6,597	239,263	399
G7	580	823,931	8.4	4.8							5,070	155,159	1,340
G8	290	802,125	9.6	4.9							6,159	180,496	1,032
G9	120	776,182	9.9	5.0							8,744	203,411	670
G10	90	773,196	10.4	5.2							5,905	207,875	428
204-1244F-4P (23.1 mbsf)													
4P-G1	595	875,610	7.5	6.0							13,151	72,967	5,255

Notes: All samples were analyzed by the natural gas analyzer. Samples from Core 204-1244C-18P were also analyzed by gas chromatography (GC). C_1 and C_2 concentrations are given as a sum for Cores 204-1244C-14P and 16P, and corrected concentrations based on GC analyses are given for Core 18P. C_1 = methane, C_2 = ethane, C_3 = propane, $i\text{-}C_4$ = isobutane, $n\text{-}C_4$ = normal butane, $i\text{-}C_5$ = isopentane, $n\text{-}C_5$ = normal pentane, $i\text{-}C_6$ = isohexane, $n\text{-}C_6$ = normal hexane, O_2 = oxygen, N_2 = nitrogen, CO_2 = carbon dioxide. Blank cells = below detection limit.

Table T11. Carbonate carbon, calcium carbonate, total carbon, organic carbon, total nitrogen, and total sulfur contents and C/N ratios, Hole 1244C.

Core, section, interval (cm)	Depth (mbsf)	Carbonate carbon (wt%)	CaCO$_3$ (wt%)	Total carbon (wt%)	Organic carbon (wt%)	Total nitrogen (wt%)	Total sulfur (wt%)	C/N
204-1244C-								
1H-3, 29–30	3.29	0.51	4.25	1.83	1.32	0.14	1.08	9.39
2H-4, 35–36	10.35	0.52	4.33	1.58	1.06	0.13	0.60	8.15
3H-3, 76–77	18.76	0.19	1.58	1.28	1.09	0.16	0.60	6.81
4H-3, 76–77	28.26	0.11	0.92	1.94	1.83	0.21	0.60	8.71
5H-3, 73–74	37.73	0.62	5.16	1.63	1.01	0.18	0.45	5.61
6H-3, 52–53	47.02	0.44	3.67	1.57	1.13	0.17	0.32	6.65
7H-3, 76–77	55.70	0.47	3.92	2.16	1.69	0.22	0.44	7.68
8H-3, 76–77	65.28	0.24	2.00	1.65	1.41	0.20	0.29	7.05
9H-3, 76–77	75.76	0.36	3.00	1.88	1.52	0.22	0.49	6.91
10H-3, 40–41	84.43	0.49	4.08	1.77	1.28	0.18	0.26	7.11
11H-3, 68–69	93.91	0.63	5.25	1.97	1.34	0.19	0.26	7.05
12H-3, 75–76	104.25	0.75	6.25	2.03	1.28	0.18	0.59	7.11
13H-3, 74–75	113.74	0.70	5.83	1.84	1.14	0.17	0.21	6.71
15H-3, 62–63	124.62	0.60	5.00	1.50	0.90	0.17	0.15	5.29
19H-3, 76–77	146.76	0.31	2.58	1.40	1.09	0.18	0.19	6.06
20H-3, 73–74	152.93	0.28	2.33	ND	ND	ND	ND	ND
21X-3, 112–113	162.92	0.24	2.00	1.26	1.02	0.14	0.16	7.29
22X-3, 64–65	171.94	0.45	3.75	1.32	0.87	0.14	0.09	6.21
23X-3, 73–74	181.63	0.39	3.25	1.32	0.93	0.15	0.16	6.20
24X-3, 59–60	190.69	0.61	5.08	2.20	1.59	0.18	0.16	8.83
25X-3, 27–28	199.67	0.40	3.33	1.96	1.56	0.20	0.33	7.80
26X-3, 73–74	209.83	0.36	3.00	1.75	1.39	0.18	0.19	7.72
27X-3, 77–78	219.57	0.51	4.25	1.57	1.06	0.16	0.14	6.63
28X-3, 73–74	229.13	0.64	5.33	1.71	1.07	0.15	0.24	7.13
29X-3, 73–74	237.99	0.64	5.33	2.26	1.62	0.18	1.17	9.00
30X-3, 31–32	248.01	0.51	4.25	1.93	1.42	0.17	1.84	8.35
31X-3, 98–99	258.28	0.13	1.08	1.40	1.27	0.17	0.89	7.47
32X-3, 75–76	267.69	0.04	0.33	1.40	1.36	0.17	1.25	8.00
33X-3, 70–71	277.24	0.08	0.67	1.36	1.28	0.16	0.78	8.00
34X-3, 53–54	286.83	0.12	1.00	1.65	1.53	0.18	1.64	8.50
35X-3, 55–56	296.58	0.05	0.42	1.26	1.21	0.16	0.85	7.56
36X-3, 21–22	305.81	0.20	1.67	1.95	1.75	0.21	0.91	8.33
37X-1, 53–54	312.73	0.21	1.75	1.44	1.23	0.17	nd	7.24
38X-3, 60–61	325.50	0.28	2.33	1.45	1.17	0.14	nd	8.36

Note: ND = not detected.

Table T12. Rock-Eval pyrolysis of samples, Hole 1244C.

Core, section, interval (cm)	Depth (mbsf)	Organic carbon (wt%)	S_1 (mg/g)	S_2 (mg/g)	Production index (S_1/[S_1+S_2])	Hydrogen index (mg S_2/g C)	T_{max} (°C)
204-1244C-							
1H-3, 29–30	3.29	1.32	0.30	1.47	0.17	111	405
4H-3, 76–77	28.26	1.83	0.48	2.95	0.14	161	407
7H-3, 76–77	55.70	1.69	0.47	2.60	0.15	154	411
9H-3, 76–77	75.76	1.52	0.39	2.08	0.16	137	413
11H-3, 68–69	93.91	1.34	0.38	1.70	0.18	127	412
13H-3, 74–75	113.74	1.14	0.28	1.25	0.18	110	408
19X-3, 76–77	146.76	1.09	0.26	1.43	0.15	131	NA
24X-3, 59–60	190.69	1.59	0.27	1.80	0.13	113	408
26X-3, 73–74	209.83	1.39	0.29	1.77	0.14	127	410
29X-3, 73–74	237.99	1.62	0.33	2.23	0.13	138	410
33X-3, 70–71	277.24	1.36	0.26	1.91	0.12	140	404
34X-3, 53–54	286.83	1.53	0.59	3.05	0.16	199	403
36X-3, 21–22	305.81	1.75	0.24	1.76	0.12	101	404

Notes: NA = not analyzed. S_1 and S_2 are as defined in **"Organic Matter Characterization,"** p. 18, in "Organic Geochemistry" in the "Explanatory Notes" chapter.

Table T13. Intervals sampled for microbiology, Holes 1244C, 1244E, and 1244F.

Core, section, interval (cm)	Depth (mbsf)
204-1244C-	
1H-1, 45–65	0.45
1H-1, 122–140	1.22
1H-2, 45–65	1.95
1H-2, 75–140	2.25
1H-3, 45–65	3.45
1H-3, 75–140	3.75
1H-4, 32–60	4.82
2H-1, 45–65	5.95
2H-1, 119–140	6.69
2H-2, 45–65	7.45
2H-2, 120–140	8.20
2H-3, 45–65	8.95
2H-3, 119–140	9.69
2H-4, 45–65	10.45
2H-4, 120–140	11.20
2H-5, 45–65	11.95
2H-5, 90–140	12.40
2H-6, 45–65	13.45
2H-6, 121–140	14.21
2H-7, 46–64	14.96
3H-1, 119–140	16.19
3H-2, 120–140	17.70
3H-3, 120–140	19.20
3H-4, 119–140	20.69
3H-5, 120–140	22.20
3H-6, 88–140	23.38
204-1244E-	
4H-5, 20–150	26.40
5H-2, 0–135	31.15
5H-5, 0–135	35.65
7H-2, 0–135	42.70
7H-5, 46–135	47.66
9H-5, 71–135	58.87
10H-5, 45–150	68.55
12H-5, 104–135	79.74
13H-5, 79–135	89.19
14H-5, 69–125	98.81
17H-5, 94–135	120.54
18H-5, 85–135	129.20
19H-5, 69–135	138.89
204-1244F-	
1H-1, 0–140	0.00
1H-2, 0–140	1.50
1H-3, 0–74	3.00
2H-1, 0–140	4.10
2H-2, 0–140	5.60
2H-3, 0–140	7.10
2H-4, 0–140	8.60
2H-5, 0–140	10.10
2H-6, 0–140	11.60
2H-7, 0–37	13.10
3H-1, 0–140	13.60
3H-2, 0–140	15.10
3H-3, 0–140	16.60
3H-4, 0–140	18.10
3H-5, 0–140	19.60
3H-6, 0–140	21.10
3H-7, 0–64	22.60

Table T14. Core quality indicators in intervals sampled for microbiology, Holes 1244C, 1244E, and 1244F.

Core, section, interval (cm)	Depth (mbsf)	PFT per sample (ag)		Microspheres per gram	
		Inside core	Outer edge	Inside core	Outer edge
204-1244C-					
2H-2, 115–120	8.15	0.00012	0.00012	NS	NS
2H-7, 39–44	14.89	0.0012	0.0012	NS	NS
204-1244E-					
4H-5, 135–145	27.55	0.0081	0.00072	BDL	6,320
5H-2, 120–130	32.35	BDL	0.0293	922	20,000
5H-5, 120–130	36.85	0.000029	0.039	BDL	9,720
7H-2, 115–125	43.85	BDL	NS	BDL	80,000
7H-5, 115–125	48.35	0.00032	0.011	4860	45,500
9H-5, 130–140	59.46	0.000044	0.0075	BDL	2,630
10H-5, 130–140	69.40	0.0014	24.28	BDL	22,000
12H-5, 130–140	80.00	0.0013	NS	BDL	26,200
13H-5, 130–140	89.70	0.0017	0.59	BDL	42,900
14H-5, 130–140	99.42	0.00058	55	1440	823
17H-5, 120–140	120.80	0.00072	6.6	BDL	3,690
18H-5, 120–135	129.55	0.096	630	BDL	22,200
19H-5, 130–135	139.50	0.11	460	BDL	2,760
204-1244F-					
1H-1, 125–135	1.25	NS	NS	BDL	9,260
1H-2, 125–135	2.75	BDL	88	NS	23,100
2H-1, 125–135	5.35	NS	NS	BDL	192,000
2H-2, 135–145	6.95	BDL	0.09	BDL	1,080,000
2H-3, 125–130	8.35	NS	NS	BDL	75,800
2H-4, 135–145	9.95	BDL	5.1	BDL	518,000
2H-5, 135–145	11.45	NS	NS	BDL	1,060
2H-6, 135–145	12.95	NS	NS	BDL	8,050
3H-1, 135–145	14.95	NS	NS	BDL	37,100
3H-2, 125–135	16.35	BDL	0.16	BDL	11,600
3H-3, 135–145	17.95	NS	NS	BDL	65,000
3H-4, 125–135	19.35	NS	NS	BDL	5,190
3H-5, 135–145	20.95	NS	NS	BDL	2,290
3H-6, 135–145	22.45	NS	NS	4310	6,580

Notes: PFT = perfluorocarbon tracer. ag = attograms. NS = not sampled, BDL = below detection limit.

Table T15. Moisture and density, Holes 1244A, 1244B, 1244C, and 1244E. (Continued on next two pages.)

Core, section, interval (cm)	Depth (mbsf)	Density (g/cm³) Bulk	Grain	Porosity (%)
204-1244A-				
1H-1, 74–76	0.74	1.562	2.658	67.1
1H-2, 74–76	2.24	1.575	2.629	65.7
1H-3, 74–76	3.74	1.619	2.710	64.7
1H-4, 72–74	5.22	1.624	2.654	63.2
1H-5, 74–76	6.74	1.627	2.714	64.3
1H-6, 74–76	8.24	1.639	2.658	62.4
1H-7, 32–34	9.32	1.671	2.710	61.6
204-1244B-				
1H-1, 60–62	0.60	1.672	2.715	61.7
1H-1, 74–76	0.74	1.613	2.686	64.6
1H-2, 74–76	2.24	1.561	2.649	66.9
1H-3, 74–76	3.74	1.605	2.637	64.0
1H-4, 74–76	5.24	1.631	2.645	62.6
1H-5, 20–22	6.20	1.645	2.647	61.8
2H-1, 74–76	7.34	1.665	2.723	62.3
2H-2, 74–76	8.84	1.651	2.652	61.5
2H-3, 74–76	10.34	1.658	2.709	62.4
2H-4, 74–76	11.84	1.653	2.709	62.7
2H-5, 74–76	13.34	1.663	2.720	62.3
2H-6, 74–76	14.84	1.652	2.637	61.1
2H-7, 49–51	16.09	1.631	2.672	63.2
3H-1, 74–76	16.84	1.602	2.622	63.8
3H-2, 74–76	18.34	1.640	2.700	63.2
3H-3, 74–76	19.84	1.585	2.635	65.2
3H-4, 74–76	21.34	1.641	2.679	62.7
3H-5, 74–76	22.84	1.667	2.675	61.1
3H-6, 74–76	24.34	1.740	2.656	56.1
3H-7, 40–42	25.50	1.664	2.677	61.3
4H-1, 10–12	25.70	1.596	2.674	65.3
4H-2, 74–76	26.52	1.623	2.660	63.4
4H-3, 74–76	28.02	1.614	2.593	62.4
4H-4, 74–76	29.52	1.620	2.656	63.5
4H-5, 74–76	31.02	1.623	2.681	63.9
4H-6, 74–76	32.52	1.585	2.685	66.2
4H-7, 106–108	34.34	1.621	2.666	63.6
4H-8, 60–62	35.38	1.665	2.682	61.3
5H-1, 30–32	35.40	1.694	2.732	60.8
5H-2, 120–122	36.81	1.680	2.721	61.4
5H-3, 70–72	37.81	1.709	2.732	59.9
5H-4, 74–76	39.35	1.708	2.732	60.0
5H-5, 74–76	40.85	1.744	2.727	57.7
5H-6, 74–76	42.35	1.681	2.713	61.1
5H-7, 64–66	43.75	1.677	2.722	61.5
5H-8, 40–42	44.54	1.719	2.713	58.8
6H-1, 11–13	44.71	1.706	2.685	59.0
6H-2, 27–29	45.12	1.651	2.702	62.6
6H-3, 74–76	46.17	1.698	2.676	59.2
6H-4, 74–76	47.67	1.657	2.687	62.0
6H-5, 108–110	49.51	1.606	2.703	65.3
6H-6, 74–76	50.67	1.690	2.726	60.9
6H-7, 74–76	52.17	1.719	2.707	58.7
6H-8, 74–76	53.55	1.528	2.655	69.1
204-1244C-				
1H-1, 78–80	0.78	1.519	2.715	70.8
1H-1, 114–116	1.14	1.742	2.807	59.7
1H-2, 28–30	1.78	1.562	2.748	68.8
1H-3, 28–30	3.28	1.583	2.685	66.3
1H-4, 28–30	4.78	1.640	2.710	63.5
2H-1, 34–36	5.84	1.625	2.701	64.2
2H-2, 34–36	7.34	1.646	2.715	63.2
2H-3, 34–36	8.84	1.631	2.708	64.0
2H-4, 34–36	10.34	1.666	2.724	62.2
2H-5, 34–36	11.84	1.679	2.724	61.5
2H-6, 34–36	13.34	1.658	2.703	62.3
2H-7, 34–36	14.84	1.646	2.723	63.4
3H-1, 74–76	15.74	1.618	2.698	64.5
3H-2, 74–76	17.24	1.625	2.707	64.3

Core, section, interval (cm)	Depth (mbsf)	Density (g/cm³) Bulk	Grain	Porosity (%)
3H-3, 74–76	18.74	1.648	2.699	62.8
3H-4, 74–76	20.24	1.661	2.700	62.0
3H-5, 74–76	21.74	1.636	2.678	63.0
3H-6, 60–62	23.10	1.633	2.698	63.6
3H-7, 60–62	24.60	1.666	2.677	61.2
4H-1, 74–76	25.24	1.726	2.720	58.6
4H-2, 80–82	26.80	1.628	2.688	63.7
4H-3, 74–76	28.24	1.619	2.626	62.9
4H-4, 90–92	29.90	1.624	2.672	63.6
4H-5, 74–76	31.24	1.689	2.677	59.7
4H-6, 74–76	32.74	1.616	2.670	64.0
4H-7, 74–76	34.24	1.647	2.673	62.2
5H-1, 60–62	34.60	1.708	2.735	60.0
5H-2, 40–42	35.90	1.766	2.738	56.7
5H-3, 74–76	37.74	1.709	2.735	60.0
5H-4, 74–76	39.24	1.678	2.710	61.2
5H-5, 74–76	40.74	1.665	2.706	61.9
5H-6, 74–76	42.24	1.740	2.712	57.6
6H-1, 70–72	44.20	1.638	2.660	62.5
6H-2, 50–52	45.50	1.677	2.713	61.3
6H-3, 50–52	47.00	1.674	2.705	61.3
6H-4, 74–76	48.74	1.677	2.693	60.9
6H-5, 74–76	50.10	1.688	2.710	60.6
6H-6, 74–76	51.60	1.696	2.662	59.0
6H-7, 40–42	52.76	1.675	2.700	61.2
7H-2, 90–92	54.34	1.604	2.669	64.8
7H-3, 74–76	55.68	1.593	2.671	65.4
7H-4, 100–102	57.44	1.612	2.665	64.1
7H-5, 80–82	58.42	1.630	2.668	63.2
7H-6, 74–76	59.86	1.678	2.714	61.3
7H-7, 74–76	61.36	1.665	2.686	61.4
8H-1, 20–22	62.70	1.677	2.697	60.9
8H-2, 60–62	63.62	1.685	2.690	60.3
8H-3, 74–76	65.26	1.723	2.697	58.2
8H-4, 74–76	66.76	1.684	2.689	60.4
8H-5, 44–46	67.96	1.683	2.690	60.4
8H-5, 90–92	68.42	1.680	2.691	60.7
8H-6, 74–76	69.76	1.647	2.675	62.3
8H-7, 6–8	70.49	1.664	2.674	61.2
9H-1, 74–76	72.74	1.661	2.649	60.8
9H-2, 86–88	74.36	1.673	2.693	61.1
9H-3, 74–76	75.74	1.694	2.737	60.9
9H-4, 90–92	77.40	1.790	2.694	54.1
9H-5, 74–76	78.74	1.699	2.703	59.8
9H-6, 74–76	80.24	1.695	2.707	60.2
9H-7, 20–22	81.20	1.686	2.675	59.9
10H-1, 88–90	82.38	1.760	2.698	56.0
10H-3, 40–42	84.43	1.754	2.722	57.0
10H-4, 74–76	86.27	1.743	2.703	57.2
10H-5, 74–76	87.77	1.716	2.699	58.7
10H-6, 50–52	89.03	1.566	2.630	66.2
10H-6, 131–133	89.84	1.622	2.647	63.2
10H-7, 54–56	90.48	1.829	2.717	52.5
11H-1, 48–50	91.48	1.698	2.699	59.7
11H-2, 64–66	92.37	1.715	2.694	58.6
11H-3, 68–70	93.91	1.715	2.676	58.2
11H-4, 74–76	95.47	1.692	2.651	58.9
11H-5, 78–80	97.01	1.771	2.674	54.7
11H-6, 74–76	98.47	1.683	2.635	59.1
11H-7, 74–76	99.89	1.685	2.677	60.0
12H-1, 58–60	101.08	1.737	2.678	56.9
12H-2, 74–76	102.74	1.682	2.654	59.6
12H-3, 74–76	104.24	1.676	2.649	59.9
12H-4, 68–70	105.68	1.623	2.600	62.0
12H-5, 74–76	107.24	1.713	2.690	58.7
12H-6, 74–76	108.74	1.713	2.668	58.1
12H-7, 74–76	110.24	1.710	2.682	58.6
13H-1, 62–64	110.62	1.697	2.696	59.8
13H-2, 74–76	112.24	1.718	2.683	58.2

Table T15 (continued).

Core, section, interval (cm)	Depth (mbsf)	Density (g/cm³) Bulk	Grain	Porosity (%)
13H-3, 74–76	113.74	1.728	2.695	57.8
13H-4, 74–76	115.24	1.692	2.658	59.1
13H-5, 74–76	116.74	1.738	2.699	57.4
13H-6, 74–76	118.24	1.755	2.715	56.8
13H-7, 60–62	119.60	1.761	2.703	56.1
15H-1, 120–122	122.20	1.740	2.699	57.3
15H-2, 80–82	123.30	1.732	2.717	58.2
15H-3, 60–62	124.60	1.742	2.693	57.0
15H-4, 74–76	126.24	1.740	2.701	57.3
15H-5, 74–76	127.74	1.736	2.719	58.0
15H-6, 74–76	129.24	1.740	2.666	56.4
19X-1, 74–76	143.74	1.690	2.699	60.3
19X-2, 74–76	145.24	1.734	2.691	57.4
19X-3, 74–76	146.74	1.755	2.709	56.6
19X-4, 74–76	148.24	1.756	2.714	56.7
19X-5, 74–76	149.74	1.788	2.716	54.9
19X-6, 40–42	150.40	1.797	2.770	55.7
20X-1, 74–76	149.94	1.733	2.681	57.2
20X-2, 74–76	151.44	1.731	2.701	57.9
20X-3, 74–76	152.94	1.771	2.730	56.2
20X-4, 50–52	154.20	1.788	2.722	55.0
20X-5, 70–72	155.90	1.823	2.726	53.1
21X-1, 58–60	159.38	1.794	2.680	53.5
21X-2, 90–92	161.20	1.863	2.711	50.3
21X-3, 112–114	162.92	1.921	2.730	47.4
21X-4, 141–143	164.71	1.845	2.727	51.8
21X-5, 64–66	165.44	1.827	2.711	52.4
22X-1, 76–78	169.06	1.972	2.763	45.5
22X-2, 98–100	170.78	1.847	2.718	51.4
22X-3, 64–66	171.94	1.815	2.704	52.9
22X-4, 42–44	173.22	1.808	2.688	52.9
22X-5, 102–104	175.32	1.847	2.643	49.2
22X-6, 22–24	176.02	1.808	2.702	53.3
23X-1, 74–76	178.64	1.726	2.642	56.6
23X-2, 74–76	180.14	1.753	2.707	56.7
23X-3, 74–76	181.64	1.763	2.729	56.6
23X-4, 74–76	183.14	1.714	2.636	57.2
23X-5, 74–76	184.64	1.759	2.690	55.9
23X-6, 74–76	186.14	1.738	2.629	55.5
24X-1, 74–76	187.84	1.763	2.649	54.5
24X-2, 74–76	189.34	1.763	2.703	56.0
24X-3, 60–62	190.70	1.772	2.721	55.9
24X-3, 102–104	191.12	1.778	2.705	55.1
24X-4, 82–84	192.42	1.745	2.668	56.1
24X-5, 109–111	194.19	1.789	2.686	54.0
24X-6, 74–76	195.34	1.770	2.701	55.5
25X-1, 90–92	197.30	1.767	2.687	55.3
25X-2, 80–82	198.70	1.739	2.660	56.3
25X-2, 113–115	199.03	1.736	2.680	57.0
25X-3, 84–86	200.24	1.777	2.680	54.5
25X-4, 25–27	201.15	1.784	2.688	54.3
25X-5, 15–17	202.55	1.790	2.698	54.2
25X-5, 74–76	203.14	1.788	2.663	53.4
25X-6, 11–13	204.01	1.797	2.673	53.2
25X-7, 26–28	205.16	1.790	2.676	53.6
26X-1, 74–76	206.84	1.809	2.754	54.7
26X-2, 80–82	208.40	1.811	2.728	53.8
26X-3, 74–76	209.84	1.696	2.720	60.4
26X-4, 74–76	211.34	1.830	2.702	52.0
26X-5, 74–76	212.84	1.818	2.694	52.4
27X-1, 20–22	216.00	1.775	2.497	49.0
27X-1, 78–80	216.58	1.811	2.727	53.8
27X-2, 90–92	218.20	1.815	2.766	54.6
27X-3, 74–76	219.54	1.795	2.716	54.4
27X-4, 88–90	221.18	1.746	2.694	56.7
27X-5, 74–76	222.54	1.762	2.719	56.5
27X-6, 62–64	223.92	1.772	2.698	55.3
28X-1, 74–76	226.14	1.729	2.680	57.4
28X-2, 74–76	227.64	1.735	2.677	57.0

Core, section, interval (cm)	Depth (mbsf)	Density (g/cm³) Bulk	Grain	Porosity (%)
28X-3, 74–76	229.14	1.718	2.695	58.5
28X-4, 74–76	230.64	1.811	2.685	52.6
28X-5, 74–76	232.14	1.811	2.703	53.1
28X-6, 60–62	233.50	1.789	2.666	53.4
28X-7, 60–62	234.50	1.801	2.661	52.6
29X-1, 30–32	235.40	1.834	2.700	51.7
29X-2, 82–84	236.58	1.819	2.718	53.1
29X-3, 74–76	238.00	1.801	2.706	53.8
29X-4, 74–76	239.50	1.819	2.638	50.7
29X-5, 74–76	241.00	1.779	2.672	54.2
29X-6, 60–62	242.36	1.787	2.683	54.0
29X-7, 13–15	243.39	1.819	2.681	52.0
30X-1, 66–68	245.36	1.671	2.610	59.2
30X-2, 87–89	247.07	1.679	2.672	60.3
30X-3, 31–33	248.01	1.718	2.720	59.1
30X-4, 96–98	250.16	1.852	2.722	51.3
30X-5, 24–26	250.94	1.696	2.678	59.4
31X-1, 68–70	254.98	1.650	2.578	59.7
31X-2, 69–71	256.49	1.737	2.725	58.1
31X-3, 98–100	258.28	1.743	2.641	55.5
31X-4, 67–69	259.47	1.803	2.704	53.6
31X-5, 55–57	260.85	1.792	2.737	55.2
32X-1, 80–82	264.80	1.706	2.710	59.6
32X-2, 74–76	266.24	1.730	2.692	57.6
32X-3, 75–77	267.69	1.763	2.708	56.1
32X-4, 81–83	269.25	1.672	2.587	58.6
32X-5, 71–73	270.65	1.677	2.596	58.4
32X-6, 67–69	272.11	1.781	2.799	57.3
33X-1, 71–73	274.31	1.714	2.737	59.7
33X-2, 71–73	275.75	1.748	2.649	55.5
33X-3, 70–72	277.24	1.735	2.641	56.0
33X-4, 123–125	279.27	1.823	2.706	52.5
33X-5, 96–98	280.50	1.736	2.742	58.5
33X-6, 91–93	281.95	1.763	2.736	56.8
33X-7, 63–65	282.67	1.832	2.895	56.8
34X-1, 56–58	283.86	1.885	2.735	49.6
34X-2, 70–72	285.50	1.741	2.832	60.3
35X-1, 24–26	293.24	1.744	2.685	56.6
35X-2, 14–16	294.64	1.176	1.261	35.8
35X-3, 55–57	296.58	1.772	2.770	57.2
35X-4, 21–23	297.74	1.842	2.795	53.8
35X-5, 83–85	299.86	1.770	2.785	57.6
35X-6, 80–82	301.33	2.066	3.247	53.1
35X-7, 46–48	301.89	1.915	2.622	44.3
36X-2, 74–76	304.84	1.999	2.704	42.0
36X-3, 22–24	305.82	1.625	2.735	64.9
36X-4, 114–116	308.24	1.821	2.763	54.1
36X-5, 36–38	308.96	1.787	2.689	54.2
36X-6, 68–70	310.78	1.749	2.688	56.4
36X-7, 41–43	311.45	1.759	2.620	53.9
37X-1, 52–54	312.72	1.756	2.620	54.1
37X-2, 30–32	314.00	1.786	2.638	52.8
38X-1, 65–67	322.55	1.822	2.723	53.0
38X-2, 48–50	323.88	1.805	2.699	53.4
38X-3, 60–62	325.50	1.842	2.760	52.9
38X-4, 74–76	327.14	1.888	2.758	50.2
38X-5, 74–76	328.64	1.859	2.750	51.6
38X-6, 102–104	330.42	1.891	2.778	50.6
38X-7, 15–17	330.77	1.819	2.717	53.1
39X-1, 44–45	331.94	1.839	2.784	53.7
204-1244E-				
1H-1, 57–59	0.57	1.554	2.681	68.0
1H-1, 119–121	1.19	1.554	2.627	67.0
1H-2, 12–14	1.62	1.596	2.637	64.5
1H-2, 56–58	2.06	1.583	2.640	65.4
1H-2, 118–120	2.68	1.608	2.662	64.4
1H-3, 19–21	3.19	1.639	2.777	65.0
1H-3, 65–67	3.65	1.659	2.843	65.1

Table T15 (continued).

Core, section, interval (cm)	Depth (mbsf)	Density (g/cm³) Bulk	Grain	Porosity (%)
1H-3, 123–125	4.23	1.662	2.692	61.8
1H-4, 9–11	4.59	1.658	2.741	63.1
1H-4, 58–60	5.08	1.690	2.790	62.3
1H-4, 119–121	5.69	1.685	2.784	62.4
1H-5, 20–22	6.20	1.658	2.713	62.5
1H-5, 67–69	6.67	1.679	2.744	61.9
1H-5, 118–120	7.18	1.676	2.710	61.3
1H-6, 36–38	7.86	1.689	2.720	60.8
2H-1, 35–37	9.05	1.659	2.750	63.2
2H-1, 87–89	9.57	1.627	2.704	64.1
2H-2, 22–24	10.42	1.673	2.741	62.2
2H-2, 66–68	10.86	1.676	2.737	61.9
2H-2, 115–117	11.35	1.689	2.748	61.4
2H-3, 19–21	11.89	1.663	2.728	62.5
2H-3, 65–67	12.35	1.657	2.750	63.4
6P-1, 14–16	39.34	1.666	2.693	61.5
6P-1, 48–50	39.68	1.662	2.738	62.8
6P-1, 83–85	40.03	1.673	2.686	60.9
11P-1, 11–13	71.71	1.576	2.592	64.8
11P-1, 40–42	72.00	1.643	2.801	65.2
11P-1, 74–76	72.34	1.674	2.736	62.0
18H-1, 62–64	123.72	1.722	2.668	57.5
18H-2, 74–76	125.34	1.762	2.712	56.3
18H-3, 44–46	126.54	1.773	2.725	55.9
18H-4, 50–52	127.35	1.735	2.721	58.1
18H-5, 60–62	128.95	1.725	2.657	57.1
18H-6, 84–86	130.69	1.746	2.692	56.8
18H-7, 40–42	131.75	1.786	2.801	57.1
19H-1, 74–76	132.94	1.780	2.822	58.0
19H-2, 80–82	134.50	1.716	2.673	58.1
19H-3, 80–82	136.00	1.748	2.711	57.1
19H-4, 74–76	137.44	1.781	2.751	56.2
19H-5, 40–42	138.60	1.794	2.775	56.0
19H-6, 74–76	140.44	1.741	2.695	57.1

Table T16. Compressional wave velocity measurements, Holes 1244A, 1244B, 1244C, and 1244E.

Core, section, interval (cm)	Depth (mbsf)	PWS1	PWS2	PWS3
204-1244A-				
1H-2, 80.5	2.31			1559
1H-4, 77.2	5.27			1564
1H-6, 77.4	8.27			1578
204-1244B-				
1H-1, 30.4	0.30			1553
1H-1, 65.6	0.66			1591
1H-1, 89.7	0.90			1538
1H-2, 64.4	2.14			1535
1H-3, 68.5	3.68			1547
1H-4, 69.9	5.20			1552
2H-1, 70.5	7.30			1567
2H-2, 79.1	8.89			1560
2H-3, 80.8	10.41			1582
2H-4, 70.2	11.80			1531
204-1244C-				
1H-3, 14.1	3.14			1551
1H-4, 20.5	4.70			1559
2H-1, 21.1	5.71			1563
2H-2, 27.5	7.28			1560
2H-3, 27.4	8.77			1576
2H-4, 28.9	10.29			1599
204-1244E-				
1H-1, 70.6	0.71			1520
1H-1, 71.2	0.71	1501		
1H-1, 71.5	0.72		1501	
1H-1, 133.1	1.33		1506	
1H-1, 133.3	1.33			1507
1H-1, 133.5	1.34	1500		
1H-2, 25.5	1.76			1512
1H-2, 26	1.76		1520	
1H-2, 26.3	1.76	1510		
1H-2, 69.3	2.19			1508
1H-2, 69.5	2.20	1514		
1H-2, 70.3	2.20		1526	
1H-2, 132.9	2.83			1517
1H-2, 133.1	2.83		1538	
1H-2, 133.3	2.83	1517		

Core, section, interval (cm)	Depth (mbsf)	PWS1	PWS2	PWS3
1H-3, 32.4	3.32			1521
1H-3, 33	3.33	1519		
1H-3, 33.1	3.33		1520	
1H-3, 78.2	3.78			1516
1H-3, 79.1	3.79	1521		
1H-3, 79.2	3.79		1544	
1H-3, 136.9	4.37		1543	
1H-3, 137.2	4.37	1528		
1H-3, 137.5	4.38			1521
1H-4, 21.2	4.71			1517
1H-4, 21.8	4.72	1527		
1H-4, 22.2	4.72		1543	
1H-4, 70.8	5.21			1518
1H-4, 71.4	5.21		1545	
1H-4, 72.2	5.22	1534		
1H-4, 131.2	5.81			1536
1H-4, 131.3	5.81	1529		
1H-4, 131.7	5.82		1539	
1H-5, 32.5	6.33			1524
1H-5, 33	6.33	1525		
1H-5, 33.6	6.34		1541	
1H-5, 81.2	6.81			1535
1H-5, 81.4	6.81		1544	
1H-5, 82	6.82	1532		
1H-5, 132.2	7.32		1557	
1H-5, 132.3	7.32	1531		
1H-5, 132.6	7.33			1532
1H-6, 49.3	7.99			1546
1H-6, 49.6	8.00	1535		
1H-6, 50.1	8.00		1556	
2H-1, 47	9.17			1536
2H-1, 47.6	9.18		1537	
2H-1, 100.6	9.71			1544
2H-2, 33.2	10.53			1558
2H-2, 78.7	10.99			1562
2H-2, 127.3	11.47			1564
2H-3, 31.6	12.02			1560
2H-3, 78.7	12.49			1544

Table T17. Thermal conductivity, Holes 1244A, 1244B, 1244C, and 1244E.

Core, section, interval (cm)	Depth (mbsf)	Thermal conductivity (W/[m·K])	Individual measurements (W/[m·K])		
204-1244A-					
1H-1, 75	0.75	0.967	0.943	0.982	0.977
1H-2, 75	2.25	0.998	1.011	1.002	0.980
1H-3, 75	3.75	0.995	0.976	1.005	1.005
204-1244B-					
1H-3, 75	3.75	0.994	1.026	0.984	0.971
2H-3, 75	10.35	1.009	1.006	0.992	1.028
2H-5, 75	13.35	0.946	0.943	0.962	0.934
3H-3, 75	19.85	0.915	0.921	0.907	0.916
3H-5, 75	22.85	0.981	0.993	0.977	0.972
4H-2, 75	26.53	0.889	0.885	0.906	0.877
4H-4, 75	29.53	0.888	0.907	0.878	0.879
4H-6, 75	32.53	0.884	0.909	0.863	0.880
5H-3, 45	37.56	0.941	0.931	0.939	0.952
5H-5, 75	40.86	0.985	1.023	0.966	0.966
6H-3, 85	46.28	0.997	1.015	0.976	1.001
204-1244C-					
4H-1, 75	25.25	1.002	1.002	1.018	0.985
4H-3, 75	28.25	0.854	0.867	0.859	0.837
4H-5, 75	31.25	1.008	0.992	1.023	1.008
5H-1, 65	34.65	1.031	1.039	1.031	1.024
5H-3, 75	37.75	0.992	0.997	0.969	1.010
5H-5, 75	40.75	0.855	0.859	0.853	0.853
6H-3, 75	47.25	0.876	0.890	0.871	0.868
7H-2, 75	54.19	0.768	0.754	0.774	0.775
7H-4, 100	57.44	0.794	0.800	0.790	0.792
7H-6, 75	59.87	0.919	0.913	0.928	0.917
8H-3, 75	65.27	0.888	0.896	0.898	0.870
9H-1, 65	72.65	0.893	0.889	0.898	0.891
9H-3, 75	75.75	0.985	0.990	0.985	0.980
9H-5, 75	78.75	0.972	0.973	0.977	0.967
10H-3, 95	84.98	0.992	1.036	0.964	0.977
11H-3, 75	93.98	0.982	0.984	0.971	0.991
12H-3, 70	104.20	0.948	0.932	0.949	0.964
12H-5, 74	107.24	0.927	0.941	0.914	0.927
13H-3, 74	113.74	0.955	0.950	0.978	0.937
15H-3, 75	124.75	0.996	1.015	0.978	0.994
19X-5, 50	149.50	0.973	0.970	0.957	0.991
20X-1, 70	149.90	0.906	0.937	0.885	0.895
20X-3, 75	152.95	1.016	1.014	1.024	1.010
20X-5, 75	155.95	1.026	1.026	1.035	1.017
21X-3, 75	162.55	1.115	1.091	1.125	1.130
22X-3, 75	172.05	1.027	1.028	1.025	1.029
22X-5, 75	175.05	0.957	0.963	0.948	0.960
23X-3, 75	181.65	1.018	1.043	1.025	0.985
24X-3, 75	190.85	1.019	1.004	1.032	1.022

Core, section, interval (cm)	Depth (mbsf)	Thermal conductivity (W/[m·K])	Individual measurements (W/[m·K])		
24X-5, 75	193.85	0.962	0.969	0.958	0.960
25X-3, 75	200.15	1.002	1.004	1.004	0.997
26X-3, 75	209.85	0.940	0.948	0.943	0.930
27X-3, 75	219.55	1.100	1.133	1.102	1.065
28X-3, 75	229.15	0.967	0.966	0.973	0.961
29X-3, 75	238.01	1.007	0.998	1.005	1.019
30X-3, 75	248.45	0.868	0.864	0.864	0.877
31X-3, 65	257.95	0.879	0.861	0.885	0.892
32X-3, 75	267.69	0.910	0.922	0.904	0.903
33X-3, 73	277.27	1.006	1.004	1.008	1.007
34X-3, 75	287.05	0.888	0.892	0.887	0.884
35X-3, 35	296.38	0.640	0.650	0.644	0.626
36X-3, 75	306.35	0.773	0.789	0.776	0.754
37X-1, 75	312.95	0.956	1.009	0.920	0.938
38X-3, 75	325.65	0.781	0.800	0.774	0.768
204-1244E-					
1H-1, 75	0.75	0.983	1.022	0.962	0.965
1H-3, 75	3.75	1.045	1.050	1.022	1.063
1H-5, 75	6.75	1.091	1.113	1.087	1.074
2H-3, 75	12.45	0.968	0.950	0.970	0.983
4H-3, 75	23.95	0.954	0.964	0.961	0.936
5H-1, 75	30.45	0.954	0.972	0.935	0.956
5H-3, 86	33.51	0.902	0.913	0.900	0.894
5H-6, 60	37.75	0.871	0.872	0.901	0.841
7H-1, 113	42.33	0.994	0.996	0.978	1.007
7H-3, 74	44.94	0.967	0.975	0.956	0.971
7H-5, 25	47.45	0.985	0.993	0.978	0.985
9H-1, 75	53.35	0.936	0.942	0.939	0.927
9H-3, 52	56.12	0.951	0.947	0.936	0.969
9H-5, 46	58.62	0.933	0.961	0.920	0.919
10H-3, 75	65.85	0.905	0.916	0.921	0.878
12H-3, 75	76.45	0.976	0.992	0.959	0.978
13H-1, 100	84.10	1.024	1.029	1.043	1.001
13H-3, 106	86.46	0.976	0.978	0.987	0.963
13H-6, 57	90.47	0.94	0.925	0.960	0.936
14H-3, 41	95.53	0.977	0.962	1.009	0.959
14H-5, 35	98.47	1.021	1.043	1.005	1.016
16H-7, 45	112.62	0.991	0.995	1.004	0.975
17H-3, 70	117.30	0.991	1.000	0.976	0.997
17H-5, 72	120.32	0.952	0.953	0.954	0.950
17H-6, 60	121.70	0.926	0.929	0.931	0.919
18H-4, 50	127.35	0.937	0.959	0.895	0.958
19H-1, 48	132.68	1.015	1.015	1.024	1.005
19H-3, 75	135.95	1.013	1.029	1.030	0.981
19H-6, 83	140.53	1.009	0.991	1.022	1.013

Table T18. Shear strength values, Holes 1244B, 1244C, and 1244E.

Core, section, interval (cm)	Depth (mbsf)	Torvane (kPa)	Torvane size	ASV (kPa)
204-1244B-				
1H-2, 70	2.20	24	M	
204-1244C-				
1H-3, 19	3.19	31	M	
10H-5, 35	87.38	142	S	
11H-6, 80	98.53	148	S	
12H-6, 98	108.98	150	S	
13H-5, 83	116.83	135	S	
13H-6, 30	117.80	118	S	
15H-3, 54	124.54	120	S	
15H-3, 130	125.30	58	S	
15H-4, 100	126.50	100	S	
15H-5, 10	127.10	63	S	
15H-5, 55	127.55	43	S	
15H-6, 40	128.90	158	S	
19H-1, 32	143.32	35	S	
19H-3, 85	146.85	87	S	
20H-1, 44	149.64	23	S	
20H-2, 53	151.23	78	S	
20H-4, 22	153.92	135	S	
204-1244E-				
1H-1, 132	1.32	28	M	
1H-1, 142	1.42			37
1H-2, 28	1.78	28	M	
1H-2, 35	1.85			25
1H-2, 37	1.87			20
1H-2, 69	2.19	32	M	
1H-2, 78	2.28			22
1H-2, 129	2.79	33	M	
1H-2, 140	2.90			25
1H-3, 33	3.33	41	M	
1H-3, 79	3.79	42	M	
1H-3, 136	4.36	55	M	
1H-4, 23	4.73	45	M	
1H-4, 71	5.21	41	M	
1H-4, 80	5.30			48
1H-4, 126	5.76	53	M	
1H-5, 14	6.14	56	M	
1H-5, 49	6.49	68	M	
1H-5, 76	6.76	63	M	
1H-5, 126	7.26	61	M	
2H-1, 41	9.11	50	M	
2H-1, 94	9.64	53	M	
2H-2, 31	10.51	55	M	
2H-2, 71	10.91	59	M	
2H-3, 70	12.40	43	M	
2H-4, 22	13.42	50	M	
2H-4, 139	14.59	71	M	

Notes: AVS = automated shear vane. M = medium, S = small.

Table T19. Temperature measurements, Holes 1245B, 1245C, and 1245E.

Site, hole, core	Depth (mbsf)	Temperature (°C)	Thermal conductivity (W/[m·K])	Tool ID
204-1244B-				
4H	35.1	6.15	0.88	12
204-1244C-				
7H	62.5	7.77	0.97	12
9H	81.5	9.13	0.92	12
12H	110.0	10.71	0.93	12
7H–8H	62.5	9.00	—	3
19X–20X	149.4	13.02	—	3
204-1244E-				
1H	00.0	3.76	1.20	11
5H	39.2	5.85	0.87	11
7H	50.7	6.39	0.99	11
9H	62.1	7.48	0.93	11
13H	92.6	9.21	0.94	11
17H	123.1	11.03	0.93	11
8Y–9H	52.6	7.04	—	2
19X–BOH	140.7	12.56	—	2

Notes: For measurements made with the APCT, the tool was at the core catcher of the core barrel for the core cited. DVTPP measurements were made in between the two cores cited. Temperatures represent the equilibrium temperature determined, as discussed in "Thermal Conductivity," p. 31, in "Physical Properties" in the "Explanatory Notes" chapter, assuming the thermal conductivity given in the table, which is the average of the nine measurements taken in the adjacent core. No thermal conductivity values are given for the DVTPP data because in situ temperatures were measured directly from the data after the tool had been in the formation for at least 30 min and equilibrium appeared to have been reached. BOH = bottom of hole. ID = identification.

Table T20. Results from degassing experiments, Holes 1244C, 1244E, and 1244F.

Core	Depth (m) Top	Depth (m) Bottom	Run time (min)	Total volume (mL)*	Volume (mL)[†] $O_2 + N_2$	C_1	CO_2	C_{2+}	Concentration (%)[‡] $O_2 + N_2$	C_1	CO_2	C_{2+}	Core length (m)	Porosity (%)	C_1 (mM)**
204-1244C-															
14P	119.5	120.5	495	1795	597.0	1191.9	6.0	NA	33.3	66.4	0.3	NA	1.00	58	57.8
16P	130.5	131.5	1230	1785	528.3	1250.5	5.4	NA	29.6	70.1	0.3	NA	0.85–1.00	57	62.3–73.3
18P	141.5	142.5	2348	2130	211.0	1917.7	1.4	0.20	9.9	90.0	0.1	0.009	1.00	56	97.7
204-1244E-															
6P	39.2	40.2	1872	945	55.8	888.3	0.9	0.01	5.9	94.0	0.1	0.001	0.96–1.00	62	39.9–41.6
11P	71.6	72.6	2999	4530	61.8	4465.2	3.0	0.08	1.4	98.6	0.1	0.002	0.92–1.00	61	203.5–221.2
15P	102.1	103.1	995	3310	868.1	2440.0	1.8	0.00	26.2	73.7	0.1	0.000	0.94–1.00	59	117.5–125.0
204-1244F-															
4P	23.1	24.1	450	595	53.0	538.8	3.2	0.01	8.9	90.6	0.5	0.002	0.89–1.00	63	23.7–26.6

Notes: * = volume of gas released. † = volume of components released. ‡ = percent of components in released gas. ** = calculated concentration in situ. Core length is reported as measured after the core was degassed and split (i.e., curated length) and as cored in subsurface. In Cores 204-1244C-14P and 16P, the value reported as C_1 includes C_1 and C_{2+} hydrocarbon gases. NA = not analyzed.

Table T21. HYACINTH pressure coring summary, Hole 1244E.

Core	Deployment number	Date (Aug 2002)	Local time (hr)	Depth			Lithology	Core recovered (cm)	Pressure (bar)	Comments
				Water (mbsl)	Core (mbsf)	BSR (mbsf)				
204-1244E-8Y	FPC 9	19	1310	895	50	124	Unconsolidated silty clay with disseminated hydrate?	92	92 (max)	Full pressure core obtained; small amounts of hydrate gas collected.

Note: BSR = bottom-simulating reflector. FPC = Fugro Pressure Corer.

Table T22. Conventional wireline logging operations summary, Hole 1244E.

Date (Aug 2002)	Local time (hr)	Tool depth (mbsf)	Remarks
20	0045		Last core on deck
20	1015–1200		Wiper trip up to 80 mbsf; back down to 250 mbsf
20	1200–1215		Hole displaced with sepiolite mud
20	1215–1400		Set back top drive; bottom of pipe put at 87.5 mbsf
20	1430		Start logging rig-up
20	1615		Start going down with triple combination (TAP/DIT/HLDT/APS/HNGS/QSST) tool string
20	1655	0.0	Stop 5 min at mudline for temperature calibration
20	1712	250.0	Tool at TD; start logging-up pass 1 at 900 ft/hr
20	1807	72.5	Tool back into pipe; speed up to 1500 ft/hr to log mudline
20	1815	0.0	End of pass 1
20	1830	250.0	Tool at TD; start logging-up pass 2 at 900 ft/hr
20	1900	72.5	End of pass 2; back down for checkshot survey
20	1905	250.0	Tool at TD for QSST checkshot survey
20	1910	250.0	End of QSST; start moving up at 1800 ft/hr
20	2010		Tool back on rig floor
20	2115		Finish rig-down
20	2115		Start logging rig-up
20	2215		Start going down with the FMS-sonic (FMS/DSI/SGT) tool string
20	2255	250.0	Tool at TD; start logging-up pass at 900 ft/hr
20	2330	72.5	Tool back into pipe; end of pass 1
20	2355	250.0	Tool at TD; start logging-up pass 2 at 900 ft/hr
21	0030	72.5	End of pass 2; speed up tool to 6000 ft/hr
21	0100		Tool back on rig floor
21	0145		Finish rig-down

Notes: TD = total depth. See Table T8, p. 102, in the "Explanatory Notes" chapter for definitions of acronyms.